10/11/29/91 JSD

SANDIA REPORT

SAND88—2730 • UC—814
Unlimited Release
Printed October 1991

Yucca Mountain Site Characterization Project

TOSPAC Calculations in Support of the COVE 2A Benchmarking Activity

John H. Gauthier, Nalini B. Zieman, Warren B. Miller

Prepared by
Sandia National Laboratories
Albuquerque, New Mexico 87185 and Livermore, California 94550
for the United States Department of Energy
under Contract DE-AC04-76DP00789

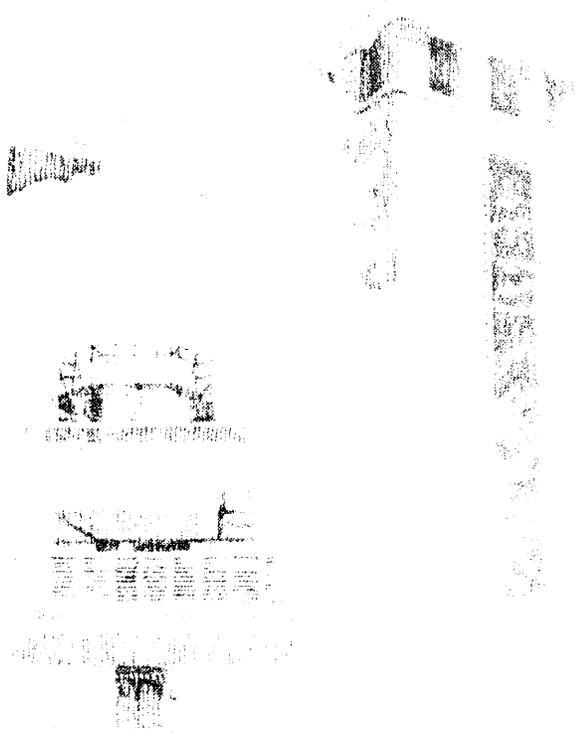

"Prepared by Yucca Mountain Site Characterization Project (YMSCP) participants as part of the Civilian Radioactive Waste Management Program (CRWM). The YMSCP is managed by the Yucca Mountain Project Office of the U.S. Department of Energy, DOE Field Office, Nevada (DOE/NV). YMSCP work is sponsored by the Office of Geologic Repositories (OGR) of the DOE Office of Civilian Radioactive Waste Management (OCRWM)."

Issued by Sandia National Laboratories, operated for the United States Department of Energy by Sandia Corporation.

Available to DOE and DOE contractors from
Office of Scientific and Technical Information
PO Box 62
Oak Ridge, TN 37831

Prices available from (615) 576-8401, FTS 626-8401

Available to the public from
National Technical Information Service
US Department of Commerce
5285 Port Royal Rd
Springfield, VA 22161

NTIS price codes
Printed copy: A10
Microfiche copy: A01

SAND--88-2730

DE92 003588

SAND88-2730
Unlimited Release
Printed October 1991

TOSPAC Calculations in Support of the COVE 2A Benchmarking Activity

John H. Gauthier
Nalini B. Zieman

SPECTRA Research Institute
Albuquerque, New Mexico

Warren B. Miller

Sandia National Laboratories
Albuquerque, New Mexico

Abstract

The purpose of the Code Verification (COVE) 2A benchmarking activity is to assess the numerical accuracy of several computer programs for the Yucca Mountain Site Characterization Project of the Department of Energy. This paper presents a brief description of the computer program TOSPAC and a discussion of the calculational effort and results generated by TOSPAC for the COVE 2A problem set. The calculations were performed twice. The initial calculations provided preliminary results for comparison with the results from other COVE 2A participants. TOSPAC was modified in response to the comparison and the final calculations included a correction and several enhancements to improve efficiency.

The work described in this report was performed for the
Yucca Mountain Site Characterization Project
under WBS 1.2.1.4.9.

Acknowledgments

The authors would like to thank Ralph Peters for his help in initially interpreting the TOSPAC results and Michael Wilson for his help in modifying the DYNAMICS module of TOSPAC and his formulation of equations for the mesh spacing and time step.

CONTENTS

TABLES

FIGURES

FIGURES
(continued)

FIGURES
(continued)

FIGURES
(continued)

FIGURES
(continued)

FIGURES
(continued)

FIGURES
(continued)

FIGURES
(continued)

FIGURES
(continued)

FIGURES
(continued)

FIGURES
(continued)

FIGURES
(continued)

FIGURES
(continued)

FIGURES
(concluded)

NUMBERING CONVENTION FOR THE FIGURES

The figures are placed after the text and are numbered as follows.

1) The first digit in the figure number is either 1, indicating the initial set of calculations, or 2, indicating the final set of calculations.

2) After a dash, the second digit, or set of digits, indicates the case number. Because steady-state plots contain 3 cases, they are indicated by a series of digits, either 1/3/5, for Cases 1, 3, and 5, or 2/4/6, for Cases 2, 4, and 6. Transient-flow cases are indicated by a single digit, either 7, 8, 9, 10, 11, or 12.

3) After a dash, the third digit is an ordinal number for the figure in its calculation set and case.

For example, Figure 1-1/3/5-6 refers to the initial set of calculations, the steady-state Cases 1, 3, and 5, and the sixth figure in this group. Figure 2-7-5 is the fifth figure for the transient-flow Case 7 of the final set of calculations.

The only exceptions to the above numbering scheme are Figures 1-1 and 2-1. They are illustrations of the calculational mesh and problem geometry for the initial and final sets of calculations, respectively.

1.0 INTRODUCTION

1.1 The COVE 2A Activity

The Yucca Mountain Site Characterization Project (YMP) of the U. S. Department of Energy (DOE) is investigating the geologic formations in the unsaturated zone at Yucca Mountain, Nevada, as the site of a potential repository for high-level radioactive waste.

To assess the long-term safety issues associated with such a potential repository, computer programs are used to model present and possible future groundwater-flow systems to predict the movement of water and radionuclides through the geologic media. The numerical accuracy and physical validity of such programs must be demonstrated for the types of geologic conditions they are used to model, as specified in 10 CFR 60 (60.21 and 60.101) (NRC, 1986) and NUREG-0856 (II.D) (Silling, 1983).

Benchmarking is the comparison of numerical solutions generated by different but equivalent computer programs. It is a method of demonstrating the numerical accuracy of these programs, particularly when modeling complex systems.

This report deals with the Code Verification (COVE) benchmarking effort, one of a series of problems being defined to compare and evaluate the flow-and-transport computer programs that may be used for Yucca Mountain performance-assessment calculations in support of a license application. COVE 2A only addresses hydrology. The COVE 2A activity is defined in *Benchmarking of Flow and Transport Codes: COVE 2A—Yucca Mountain Hydrology*, YMP Problem Definition Memo 72-6, Sandia National Laboratories, Albuquerque, New Mexico, 10 January 1986. The major purpose of the COVE 2A effort is to test the capabilities of hydrologic programs on isothermal problems that are representative of the conditions expected at Yucca Mountain.

This report presents a description of the calculational effort and the results obtained by applying the computer program TOSPAC (Dudley et al., 1988) to the COVE 2A problems.

1.2 The COVE 2A Problem Set

The COVE 2A problem set has been selected to investigate the ability of the programs being benchmarked to accurately model water flow in a partially saturated regime. Table 1-1 presents the 12 cases of the COVE 2A problem set.

TABLE 1-1
THE COVE 2A PROBLEM SET

Case	Flux at Ground Surface(mm/yr)	Calico Hills (CHn) Property	Time Domain
1	0.1	zeolitic	steady
2	0.1	vitric	steady
3	0.5	zeolitic	steady
4	0.5	vitric	steady
5	4.0	zeolitic	steady
6	4.0	vitric	steady
7	0.1 → 0.2	zeolitic	nonsteady
8	0.1 → 0.2	vitric	nonsteady
9	0.5 → 1.0	zeolitic	nonsteady
10	0.5 → 1.0	vitric	nonsteady
11	4.0 → 8.0	zeolitic	nonsteady
12	4.0 → 8.0	vitric	nonsteady

The problems examine one-dimensional, vertical, isothermal flow through a stratigraphy of five fractured materials. The stratigraphy is a simplified representation of drill hole USW G-4 at Yucca Mountain (Ortiz et al., 1985). The stratigraphy is presented in Figure 1-1 and repeated in Figure 2-1.

Sensitivity of the numerical solution techniques to sharp contacts between materials with very different hydrologic characteristics is investigated by comparing calculations that use the properties of either the zeolitized Calico Hills Unit (CHnz) or the vitrified Calico Hills Unit (CHnv). At USW G-4, the Calico Hills Unit is primarily zeolitized.

The media through which flow occurs are described with a composite-porosity model (Peters and Klavetter, 1988). Hydrologic properties are specified by saturation and hydraulic-conductivity characteristic curves. These curves are defined according to a method derived by Mualem (1976) and applied in a form developed by van Genuchten (1980). Hydrologic properties are defined separately for the matrix and the fractures; the bulk properties are calculated as the area-weighted average of the two. Table 1-2 presents the hydrologic properties assigned to the various geologic units in the COVE 2A stratigraphy.

The hydrologic cases are defined for both steady and nonsteady flow. The range of fluxes prescribed at the ground surface has been selected to simulate different combinations of matrix and fracture flow. A flux of 0.1 mm/yr (Cases 1 and 2) should produce flow predominantly in the matrix; 4 mm/yr (Cases 5 and 6) should produce flow predominantly in the fractures. The 0.5 mm/yr flux (Cases 3 and 4) is close to the transition between matrix and fracture flow in most of the geohydrologic units. The 0.5 to 1 mm/yr transient-flow cases (Cases 9 and 10) cross from predominantly matrix flow to

TABLE 1-2

HYDROLOGIC PROPERTIES USED FOR THE COVE 2A CALCULATIONS

Matrix Properties

Unit	Sample Code	Grain Density (g/cm^3)	Porosity n_m	Hydraulic Conductivity $K_{m,h}$ (m/s)	Residual Saturation S_r	van Genuchten Parameters α (10^{-2}/m)	β
TCw	G4-1	2.49	0.08	9.7×10^{-12}	0.002	0.821	1.558
PTn	GU3-7	2.35	0.40	3.9×10^{-07}	0.100	1.50	6.872
TSw1	G4-6	2.58	0.11	1.9×10^{-11}	0.080	0.567	1.798
TSw2-3	G4-6	2.58	0.11	1.9×10^{-11}	0.080	0.567	1.798
CHnv	GU3-14	2.37	0.46	2.7×10^{-07}	0.041	1.60	3.872
CHnz	G4-11	2.23	0.28	2.0×10^{-11}	0.110	0.308	1.602

Fracture Properties

Unit	Sample Code	Horizontal Stress (bars)	Fracture Aperture (μm)	Fracture Conductivity (10^{-5}m/s)	Fracture Density (No./m^3)	Fracture Porosity n_f (10^{-5})	Fracture Compressibility $\partial n_f/\partial\sigma'$ (10^{-8}/m)	Bulk Fracture Conductivity $K_{f,b}$ (10^{-9}m/s)
TCw	G4-2F	1.1	6.74	3.8	20	14.	132.	5.3
PTn	G4-3F	3.3	27.0	61.	1	2.7	19.	16.
TSw1	G4-2F	9.5	5.13	2.2	8	4.1	5.6	0.90
TSw2-3	G4-2F	21.9	4.55	1.7	40	18.	12.	3.1
CHnv	G4-4F	34.3	15.5	20.	3	4.6	2.8	9.2
CHnz	G4-4F	34.3	15.5	20.	3	4.6	2.8	9.2

Fracture-saturation coefficients are $S_r = 0.0395$, $\alpha = 1.2851$/m, and $\beta = 4.23$.

Bulk-Rock Compressibilities

Unit	TCw	PTn	TSw1	TSw2-3	CHnv	CHnz
Coefficient of Consolidation α'_{bulk} (10^{-7}/m)	6.2	82.	12.	5.8	39.	26.

The compressibility of water (β'_w) is 9.8×10^{-7}/m.

predominantly fracture flow. The other nonsteady cases examine transient flow predominantly in the matrix (Cases 7 and 8) or in the fractures (Cases 11 and 12).

The physical constants used by TOSPAC for the COVE 2A calculations are presented in Table 1-3.

TABLE 1-3
PHYSICAL CONSTANTS USED BY TOSPAC FOR THE COVE 2A CALCULATIONS

Acceleration Resulting from Gravity	9.8 m/s^2
Density of Water	(implicit in β'_w)
Viscosity of Water	(implicit in the characteristic curves)
Seconds per Year	3.15576×10^7
Days per Year	365.25

Problem Definition Memo 72-6 requires that results be generated at a number of specified problem times and 75 specified elevations so that results from different participants can be compared. The Problem Definition Memo does not specify a flow model, a solution technique, or parameters associated with a solution technique: time step, the degree of implicitness in the equations, mesh-point spacing, etc., are left to the discretion of the participant.

1.3 Two Sets of Calculations

The COVE 2A problem set was taken from a number of problems that TOSPAC had already solved. TOSPAC was being developed at the time and was primarily being used to better understand the highly nonlinear differential equations that model flow in an unsaturated regime. When the COVE 2A benchmarking activity began, the algorithms within TOSPAC were becoming finalized. TOSPAC was included in COVE 2A, not to determine if it could perform the calculations, but to measure its accuracy and efficiency with respect to other programs.

After the COVE 2A participants performed the calculations, it was discovered that the TOSPAC calculations could be improved in several areas. First, an error existed in the calculation of the water velocity in the fractures. Second, the transient-flow calculation was marginally stable, resulting in long computer run times for the transient-flow solver (the DYNAMICS module) when compared with some of the other participating programs. Finally, work on another project led to analytic formulas for selecting appropriate mesh-point spacings and time steps. The formulas indicated that the mesh spacings

used in the transient-flow calculations were too large to guarantee accuracy. The formulas also indicated that, if the calculations were more stable, the time steps could have been longer and still preserved accuracy.

The TOSPAC hydrology modules were modified to correct the water velocity error and improve efficiency. The input data files were modified to incorporate a new calculational mesh. The COVE 2A problems, still as originally defined, were then recalculated. The first set of calculations is described in Section 3, and the second set of calculations is described in Section 4.

2.0 TOSPAC

2.1 General Description

TOSPAC is a computer program that models partially saturated groundwater flow with the transport of contaminants. TOSPAC is an acronym for the "Total Systems Performance Assessment Code." The program was written at Sandia National Laboratories for the Nevada Nuclear Waste Storage Investigations project, the predecessor to the YMP.

TOSPAC includes three calculational modules: a steady-state-flow solver (STEADY) that solves Darcy's law; a transient-flow solver (DYNAMICS) that solves Richards' Equation; and a transport solver (TRANS) that solves a general advection/dispersion equation.

All three calculational modules of TOSPAC configure the differential equations as boundary value problems. All three modules use the finite-difference method on an Eulerian mesh. The hydrology modules, STEADY and DYNAMICS, solve for pressure head, with hydraulic conductivity and water storage capacity (capacitance) specified as functions of pressure head. The transport module solves for contaminant concentration. TRANS uses the average linear water velocity and saturation results from STEADY as the hydrologic background for transport.

The STEADY and DYNAMICS modules were designed to handle site-scale problems involving flow through partially saturated, fractured, stratified media. DYNAMICS allows boundary conditions to change with time.

TRANS was designed to handle transport of multiple, decaying contaminants (e.g., radionuclides) with the matrix and fractures coupled. Contaminants can be introduced at a boundary or at an internal source region, and time-dependent transport boundary conditions are allowed. Solubility-dominated or congruent-leach source terms can be specified. Adsorption and precipitation of contaminants are modeled. TRANS computes both the amount of contaminants that cross problem boundaries and, if the contaminant decays, the actual amount that is outside problem boundaries at a given time (i.e., TRANS continues to compute decay and generation of daughter products of the departed contaminant).

In the interest of efficiency, and in the absence of some basic physics, TOSPAC incorporates simplifying assumptions. First, TOSPAC does not handle temperature effects, hysteresis effects, two-phase flow, or colloidal transport. At present only one-dimensional, vertical problems can be solved (a version of TOSPAC that solves problems with arbitrary flow paths exists, but has not been fully tested), and transport is only simulated

with steady-state-flow fields. Also, the composite-porosity model used by TOSPAC assumes that the pressure heads in the matrix and the fractures are equal. This condition is not valid for all transient flow conditions; however, it is valid for many problems (Dudley et al., 1988).

The mathematical and physical bases of TOSPAC are described by Dudley et al. (1988). A user's manual, *Total System Performance Assessment Code (TOSPAC) Volume 2: User's Guide*, SAND85-0004, by J.H. Gauthier, M.L. Wilson, R.R. Peters, and A.L. Dudley, is in preparation. A compendium of analyses using TOSPAC for the YMP is reported by Peters (1988).

The TRANS module in TOSPAC was not used in the COVE 2A project and is not discussed further in this report. Dudley et al. (1988) provide more information about this module.

2.2 Governing Equations

The STEADY module in TOSPAC solves the divergence of Darcy's law, which is equivalent to the conservation-of-mass formulation:

$$0 = -\nabla \cdot \mathbf{q} - \beta'_w \nabla\psi \cdot \mathbf{q}$$

$$- K\frac{\partial^2\psi}{\partial z^2} + \left(\frac{\partial K}{\partial z} + \beta'_w K\frac{\partial\psi}{\partial z}\right)\left(\frac{\partial\psi}{\partial z} + 1\right) , \qquad (1)$$

where $\mathbf{q}$ is the flux (also known as the Darcy velocity or specific discharge), β'_w the water-compressibility coefficient, ψ the pressure head, K the hydraulic conductivity, and z is the elevation above the water table.

The water-compressibility coefficient is defined by Peters and Klavetter (1988) as the following:

$$\beta'_w = \frac{1}{\rho}\left(\frac{\partial\rho}{\partial\psi}\right) , \qquad (2)$$

where ρ is the density of water. (For the initial calculations of the steady-state cases, β'_w was 0; i.e., the effect of water compressibility on the hydraulic conductivity was not considered. For the initial calculations of the transient-flow cases, β'_w was specified in the water-storage-capacity coefficient C, defined in Equation 5, but again, not in the

hydraulic conductivity. For the final calculations, β'_w was specified in both the water-storage capacity coefficient and the hydraulic-conductivity term.)

The hydraulic conductivity is calculated as a function of pressure head as follows (van Genuchten, 1980):

$$K(\psi) = K_s(1 + |\alpha\psi|^{\beta})^{-\frac{\lambda}{2}}\left(1 - \left[\frac{|\alpha\psi|^{\beta}}{1 + |\alpha\psi|^{\beta}}\right]^{\lambda}\right)^2 , \tag{3}$$

where K_s is the hydraulic conductivity at saturation, α and β are curve-fit parameters, and λ is $1 - 1/\beta$.

The DYNAMICS module in TOSPAC solves a generalization of Richards' equation, written as follows:

$$C\frac{\partial\psi}{\partial t} = K\frac{\partial^2\psi}{\partial z^2} + \left(\frac{\partial K}{\partial z} + \beta'_w K\frac{\partial\psi}{\partial z}\right)\left(\frac{\partial\psi}{\partial z} + 1\right) , \tag{4}$$

where C is the water-storage-capacity coefficient and t is time. Notice that, written in this form, the right-hand side of Equation 4 is the same as the right-hand side of Equation 1. C is defined as follows (Peters and Klavetter, 1988):

$$\begin{aligned} C = {} & n_m\frac{\partial S_m}{\partial\psi} + n_f\frac{\partial S_f}{\partial\psi} + \beta'_w(S_m n_m + S_f n_f) \\ & + \alpha'_{bulk}\frac{(S_m n_m + S_f n_f)}{(n_m + n_f)}\left[S_m - n_f(S_m - S_f)\right] \\ & - \frac{\partial n_f}{\partial\sigma'}\frac{(S_m n_m + S_f n_f)}{(n_m + n_f)}(S_m - S_f) , \end{aligned} \tag{5}$$

where n is the porosity, S is the saturation, α'_{bulk} is the coefficient of consolidation of the medium, and $\partial n_f/\partial\sigma'$ is the fracture-compressibility term. The subscripts m and f indicate matrix and fracture, respectively.

In Equation 5, the saturation is also a function of pressure head and is calculated as follows (van Genuchten, 1980):

$$S(\psi) = (S_s - S_r)\left[\frac{1}{1 + |\alpha\psi|^{\beta}}\right]^{\lambda} + S_r \ , \tag{6}$$

where S_s is the full saturation (typically 1) and S_r is the residual saturation.

2.3 Numerical Technique

This section presents a very brief description of the numerical techniques used in TOSPAC. Dudley et al. (1988) give a more complete discussion.

The STEADY and DYNAMICS modules both use the finite-difference technique with the physical domain represented by a one-dimensional Eulerian mesh. Equation 1 (STEADY) and Equation 4 (DYNAMICS) are spatially center-differenced using three mesh points. Equation 1 is differenced as follows:

$$\begin{aligned} 0 = & \frac{2K_j}{z_{j+1} - z_{j-1}}\left(\frac{\Delta\psi_{j+1}}{\Delta z_{j+1}} - \frac{\Delta\psi_j}{\Delta z_j}\right) \\ & + \frac{\Delta K_{j+1} + \beta'_w K_{j+1/2}\Delta\psi_{j+1}}{z_{j+1} - z_{j-1}}\left(\frac{\Delta\psi_{j+1}}{\Delta z_{j+1}} + 1\right) \\ & + \frac{\Delta K_j + \beta'_w K_{j-1/2}\Delta\psi_j}{z_{j+1} - z_{j-1}}\left(\frac{\Delta\psi_j}{\Delta z_j} + 1\right) \ , \end{aligned} \tag{7}$$

where $\Delta\psi_j = \psi_j - \psi_{j-1}$, $K_{j+1/2} = (K_j + K_{j+1})/2$, etc.

The differencing of Equation 4 adds forward differencing in time:

$$\begin{aligned} C_{j,n+\Omega}\frac{\psi_{j,n+1} - \psi_{j,n}}{t_{n+1} - t_n} = & \frac{2K_{j,n+\Omega}}{z_{j+1} - z_{j-1}}\left(\frac{\Delta\psi_{j+1,n+\Omega}}{\Delta z_{j+1}} - \frac{\Delta\psi_{j,n+\Omega}}{\Delta z_j}\right) \\ & + \frac{\Delta K_{j+1,n+\Omega} + \beta'_w K_{j+1/2,n+\Omega}\Delta\psi_{j+1,n+\Omega}}{z_{j+1} - z_{j-1}}\left(\frac{\Delta\psi_{j+1,n+\Omega}}{\Delta z_{j+1}} + 1\right) \\ & + \frac{\Delta K_{j,n+\Omega} + \beta'_w K_{j-1/2,n+\Omega}\Delta\psi_{j,n+\Omega}}{z_{j+1} - z_{j-1}}\left(\frac{\Delta\psi_{j,n+\Omega}}{\Delta z_j} + 1\right) \ . \end{aligned} \tag{8}$$

The subscript n refers to values at the nth time, t_n. Most quantities have time subscripts $n + \Omega$, which is meant to indicate a value at time $t_{n+\Omega}$. A value at an intermediate time is obtained by a weighted average of the values at t_n and t_{n+1}: $K_{j,n+\Omega} = (1 - \Omega)K_{j,n} + \Omega K_{j,n+1}$, with Ω between 0 and 1. Values at intermediate spatial positions are then handled as follows: $K_{j+1/2,n+\Omega} = \frac{1}{2}(K_{j,n+\Omega} + K_{j+1,n+\Omega}) = \frac{1}{2}((1 - \Omega)K_{j,n} + \Omega K_{j,n+1} + (1 - \Omega)K_{j+1,n} + \Omega K_{j+1,n+1})$,

Centered spatial differencing is used for two reasons. First, when the mesh points are equally spaced, the truncation error is least for centered differencing (however, this result does not hold for mesh-point spacings that are nonuniform). Second, centered differencing allows water flux to be calculated in a self-consistent manner. For example, with an upstream-differencing scheme, the first-derivative term in Equations 1 and 4 is differenced across different mesh points from the second-derivative term, and no method exists to balance the contribution of the various mesh points when calculating the flux. The flux calculation used in TOSPAC is shown in Equation 11.

The implicitness factor Ω is added to forward time differencing because it is important to the stability and the accuracy of the numerical solution. The greatest stability is achieved with $\Omega = 1$. Unfortunately, this stability does not come without a price, and considerable numerical dispersion can often be observed. Truncation error is minimized, at least to first order, by calculating the time-dependent variables at the middle of the time step ($\Omega = 0.5$).

For the initial calculations, a Picard-iteration scheme in which every iteration is a time step was used and Ω was equal to 0. For the final set of calculations, a Picard iteration with $\Omega = 0$ was used for the first guess at a new time step, then a Newton subiteration was performed to refine the solution at the new time step. The Newton subiteration used $\Omega = 0.6$ for Cases 7 and 8 (instabilities occurred when these cases were solved with $\Omega = 0.5$), and $\Omega = 0.5$ for Cases 9 through 12.

To solve Equations 7 and 8, a linear system $\mathbf{A}\Psi = \mathbf{d}$ was constructed, where $\mathbf{A}$ is a tridiagonal matrix, Ψ is the pressure head vector to be solved for, and $\mathbf{d}$ is the inhomogenous vector. The equations that define the components of $\mathbf{A}$ and $\mathbf{d}$ are given by Dudley et al. (1988). In STEADY, the linear system is solved, reconstructed, and resolved to convergence, with stability controls interfering where necessary. In DYNAMICS, each solution of the linear system corresponds to a time step. (The subiteration formulation used in DYNAMICS for the final calculations is given in Equation 9.)

STEADY is designed as a hybrid boundary-value problem (BVP) and initial-value problem (IVP). STEADY attempts to solve each geologic unit as a BVP; however, when stability problems occur, STEADY fixes a new boundary immediately below the instability and forms a new BVP, thus marching up the mesh in the manner of an IVP.

Indeed, the steady-state cases can be solved using only IVP techniques. The hybrid implementation used in STEADY allows a consistent and stable steady-state solution to be calculated on a mesh defined primarily for a transient-flow calculation. Thus the STEADY solution can be used immediat ly as an initial condition for a DYNAMICS calculation.

DYNAMICS is set up as a BVP in space and an IVP in time. As mentioned, the version of the DYNAMICS module used for the initial calculations uses a Picard iteration at each time step. DYNAMICS was then modified for the final set of calculations to perform a subiteration based on Newton's method (although the initial time step is still made with a Picard iteration). The general form of Newton's method (also called a Newton/Raphson iterative method) is as follows:

$$\Psi_{k+1} = \Psi_k - \mathbf{J}(\Psi)^{-1}\mathbf{G}(\Psi_k) \ , \tag{9}$$

where Ψ_k is the pressure head solution at the k^{th} iteration, $\mathbf{J}(\Psi)^{-1}$ is the inverted Jacobian matrix of Ψ, and $\mathbf{G}(\Psi_k)$ is a root of the equation we are trying to solve (Richards' equation); i.e.,

$$g(\psi) = K\frac{\partial^2\psi}{\partial z^2} + \frac{\partial K}{\partial z}\left[\frac{\partial\psi}{\partial z} + 1\right] - C(\psi)\frac{\partial\psi}{\partial t} \ . \tag{10}$$

Although the addition of Newton subiteration causes DYNAMICS to perform more work at each time step, it allows much longer time steps (Section 4).

The convergence criterion for both the steady-state and transient-flow cases of the initial calculations was that the pressure head could not vary at any mesh point by more than 10^{-6} from one iteration to the next. For the final calculations this tolerance was relaxed to 10^{-2} for the steady-state cases only. The weaker tolerance caused less interference by STEADY's stability controls; execution times were shorter with no loss of accuracy.

Two major dependent variables, the flux and the average linear velocity, are calculated using the above solutions. The flux is calculated from the pressure head and the hydraulic conductivity using Darcy's law, averaging over three mesh points in a manner consistent with the difference equations (Equations 7 and 8), as follows:

$$q_j = -\frac{1}{2}\left[K_{j+1/2}\left(\frac{\Delta\psi_{j+1}}{\Delta z_{j+1}} + 1\right) + K_{j-1/2}\left(\frac{\Delta\psi_j}{\Delta z_j} + 1\right)\right] . \tag{11}$$

where q_j is the flux at mesh point j, $K_{j+1/2} = (K_{j+1} + K_j)/2$, $\Delta\psi_{j+1} = \psi_{j+1} - \psi_j$, etc.

Equation 11 calculates the composite flux, i.e., the flux through both the matrix and the fractures. The flux through only the matrix is calculated in the same manner, using the hydraulic conductivity in the matrix, i.e., $K_{m,j+1}$. The flux through the fractures is calculated similarly, using the hydraulic conductivity in the fractures, i.e., $K_{f,j+1}$.

The average linear velocity of a particle of water at mesh point j is calculated as the flux (q_j, taken from Equation 11) divided by the area available for flow (A_j):

$$v_j = \frac{q_j}{A_j} \ . \tag{12}$$

In one dimension, flux has units of length over time (L/T). For Equation 12 to return a velocity, flux must have units of L^3/T. The assumption is that flux occurs through a unit area. Conceptually, flow is not rigorously one-dimensional, but rather through a column, or a "flow tube." The area available for flow is the fraction of this unit area through which flow actually occurs. A_j is calculated by averaging over three mesh points in a manner consistent with the difference equations, as follows:

$$A_j = \frac{1}{4}\left[n_{j+1}(S_{j+1} - S_{r,j+1}) + 2n_j(S_j - S_{r,j}) + n_{j-1}(S_{j-1} - S_{r,j-1})\right] \ , \tag{13}$$

where n_{j+1} is the porosity at mesh point $j+1$, S_{j+1} is the saturation at the mesh point, and $S_{r,j+1}$ is the residual saturation.

Again, this equation is used for the average linear velocity of water in the composite material. To calculate the average linear velocity in the matrix, the flux in the matrix is divided by the area available for flow in the matrix; to calculate the average linear velocity in the fractures, the flux in the fractures is divided by the area available for flow in the fractures.

2.4 Boundary Conditions

Both STEADY and DYNAMICS allow boundary conditions to be specified either in terms of flux or pressure head. However, STEADY requires that the boundary conditions be consistent. For example, if in a steady-state calculation a flux is specified at the top boundary and a different flux is specified at the bottom boundary, STEADY will report an error.

For the COVE 2A problems, boundary conditions are defined as follows:

$$\psi_{jmin} = 0,$$
$$\psi_{jmax} = \left[\frac{q}{\frac{1}{2}(K_{jmax} + K_{jmax-1})} - 1\right](z_{jmax} - z_{jmax-1}) \ , \tag{14}$$

where the subscript $jmin$ indicates the mesh point at the lower boundary, $jmax$ indicates the mesh point at the upper boundary, and $jmax - 1$ indicates the mesh point immediately below the upper boundary. The lower boundary condition corresponds to the water table. For the upper boundary condition, the flux q is specified and bounds on the pressure head are set. An iterative bisection scheme is then used to settle on an accurate answer. This technique is necessary because K_{jmax} is a nonlinear function of ψ_{jmax}, the value we are trying to find.

In the version of DYNAMICS used for the final calculations, the specification of both flux and pressure-head boundary conditions is included in the Newton-subiteration scheme (Dudley et al., 1988).

2.5 Time-Step Control

STEADY solves for the steady-state pressure head directly; it does not include a time-dependent term and therefore has no time-step control.

The time step in DYNAMICS was controlled differently for the initial and final sets of calculations. For the initial calculations, the time step was based on a Courant condition. The algorithm is as follows.

The first time step is supplied by the user; subsequent time steps are increased by a factor of 1.5 until a Courant condition is reached. This Courant condition limits the time step to some fraction of the minimum cell-transit time and is calculated using the following equation:

$$\Delta t_{n+1} = \min\left(f\frac{\Delta z_j}{v_{j-1/2,n}}\right) \ , \tag{15}$$

where Δt_{n+1} is the next time step (the time between time step n and time step $n + 1$); f is the Courant factor, discussed below; Δz_j is the distance between adjacent mesh points; and $v_{j-1/2,n}$ is the average linear velocity between adjacent mesh points at time step n.

In classical flow problems with explicit difference equations, the Courant factor is usually set to 0.5, meaning that a given particle of fluid can traverse, at most, one-half the distance between mesh points which have the shortest transit time of the entire problem during any time step. When the COVE 2A problem set was being conceived, f was set equal to 10 for predominantly matrix-flow conditions and to 0.05 for predominantly fracture-flow conditions. For the initial set of calculations, the fracture flow f was relaxed slightly to 0.1 and the matrix flow f was kept at 10. (Section 3.3 contains a discussion of the subsequent degradation in behavior of the solution process.)

"Predominance" of matrix or fracture flow is determined as follows: if the flux in the fractures is $\geq$ 1% of the imposed flux, then fracture flow is said to predominate; otherwise matrix flow is said to predominate. The 1% value is arbitrary.

In the interests of efficiency, Equation 15 is not calculated for every mesh point, but rather only for mesh points at which total flux has changed over the previous time step. If the flux changes more than 1% in any given mesh point, then that point is used as one of the set to calculate the next time step.

The above algorithm is insufficient for preventing instabilities in the solution when used with a Picard-iteration scheme, as in the initial calculations. To control instabilities, the following algorithm works in concert with the Courant-condition time-step control:

1) instabilities are identified when the Courant condition indicates a spike in the velocity (i.e., a plunge in the calculated time step when compared with the previous time step, specifically when $\Delta t_{n+1} < \frac{1}{2}\Delta t_n$);

2) the pressure-head solution is returned to that used in the previous time step (the last time at which a stable solution is known), and the time step is repeated with a time step of one-half the previous time step;

3) for five iterations the time step is not allowed to exceed the reduced time step;

4) after five iterations the time step is allowed to become up to 50% greater than the previous time step until instabilities again occur.

In the initial calculations, for a predominantly fracture-flow problem, an instability typically appeared before the true Courant condition was realized; thus the time step was controlled for the most part by the stability-control algorithm.

For the final calculations, the Courant-condition control and the stability controls were retained in DYNAMICS, but in a subordinate role. The dominant time-step control was—and still is—based on limiting the temporal change of the major variables in Equation 4 (the pressure head and the hydraulic conductivity) as shown in the following equation:

$$\Delta t_{n+1} = \min\left(f\frac{K_{j,n}}{K_{j,n} - K_{j,n_1}}, f\frac{\psi_{j,n}}{\psi_{j,n} - \psi_{j,n-1}} \right) , \qquad (16)$$

where $K_{j,n} - K_{j,n_1}$ is an approximation for the time derivative of the hydraulic conductivity (also noted as $\dot{K}$), $\psi_{j,n} - \psi_{j,n_1}$ is an approximation for the time derivative of the pressure head (also noted as $\dot{\psi}$), and f is now the "time-step factor," set to 0.1 for the COVE 2A problems.

Because the hydraulic conductivity is typically more nonlinear than the pressure head in an unsaturated-flow problem, the first term in Equation 16 should prevail. The pressure-head term is a precaution for situations where the derivative of the hydraulic conductivity approaches 0, such as near saturation.

This derivative-based time-step control also includes a precaution against taking time steps so long that an excessive number of subiterations are performed to converge on a solution: if more than five Newton subiterations are performed at any single time step, the previous time step is repeated with a reduced time step. This additional control was never required in the final calculations.

The derivative-based time-step control requires that the first time step be specified; the Courant-condition time-step control is used for this purpose. Thereafter the Courant condition and its stability-control algorithm are used only when they produce a time step greater than the $K/\dot{K}$ or $\psi/\dot{\psi}$ value. The reason for retaining these time-step controls is that near a pressure head of 0, the $\psi/\dot{\psi}$ term goes to 0, while the $K/\dot{K}$ term goes to infinity because the derivative of the hydraulic conductivity goes to 0—both undesirable situations. After the first time step in the final set of calculations, however, the time step was never set by the Courant condition or its stability-control algorithm.

2.6 Some Notes on Accuracy

The intent of this section is to specify what an accurate solution is for both the steady-state and the transient-flow COVE 2A cases, and then to determine what mesh-point spacings and time steps guarantee this accuracy.

In steady-state flow in one dimension, the calculated flux should exactly match the imposed flux. Therefore, to assess the accuracy of a calculation, one need only check the agreement between the calculated and the imposed flux. With STEADY, deviations between the calculated and the imposed flux can be minimized by closer spacing of mesh points. If the accuracy of a solution is not acceptable, the calculational mesh can be

modified and a new solution can be calculated. This process can be repeated until an acceptable solution is found.

Section 4.2 describes analytic inequalities that were developed by Dudley et al. (1988) to bound the mesh-point spacing for steady-state calculations. These inequalities do not depend on the solution technique (other than the assumption that a calculational mesh is required), and errors introduced by the solution technique are not considered. Further, the inequalities show that infinitesimal mesh-point spacings are required at material boundaries while arbitrarily large spacings are acceptable in other regions—mesh designs that are difficult to implement. However, with the exception of the regions near the boundaries between adjacent geologic units, the calculational meshes constructed for both the initial and final sets of calculations were acceptable for accurate steady-state calculations, based on the inequalities in Section 4.2.

For transient-flow calculations, the generally accepted measure of accuracy is mass balance. The weakness of relying on mass balance is that it can be constant for a given calculation, and yet essential elements of the dynamics (e.g., speed of propagation) may be incorrect.

A mass-balance measure has not been implemented in DYNAMICS. The measure of accuracy chosen for transient-flow calculations is the shape of the flux front as it proceeds down the column. Dudley et al. (1988) give a formula for calculating the shape of a pressure-head pulse passing through a single material, when beginning at a flux of q_0 and ending at a flux of q_1. Because flux is calculated from pressure head, the formula indirectly gives the shape of a flux front:

$$\frac{d\psi}{du} = 1 + \frac{q_0 + (\theta(\psi) - \theta_0)v_{fr}}{K(\psi)} , \tag{17}$$

where $\theta(\psi)$ is the moisture content at a given pressure head, θ_0 is the initial moisture content of the material, $K(\psi)$ is the conductivity at a given pressure head, v_{fr} is the velocity of the flux front, and $u = -z + v_{fr}t$. In general, for a flux front through a single material, v_{fr} can be described as follows:

$$v_{fr} = (q_1 - q_0)/(\theta_1 - \theta_0) , \tag{18}$$

where θ_1 is the moisture content after the front passes.

Equation 17 can be solved by a numerical integration for pressure head at various elevations. Pressure-head solutions were calculated using Equation 17 for several different pairs of fluxes through several different materials. The calculations were repeated using DYNAMICS. Agreement between the flux-front shape calculated by Equation 17 and by

DYNAMICS was generally excellent given the following conditions on the DYNAMICS solution:

1) the time step was sufficiently small,
2) the mesh spacing was sufficiently small, and
3) the truncation error of the difference equations was minimized.

Analytic inequalities were developed to determine what is "sufficiently small" for time steps and mesh spacings. These inequalities, given in Sections 4.2 and 4.3, should be useful for any finite-difference or finite-element solution technique used on these problems.

According to these inequalities, the mesh-point spacings used for the initial transient-flow calculations were too coarse to ensure accuracy. The time steps, however, were satisfactory. (Actually, the time steps were shorter than necessary, resulting in too much computer time being used. These small time steps were caused by numerical instabilities in the solution. If a finer mesh had been used, the instabilities could possibly have been reduced and the time steps could possibly have been lengthened.)

For the final calculations, mesh spacings and time steps were defined on the basis of these inequalities. Indeed, the mesh developed for Case 12 was satisfactory for all the cases and was used in all the final calculations.

The COVE 2A Problem Definition Memo requires that values for each hydrologic variable be saved at 75 locations in the mesh. Plots based on these 75 data points lack resolution and can be misleading in two respects:

1) numerical instabilities, such as those evident in Figure 1-12-1, can be lost, and
2) the true steepness of the flux front—our measure of accuracy—can be lost.

The plots contained in this report show values taken at every mesh point. A report comparing the results produced by all the COVE 2A participants is planned, and that report will base the comparison on values taken at the 75 data locations. Thus the plots herein will appear different from the plots in the comparison report.

3.0 INITIAL CALCULATIONS

3.1 Changes to the Computational Modules of TOSPAC

When the initial calculations were performed, TOSPAC was still under developement. No modifications were made to the computational sections of the version of STEADY that existed at the time; a single modification was made to the computational sections of DYNAMICS.

DYNAMICS was "vectorized" so that it could take advantage of pipeline processing on a CRAY computer. The vectorized version of DYNAMICS was only used on Cases 9 through 12; Cases 7 and 8 were executed on a VAX 8650 computer with a nonvectorized version of DYNAMICS. Vectorizing includes removing conditional statements, subroutine and function calls, and array dependencies from FORTRAN DO loops. Then, upon compilation, passes through the DO loop can be separated and sent to different processors where they can be executed in parallel. A preliminary calculation of the Case 10 problem indicated that, if solved on the VAX 8650, it would take approximately 50 hours of central processing unit (CPU) time. The vectorized version took less than 1 hour on a CRAY X/MP. Of this improvement, approximately half was due to the inherently faster processing of the CRAY and half was due to the vectorizing.

DYNAMICS was not very efficient at the beginning of the COVE 2A project; it was vectorized in a piecemeal fashion. First, the matrix setup subroutine (PICARD) was vectorized with surprisingly little improvement in execution speed. Next, the subroutine that calculates flux and average linear water velocity (GETOUT) and then the time-step control subroutine (TMCNTL) were vectorized. Finally, the subroutine that computes the van Genuchten functions for saturation, hydraulic conductivity, and their derivatives (GETCRV) was vectorized; here the largest increase in speed was realized: approximately a factor of seven. Minimizing the repetition of mathematical operations in these same subroutines made up for some of the improvement in run times. However, the important lesson learned from vectorizing was that computing the van Genuchten functions for saturation and hydraulic conductivity (and their derivatives), with all their divisions and exponentiations, for every mesh point at every iteration takes approximately 80% of the CPU time on a VAX 8650 computer.

3.2 Calculational Mesh

Table 3-1 presents the number of mesh points used to define the calculational meshes in the initial COVE 2A calculations. Figure 1-1 shows the calculational mesh as well as the geologic units and material assignments that compose the problem geometry for Case 1. Meshes for the other cases were similarly configured. In Figure 1-1, each rectangle in the

mesh column indicates ten mesh points. The bottoms of the columns (−0.1 m) correspond to the bottom of the mesh. (The water table corresponds to an elevation of 0.0 m. The version of TOSPAC used in the initial calculations imposed the lower-boundary condition at the second mesh point; TOSPAC was modified for the final calculations to impose the lower-boundary condition at the first mesh point.) The tops of the columns (530.4 m) correspond to the top of the mesh, the ground surface.

TABLE 3-1
NUMBER OF MESH POINTS FOR EACH CASE OF THE INITIAL SET OF CALCULATIONS

Case	Number of Mesh Points	Number of Submeshes[a]
1	811	16
2	813	16
3	811	16
4	813	16
5	893[b]	16
6	895[b]	16
7	811	16
8	811	16
9	811	16
10	811	16
11	847[b]	16
12	522[c]	21

a. Submeshes are regions of the mesh with mesh points spaced differently from adjacent regions.

b. The increase in the number of cells was due to fine tuning the mesh.

c. Mesh for Case 12 was constructed with a reduced number of mesh points because of extremely long run times.

The calculational meshes were created as follows. A uniform mesh was created as a starting point. It was known from previous experience that the transient-flow cases require a large number of mesh points. Because the fractures tend to desaturate over an interval from 0 to −1 meters of pressure head, it was deduced that the maximum mesh-point spacing to resolve this desaturation should be 1 meter. Hence the uniform mesh used 531 mesh points, spaced 1 meter apart.

Previous experience also suggested that to achieve satisfactory steady-state results, mesh points must be spaced closer together in two regions:

1) at interfaces between geologic units where material hydrologic properties are discontinuous and

2) immediately above interfaces where relatively impermeable geologic units lie on top of highly conductive units (asymptotes in the pressure-head solution occur in these regions, for example, in the region immediately above the TSw2/CHnv interface and the region immediately above the TCw/PTn interface in Figure 1-12-2).

Therefore, beginning with the uniform mesh, more mesh points were inserted in these regions. Then the steady-state cases were executed one at a time. For the steady-state cases there is a check on the accuracy of the answer—the flux calculated at each mesh point should be the same as the imposed flux. Each steady-state solution was examined for deviations in the calculated flux from the imposed flux, and when a deviation was deemed significant (typically above 10%), more mesh points were added in the region of the deviation. Then the process was repeated, until by trial and error a suitable mesh consisting of 811 mesh points was created for the steady-state cases. (The 813-point mesh was virtually identical—the additional two points were inserted by mistake.)

The steady-flow cases were also the initial conditions for the transient-flow cases. Thus the steady-state solutions of the final transient-flow fluxes (0.2 mm/yr for Cases 7 and 8, 1 mm/yr for Cases 9 and 10, and 8 mm/yr for Cases 11 and 12) were also calculated to determine suitability of the mesh.

Originally, the intention was to have a single mesh to use in all the calculations. However, the use of a single mesh became less of a priority at this point, and the meshes for Cases 5, 6, 11, and 12 were changed without running the other cases again.

The number of mesh points for Case 12 was arbitrarily reduced because the computer time to execute it was projected to be extremely long. The greater mesh-point spacing led to somewhat poorer results, as shown in Figure 1-12-1, but the results compare favorably with those for Case 11, as shown in Figure 1-11-1. (In fact, according to the inequalities given in Section 4.2, the mesh used for Case 11 was also too coarse.)

3.3 Time Step

As discussed in Section 2.5, DYNAMICS incorporates an automatic time-step controller. For the initial set of calculations the controller responded to two requirements:

1) Courant condition, and
2) stability.

In practice, for predominantly matrix flow, times were controlled by a Courant condition. Equation 13 and the discussion in Section 2.5 provide information about the Courant condition.

The Courant-condition factors for the initial calculations were set as follows:

matrix flow: $f = 10$,
fracture flow: $f = 0.1$.

A more conservative $f = 0.05$ for fracture flow was used in the original solution of these problems (before the COVE 2A project began). It was hoped that the $f = 0.1$ setting would result in longer time steps and, therefore, shorter run times. However, the attempt to take longer time steps resulted in greater numerical instability. And, in practice, for predominantly fracture flow, the time step was dominated by stability controls. The algorithm given in Section 2.5 provides information about the stability controls.

For Cases 7 and 8, which exhibit predominantly matrix flow, time steps were on the order of several hundred years when the time-step controller was using mesh points in TSw2. For Cases 11 and 12, which exhibit predominantly fracture flow, time steps were on the order of a few hours when the time-step controller was using mesh points in TSw2. These very small time steps were caused by the stability controls in the time-step controller. The result was over 100,000 iterations in some of the problems with fracture flow.

3.4 Run-Time Information

Table 3-2 shows run-time information for the initial set of calculations. The transient-flow cases involving fracture flow were executed on a CRAY X/MP computer because of excessive run times on a VAX 8650 computer (it was estimated that Case 10 would take approximately 50 hours of VAX CPU time).

3.5 Results

This subsection contains a brief interpretation of the results from the initial set of calculations. The emphasis is on tying significant features of the results back to the governing equations (Section 2.1). A similar problem set was used in the example section of the report by Dudley et al. (1988), and a more complete discussion is contained therein.

TABLE 3-2
RUN-TIME INFORMATION FOR THE INITIAL SET OF CALCULATIONS

Case	Number of Mesh Points	Computer	Number of Time Steps	CPU Time (sec)
1	811	VAX 8650	16*	35
2	813	VAX 8650	25*	44
3	811	VAX 8650	105*	99
4	813	VAX 8650	95*	110
5	893	VAX 8650	140*	204
6	895	VAX 8650	105*	155
7	811	VAX 8650	515	714
8	811	VAX 8650	496	676
9	811	CRAY X/MP	49,540	875
10	811	CRAY X/MP	164,136	2885
11	847	CRAY X/MP	6315	120
12	522	CRAY X/MP	213,914	3070

* Iterations rather than time steps (STEADY does not implement time). Also, because STEADY iterates over only a portion of the mesh at one time, this number has been adjusted to represent iteration over the entire mesh.

Examination of the results of the initial calculations as part of the COVE 2A benchmarking activity revealed several problems.

1) The average linear velocity of water in the fractures was calculated incorrectly, most significantly in the 0.1 mm/yr flux cases (Figures 1-1/3/5-6, 1-2/4/6-6, 1-7-6, and 1-8-6).

2) In the transient-flow cases the flux upper-boundary condition is unstable. The instability is most noticeable in Figures 1-7-1 and 1-8-1, but also is apparent in Figures 1-9-1 and 1-10-1).

3) In Case 6 the calculated flux deviates markedly from the imposed flux near the TSw2/CHnv interface (Figure 1-2/4/6-1).

The average linear velocity is calculated by dividing the flux by the area available for flow (Equations 12 and 13). In TOSPAC, for the initial COVE 2A calculations, the area available for flow was calculated using an approximation for the residual saturation parameter (S_r in Equation 13). The value was approximated because, at the time, TOSPAC allowed a number of different methods for specifying hydrologic-property data and not all methods required specifing the residual saturation explicitly. The approximation consisted of identifying a saturation level that caused a hydraulic conductivity close to the lowest machine precision available—in practice, a value in the neighborhood of 10^{-25}. This saturation was approximately 0.1% above the exact residual saturation. At

very low pressure heads, when saturation approached residual saturation, the slight inaccuracy inherent in the residual-saturation approximation caused errors of several orders of magnitude in the average linear velocities.

The error had not been discovered because it was only apparent at the extreme lower values of the velocity of water in the fractures. Investigation of results in this region of the solution are easily dismissed as insignificant, or in the province of numerical noise (errors caused by round-off of numbers or loss of precision when very small numbers are added or subtracted from very large numbers). The error was only discovered after the preliminary results from all the participants had been plotted together. It is unlikely that the error would have been found without having gone through this process of direct comparison of results from the same problems.

The velocity calculation was corrected for the final set of calculations by modifying TOSPAC to require that the exact value of the residual saturation be entered explicity in all hydrologic-property data, and to use this exact value in calculating the area available for flow.

The flux boundary-condition instability was caused by a combination of the implementation and the Picard-iteration solution technique. As shown in Equation 14, the flux boundary condition was actually calculated as a pressure head, linearly interpolated from the next interior mesh point, $jmax - 1$. Hence, the boundary-condition pressure head was not actually the pressure head at the the uppermost mesh point, $jmax$, but rather the pressure head at a midpoint between the uppermost mesh point and the next interior mesh point. Thus, when a Picard iteration was taken, an inaccuracy was added to the calculation. The inaccuracy tended to be self-correcting, however, because when the pressure head at the next interior mesh point was perturbed in one direction, the boundary-condition error was in the other direction. Further, the inaccuracy developed only when the solution dictated different pressure-head values at the uppermost and the next-interior mesh points. If the pressure heads were the same (as in Cases 9 through 12) there was no error.

When a Newton-subiteration technique was added for the final calculations, it was implemented so that the boundary mesh points were included in the subiteration. The subiteration caused the inaccurate pressure head to settle on a more accurate value. Essentially, the boundary condition was moved to the outer mesh point, and the instability was cured. Section 4 covers this modification more fully.

The spike in the Case 6 flux profile was a mesh-refinement problem. The introduction of more mesh points in this area reduced the magnitude of the deviation. (Other Project participants used coarser meshes and some of their solutions did not exhibit these spikes in the steady-state cases or oscillations in the transient-flow cases. Other solution techniques can inherently perform more smoothing or averaging across mesh points than

three-point finite differencing does. Also, if only a subset of data points are plotted—e.g., 75—these spikes or oscillations can disappear.)

3.5.1 Cases 1, 3, and 5

Figure 1-1/3/5-1 shows the normalized flux (the calculated flux at a point divided by the imposed flux) plotted against distance above the water table—i.e., elevation—for Cases 1, 3 and 5. For one-dimensional, steady-state calculations such as these, the flux is a check of the correctness of the solution; the calculated flux should equal the flux imposed at the boundary. The flux is also a sensitive measure of the smoothness of the pressure-head solution—tiny variations, oscillations, or spikes in the pressure head are magnified in the flux.

Figure 1-1/3/5-1 indicates that the solutions are correct to within approximately 5%. The single notable deviation in flux occurs in Case 5 results at the interface between units PTn and TSw1. A finer mesh spacing in this region would have reduced this spike.

Figure 1-1/3/5-2 shows the corresponding plot of pressure head versus distance above the water table for Cases 1, 3, and 5. In general, the pressure head decreases to large negative values as the flux is decreased. Rapid changes in pressure head can be seen at interfaces between units that have very different hydraulic conductivities, such as at the TCw/PTn interface and the PTn/TSw1 interface. For a flux of 4 mm/yr the pressure head change at the TCw/PTn interface is almost discontinuous. For a 4 mm/yr flux, Unit TCw with its saturated conductivity of 0.6 mm/yr is saturated in the matrix, and the pressure head is near 0 in this unit. The PTn unit with saturated conductivity of approximately 10,000 mm/yr would be near residual saturation if not for the influence of TSw1, and the pressure head tends toward very negative values. The pressure-head discontinuity moderates as the flux is reduced to 0.1 mm/yr, which is less than the matrix conductivities of both of these units, neither unit being saturated at this flux. Note that, for a flux of 4 mm/yr, the pressure head is near 0 in all the units (except PTn) indicating that both the matrix and the fractures are carrying water.

In Figure 1-1/3/5-3 matrix saturation is plotted against distance above the water table for Cases 1, 3, and 5. The pressure-head solution was used to calculate the matrix saturation directly using the van Genuchten formulation for the saturation characteristic curves. For a flux of 4 mm/yr, the matrix is near full saturation in all regions except at the interface of PTn and TSw. Matrix saturation drops sharply in Unit PTn for this flux, corresponding to the almost discontinuous drop in pressure head in this unit. In general, matrix saturation does not change significantly in TCw, TSw1, TSw2, and CHnz, because these units have similar saturation characteristic curves and the pressure head does not vary much in them.

Figure 1-1/3/5-4 shows hydraulic conductivity versus distance above the water table for the three CHnz cases. The hydraulic conductivity is for the composite (matrix and fractures) material; it was calculated separately for the matrix and the fractures from the van Genuchten formulation for the characteristic curves, and these values were area-weighted for the composite value. Large sections of the column show a constant hydraulic conductivity, which not coincidentally equals the flux. These areas also show a constant pressure head (Figure 1-1/3/5-2) and are termed the "characteristic solution" by Dudley et al. (1988). This solution is also sometimes called the "unit head gradient." Sharp changes in hydraulic conductivity occur at the interfaces of PTn with TCw and TSw1.

The spikes visible at the unit interfaces of the 4 mm/yr profile are an adjustment needed to maintain the characteristic solution over a discontinuous change in hydrologic properties. At these points the term describing spatial change in pressure head in Equation 1 is significant, and thus the value of the conductivity coefficient decreases. The 4 mm/yr case involves the most nonlinear part of the hydraulic-conductivity characteristic curve for Units TSw1, TSw2, and CHnz, and thus the adjustment is most noticeable in this profile.

Figures 1-1/3/5-5 and 1-1/3/5-6 are plots of the average linear velocity of water in the matrix and in the fractures, respectively, versus distance above the water table for Cases 1, 3, and 5. As seen in Figure 1-1/3/5-3, matrix saturation does not change much for most cases as the flux is varied. The water velocity in the matrix thus varies approximately linearly with the flux until the matrix is saturated. PTn is the exception to this situation. For a flux of 0.1 mm/yr, PTn has a very low saturation resulting in a high matrix water velocity. The water velocity of the matrix decreases for a flux of 0.5 mm/yr because PTn now becomes nearly saturated. It increases again for 4 mm/yr because the saturation has not changed but the flux has increased.

Regardless of flux, there is some water movement in the fractures near the water table, where the prescribed boundary condition of 0 pressure head causes the fracture saturation to increase as the water table is approached. At a flux of 0.1 mm/yr, fracture flow is negligible except near the water table. At 0.5 mm/yr, fracture flow becomes significant in TCw, which has a matrix conductivity of 0.3 mm/yr. At 4 mm/yr, the water velocity is much greater in the fractures than in the matrix in the units with matrix conductivities are less than 4 mm/yr (TCw, TSw1, TSw2, and CHnz). (As mentioned above, the velocity of water in the fractures as shown in these plots is only qualitatively correct.)

3.5.2 Cases 2, 4, and 6

Normalized flux versus distance above the water table for Cases 2, 4, and 6 is shown in Figure 1-2/4/6-1. These curves are similar to those in Figure 1-1/3/5-1, and show that the calculated flux generally agrees with the imposed flux, indicating accurate pressure-head solutions. In Case 6 (CHnv, 4 mm/yr flux), there is a spike representing approximately an 8% discrepancy between calculated and imposed flux (the guideline used was that any disagreement should be less than 10%). This deviation can be controlled by using a finer mesh spacing, as shown in the final set of calculations.

Figure 1-2/4/6-2 shows pressure head plotted against distance above the water table for Cases 2, 4, and 6. These plots are generally similar to those for the CHnz cases (Figure 1-1/3/5-2) except in the lower part of TSw2 and into CHnv. CHnv has a large saturated matrix conductivity (8,400 mm/yr) compared with the applied flux (the saturated matrix conductivity of CHnz is 0.6 mm/yr), which causes the pressure head to decrease rapidly above the water table. Note the almost discontinuous change in pressure head at the interface between TSw2 and CHnv for an imposed flux of 4 mm/yr; this effect has already been discussed for the TCw/PTn interface.

Matrix saturation versus distance above the water table is shown in Figure 1-2/4/6-3. Compared with Figure 1-1/3/5-3, the major difference is that CHnv is much less saturated than CHnz. At pressure heads between -10 and -100 meters, the characteristic curves for the CHnv matrix show much greater hydraulic conductivity and much less saturation that the characteristic curves for the CHnz matrix. (The saturation curve for the CHnv matrix shows a rapid decrease in saturation beginning at approximately -10 meters, whereas the curve for the CHnz matrix shows a more gradual decrease beginning at approximately -100 meters. The hydraulic conductivity curve for the CHnv matrix also shows an abrupt decrease at -10 meters; however, the saturated hydraulic conductivity for the CHnv matrix is much greater than it is for the CHnz matrix, and therefore, the hydraulic conductivity for the CHnv matrix remains greater than that of the CHnz matrix over most of the -10 to -100 meter range in pressure head.) Because the hydraulic conductivity is greater, CHnv retains less water than CHnz. Less water corresponds to lower pressure heads. Lower pressure heads correspond to even lower saturation values to be taken from the saturation characteristic curve.

The composite hydraulic conductivity curves for the three CHnv cases shown in Figure 1-2/4/6-4 are essentially identical to those for the CHnz cases, except near and below the TSw2/CHnv interface. As is expected, a comparison of these plots to the pressure-head plots reveals a discontinuity at this interface for a flux of 4 mm/yr.

Figures 1-2/4/6-5 and 1-2/4/6-6 show the average linear velocities in the matrix and in the fractures, respectively. When compared with the CHnz cases, the water velocity in the CHnv matrix is greater than that in CHnz, primarily because the average linear velocity is calculated by dividing the flux by the area available for flow, and for a given flux,

CHnv has less area available for flow than CHnz. (The area available for flow is calculated as the porosity times the saturation minus the residual saturation. Although the porosity of CHnv is almost twice the porosity of CHnz, the saturation values are much lower in CHnv at the pressure heads being considered.) In the CHnv fractures, there is virtually no water movement at any of the fluxes (except near the water table, where the boundary condition encroaches).

3.5.3 Case 7

Figures 1-7-1 through 1-7-12 are the output plots for Case 7, where the CHn unit is zeolitized, and the flux change is from 0.1 to 0.2 mm/yr. Throughout this flux range, flow occurs predominantly in the matrix (except near the water table).

Figure 1-7-1 shows the normalized flux versus distance above the water table for this case. The flux is increased instantaneously at the top of TCw and is seen to disperse quickly as it passes through Units TCw and PTn. The front appears to pause and rebuild itself at the PTn/TSw1 interface. It again disperses after entering TSw1, and the flux change thereafter occurs almost simultaneously in the lower three units.

It can be seen from Figure 1-7-1 that, as the flux approaches the new steady state of 0.2 mm/yr, the rate of approach decreases. This occurrence can be explained by the decreasing gradient of the pressure head with time, as seen in Figure 1-7-2.

A slight instability can be noticed at the upper flux boundary of 0.2 mm/yr. The instability has been corrected, as can be seen in the corresponding plot for the final set of calculations (Figure 2-7-1).

The plot of pressure head versus distance at progressive times for Case 7 is seen in Figure 1-7-2. The pressure head increases in concert with the flux. This change is marked in the TSw units, where the magnitude of the pressure head at 200,000 years is approximately half its initial value. The hydraulic conductivity characteristic curve for TSw is relatively linear for this range in pressure head, which would indicate that the pressure head should vary with the flux, i.e. by a factor of 2. Smaller changes in pressure head occur in CHnz and TCw, partly because of the greater variability in hydraulic conductivity with respect to pressure head and, in CHnz, partly because the pressure head is constrained at the water table. Dudley et al. (1988) give more details on the conductivity curves. PTn, however, has a fairly large increase in pressure head, necessitated by the large pressure head change required to increase the flux from 0.1 to 0.2 mm/yr in the TSw units below it. Overcoming this pressure-head "dam" is the reason that the flux front attempts to rebuild in PTn.

Figure 1-7-3 shows the matrix saturation profiles over distance above the water table. The general tendency is for the saturation to slowly increase over time. This increase is slight in CHnz and greater in the TSw units. PTn shows the greatest change going from approximately 10% to 60% saturation at 200,000 years. This effect is due to the influence of the TSw units below, where large pressure head changes occur, as seen in Figure 1-7-2. This jump in pressure head causes a large increase in saturation at the PTn/TSw1 interface, which extends into the PTn layer. The saturation increase in CHnz is moderated by the fixed saturation at the bottom (a pressure head of 0 forces complete saturation).

To a large extent, the time needed to fill PTn to the new saturation level determines the 200,000 years required to go from one steady state to another. Because the porosity of the PTn matrix is approximately 50% and the change in saturation is approximately 40%, approximately 20% of the total volume of PTn fills with water. PTn is about 40 meters thick; thus, in a one-dimensional column a meter square, approximately 8 cubic meters of water must be added to PTn. At an infiltration of 0.2 mm/yr, or 6.34×10^{-12} m/s (over a square meter), it should take approximately 10^{12} seconds, or 300,000 years, to fill PTn.

The next plot, Figure 1-7-4, shows profiles of the hydraulic conductivity versus distance. These results follow the same pattern as the pressure-head and matrix-saturation plots, with the greatest increase occurring in PTn, where the TSw1-induced increase in pressure head raises the conductivity more than might have been anticipated.

The average linear velocities of water in the matrix and in the fractures for Case 7 are shown in Figures 1-7-5 and 1-7-6. For the matrix water, the increase in the average linear velocity occurs relatively abruptly in TCw, then more gradually in the lower four units. The behavior is similar to that shown in the flux profiles (Figure 1-7-1), except in PTn. The velocity decreases downward through PTn because the pressure head (and hence the saturation) at the lower boundary is determined by TSw1. Figures 1-7-2 and 1-7-3 show how the interface with TSw1 acts like an internal boundary condition on PTn. The unusual behavior, however, is not the spatial decrease in velocity, but rather the temporal decrease. Close examination of Figure 1-7-5 shows that the velocity of water in PTn first increases in time, then decreases significantly. The decrease is attributable to the increase in the area available for flow in PTn. At the PTn/TSw1 interface, the saturation in PTn goes from less than 15%—residual saturation is 10%—to over 60% (Figure 1-7-3). From Equation 12, when the flux increases by a factor of 2 and the area available for flow increases by almost a factor of 20, the average linear velocity decreases by almost an order of magnitude.

For the low fluxes in Case 7, water flow is predominantly in the matrix, not the fractures (except near the water table). Figure 1-7-6 reflects this fact—qualitatively. Because of the error in the velocity calculation discussed at the beginning of this subsection, the lowest velocity values are approximately five orders of magnitude too low.

Figures 1-7-7 through 1-7-12 show the flux, pressure head, saturation, hydraulic conductivity, and average linear velocity plotted against time at specified elevations above the water table. The first such plot, Figure 1-7-7, shows the normalized flux profiles. The increase in flux can be seen advancing progressively down the mountain with time. At the bottom of the topmost unit (TCw), the calculated flux becomes equal to the imposed flux in approximately 3,000 years; the new steady state of 0.2 mm/yr occurs in all units at around 200,000 years.

Instabilities are noticeable in the 465.7-m (0.2 meters above the lower boundary of PTn) and 503.4-m (0.2 meters below the upper boundary of PTn) elevation lines. The instabilities are the result of the Picard-iteration solution technique being inadequate to calculate an accurate solution near major discontinuities in the material properties (the TCw/PTn interface). As discussed in Section 2.5, the time-step length for the initial calculations was determined primarily by the stability-control algorithm, and these instabilities are signs of why the stability-control algorithm was operating.

Figure 1-7-8 shows the pressure head versus time plots. As in the normalized flux plots, this plot also shows agreement with the plot of pressure head versus distance (Figure 1-7-2). The greatest pressure-head change is in the TSw units. Notice that the instabilities in the 465.7- and 503.4-m lines in Figure 1-7-7 are not apparent in Figure 1-7-8, an indication of the sensitivity of the flux.

Temporal change in matrix saturation at different elevations is shown in Figure 1-7-9. All the units except PTn show a slow, gradual increase in saturation as the flux front disperses through them. In PTn the change is more dramatic: the 465.7-m line rises sharply beginning at approximately 2,000 years and lasting until 200,000 years. This response is explained by the large pressure-head increase occurring in the TSw units below.

Figure 1-7-10 shows hydraulic conductivity versus time. In keeping with the trend shown in the pressure-head plot, hydraulic conductivity increases with time as the units become more saturated.

Figure 1-7-11 shows the average linear velocity of water in the matrix. For the most part, as time progresses, the flux increases more than the area available for flow, and therefore the average linear velocity of water in the matrix increases. The large increase in saturation in PTn, as detailed in the discussions of Figures 1-7-3 and 1-7-5, causes the average linear velocity of water in the matrix to decrease, as is evident in the curves representing elevations of 503.4 and 465.7 m.

The average linear velocity of water in the fractures is seen in Figure 1-7-12. Although quantitatively the velocities are in error, qualitatively they indicate the correct situation. The only significant water flow occurs at the water table; there is no appreciable fracture

flow in any of the units for the fluxes considered in this case. (Figures 2-7-6 and 2-7-12 show the quantitatively correct fracture-water velocities.)

3.5.4 Case 8

Figure 1-8-1 shows the normalized flux plotted against distance for a flux change of 0.1 to 0.2 mm/yr, where the bottom unit is vitric (CHnv). The characteristic curves for CHnv and CHnz are significantly different, although Figure 1-8-1 is quite similar to Figure 1-7-1. The flux change in the lower units in both Cases 7 and 8 is dominated by the pressure-head change at the PTn/TSw1 interface. The large pressure-head change at this interface causes a substantial change in saturation in PTn, and as explained in the discussion of Figure 1-7-3, it is this change in saturation that determines that time scale for this problem. Thus, the flux-change profiles are virtually independent of whether CHnv or CHnz is considered as the lowest unit.

Figures 1-8-2, 1-8-3, and 1-8-4 show the pressure head, matrix saturation, and hydraulic conductivity, respectively, versus distance above the water table. These plots are similar to the corresponding CHnz plots (Figures 1-7-2, 1-7-3, and 1-7-4) except in CHnv and the lower part of TSw2. In CHnv there is no visible change in these three quantities as time progresses. Matrix saturation and hydraulic conductivity do not visibly change in time, because pressure head does not visibly change in time. Examination of Equation 4 shows that the $\partial\psi/\partial z$ derivative and second derivative account for most of the necessary change in flux.

Figures 1-8-5 and 1-8-6 present the average linear water velocity in the matrix and the fractures, respectively, plotted against distance above the water table at successive times. The primary difference in matrix-water velocities between the CHnz and CHnv cases occurs in the CHn unit. At the top of the CHnv unit, matrix-water velocities are greater than in the CHnz unit (approaching an order of magnitude greater). Because the flux through the matrix is approximately the same in both cases, the different velocities can be attributed to differences in the area available for flow. In the upper part of CHnv, the area available for flow is constrained by the low matrix saturation. Near the water table, where both CHnz (Case 7) and CHnv (Case 8) are saturated, the water velocity is approximately a factor of 2 greater in CHnz. This difference occurs because at full saturation the area available for flow is constrained by the porosity, and the porosity of CHnz is approximately half the porosity of CHnv.

Velocity of the fracture water (in Case 8 as in Case 7) remains negligible in all units, because although the fractures are desaturated and have very little area available for flow, the flux in the fractures is vanishingly small (Equation 12). (Figure 2-8-6 shows fracture-water velocities that are more quantitatively correct.)

Figures 1-8-7 through 1-8-12 show the same quantities discussed above, plotted against time at specified elevations. The normalized flux profiles shown in Figure 1-8-7 are similar to those for the CHnz case (as compared with Figure 1-7-7). The flux change occurs slightly faster at the lower elevations in Case 8. Indeed, the flux change occurs simultaneously at elevations of 0 and 130.5 m in Figure 1-8-7. These elevation lines overlap in Figure 1-8-7, but are distinct in Figure 1-7-7, indicating that the flux front passes through CHnv faster than through CHnz (although both are dominated by the rate at which the new flux exits PTn).

The pressure-head plots are also similar in the CHnv and CHnz cases (Figures 1-8-8 and 1-7-8). In Figure 1-8-8, immediately above the TSw2/CHnv interface (130.5-m elevation), the pressure head is more negative than in Figure 1-7-8, and it is nearly constant over time. That the influence of CHnv extends well into TSw2 is evinced by the 219.5-m elevation line, which is also more negative than the corresponding line in Figure 1-7-8.

Matrix saturation versus time is seen in Figure 1-8-9. The matrix is approximately 80 to 90% saturated in the welded units (TCw, TSw1, and TSw2), with a slight increase in saturation as time progresses. The 130.5- and 219.5-m lines indicate lower saturation at these elevations than in the CHnz case. The greatest increase in saturation occurs immediately above the PTn/TSw1 interface at the 465.8-m elevation line, and the change in saturation at this elevation lasts almost the duration of the problem, from approximately 2,000 to 200,000 years.

Figure 1-8-10 shows the hydraulic-conductivity plots. The 130.5- and 219.5-m elevation lines are somehwat different from the corresponding lines in Figure 1-7-10, showing how the influence of the highly-conductive CHnv Unit extends into TSw2. The increase in hydraulic conductivity in PTn (465.7- and 503.4-m elevation lines) is significant because of the large jump in pressure head (and hence, saturation) in this unit.

The average linear velocity of water in the matrix and the fractures over time is presented in Figures 1-8-11 and 1-8-12. Because flow is primarily in the matrix, the average linear velocities respond primarily to the level of matrix porosity and saturation. The only significant fracture-water velocities are seen at the water table, where the fractures are fully saturated. (Figures 2-8-6 and 2-8-12 contain the quantitatively correct fracture-water velocities.)

3.5.5 Case 9

Figures 1-9-1 through 1-9-12 present the required output plots for COVE 2A Case 9. This case has CHnz as the bottom unit and a flux of 1 mm/yr imposed at the top of the vertical column, on an initial steady-state flux of 0.5 mm/yr. This change in flux

causes a transition from predominantly matrix to predominantly fracture flow in TSw1, TSw2, and CHnz. TCw begins in predominantly fracture flow; PTn begins in predominantly matrix flow and, because its saturated matrix conductivity is sufficiently large, it remains in predominantly matrix flow.

The plot of normalized flux versus distance above the water table is shown in Figure 1-9-1. Contrasting this plot with the corresponding plots for the flux change from 0.1 to 0.2 mm/yr, the most obvious difference is the time required to go from the initial to the final state. This process takes approximately 450 years in Case 9 as opposed to approximately 200,000 years in Case 7.

Another significant difference between this case and Case 7 is that the flux pulse does not disperse down the mountain, but rather proceeds as a near step function. The steepness of the flux front is dependent to a certain extent on scaling (flux is calculated from pressure head: the pressure-head change is only 8 meters in TSw1 for Case 9, whereas in Cases 7 and 8 it is approximately 40 meters), but other factors are also involved, as indicated in Equation 17. For a discussion of flux-front shape, see Dudley et al. (1988).

The shape of the flux front in PTn is the exception to the step-function shape. This situation should be analogous to the situation that exists in Case 7—a large pressure head jump required to support the flow in TSw1 should cause a significant pressure head jump in PTn, and therefore, a long filling time to increase the saturation in this unit. Examination of Figure 1-9-1 reveals that it takes approximately 250 years of the total problem time of 450 years for the flux pulse to pass through PTn. However, because the lower half of PTn is nearly saturated at the beginning of the problem (Figure 1-9-3), the damming effect occurs near the top of PTn. Although the flux front begins to disperse in TSw1 similarly to the situation in Case 7 when the flux at the PTn/TSw1 interface reaches approximately 0.6 mm/yr (a normalized value of approximately 0.6 on the plot, corresponding to a pressure head of -1 meter), incipient fracture flow causes an abrupt change in the hydraulic conductivity and capacitance for TSw1. The wetting of PTn ceases because the pressure-head change is virtually complete. The flux in PTn and the upper part of TSw1 (where the matrix is saturated) rapidly climbs to the imposed value of 1 mm/yr, and the flux front forms a step-function shape immediately above the point in TSw1 where the matrix is not yet fully saturated. The pulse then proceeds through the lower units as a sharp front, with predominantly matrix flow ahead of the front and significant fracture flow behind it.

The pressure-head profiles for Case 9 are presented in Figure 1-9-2. The change in pressure head is quite small compared to Cases 7 and 8. For the TSw1 unit in Case 9, the difference between the initial and final states is typically 8 meters of pressure head; in Cases 7 and 8, the difference is approximately 40 meters. In upper TCw, the pressure head change is not visible at the scale of the plot. The TCw matrix has a saturated conductivity of approximately 0.3 mm/yr; at the initial condition of 0.5 mm/yr, there is

already flow in the fractures. To go from 0.5 to 1 mm/yr in a fracture-flow regime requires a pressure-head change of only about 0.1 meters with the characteristic curves being used.

The hydraulic-conductivity plot (Figure 1-9-4) shows that the conductivity doubles with the flux in most units, indicating that the conductivity term in Equation 4 is the major contributor to the doubling of the flux in this case. Again, an exception is PTn, which has a conductivity several orders of magnitude greater than the imposed flux. Flow in this unit is controlled by the $\partial\psi/\partial z$ term from Equation 4, and the PTn/TSw1 dam (effectively an interior boundary condition), and no change in conductivity is required. Another exception occurs at the hydrologic-unit interfaces, where the pressure head must adjust between discontinuous hydrologic properties. At these interfaces, the $\partial\psi/\partial z$ term in Equation 4 becomes significant, and there is a drop in the value of the conductivity coefficient. The decrease in conductivity is most noticeable at values where it varies most nonlinearly with pressure head—i.e., during fracture flow. The spikes in conductivity at the TSw1/TSw2 and TSw2/CHnz interfaces in Figure 1-9-4 reflect this observation. Note that the spikes only occur at conductivities reflecting predominantly fracture flow and not at conductivities reflecting matrix flow.

The average linear velocities of water in the matrix and the fractures versus distance above the water table are shown in Figures 1-9-5 and 1-9-6. In the lower units, the matrix-water velocity shows a curious pattern of increase as time progresses: the velocity doubles with the doubling flux, then abruptly drops back to a lower level, forming the "fins" shown in Figure 1-9-5. As the pressure-head pulse passes, the pressure head goes from -8 to near 0 meters and the water velocity is doubled. This doubling takes place almost entirely in the matrix, because there is insignificant saturation in the fractures over most of this pressure-head change. Insignificant saturation implies insignificant conductivity. However, at about -1 meters the fractures begin to wet, and substantial flow initiates. At this point, matrix-water velocity subsides, and fracture-water velocity increases abruptly as shown in the sudden jump in the velocity curves in Figure 1-9-6.

Neither TCw nor PTn shows the velocity fins, because TCw starts and stays in predominantly fracture flow (except near the interface with PTn) and PTn starts and stays in predominantly matrix flow. Fracture velocity approximately doubles in TCw; matrix velocity approximately doubles in PTn.

Figure 1-9-6 indicates qualitatively that fracture flow initially occurs only in the upper reaches of TCw and in the lowermost reaches of CHnz, near the water table. In TSw1, TSw2, and CHnz, fracture flow is abruptly initiated as the flux front passes through the column. If this figure is superimposed on Figure 1-9-5, it can be seen that the fracture velocity initiates exactly as the matrix velocity begins to fall after the crest of the matrix/fracture transfer fin. There is no appreciable fracture flow in PTn, hence no appreciable fracture-water velocity.

The same six physical quantities discussed above are plotted against time at specified elevations in the next six figures. Normalized flux versus time is shown in Figure 1-9-7. At all elevations, the value of the normalized flux jumps from 0.5 to 1 as the flux front passes down the mountain. (Elevations 503.4 and 503.8 m appear to show a more gradual climb than the others; however, the reduced slope is an artifact of the logarithmic time scaling.) The wetting of PTn is evinced by the long leading edges to the 465.3- and 465.7-m elevation lines. When the flux reaches the value of the saturated matrix conductivity in TSw1—about 0.6 mm/yr, coincidentally matching the nondimenional 0.6 value on the normalized scale—the abrupt transfer to fracture flow causes an abrupt increase in the flux. It is interesting to contrast this plot and its abrupt change in flux over time with Figure 1-7-7 and its gradual flux change over time.

Figure 1-9-8 presents pressure head plotted against time. At the 503.8-m elevation line, no perceptible change in pressure head occurs until about 30 years have elapsed. A gradual increase in the pressure head is then shown by the elevations in the neighborhood of PTn. This gradual increase corresponds to the 250 years it takes to wet PTn. More abrupt jumps in pressure head occur in the units below PTn.

Figure 1-9-9 presents matrix saturation versus time. The plot shows how near to complete saturation the matrix is throughout the problem. The 503.4- and 503.8-m elevation lines (immediately below and above the TCw/PTn interface) are farthest from complete saturation, but they are still over 90% saturated, and during the course of the problem the saturation increases only a few percent in this area. (The matrix is unsaturated at this interface because the large matrix conductivity of PTn drains TCw.)

Hydraulic conductivity versus time is shown in Figure 1-9-10. Elevation lines 465.7 and 503.4 m, within PTn, show the greatest conductivity. Conductivity changes little over time at these elevations; the conductivity at 503.4 m increases slightly with the increased matrix saturation beginning at about 50 years. The 503.8-m elevation line shows a similar increase, but the conductivity of the welded TCw Unit is much lower. Figure 1-9-2 shows the steep pressure-head gradient needed to support 0.5 to 1 mm/yr flow with the low conductivity at this elevation. The lower elevations, 130.5, 219.5, 335.6, and 465.3 m show sharp increases in conductivity as the flux front passes. The 219.5- and 465.3-m elevation lines increase to a greater conductivity than the 130.5- and 335.6-m elevation lines because both are immediately adjacent to interfaces where the pressure head changes with distance, thus mitigating the conductivity term in Equation 4 (as discussed previously).

Figures 1-9-11 and 1-9-12 show the time plots of the average linear velocity of water in the matrix and the fractures. The matrix/fracture transfer fins in the matrix velocity, evident in Figure 1-9-5, are less evident in Figure 1-9-11. Because the transient-flow cases with fracture flow took tens of thousands of time steps (Table 3-2), only every hundredth time step was recorded to produce these plots; therefore resolution suffered.

In Figure 1-9-11, however, a matrix/fracture transfer fin can be seen at the 219.5-m elevation line, and a vestigial fin can be seen at the 465.3-m elevation line (a large fin would not be expected so close to PTn because there is not enough space for it to develop). (In the final set of calculations every tenth time step was recorded, and the fins are clearer in Figure 2-9-11.) Fins are not expected to be seen in the 0-, 465.7-, 503.4-, or 503.8-m elevation lines because these elevations exhibit no switch from predominantly matrix flow to predominantly fracture flow.

For the fractures, the sudden jump in average linear velocity is pronounced at all elevations shown in Figure 1-9-12, except in the neighborhood of the TCw/PTn interface where fracture flow is negligible. Note that the fracture-water velocity doubles at the 0-m elevation (the water table), as it should for a saturated regime. Again, more accurate fracture-water-velocity values, especially at elevations with low saturations, are given in Figures 2-9-6 and 2-9-12.

3.5.6 Case 10

The next set of Figures, 1-10-1 through 1-10-12, shows the elevation and time plots for Case 10, where a flux of 1 mm/yr is imposed on an initial steady state of 0.5 mm/yr and the bottom unit is now CHnv. Unlike the cases for a flux change of 0.1 to 0.2 mm/yr, where the water flow histories for CHnz and CHnv were similar, the CHnz and the CHnv cases are considerably different.

Normalized flux versus distance above the water table at different times is presented in Figure 1-10-1. The influence of CHnv can be seen at the TSw2/CHnv interface and extending upwards into TSw2. The flux change is retarded as the front approaches this interface. Overall, approximately 1,500 years elapse before the new steady state is reached, as compared to 450 years for the CHnz case.

Examination of the pressure-head profiles in Figure 1-10-2 and the matrix-saturation profiles in Figure 1-10-3 helps to explain the retardation of the flux front. The pressure head at the TSw2/CHnv interface is almost -130 meters, which means that CHnv is strongly draining the TSw2 Unit. Figure 1-10-2 indicates that the influence actually extends up into TSw1. The matrix saturation drops dramatically at the TSw2/CHnv interface (Figure 1-10-3), and creates a region in the lower half of TSw2 that must be filled with water in order for the flux to change. In Case 9 only one region, in the neighborhood of the TCw/PTn interface, must fill with water to support the new flux (Figure 1-9-3); in Case 10 there are two regions. Thus the flux pulse takes almost 1,000 years longer to traverse the column in Case 10 than it does in Case 9.

The flux pulse not only takes longer to cross CHnv than it does to cross CHnz, but it also changes character. Across CHnv the flux front spreads until the change in flux is

nearly simultaneous through most of the unit. Much of the spreading is caused by the filling of the lower region of TSw2, which imposes a water-flow constraint. However, using Equation 17 it can be shown that the width of the flux front in CHnv should be approximately 400 meters; using Equation 18 the transit time is shown to be on the order of 1,000 years. Thus, even without the TSw2/CHnv interface, the flux front would spread in CHnv.

Hydraulic conductivity versus elevation is presented in Figure 1-10-4. The upper three units in this case and Case 9 show similar conductivity levels. In Case 10 the conductivity is much lower at the TSw2/CHnv interface than at the TSw2/CHnz interface in Case 9. The low conductivity impedes the filling of the lower half of TSw2 and further slows the flux pulse.

Interestingly, matrix saturation and conductivity levels in CHnv are quite similar to levels shown in CHnv in Case 8 (Figures 1-8-3 and 1-8-4), despite an order of magnitude difference in flux. The fluxes being considered are still far removed from the saturated conductivity of CHnv (8,400 mm/yr), and the discussion of behavior of CHnv in Case 8 applies for this case.

Matrix-water and fracture-water average linear velocities are presented in Figures 1-10-5 and 1-10-6, respectively. In Figure 1-10-5, as in Figure 1-9-5, matrix/fracture transfer fins are visible, although not in PTn or CHnv because no appreciable fracture flow occurs in these units (except near the water table in CHnv). As shown in Figure 1-10-6, fracture-water velocity in CHnv is negligible. (Figure 2-10-6 shows fracture-water velocity values that are more accurate than those shown in Figure 1-10-6.) The discussion of the average linear water velocity in CHnv given for Case 8 also applies here.

Figure 1-10-7 shows normalized flux plotted against time at specified elevations. Of note is the 300-year-long ramp on the leading edge of the 465.3- and 465.7-m elevation lines. These lines occur near the bottom of PTn, and the ramp corresponds to the wetting of PTn. The elevation lines at 503.4 and 503.8 m, near the top of PTn, do not reach the final flux level until PTn is fully saturated. The change from initial to final state in the TSw units is rapid (219.5- and 335.6-m elevation lines); the change in CHnv is more gradual, and occurs at nearly the same time throughout the unit, as evinced by the 130.5-m elevation line (immediately above CHnv) and the 0-m elevation line. The simultaneous nature of the flux change over the width of unit shows the spreading of the flux front described above.

Figure 1-10-8, the change in pressure head with time, shows that the pressure head just above the TSw2/CHnv interface (at an elevation of 130.5 m) is about -130 meters, indicating that CHnv is exerting a strong suction on TSw2. The pressure head change itself is seen to be slight at nearly all the selected elevations; only the 219.5-m curve in TSw2 shows any significant change over time.

Matrix saturation and hydraulic conductivity are shown in Figures 1-10-9 and 1-10-10. For the upper units, the discussion for the corresponding figures for Case 9 suffices. For the lower units, the discontinuity in hydrologic properties at the TSw2/CHnv interface is of interest. Immediately above CHnv (the 130.5-m elevation line), the pressure head is -130 meters, but the matrix saturation is still 83%. Just 0.2 meters away, in CHnv proper, the matrix saturation is approximately 10% (Figure 1-10-3).

Figures 1-10-11 and 1-10-12 present average linear velocities in the matrix and in the fractures versus time. Again the discussion for the corresponding figures for Case 9 is applicable for the upper units. In Figure 1-10-11, the 130.5-m line shows a gradual doubling of matrix velocity with no matrix/fracture transfer fin. (Figures 2-10-6 and 2-10-12 show the quantitatively correct fracture-water velocities.)

3.5.7 Case 11

The Case 11 problem consists of a flux of 8 mm/yr imposed at the upper boundary on a steady-state flow of 4 mm/yr, with CHnz as the lowermost unit. Fracture flow predominates through all the units except PTn throughout the course of the problem.

The normalized flux versus elevation at specified times is presented in Figure 1-11-1. The time taken for the transition from 4 to 8 mm/yr for the entire column is approximately 3 years. The flux front proceeds abruptly in both time and space, except in PTn and TSw1. The constriction in flow at the TCw/PTn interface and the wetting of PTn are discussed above for Cases 9 and 10 and are similar for this case. However, the time scale for the process is greatly reduced, primarily because the changes in pressure head and saturation in PTn are slight (as discussed for Figures 1-11-8 and 1-11-9).

Several instabilities are seen in the flux profiles in Figure 1-11-1: at the TSw1/TSw2 interface, at the water table, and at the peak of the flux front in the lower geologic units. The instabilities at the flux-front peak are caused by the inability of the difference equations to track a change that occurs at a smaller scale than the spacing of the mesh points; the effect (sometimes called Gibb's phenomenon) can be mitigated by a finer mesh spacing. The other instabilities are inherent in highly nonlinear problems being solved with a Picard-iteration scheme; these have been eliminated by the use of Newton's method in the final set of calculations (Figure 2-11-1).

Figure 1-11-2 presents the plot of pressure head versus distance above the water table. At this scale, there is no perceptible change in pressure head in any of the units. In fact, in the TSw units, the pressure head changes approximately 0.1 meters to cause the flux to double. This effect is caused by the highly nonlinear characteristic curves being used to model the fractures.

The plots of matrix saturation versus elevation, Figure 1-11-3, show that the matrix is essentially saturated, except at the TCw/PTn interface. Saturation change is primarily in the fractures: the fractures occupy approximately 0.01% of the volume, and therefore, any change would be undectable at this scale. It also follows that a doubling in flux occurs with the introduction of only a small amount of water.

Figure 1-11-4 shows the hydraulic conductivity change with distance above the water table. In all units except PTn, the conductivity doubles with the flux (and therefore the conductivity term dominates in Equation 4); in PTn, the conductivity is much greater than the flux and, as in Cases 7 and 8, flow is primarily driven by the spatial change in pressure head—i.e., small changes in a near-zero gradient. The discussion of Figure 1-9-4 includes an explanation of the spikes at the TSw1/TSw2 and TSw2/CHnz interfaces. At the TCw/PTn interface the conductivity values are relatively low because the suction of PTn partially desaturates the bottom of TCw.

The variation of matrix-water velocities with distance above the water table is shown in Figure 1-11-5. The average linear velocity in the matrix is essentially constant for each unit, because flow is predominantly in the fractures. In PTn, the flow is predominantly in the matrix, and the velocity increases in proportion to the flux. The velocity spike at the TCw/PTn interface is in response to the decreased area available for flow caused by PTn draining TCw.

The average linear velocity of water in the fractures is shown in Figure 1-11-6. In the units where significant fracture flow occurs (TCw, TSw1, TSw2, and CHnz) the water velocities are much greater in the fractures than in the matrix. The maximum area available for flow in the fractures is between two and four orders of magnitude lower than the maximum area available for flow in the matrix, and much of difference between fracture-water and matrix-water velocity is attributable to this disparity in area (at higher fluxes, however, the flux component of the velocity equation would begin to dominate). PTn, with its highly conductive matrix, does not show fracture flow.

Figure 1-11-6 also shows that velocity in the fractures approximately doubles as the flux doubles, indicating that the saturation of the fractures is not changing significantly (i.e., that the area available for flow is not changing significantly).

The normalized flux versus time at specified elevations is presented in Figure 1-11-7. All elevations show a relatively quick transition from the initial to the final flux (differences in the slope of the elevation lines are due primarily to the logarithmic time scale). The leading edge of each elevation line shows less radius of curvature than the trailing edge; i.e., the flux change initially proceeds quickly but slows as the flux approaches 8 mm/yr. Capacitance increases as the fractures increase in saturation (in TSw2 at -0.95 meters of pressure head, corresponding to 4 mm/yr of flux, the capacitance coefficient is approximately 2.3×10^{-4}; at -0.85 meters of pressure head, corresponding to 8 mm/yr of flux, the capacitance coefficient is approximately 2.6×10^{-4}). However, the slowing in the

flux change in TSw2 is probably due to a slowing in the flux change in PTn, as can be surmised from the shape of the 6-month time line in Figure 1-11-1.

The plot of pressure head versus time is shown in Figure 1-11-8. At the scale used for the pressure-head axis, the pressure-head change is virtually imperceptible for most of the elevation lines. The exception is at an elevation of 503.8 m, in TCw, where PTn applies suction that desaturates the lower part of the unit and forces predominantly matrix flow. At an elevation of 503.4 m the pressure head changes slightly as PTn is wetted. The other elevations are predominantly experiencing fracture flow, and the pressure-head change is only about 0.1 meters.

Matrix saturation versus time is presented in Figure 1-11-9. Confirming what has already been seen in Figure 1-11-3, the matrix-saturation changes are imperceptible at most elevations, with the exception of the TCw/PTn interface. The 503.8-m elevation line immediately above the TCw/PTn interface shows an increase in saturation of approximately 1%.

The hydraulic-conductivity change over time is presented in Figure 1-11-10. At most elevations presented, the hydraulic conductivity doubles in concert with the flux, implying that the spatial derivative of pressure head is a constant (i.e., the characteristic solution or unit-head gradient). The conductivity change is imperceptible at elevations in the neighborhood of PTn, where flow is controlled by the spatial derivative of the pressure head.

Figures 1-11-11 and 1-11-12 show the average linear water velocities in the matrix and in the fractures, respectively. The changes in matrix-water velocity over time occur at elevations of 0, 465.7, 503.4, and 503.8 m. The doubling of the matrix-water velocity at the water table is an indication that the pressure-head gradient doubles at this point. (In a saturated-flow problem, the conductivity is a constant and the area available for flow is virtually a constant; hence the velocity could only vary with the pressure-head gradient.) At the 130.5-, 219.5-, and 335.6-m elevations the change in velocity is reflected in the fracture water. The fracture-water velocity doubles at all elevations shown; however, some of the velocities are minuscule—notably, those at the elevations in or just above PTn—and have no effect on the overall flow. Again, see the corresponding figure in the final set of calculations for more quantitatively correct values.

3.5.8 Case 12

The last case considers transient flow with a flux change from 4 to 8 mm/yr and a vitric bottom unit, CHnv. As in the previous case, flow is predominantly in the fractures in units other than the high-conductance and high-capacitance units, PTn and, in this instance, CHnv.

Normalized flux versus distance above the water table is shown in Figure 1-12-1. As in Case 11, there are instabilities (notably in the 1.5-year time line). As in the contrast between Cases 10 and 9, the flux front is greatly retarded in Case 12 in CHnv when compared with Case 11 in CHnz. Transition from initial to final state in the column takes 150 years for this case, whereas it takes 3 years for Case 11.

The plot of the pressure head versus distance above the water table, shown in Figure 1-12-2, is different from the corresponding plot for Case 11 (Figure 1-11-2) starting at the TSw2/CHn interface and continuing into CHn. The pressure head drops from near 0 to about -120 meters at the TSw2/CHnv interface. The effect is similar to the TCw/PTn interface where a highly conductive unit applies a suction force on a relatively impermeable unit, as presented in the discussion of Figure 1-9-1. The large spatial change in pressure head seen in CHnv is a major factor in determining the flux when Equation 4 is solved. Figure 1-12-2 is similar to Figure 1-11-2 in that temporal changes in pressure head are for the most part indiscernible at the scale of the plot. (This scaling was necessary to show the extreme values.)

The matrix-saturation plot (Figure 1-12-3) shows that the matrix is saturated except at the TCw/PTn and TSw2/CHnv interfaces. The only changes in saturation over time are visible in the neighborhood of the TSw2/CHnv interface. The change in saturation corresponds to the slight change in pressure head at this same interface. The matrix is approximately 25% saturated at the top of CHnv. Contrast this value with the values in CHnz (Figure 1-11-3), which is saturated at these fluxes.

Figure 1-12-4 presents the hydraulic conductivity change over distance above the water table. Conductivity does not change significantly with time in PTn and CHnv, for reasons discussed in Case 9. The conductivity in CHnv does change spatially because of the increasing saturation caused by the presence of the water table. In the other units, the conductivity doubles with the doubling flux, and the conductivity spikes noticeably at several unit interfaces (Section 3.5.1).

Figure 1-12-5 shows the average linear velocity profiles for water in the matrix. The velocity of the matrix water does not change significantly in the predominantly fracture-flow units (TCw, TSw1, and TSw2). In PTn and CHnv, the velocity doubles as the flux doubles. In this instance, the doubling is expected because the matrix saturation does not change.

Average linear water velocity in the fractures is shown in Figure 1-12-6. The water velocity doubles with the flux in TCw, TSw1, and TSw2, indicating that the saturation in the fractures changes little. Fracture-water velocity is negligible in PTn and CHnv; however, the velocity also doubles in these units. (Figures 2-12-6 and 2-12-12 present the quantitatively correct fracture-water velocities.)

Figures 1-12-7 through 1-12-12 present the time plots for the variables specified above. These plots are virtually identical to the corresponding Case 11 plots, except at the 130.5-m elevation where the vitric properties used for CHn exert their influence. (Notice the difference in time scales between the Case 11 and the Case 12 plots.)

Figure 1-12-7 presents normalized flux with respect to time. Although the upper four elevations are similar to those shown in the corresponding plot for Case 11 (Figure 1-11-7), the resolution is poor because only every hundredth time step was recorded. The lower two elevations (130.5 m and 219.5 m) show the prolonged times associated with the constriction in flow at the TSw2/CHnv interface.

Contrasting Figures 1-12-8, 1-12-9, and 1-12-10 with the corresponding figures for Case 11 shows that the major difference is in the position of the 130.5-m elevation line. This elevation is immediately above the TSw2/CHnv interface and reflects the tremendous suction exerted by CHnv; pressure head, matrix saturation, and hydraulic conductivity are all significantly reduced from the values in the Case 11 figures. The 130.5-m elevation line in the three figures also tends to mimic (at a later time) the shape of the 503.8-m elevation line, which occurs in similar circumstances immediately above TCw/PTn interface.

The plots of average linear velocity versus time (Figures 1-12-11 and 1-12-12) show that matrix-water velocity is significant at both the 0- and 130.5-m elevation lines when compared with the corresponding Case 11 figures; however, fracture-water velocity at these elevations is greatly reduced. The increased matrix-water velocity at the water table is attributable to the greater matrix conductivity term for the CHnv unit in Equation 4. The fracture-water velocity is less because more of the flux is therefore carried by the matrix.

4.0 FINAL CALCULATIONS

4.1 Changes to the Computational Modules of TOSPAC

Errors and peculiarities in the initial set of calculations led to several changes in the computational modules of TOSPAC. These errors and the resulting modifications were discussed in Section 3.5.

In addition, the initial calculations showed that TOSPAC was inefficient. For the final calculations, efficiency was important for two reasons. First, a new analytic formula for calculating mesh-point spacing (Section 4.2) indicated that over 2,000 mesh points were necessary to ensure an accurate solution—raising the prospect of increasing computer times by a factor of three. Second, the compressibility-of-water coefficient (β'_w) in both the capacitance terms and the conductivity terms in Equations 1 (STEADY) and 4 (DYNAMICS) were activated. (The improvement in accuracy for the COVE 2A problems was insignificant, as a comparison of the results of the initial and final calculations shows; however, the solution required approximately twice as many evaluations of the van Genuchten functions and therefore approximately twice as much computer time.)

Efficiency modifications made to STEADY before beginning the final set of calculations were as follows.

1) The region of the mesh being iterated as a boundary-value problem (Section 2.3) was restricted to a maximum of 120 mesh points. This modification caused the solution technique to look more like an initial-value problem and minimized the work done in slowly converging regions of the mesh.

2) The convergence criterion for the region of the mesh being iterated as a boundary-value problem was increased from 10^{-6} to 10^{-2}. At first glance, this modification appeared to be self-defeating, potentially causing errors in the solution. However, the stability controls introduce an error whenever they are enacted; this modification allows the region of the mesh being iterated to "converge" more easily, and the stability controls are not enacted unnecessarily. Thus, STEADY executes faster with no degradation in accuracy.

Efficiency-related modifications made to DYNAMICS before the final set of calculations were more significant than those made to STEADY:

1) The solution technique used in DYNAMICS was modified by the implementation of Newton's method (Section 2.3). Newton's method allowed greater stability in the calculations. This stability was a mixed blessing: greater stability allows larger time steps and greater mesh point spacing; however, what is allowed is much greater than

what is required for an accurate solution. With $\Omega = 1$ and large time steps, a significant amount of spreading could be seen in the flux profiles of the cases dominated by fracture flow. The final set of calculations were executed with $\Omega = 0.5$ for the predominantly fracture-flow cases, with time steps and mesh-point spacing bounded as discussed below.

2) Analytic bounds on the time step and the mesh spacing were developed (Sections 4.2 and 4.3). The time-step bounds were used to develop a new time-step controller for DYNAMICS (Section 2.5). The mesh-spacing bounds created a need to rethink the question of accuracy and efficiency. The number of mesh points required for an accurate solution demanded a more efficient solution technique for DYNAMICS. However, a large number of mesh points do not guarantee an accurate solution. The Picard-iteration technique used in the initial set of calculations was assumed to be accurate primarily because its unstable nature caused exceedingly small time steps. The implementation of Newton's method allowed very large time steps to be taken, and when $\Omega > 0.5$, exceedingly large time steps can be taken, thus requiring the time-step bounds.

Because of the vectorization effort in the initial set of calculations, it was known that improving the evaluation of the van Genuchten functions could significantly aid efficiency. Unfortunately, there was not enough time before the final calculations to investigate this matter. After performing the final calculations, DYNAMICS was modified to create a table of the van Genuchten-function values. Rather than evaluate the van Genuchten functions at each iteration, a table look-up and linear interpolation was performed. Preliminary results show that run times could have been decreased by a factor of four from those presented in Section 4.4.

4.2 Calculational Mesh

For the final set of calculations, the mesh was created using analytic formulations based on length scales inherent in Equations 1 and 4. This section gives a brief overview of the subject. Dudley et al. (1988) give a more rigorous treatment in Section 2.3 of their report.

For STEADY calculations, Darcy's law yields two restrictions for selecting appropriate, general mesh-point spacings:

$$\Delta z < \left| \frac{\psi}{1 + q/K} \right| \text{ and}$$

$$\Delta z < \left| \frac{K/K'}{1 + q/K} \right| , \tag{19}$$

where Δz is the mesh-point spacing and K' is the derivative of hydraulic conductivity with respect to pressure head.

These two restrictions work best for the case where the pressure-head solution approaches the characteristic solution (the pressure head at which the hydraulic conductivity equals the flux, also called the unit head gradient) in a nonlinear manner, i.e., where $\Delta\psi \gg \Delta z$. This situation occurs in a geologic unit that must carry the imposed flux at high pressure heads immediately above a geologic unit that can carry the imposed flux at very low pressure heads, e.g., Case 6 at the TSw2/CHnv interface where CHnv is applying a suction to drain TSw2 (Figure 2-2/4/6-2).

For the special case where the pressure-head solution asymptotically approaches the characteristic solution (the transition point between $\Delta\psi \gg \Delta z$ and $\Delta\psi = 0$) the following equation holds:

$$\Delta z < \left| \frac{q}{K'^c} \right| , \tag{20}$$

where K'^c is the derivative of hydraulic conductivity with respect to the pressure head at the characteristic solution. (Steady-state solutions in one dimension always reach the characteristic solution if the geologic unit is thick enough.)

Sometimes a steady-state solution offers no appropriate length scale. Where the pressure-head solution changes in a linear manner (most obviously where $\Delta\psi \approx -\Delta z$ and $\Delta\psi = 0$) any two points can determine a line, and the length scale is undefined. The $\Delta\psi \approx -\Delta z$ situation occurs in a geologic unit that can carry the imposed flux at very low pressure heads immediately above a geologic unit that must carry the imposed flux at high pressure heads. Consider, for example, Case 6 where TSw1 is applying a pressure to dam PTn immediately above it. The $\Delta\psi = 0$ situation occurs at the characteristic solution. Also consider Case 5, where most of TCw, TSw1, TSw2, and CHnz are at a constant pressure head.

These situations do not necessarily imply that mesh points can be spaced as far apart as possible. Prudence dictates a reasonable spacing to ascertain that areas where linearity may be violated have not been missed. Also, there could be length scales in the transient-flow or transport solution (these calculations could use the same mesh) that should not be overlooked.

For DYNAMICS calculations, the mesh-point spacing can be approximated in terms of the radii of curvature of the leading and trailing edges of a flux pulse. This approximation is as follows:

$$\Delta z < \min\left\{\left|\frac{q_0}{K_0' + C_0 v_{fr}}\right|, \left|\frac{q_1}{K_1' + C_1 v_{fr}}\right|\right\} , \tag{21}$$

where z is elevation, Δz is a measure of the mesh-point spacing, q is flux, K' is the derivative of hydraulic conductivity with respect to pressure head, C is storage capacity, v_{fr} is the velocity of the flux front, and the subscripts 0 and 1 imply that these parameters occur at the leading and trailing edges of the flux front, respectively.

It should be noted that in Equations 19 through 21 several variables appear that can only be exactly defined when a solution is known.

By using Equations 19 through 21 and information gained during the initial set of calculations, a single mesh was defined for all cases—steady-state and transient—of the final set of calculations. Requiring the finest mesh were Cases 9, 10, 11, and 12 in the welded units, with the radii of curvature being approximately 0.3 meters. The mesh was constructed with an average spacing of 0.25 meters and contained 2303 mesh points, approximately three times as many as used in the initial calculations.

The calculational mesh is presented in Figure 2-1, along with the geologic units and material assignments that compose the problem geometry. Each rectangle in the mesh column indicates ten mesh points. The bottoms of the columns (0.0 m on the plot) correspond to the water table; the tops (530.4 m) correspond to the ground surface.

4.3 Time Step

Given the above bound on the mesh spacing for a transient-flow calculation, the following upper bound on the time step can be calculated:

$$\Delta t < \frac{\Delta z}{|v_{fr}|} . \tag{22}$$

This inequality states that the time step should be less than the amount of time it takes the flux front to cross the distance between adjacent mesh points.

It is not possible to calculate v_{fr} for the general case. However, using this inequality, time-step controllers based on several different time-dependent characteristics of the unsaturated-flow model were tested. The time-step controller that most closely follows the upper bound in Equation 22 is as follows:

$$\Delta t = f\frac{K}{\dot{K}}\ , \tag{23}$$

with $f = 0.1$. Implementation of the entire time-step controller is discussed in Section 2.5. The transient-flow cases in the final calculations used this time-step controller almost exclusively, despite other facets of the implementation.

For Case 11 with the mesh defined in Section 4.2, Equation 22 specifies that the time step when the flux front is in Unit TSw1 should be less than 0.8 days. Using Equation 23, the time step is 0.7 days.

4.4 Run-Time Information

Table 4-1 presents the run-time information for the final calculations.

TABLE 4-1
RUN-TIME INFORMATION FOR THE FINAL SET OF CALCULATIONS

Case	Number of Mesh Points	Computer	Number of Time Steps	CPU Time (sec)
1-6	2303	VAX 8650	≈ 200*	<160
7	2303	VAX 8650	124	1056
8	2303	VAX 8650	124	985
9	2303	VAX 8650	2327	24,142
10	2303	VAX 8650	1672	17,389
11	2303	VAX 8650	861	7301
12	2303	VAX 8650	1070	9164

* Iterations rather than time steps (STEADY does not implement time). Also, because STEADY iterates over only a portion of the mesh at one time, this number has been adjusted to represent iteration over the entire mesh.

Cases 1 through 12 were run on a VAX 8650 computer. All 12 cases used the same calculational mesh with 2303 mesh points; this mesh is approximately three times as large as the mesh used in the initial calculations and would have led to a factor of three increase in run time if the efficiency of STEADY and DYNAMICS had not been improved. (With a general linear-system solver this mesh increase would cause a factor of nine increase in run time—a quadratic function of the size of the mesh. However, TOSPAC uses a simple tridiagonal-matrix solver that allows an increase in run time that is a linear function of the size of the the mesh.)

In general, the final steady-state runs took approximately one-half as long as the initial runs, and the final transient-flow runs took approximately one-eighth the time of the initial runs (corrected for the different speeds of the CRAY X/MP and the VAX 8650). The number of time steps given in Table 4-1 for the transient-flow cases is not the total number of iterations: at each time step the Newton's method performed approximately four subiterations.

The time-step factor was 0.1 for all the transient-flow cases; however, the implicitness factor was set to 0.6 for Cases 7 and 8, and 0.5 for Cases 9 through 12. The implicitness factor $\Omega = 0.5$ minimizes truncation error, but is less stable than larger factors. This setting caused spikes in the flux profiles in Cases 7 and 8 (and these cases should have been the most stable, which is somewhat of a paradox). Two calculations were made for Case 7, one with a reduced time-step factor (0.05) and the other with an increased implicitness factor (0.6). In both calculations the spikes disappeared and virtually identical results were returned. Because the increased implicitness factor required much less computer time to be used, these calculations are the ones reported.

As mentioned in Section 4.1, using a table look-up method to evaluate the van Genuchten functions should reduce computer times by another factor of four.

4.5 Comparison of Results from Initial and Final Calculations

The results of the final set of calculations are virtually identical to the results of the initial set of calculations. The major exception to this statement is that the error in calculating the average linear water velocity in the fractures was corrected, leading to quantitatively different results at low pressure heads. Qualitatively, the results are the same. Improvements in numerical stability also improved the appearance of the results, but improvement in the accuracy of the initial calculations was minimal.

The remainder of this section examines each COVE 2A case, and discusses any visible difference between the corresponding figures for the initial and final calculations.

4.5.1 Cases 1, 3, and 5

The normalized-flux profiles presented in Figures 1-1/3/5-1 and 2-1/3/5-1 show minor differences in the placement and magnitude of the deviations between the calculated and the imposed flux. The largest improvement was in the 4 mm/yr case, where the initial calculation deviated by about 8%, while the final calculation deviated by about 1.5%.

The deviations in the calculated flux signal inaccuracy in the pressure-head solution. Flux is very sensitive to inaccuracy in the pressure head, and in these cases the pressure-head inaccuracies are imperceptible (Figures 1-1/3/5-2 and 2-1/3/5-2).

The mesh spacing for the final calculations was finer than for the initial calculations, and hence, the results were slightly more accurate. However, inaccuracy in the calculated flux can also be an artifact of the stability controls and the stepwise solution technique used in STEADY (Section 2.3). The stability controls were activated less often in the final calculations, reducing the magnitude of the deviations, but the stepwise solution technique was activated more often, increasing the number of deviations.

The improved accuracy in the pressure head translates into better hydraulic conductivity and velocity profiles (Figures 1-1/3/5-4 through 1-1/3/5-6 and 2-1/3/5-4 through 2-1/3/5-6).

4.5.2 Cases 2, 4, and 6

The differences between the initial and final calculations are substantially the same for Cases 1, 3, and 5. The improvement in the magnitude of the calculated-flux deviations was the same as in the CHnz cases, but the placement of the deviations differed (Figures 1-2/4/6-1 and 2-1/3/5-1.)

4.5.3 Case 7

Figure 2-7-1 lacks the instability in the imposed flux noticeable in Figure 1-7-1 at the upper boundary. This instability is even more pronounced in Figure 1-7-7, as is an instability at the PTn/TSw1 interface that had not been apparent in Figure 1-7-1. Figure 2-7-7 shows no instabilities.

The upper boundary instability was caused by the application of the boundary condition in the Picard-iteration technique (as discussed at the beginning of Section 3.5); implementation of Newton's method, with the inclusion of the boundary condition in each Newton subiteration, fixed this problem. The instabilities in PTn were also caused

by the Picard-iteration technique and were present when this problem was solved using Newton's method with a 0.5 implicitness factor. Using Newton's method with a 0.6 implicitness factor allowed the stable calculation shown in Figures 2-7-1 and 2-7-7.

Although the instabilities in the initial calculation of Case 7 are quite noticeable in the flux profiles, they are not noticeable in the other plots. By comparing Figure 1-7-1 with Figure 2-7-1, it can be seen that the instabilities have no obvious effect on the flux-pulse shape or flux-pulse propagation.

The remaining figures containing the final Case 7 results are virtually identical to the corresponding figures containing the initial results.

4.5.4 Case 8

Other than the correction in the boundary-condition instability exhibited in the initial Case 8 flux profiles, the final Case 8 figures show no apparent differences between the initial and final calculations.

4.5.5 Case 9

With the exception of the correction of the fracture-water-velocity calculation, the differences in results between the initial and final calculations for Cases 7 and 8 were primarily superficial. Figure 2-9-1, however, when compared with Figure 1-9-1, shows a different propagation speed for the flux pulse as it passes through PTn. The time line showing the flux pulse at 300 years is approximately 10 meters further down the column in Figure 1-9-1 than it is in Figure 2-9-1. Because the velocity of the flux pulse is approximately 1 m/yr (it can be estimated by taking the distance between the 300-year and the 350-year time lines—approximately 50 m—and dividing by 50 years), the difference is approximately 10 years. Because the pulse spends somewhat over 100 years passing through PTn, the difference is approximately 10%. Based on the finer mesh in the final calculations, plus the minimization of the truncation error (to first order) with the implementation of Newton's method, it is assumed that the final results are more accurate (as discussed in Section 2.6). A more thorough investigation would involve performing both calculations again with finer mesh spacings and shorter time steps, and then determining to what solution the different methods are converging (if they are indeed converging).

The shift in time lines after 300 years is reflected in the other elevation plots (Figures 1-9-2 through 1-9-6 and Figures 2-9-2 through 2-9-6). The time plots (Figures 1-9-8 through 1-9-12 and Figures 2-9-7 through 2-9-12) show little difference.

For the final calculations, the time-data points were saved at every 10 iterations, as opposed to being saved at every 100 iterations for the initial calculations; because fewer time steps were taken in the final calculations, the time-data curves of the two calculational sets have approximately the same resolution. Notice, however, that the matrix/fracture-transfer fins are evident in Figure 2-9-11 at the appropriate elevations.

4.5.6 Case 10

The results of the final and initial calculations for Case 10 are essentially identical. The Case 9 results showed a difference between flux-pulse velocities in the initial and final calculations through PTn. This difference is not evident in the Case 10 results. Comparison of Figures 1-9-2 and 1-10-2 (or Figures 2-9-2 and 2-10-2) shows that the CHnv unit applies a suction that extends virtually to the PTn/TSw1 interface. This suction keeps the flow predominantly in the matrix for a longer period of time in Case 10. Except at complete saturation, the characteristic curves for TSw1 are less nonlinear for a matrix-flow solution than a fracture-flow solution (as is the case for all the characteristic curves in this problem set). Given the same mesh and time step, the Case 10 results should be slightly more accurate than the the Case 9 results. Thus the results of the initial calculations and the results of the final calculations present a closer match in Case 10 than in Case 9.

4.5.7 Case 11

The most noticeable difference between the results of the initial and final calculations for Case 11 is the "wiggles" in the time lines of the initial-calculation results. These instabilities are evident in most of the elevation plots (Figures 1-11-1 through 1-11-6) and the plot of normalized flux versus time (Figure 1-11-7). The 1.5-year time line in Figure 2-11-1 shows an incipient instability in the form of a slight irregularity immediately above the inflection point in the flux pulse. This irregularity disappears with $\Omega > 0.5$ or with the time-step factor $f < 0.1$. Most of the plots of the final calculations, however, are free of any sign of instability. The instabilities were discussed in Section 3.5. The corrective measures were discussed in Section 4.1.

Perhaps the most surprising observation concerning the Case 11 results is the lack of significant differences between the final and initial calculations given the instabilities in the initial results.

4.5.8 Case 12

The comparison of the Case 11 initial and final calculations is also valid for the Case 12 calculations. The time plots for the initial calculations of Case 12 (Figures 1-12-7 through 1-12-12) show very coarse spacing of data points at early times. The time plots for the final calculations of Case 12 show coarse spacing of data points at late times. Time results were not taken at every time step; however, the initial calculations were probably taking too few time steps at early times and too many at late times. The results of the initial set of calculations still compare well with the results of the final set of calculations.

5.0 CONCLUSION

Because TOSPAC was used to define the COVE 2A problems, there was never a question that it would be able to solve the complete problem set. The questions about TOSPAC participation in the COVE 2A activity involved whether it was correct, accurate, and efficient when compared with other computer programs that model unsaturated flow.

TOSPAC did contain a major flaw in calculating the average linear velocity of water in fractures. It is unlikely that this flaw would have been detected without COVE 2A or a similar benchmarking effort.

With the exception of the velocity error, the accuracy of TOSPAC was generally acceptable, though not outstanding, for the initial calculations. The accuracy of TOSPAC was improved for the final calculations with the improved mesh-point spacing, with the improved time-step control, and with the consideration of the water compressibility in the conductivity term of Equations 1 and 4 (although water compressibility is not a significant factor for the COVE 2A problems).

The initial calculations were marginally efficient. Improved efficiency became necessary when TOSPAC was modified to include the compressibility of water and when it was discovered that the mesh should contain several thousand points to ensure accuracy. The major obstacle to an efficient calculation, however, was still numerical stability.

Most of the work done in the DYNAMICS module of TOSPAC was in evaluating the Mualem-based, van Genuchten-defined functions for saturation, hydraulic conductivity, and their derivatives. In the initial calculations, numerical instability caused DYNAMICS to evaluate these functions more often than they would have to be evaluated in a stable calculation. DYNAMICS was modified for efficiency by implementing a subiteration scheme based on Newton's method, which directly improved stability. Indeed, complete foward-differencing in time created a very stable calculation—at the expense of accuracy. Center-differencing in time afforded the best accuracy with acceptable stability. Execution times on a VAX 8650 computer were decreased by approximately an order of magnitude.

REFERENCES

Dudley, A.L., R.R. Peters, J.H. Gauthier, M.L. Wilson, M.S. Tierney, and E.A. Klavetter, *Total System Performance Assessment Code (TOSPAC) Volume 1: Physical and Mathematical Bases*, SAND85-0002, Sandia National Laboratories, Albuquerque, New Mexico, 1988. (NNA.881202.0211)

Mualem, Y., A new model for predicting the hydraulic conductivity of unsaturated porous materials, *Water Resour. Res.*, *12*(3), 513-522, 1976. (NNA.890522.0250)

NRC (U.S. Nuclear Regulatory Commission), Disposal of high-level radioactive wastes in geologic repositories, *Code of Federal Regulations, Energy*, Title 10, Part 60, Washington, D.C., 1986. (NNA.870406.0488)

Ortiz, T.S., R.L. Williams, F.B. Nimick, B.C. Whittet, and D.L. South, *A Three-Dimensional Model of Reference Thermal/Mechanical and Hydrological Stratigraphy at Yucca Mountain, Southern Nevada*, SAND84-1076, Sandia National Laboratories, Albuquerque, New Mexico, 1985. (NNA.890315.0013)

Peters, R.R., and E.A. Klavetter, A continuum model for water movement in an unsaturated fractured rock mass, *Water Resour. Res.*, *21*(3), 416-430, 1988. (NNA.870323.0453)

Peters, R.R., *Hydrologic Technical Correspondence in Support of the Site Characteristic Plan*, SAND88-2784, Sandia National Laboratories, Albuquerque, New Mexico, 1988. (NNA.881202.0204)

Silling, S.A., *Final Technical Position on Documentation of Computer Codes for High-Level Waste Management*, NUREG-0856 (II.D), U.S. Nuclear Regulatory Commission, Washington, D.C., 1983. (NNA.871104.0034)

van Genuchten, M., A closed-form equation for predicting the hydraulic conductivity of unsaturated soils, *Soil Sci. Soc. Am. J.*, *44*, 892-898, 1980. (NNA.890522.0287)

Appendix A
DATA RELEVANT TO THE REFERENCE INFORMATION BASE

A.1 Information from the Reference Information Base Used in this Report

This report contains no information from the Reference Information Base.

A.2 Candidate Information for the Reference Information Base

This report contains no candidate information from the Reference Information Base.

A.3 Candidate Information for the Site and Engineering Properties Data Base

This report contains no candidate information from the Site and Engineering Properties Data Base.

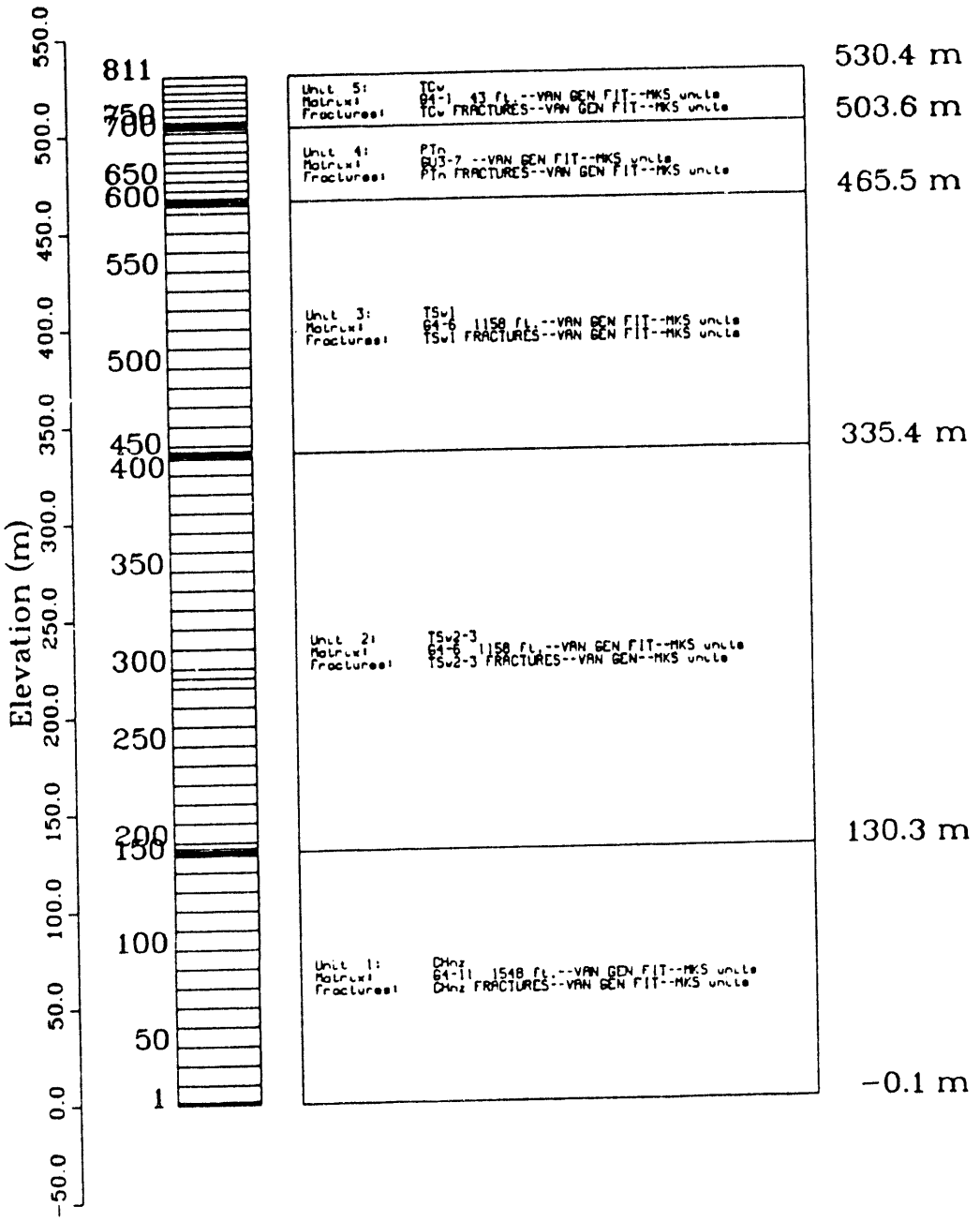

Figure 1-1. The calculational mesh (left-hand column) and the geohydrologic unit stratigraphy (right-hand column) used for Case 1 of the initial set of calculations.

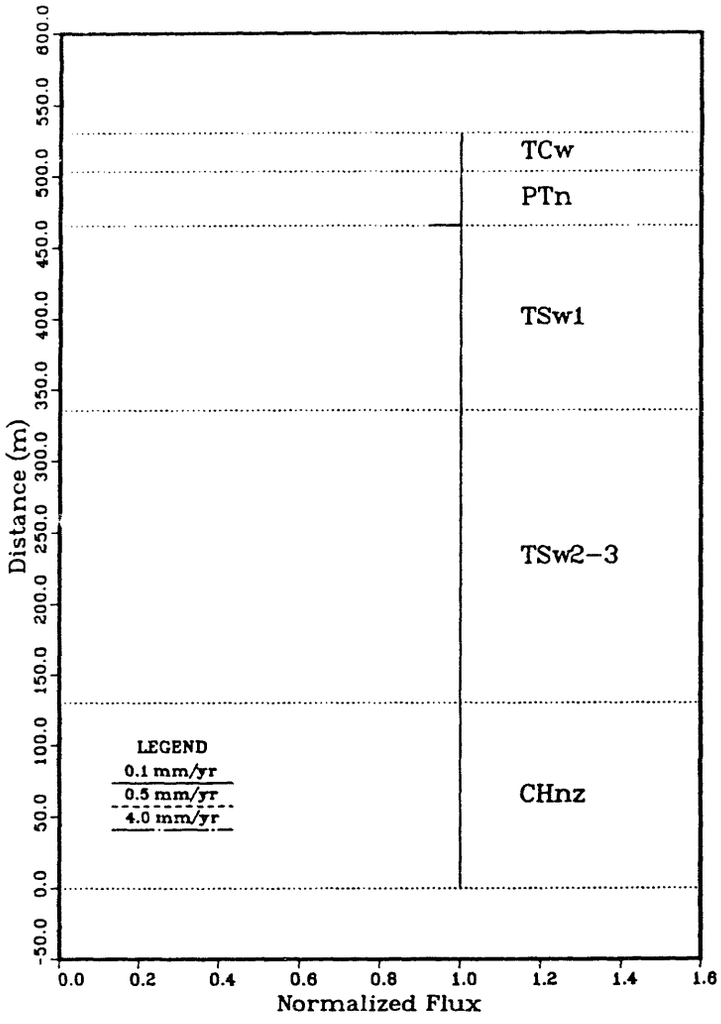

Figure 1-1/3/5-1. Normalized flux (calculated flux divided by imposed flux) versus distance above the water table; initial set of calculations; Cases 1, 3, and 5.

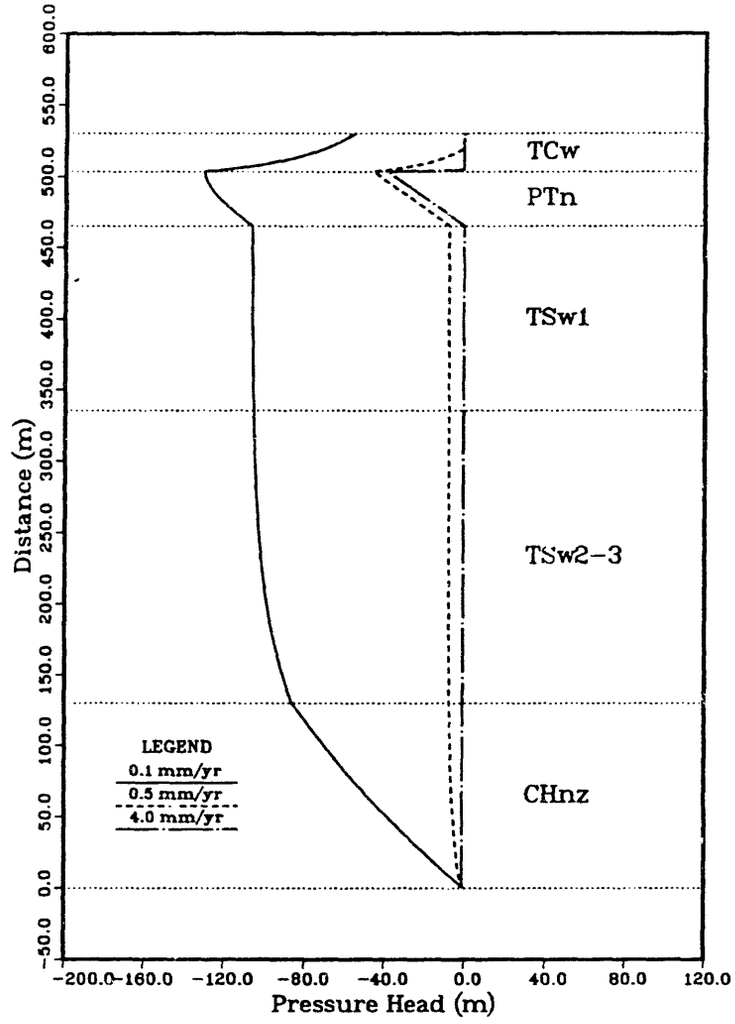

Figure 1-1/3/5-2. Pressure head versus distance above the water table; initial set of calculations; Cases 1, 3, and 5.

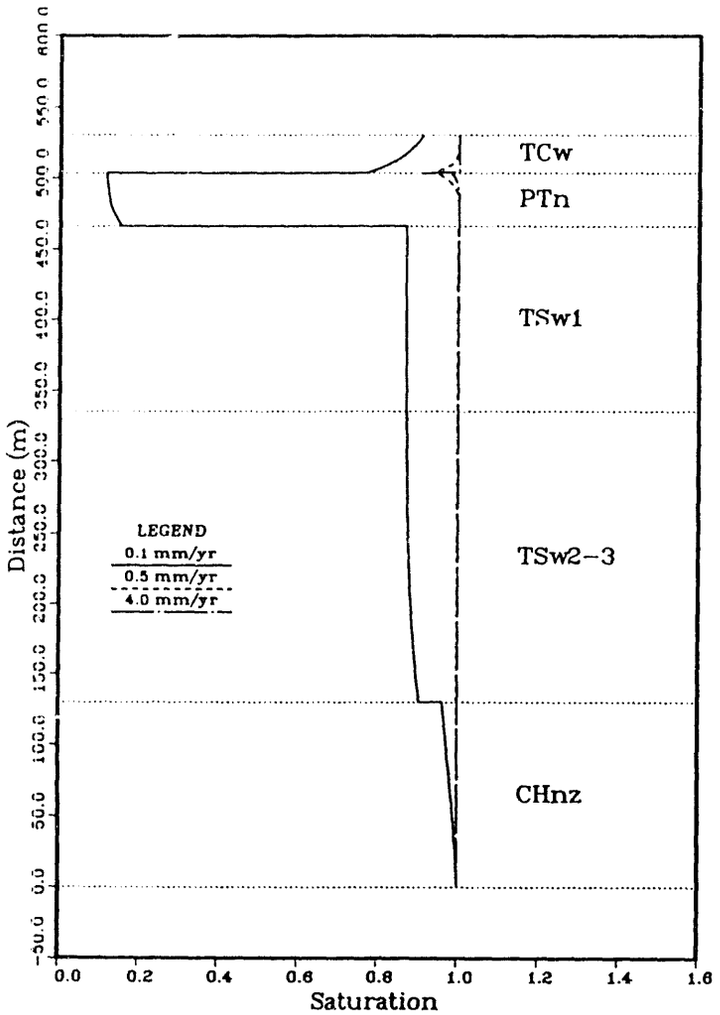

Figure 1-1/3/5-3. Matrix saturation versus distance above the water table; initial set of calculations; Cases 1, 3, and 5.

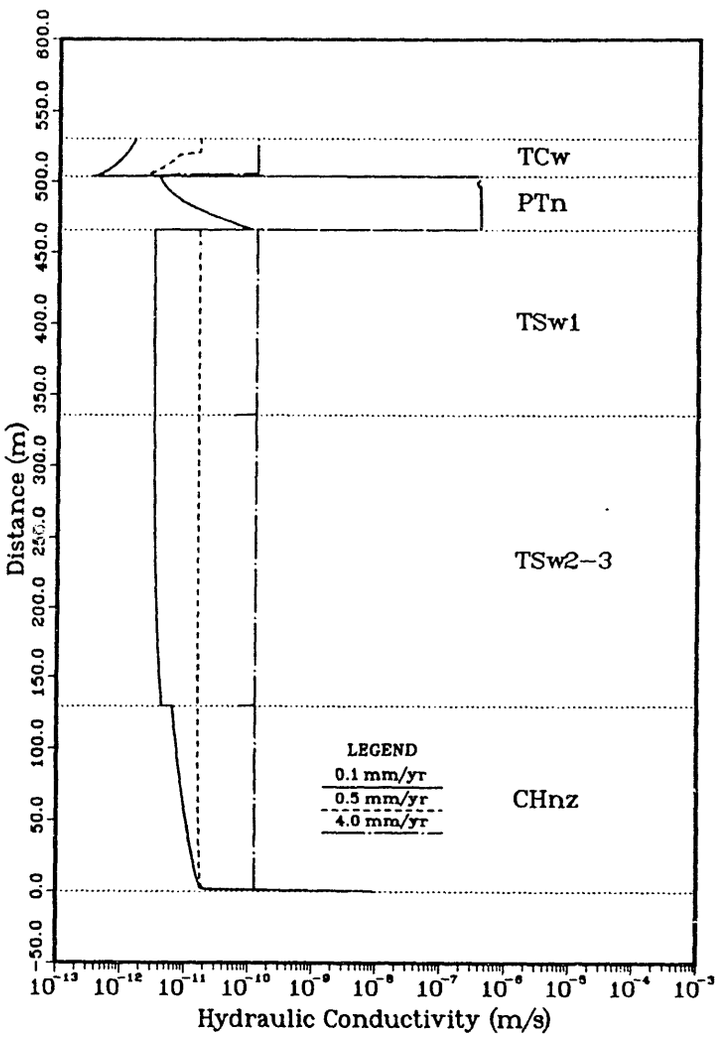

Figure 1-1/3/5-4. Hydraulic conductivity versus distance above the water table; initial set of calculations; Cases 1, 3, and 5.

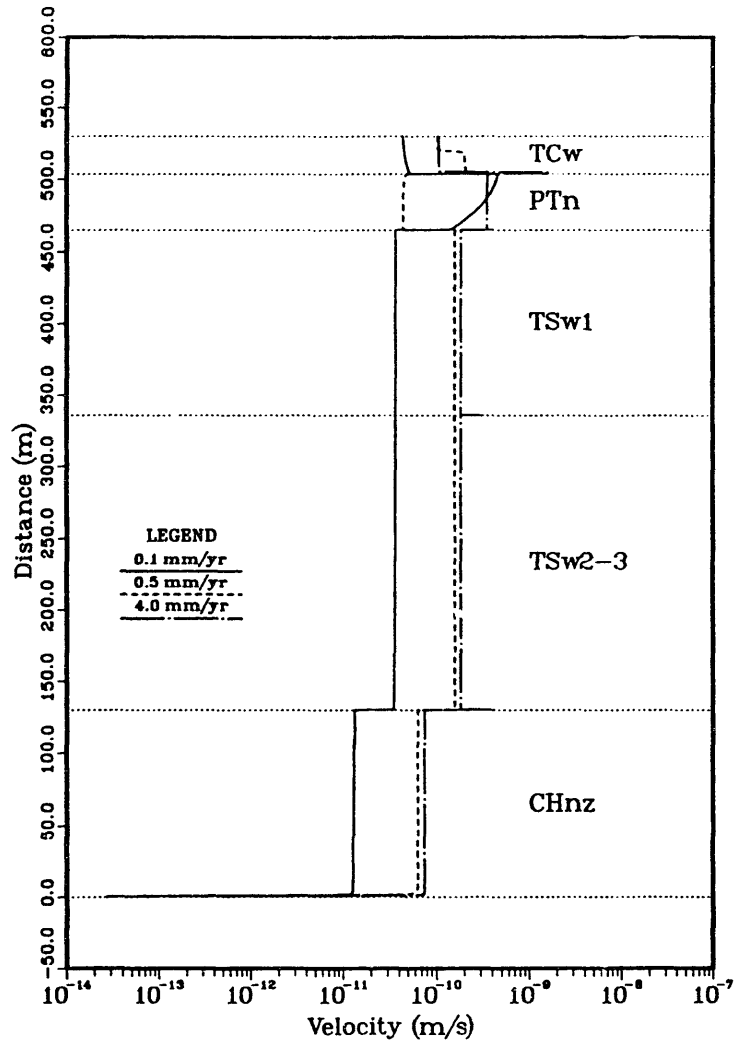

Figure 1-1/3/5-5. Average linear velocity of water in the matrix versus distance above the water table; initial set of calculations; Cases 1, 3, and 5.

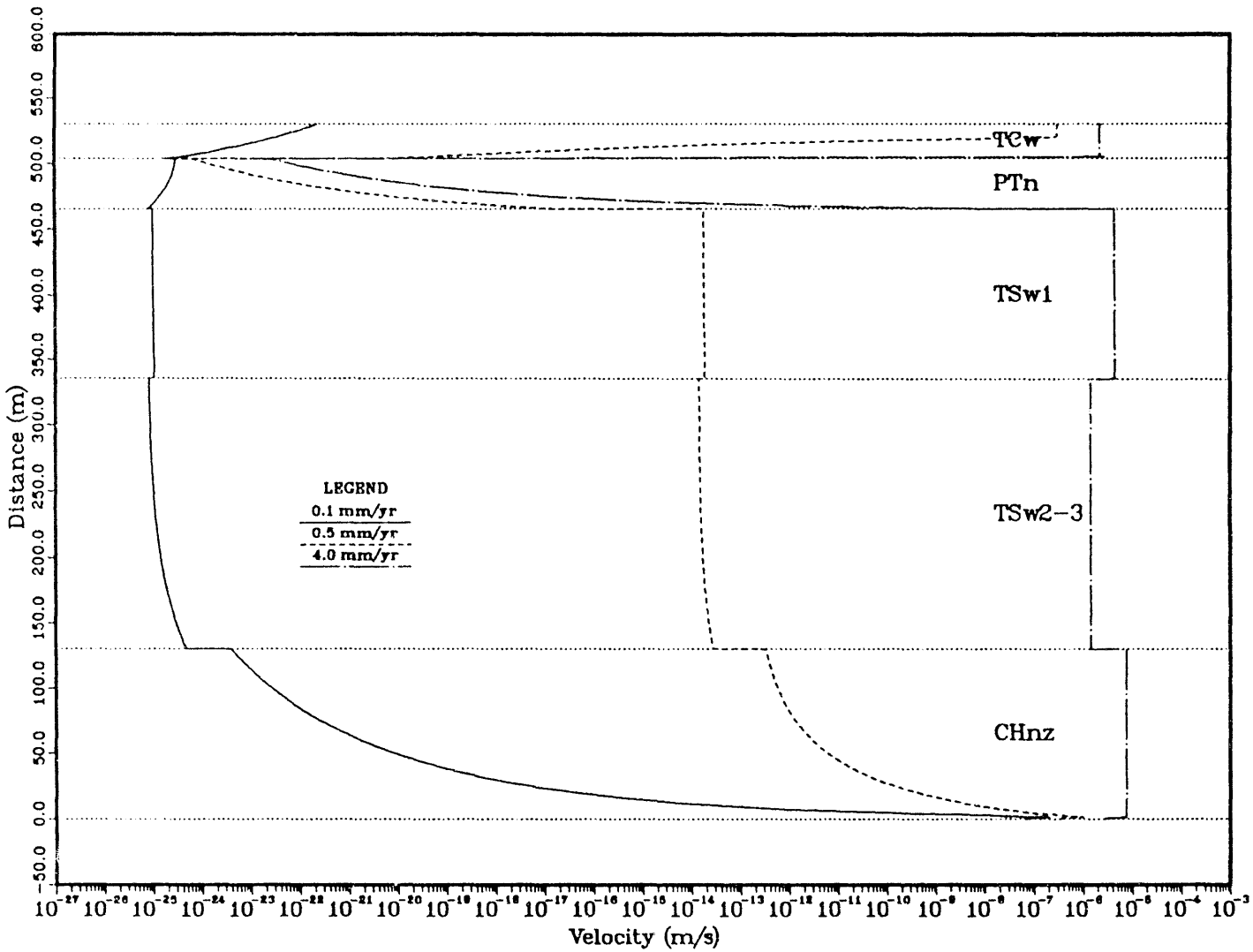

Figure 1-1/3/5-6. Average linear velocity of water in the fractures versus distance above the water table; initial set of calculations; Cases 1, 3, and 5.

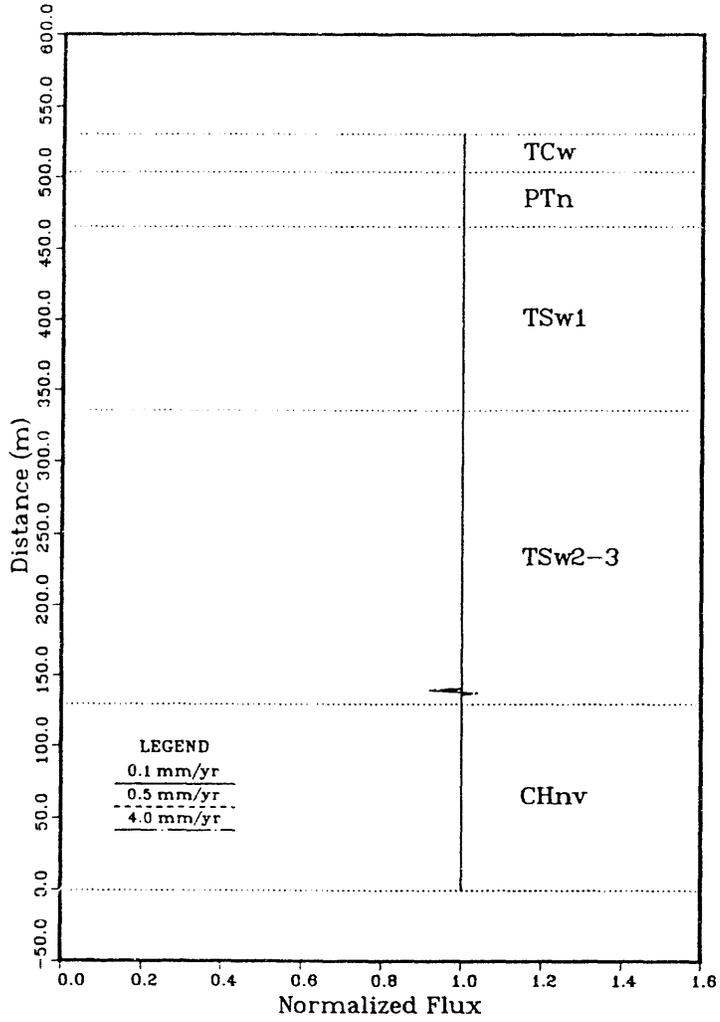

Figure 1-2/4/6-1. Normalized flux (calculated flux divided by imposed flux) versus distance above the water table; initial set of calculations; Cases 2, 4, and 6.

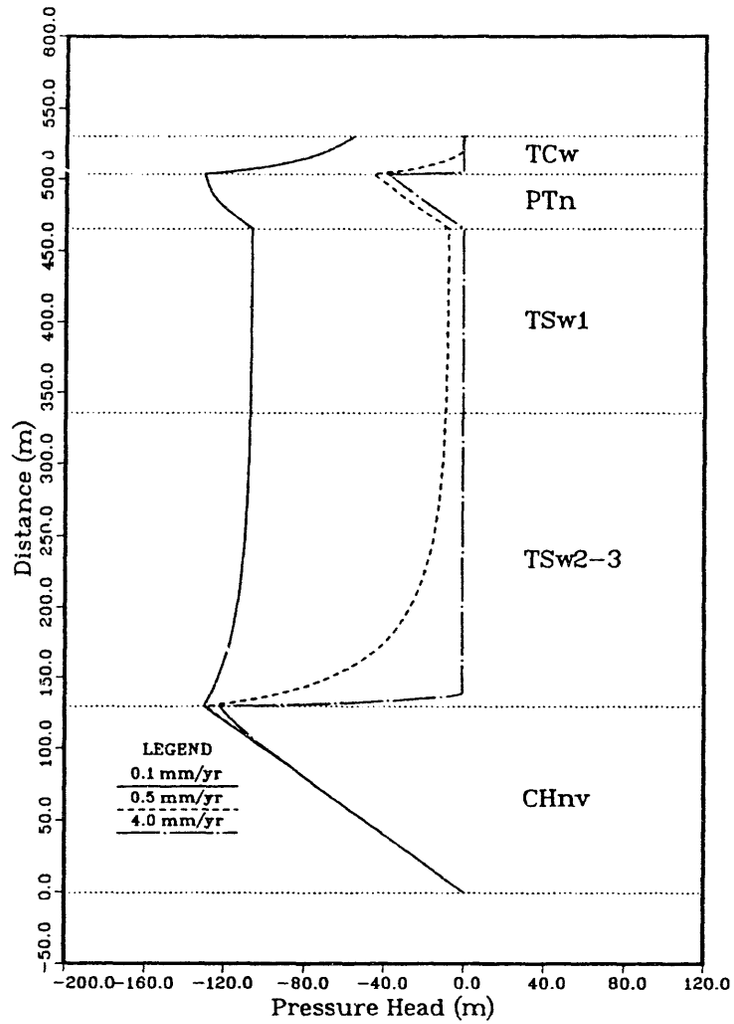

Figure 1-2/4/6-2. Pressure head versus distance above the water table; initial set of calculations; Cases 2, 4, and 6.

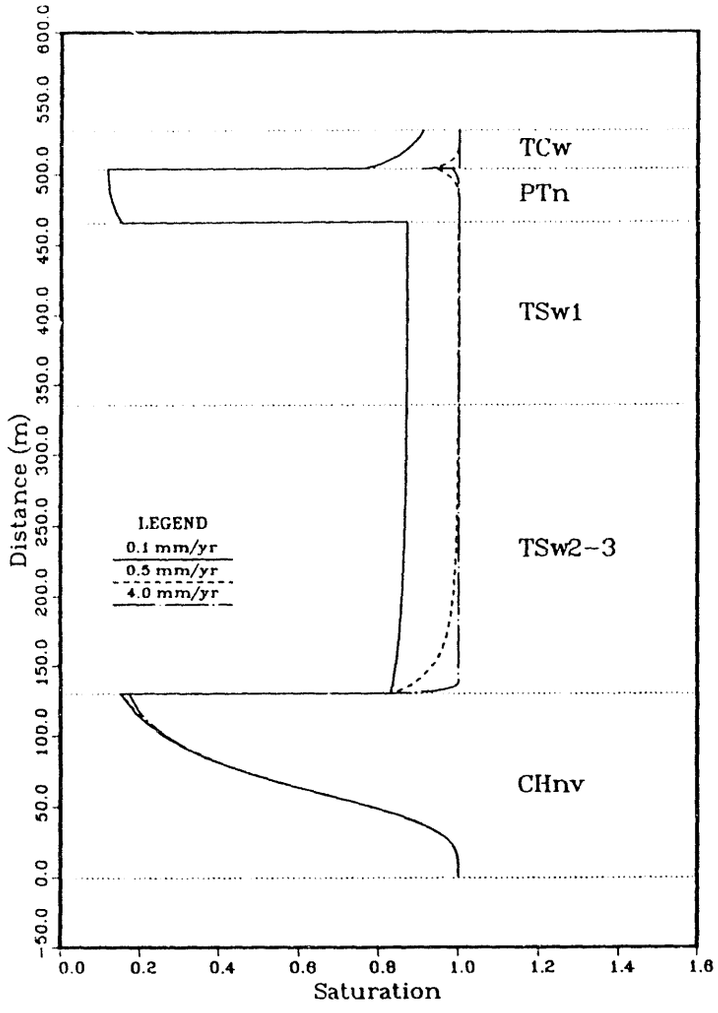

Figure 1-2/4/6-3. Matrix saturation versus distance above the water table; initial set of calculations; Cases 2, 4, and 6.

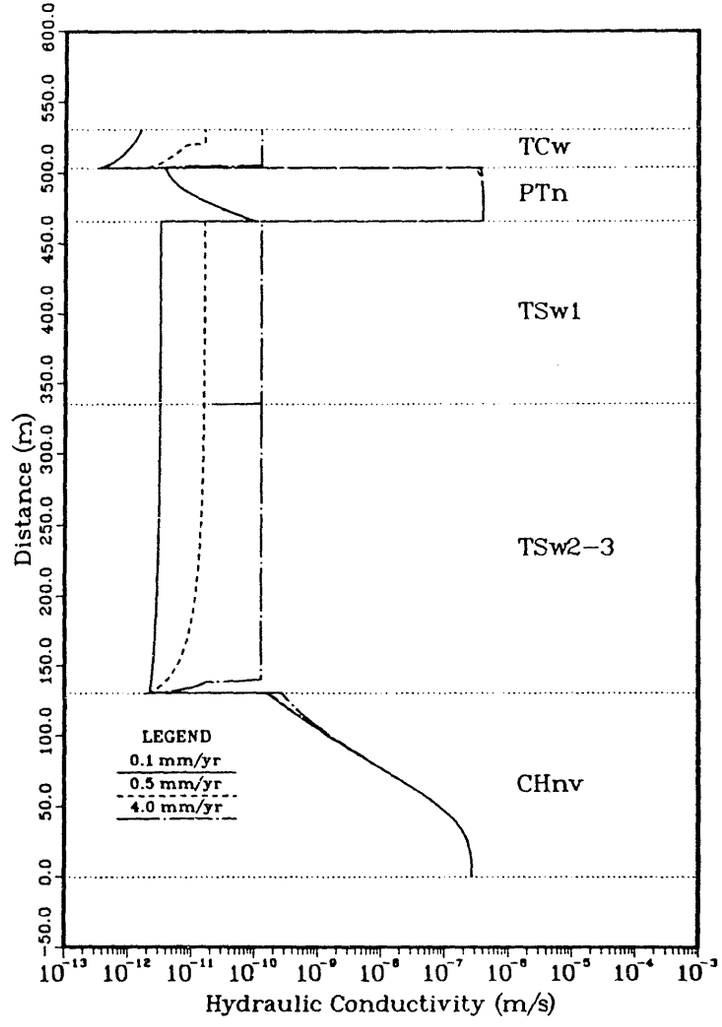

Figure 1-2/4/6-4. Hydraulic conductivity versus distance above the water table; initial set of calculations; Cases 2, 4, and 6.

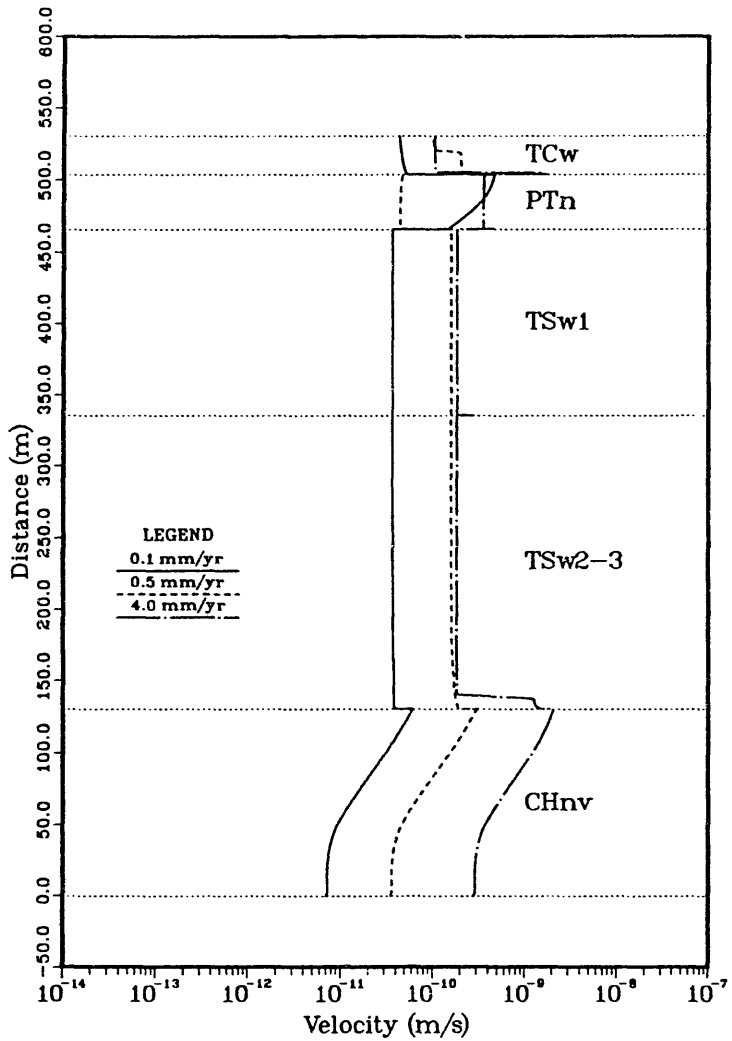

Figure 1-2/4/6-5. Average linear velocity of water in the matrix versus distance above the water table; initial set of calculations; Cases 2, 4, and 6.

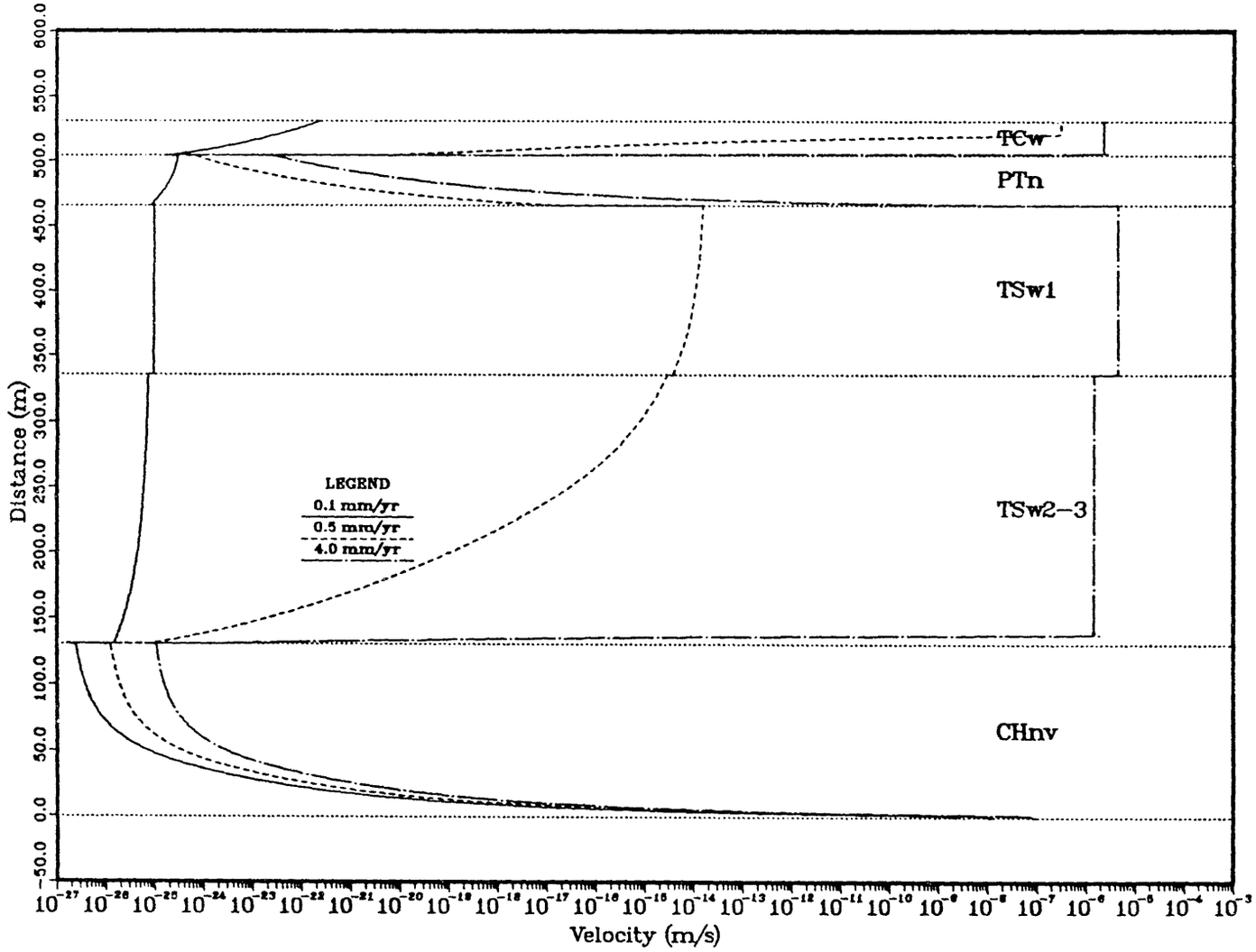

Figure 1-2/4/6-6. Average linear velocity of water in the fractures versus distance above the water table; initial set of calculations; Cases 2, 4, and 6.

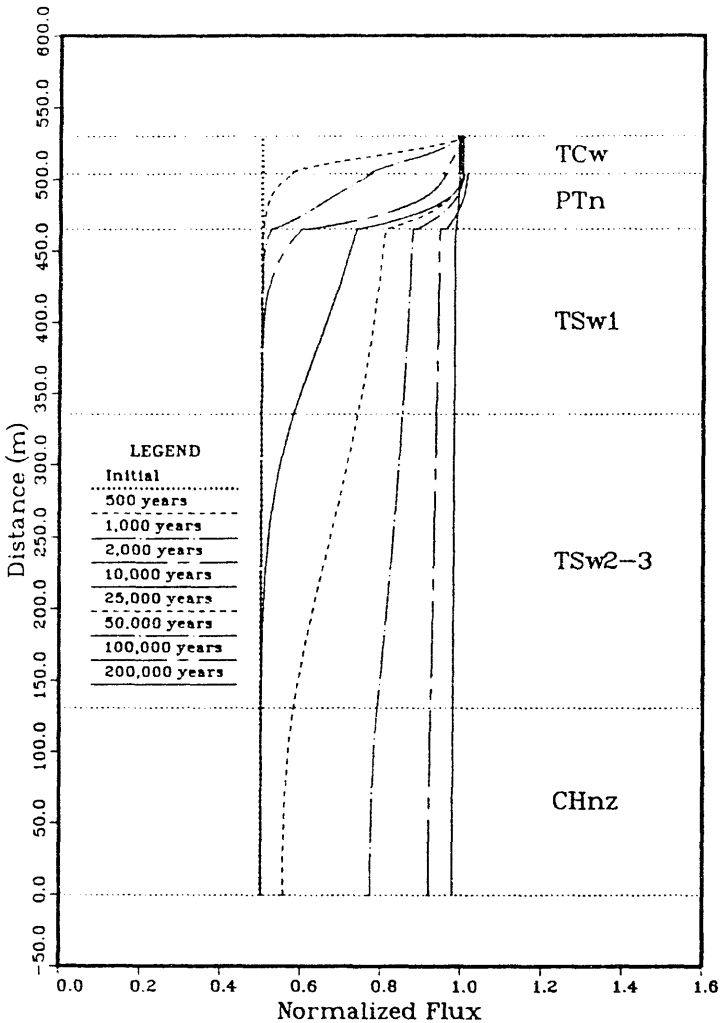

Figure 1-7-1. Normalized flux (calculated flux divided by imposed flux) versus distance above the water table at specified times; initial set of calculations; Case 7.

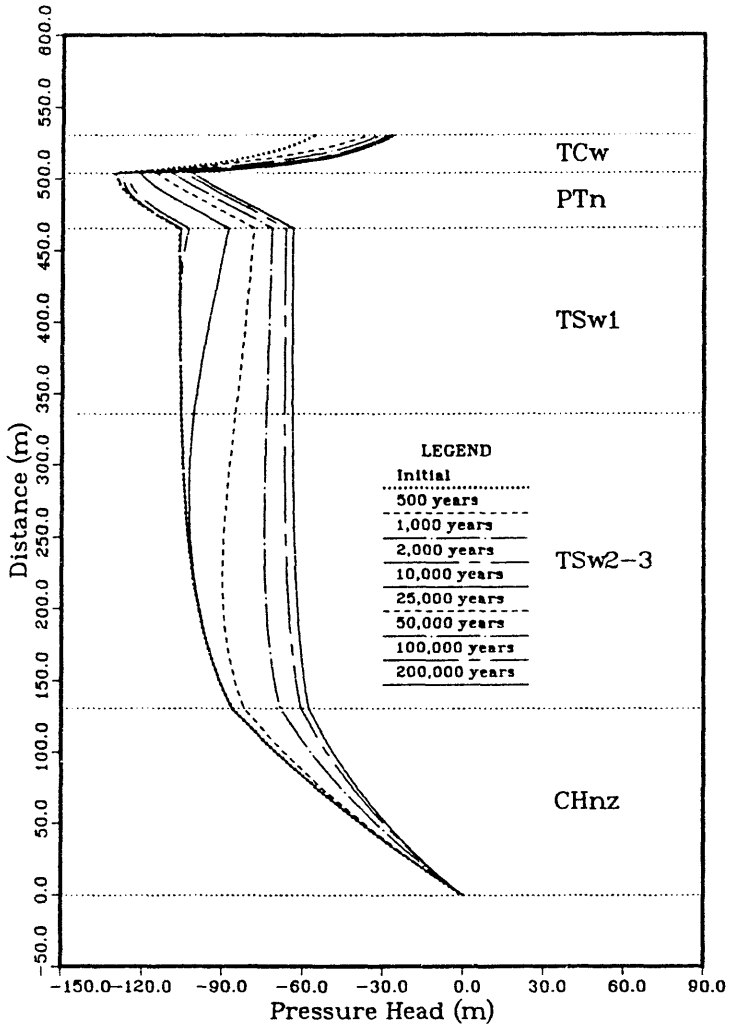

Figure 1-7-2. Pressure head versus distance above the water table at specified times; initial set of calculations; Case 7.

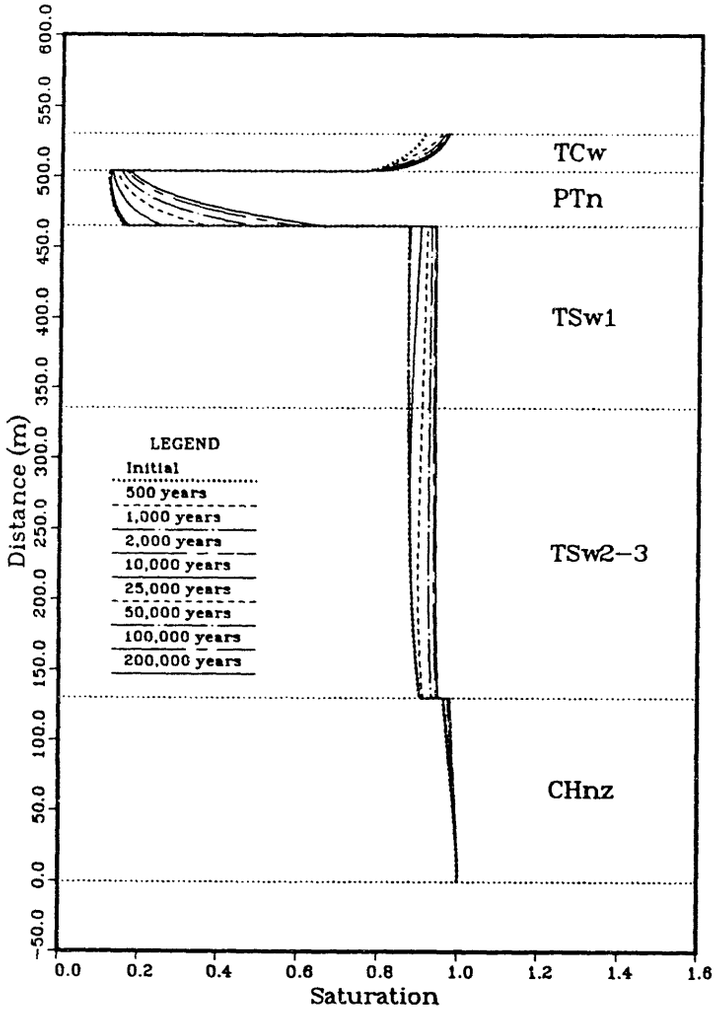

Figure 1-7-3. Matrix saturation versus distance above the water table at specified times; initial set of calculations; Case 7.

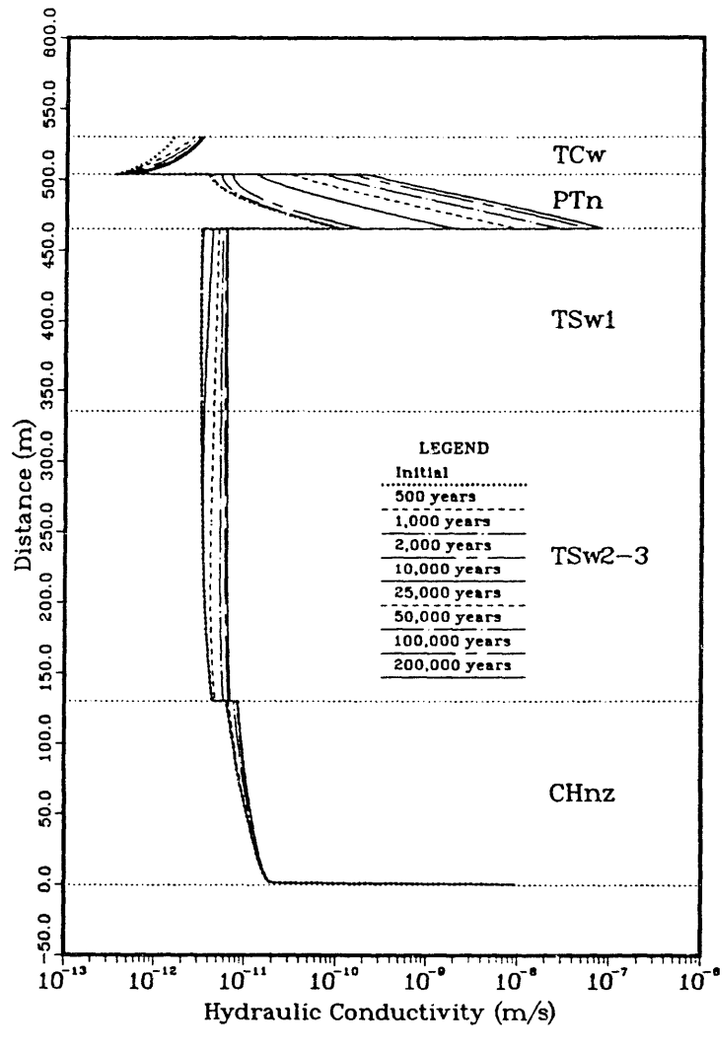

Figure 1-7-4. Hydraulic conductivity versus distance above the water table at specified times; initial set of calculations; Case 7.

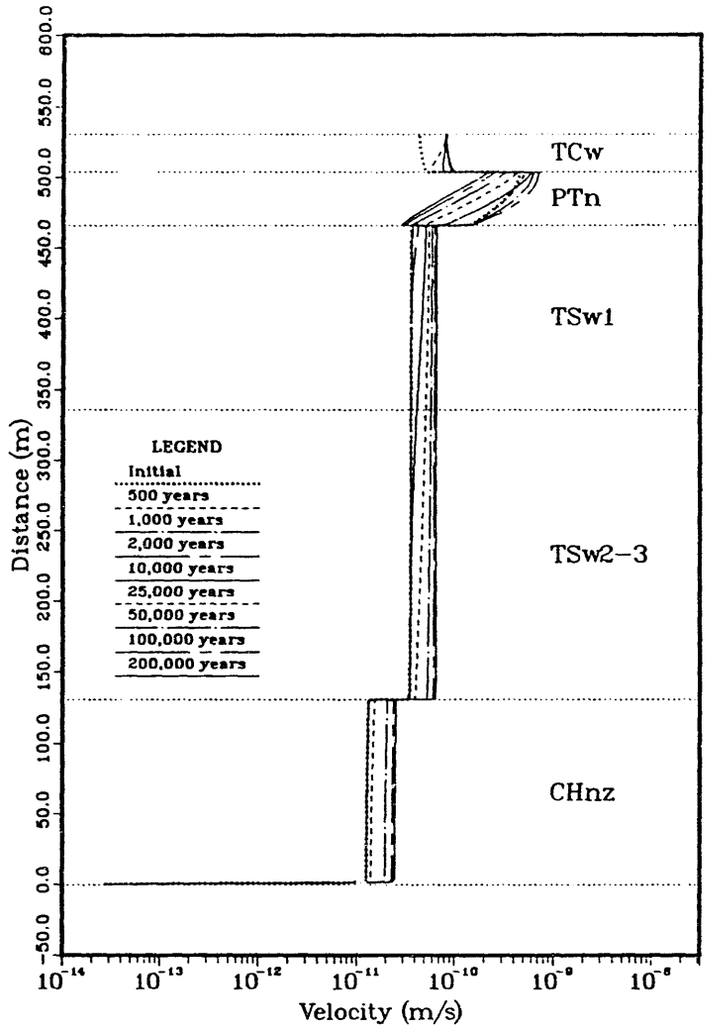

Figure 1-7-5. Average linear velocity of water in the matrix versus distance above the water table at specified times; initial set of calculations; Case 7.

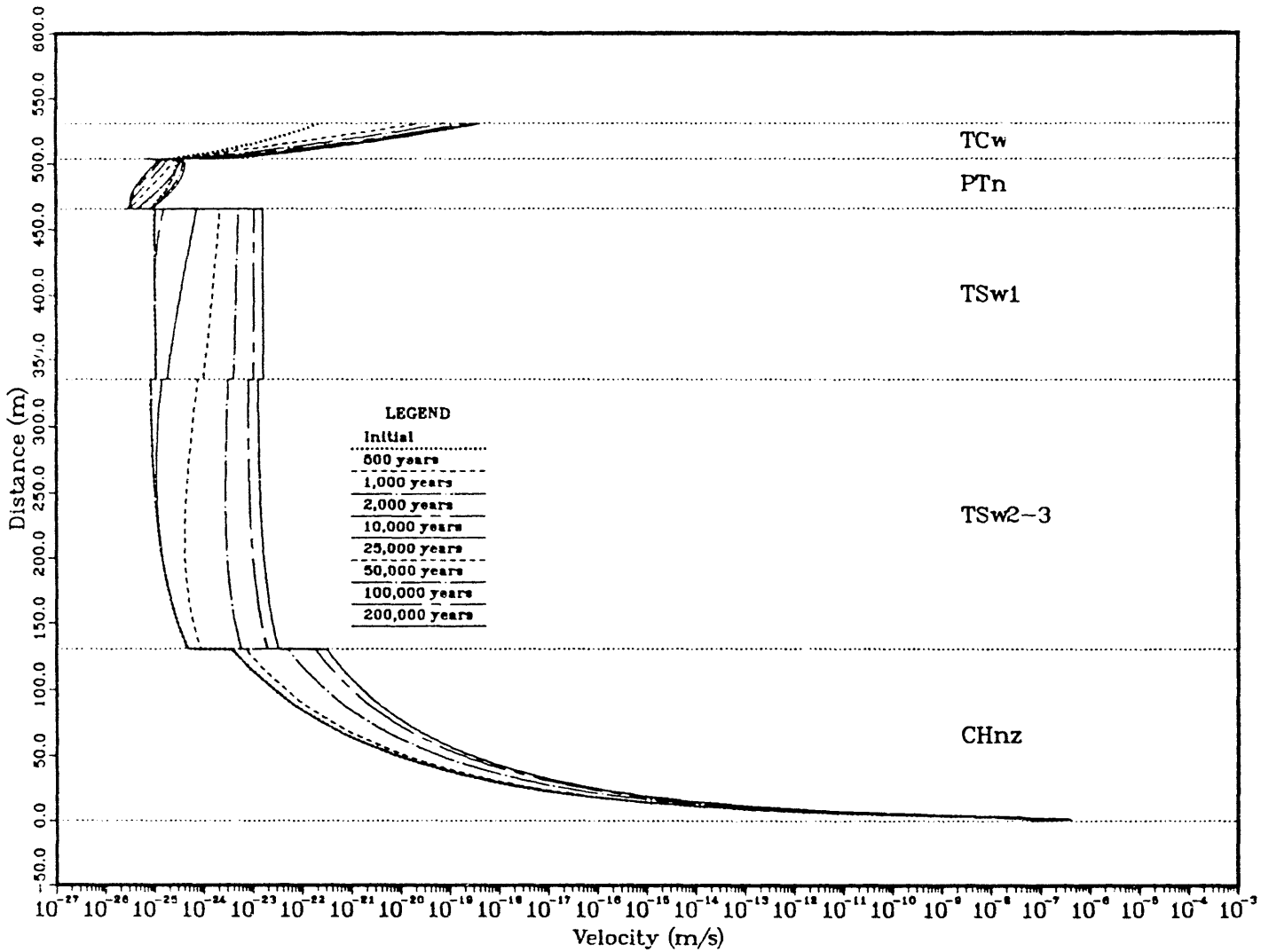

Figure 1-7-6. Average linear velocity of water in the fractures versus distance above the water table at specified times; initial set of calculations; Case 7.

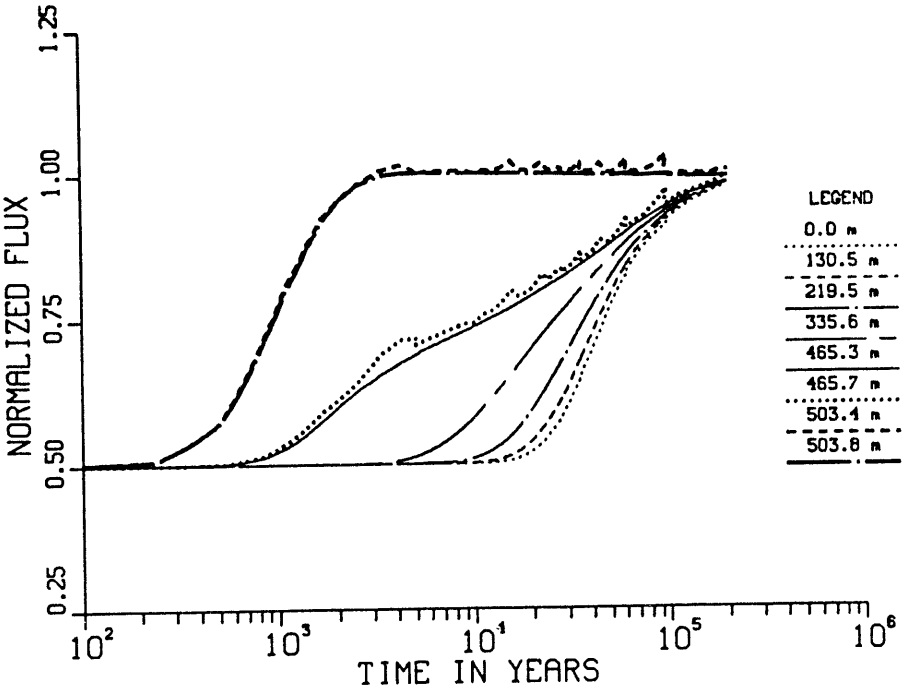

Figure 1-7-7. Normalized flux (calculated flux divided by imposed flux) versus time at specified distances above the water table; initial set of calculations; Case 7.

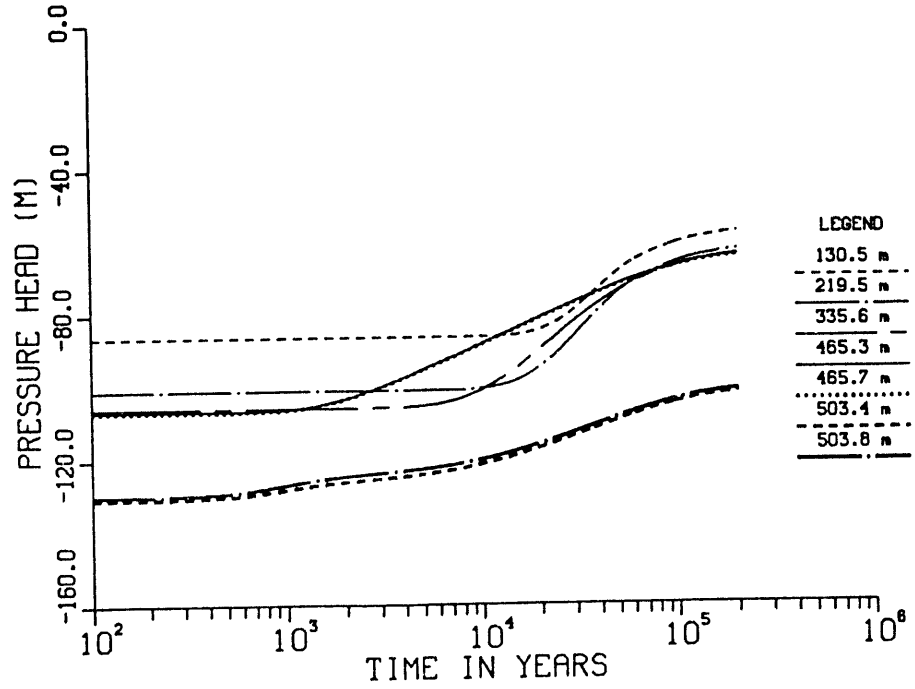

Figure 1-7-8. Pressure head versus time at specified distances above the water table; initial set of calculations; Case 7.

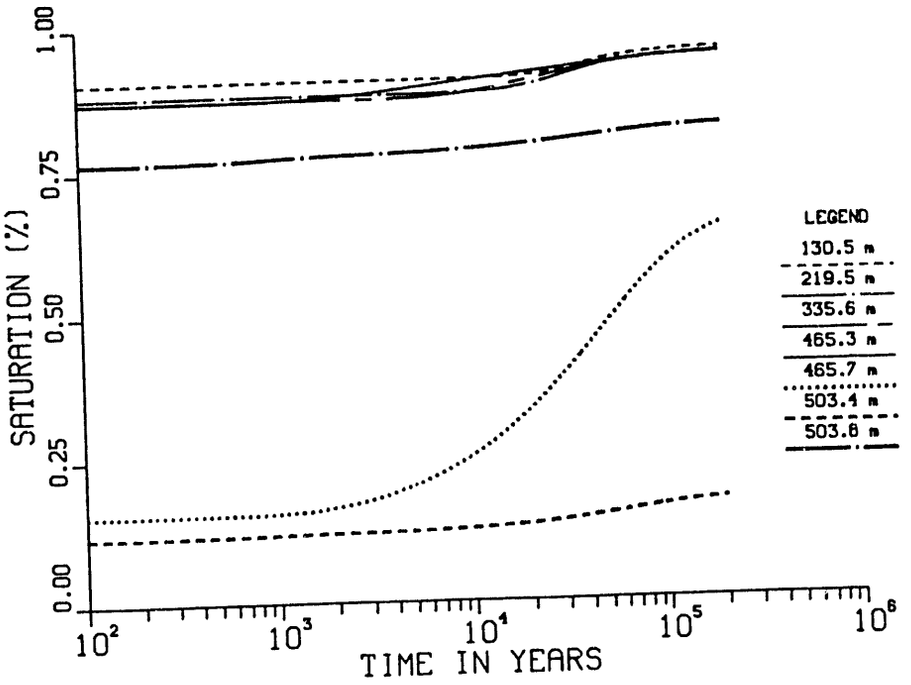

Figure 1-7-9. Matrix saturation versus time at specified distances above the water table; initial set of calculations; Case 7.

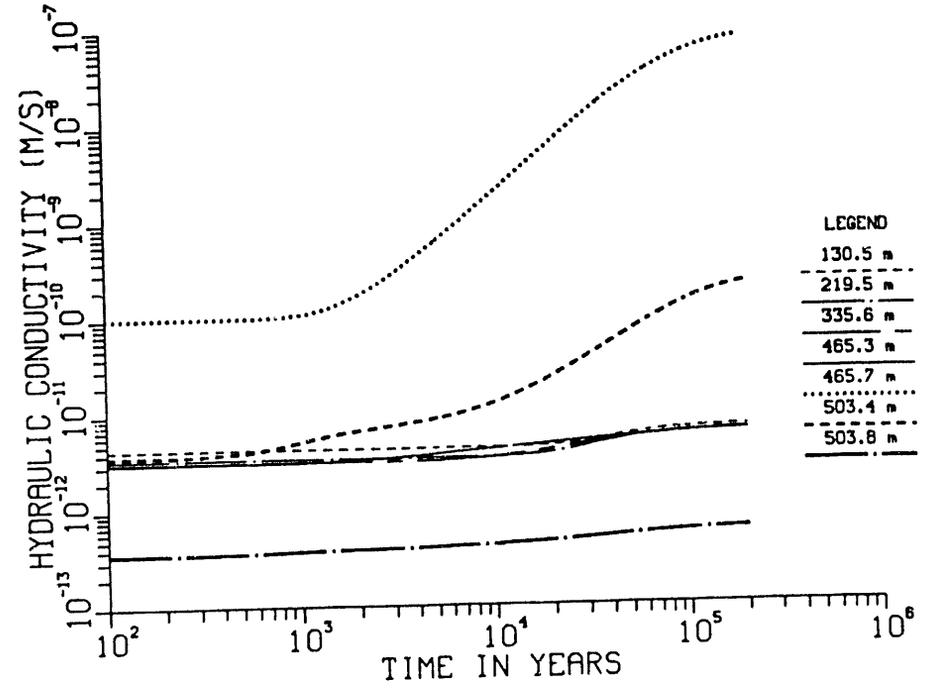

Figure 1-7-10. Hydraulic conductivity versus time at specified distances above the water table; initial set of calculations; Case 7.

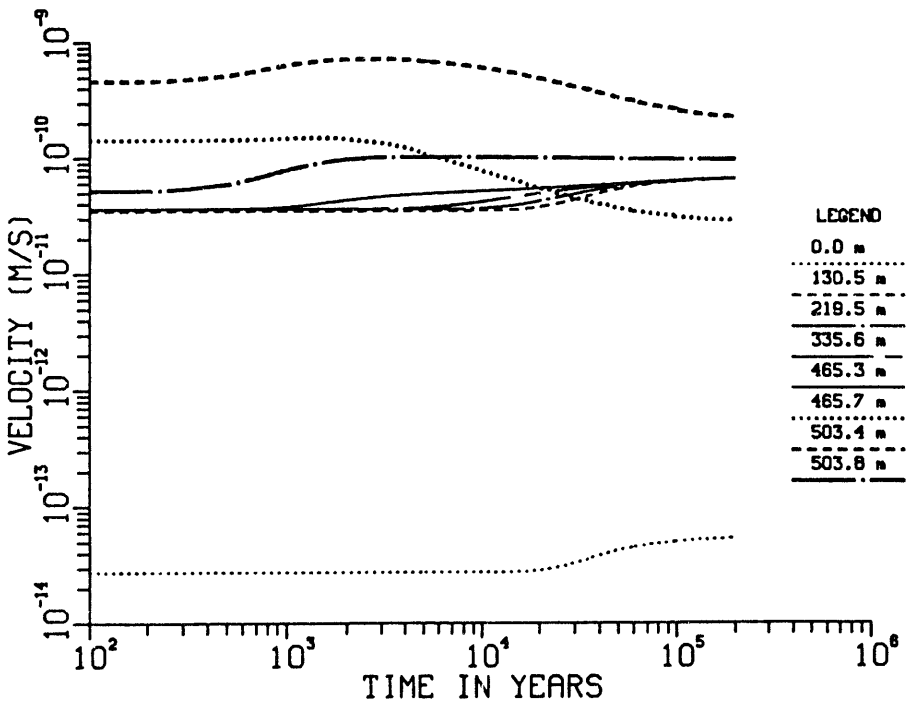

Figure 1-7-11. Average linear velocity of water in the matrix versus time at specified distances above the water table; initial set of calculations; Case 7.

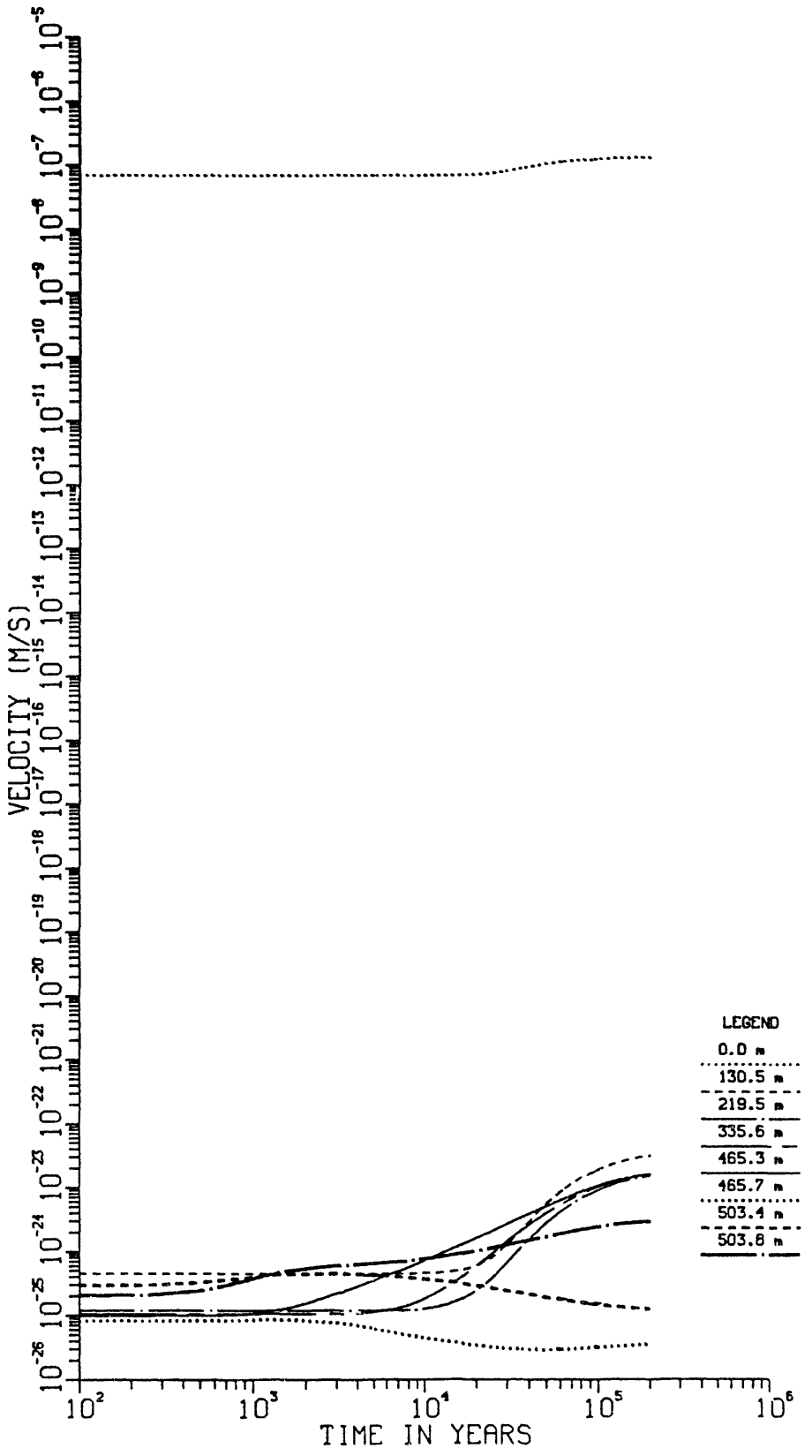

Figure 1-7-12. Average linear velocity of water in the fractures versus time at specified distances above the water table; initial set of calculations; Case 7.

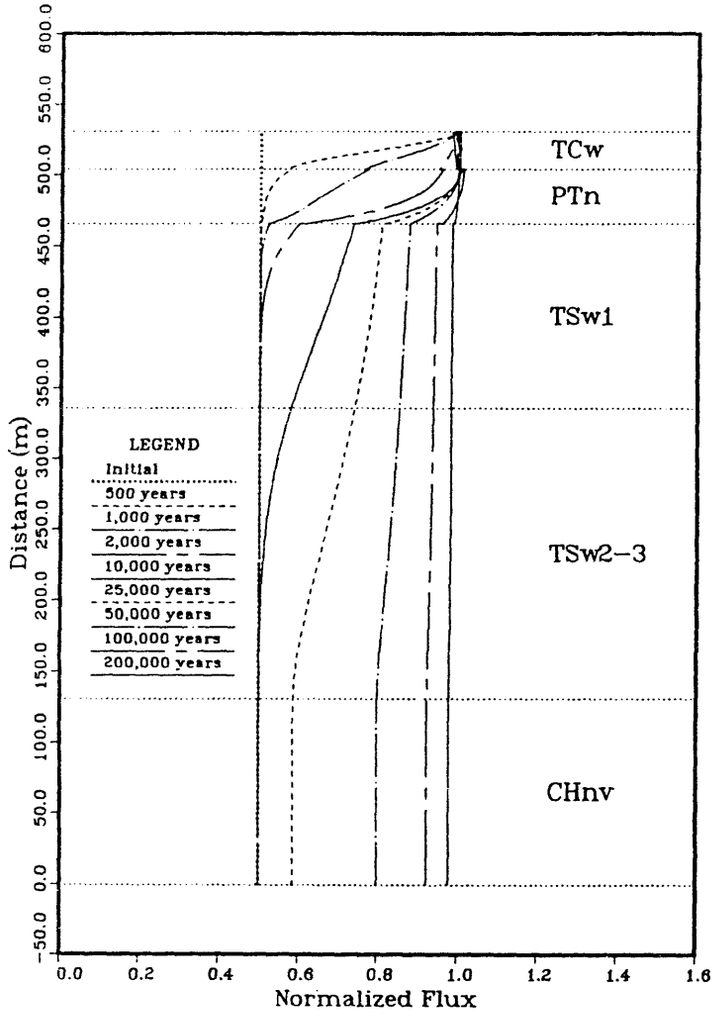

Figure 1-8-1. Normalized flux (calculated flux divided by imposed flux) versus distance above the water table at specified times; initial set of calculations; Case 8.

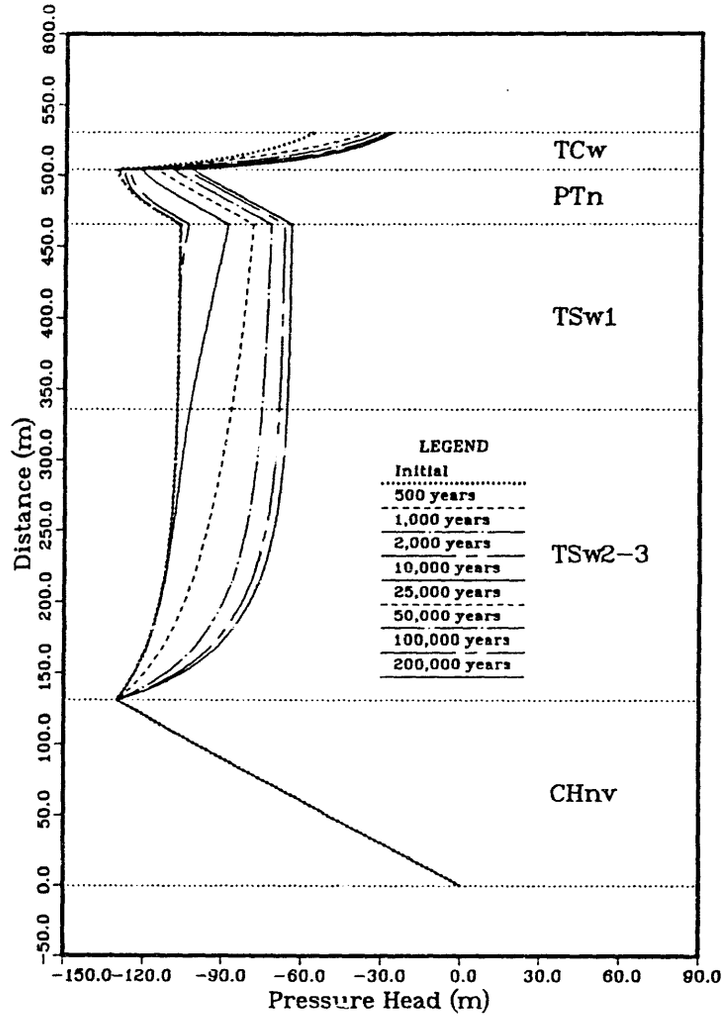

Figure 1-8-2. Pressure head versus distance above the water table at specified times; initial set of calculations; Case 8.

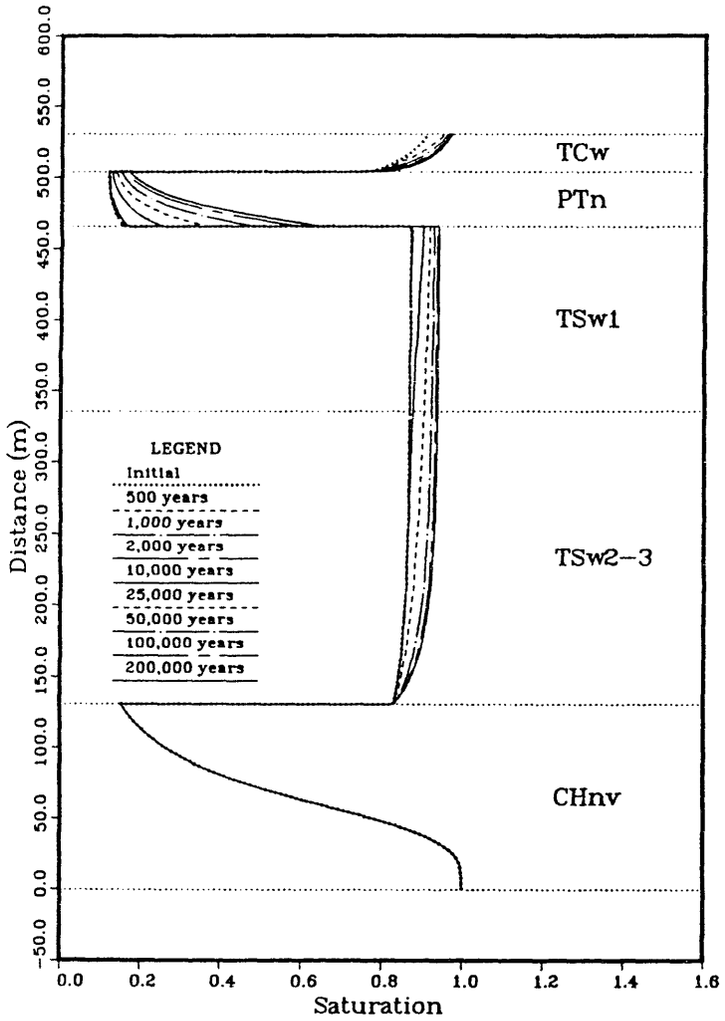

Figure 1-8-3. Matrix saturation versus distance above the water table at specified times; initial set of calculations; Case 8.

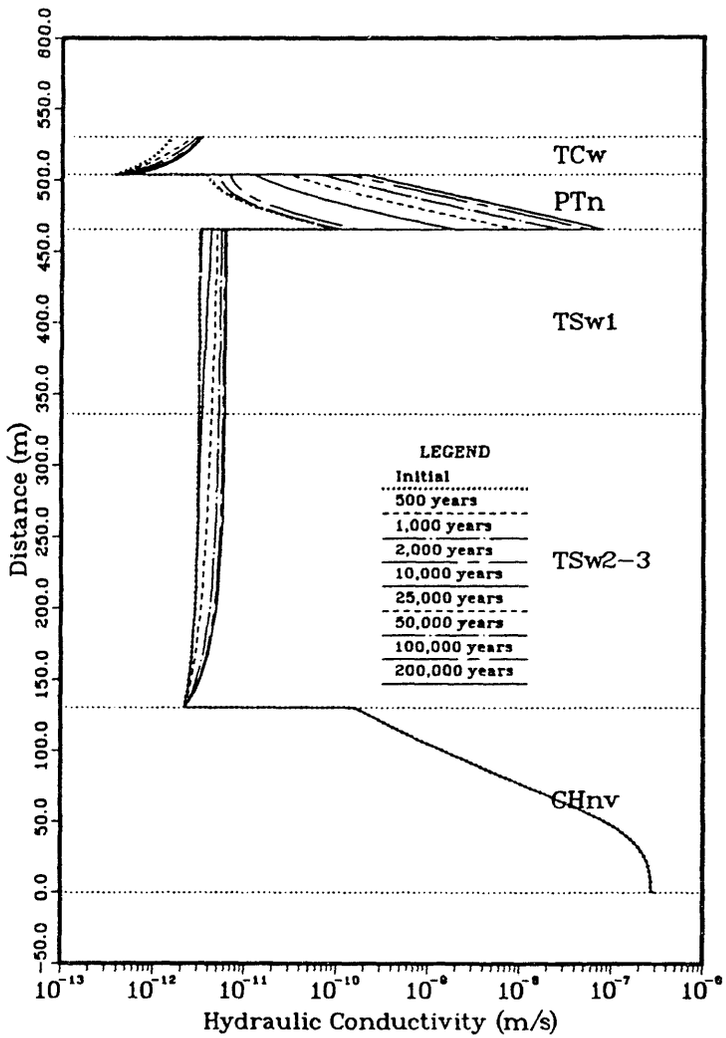

Figure 1-8-4. Hydraulic conductivity versus distance above the water table at specified times; initial set of calculations; Case 8.

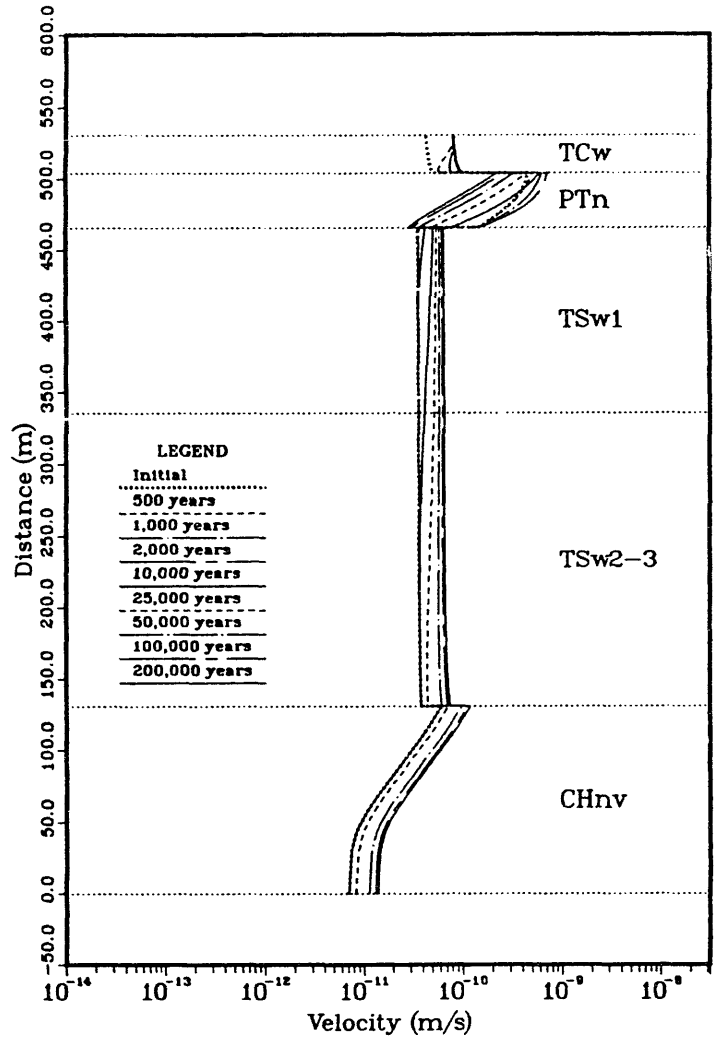

Figure 1-8-5. Average linear velocity of water in the matrix versus distance above the water table at specified times; initial set of calculations; Case 8.

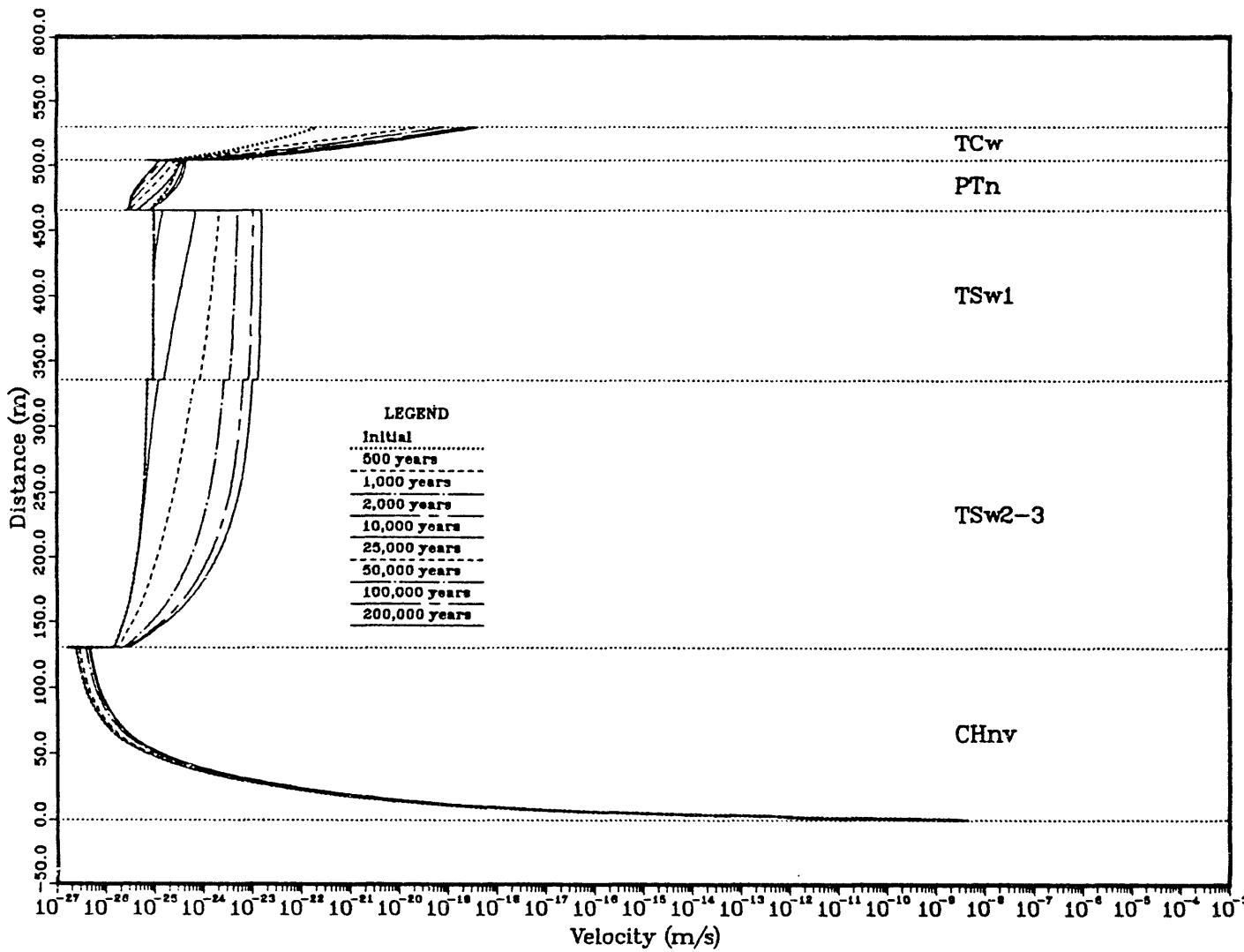

Figure 1-8-6. Average linear velocity of water in the fractures versus distance above the water table at specified times; initial set of calculations; Case 8.

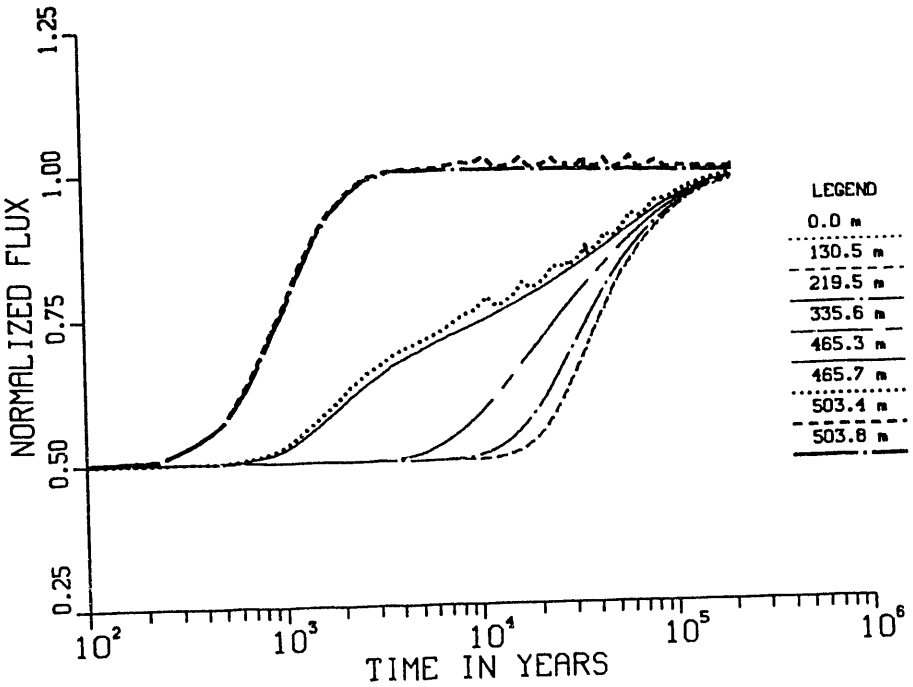

Figure 1-8-7. Normalized flux (calculated flux divided by imposed flux) versus time at specified distances above the water table; initial set of calculations; Case 8.

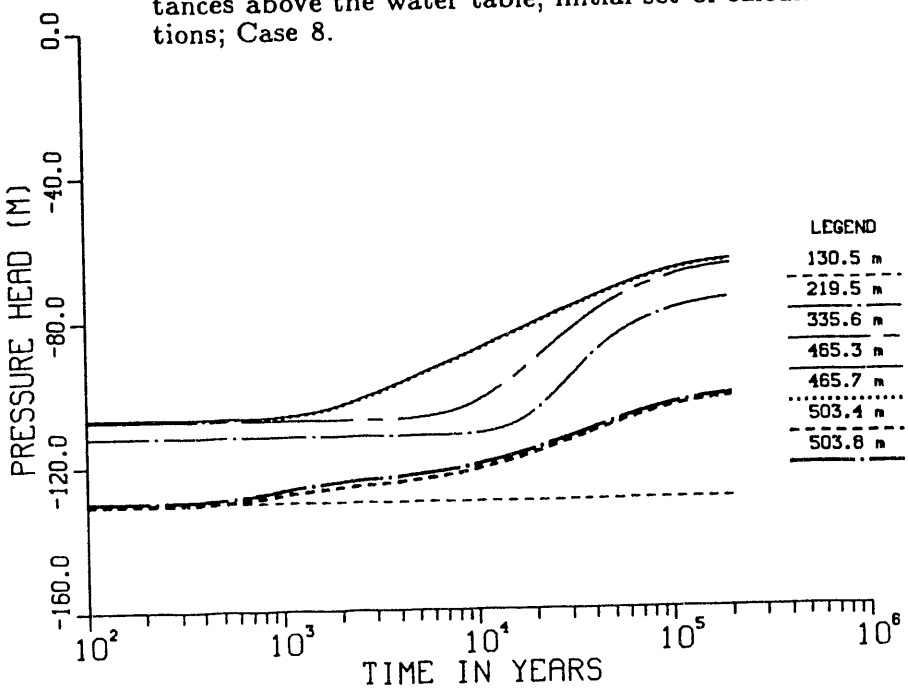

Figure 1-8-8. Pressure head versus time at specified distances above the water table; initial set of calculations; Case 8.

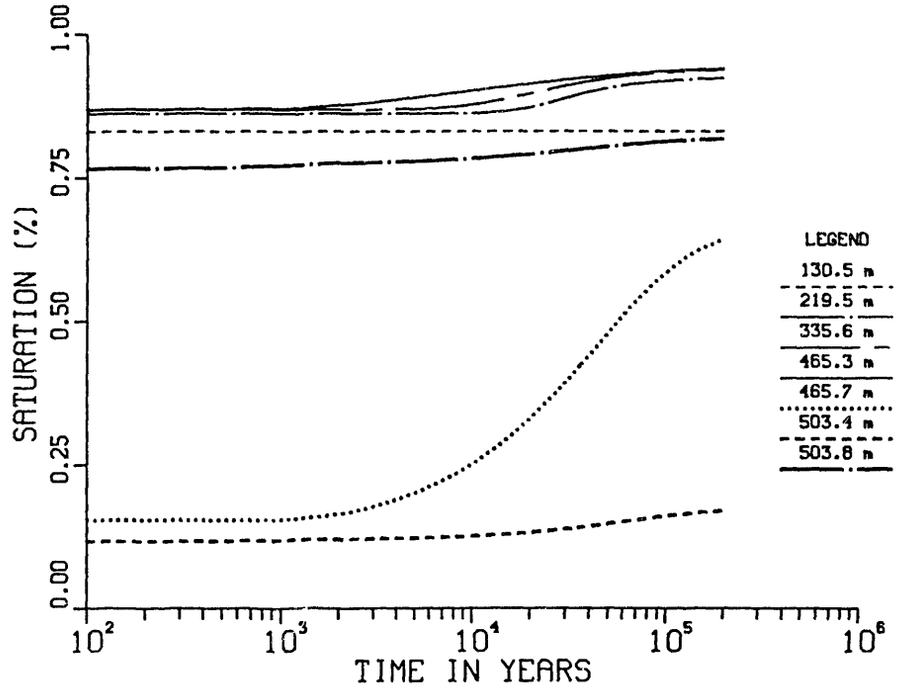

Figure 1-8-9. Matrix saturation versus time at specified distances above the water table; initial set of calculations; Case 8.

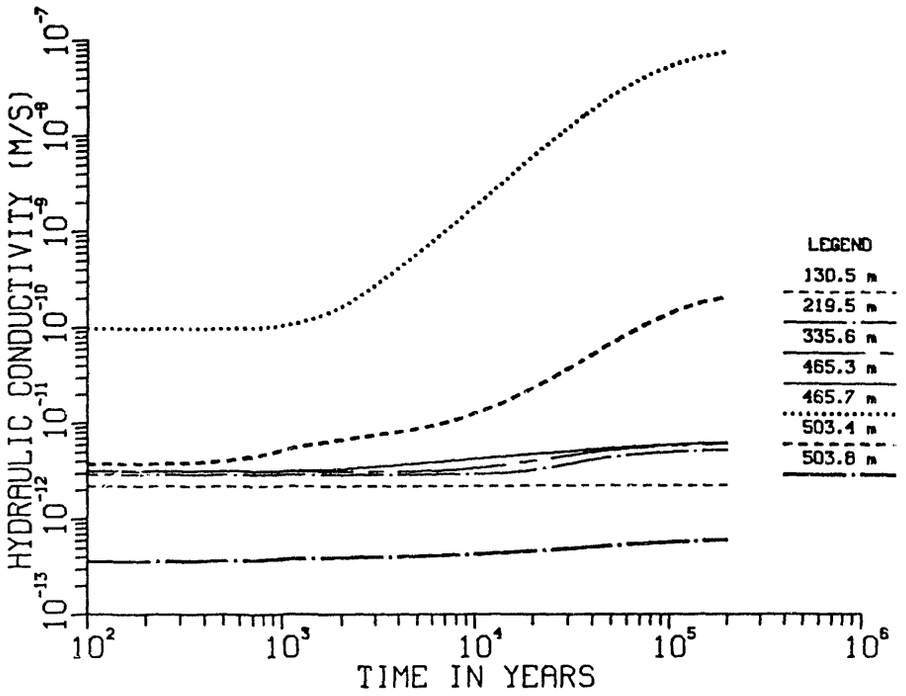

Figure 1-8-10. Hydraulic conductivity versus time at specified distances above the water table; initial set of calculations; Case 8.

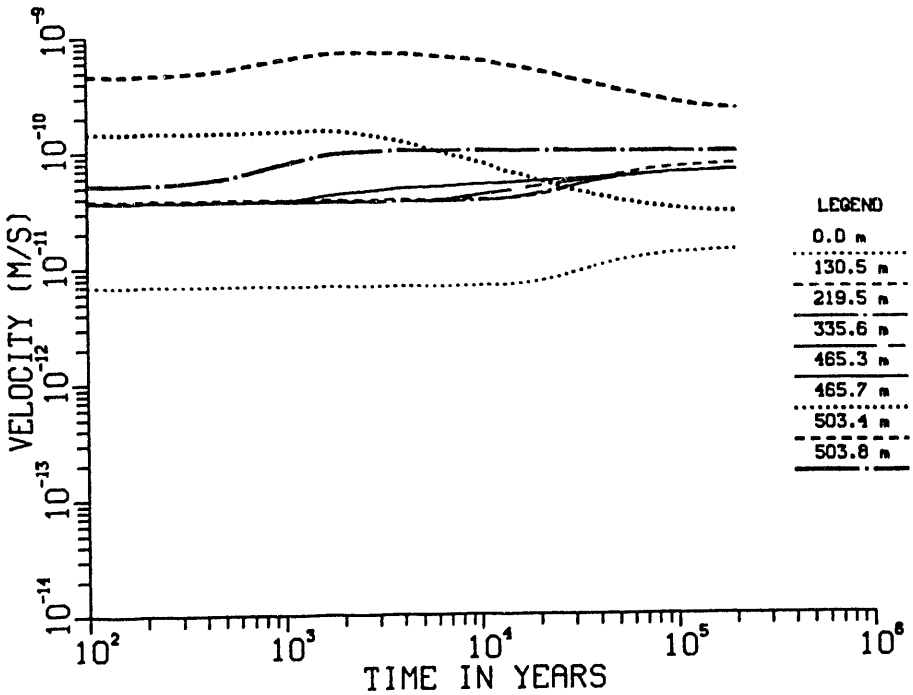

Figure 1-8-11. Average linear velocity of water in the matrix versus time at specified distances above the water table; initial set of calculations; Case 8.

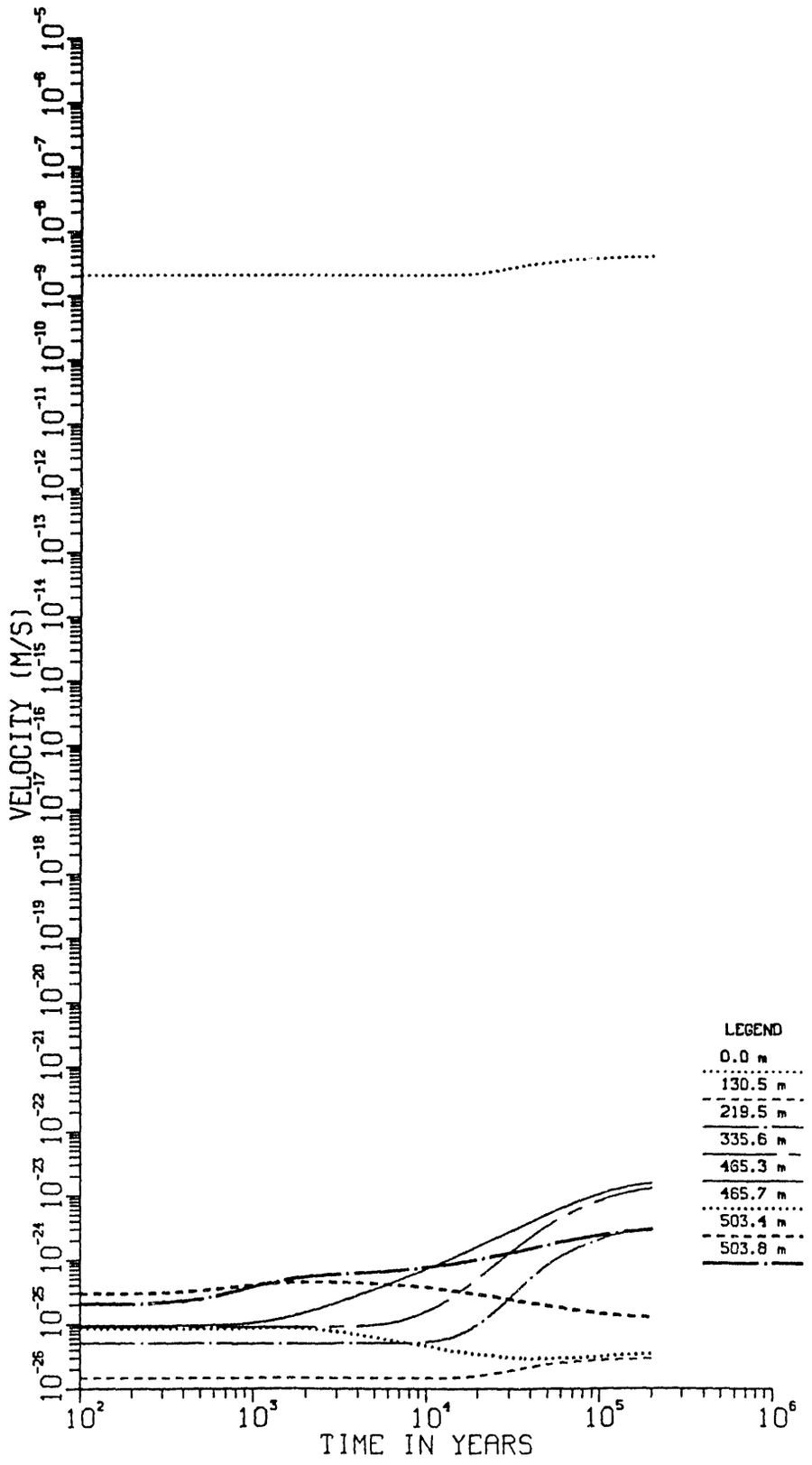

Figure 1-8-12. Average linear velocity of water in the fractures versus time at specified distances above the water table; initial set of calculations; Case 8.

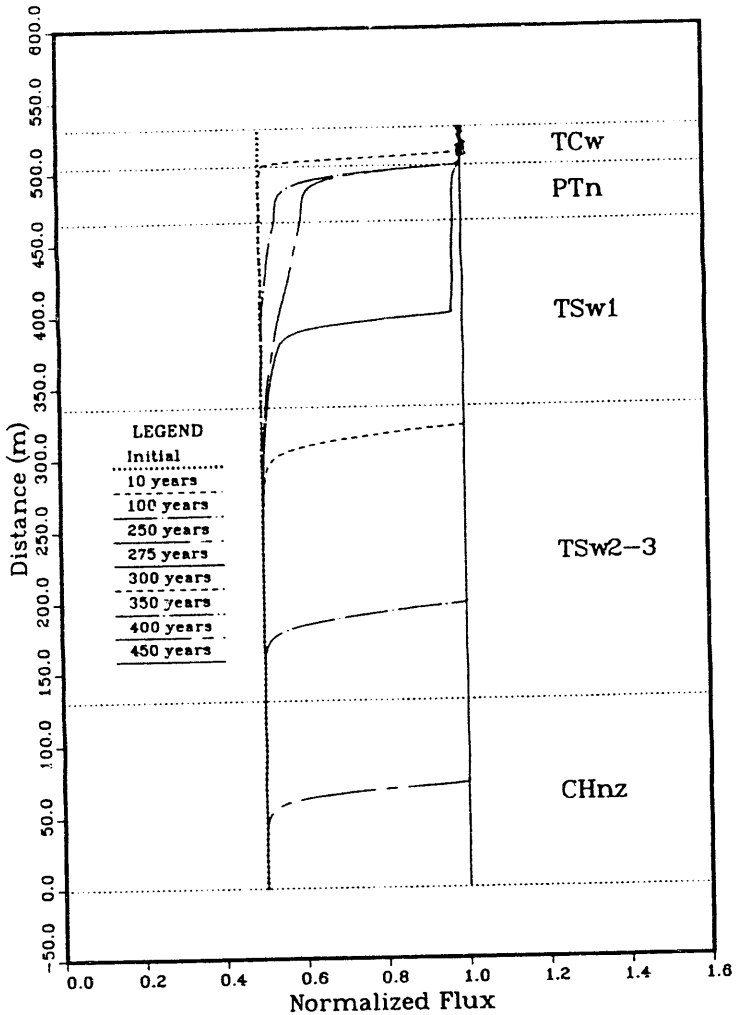

Figure 1-9-1. Normalized flux (calculated flux divided by imposed flux) versus distance above the water table at specified times; initial set of calculations; Case 9.

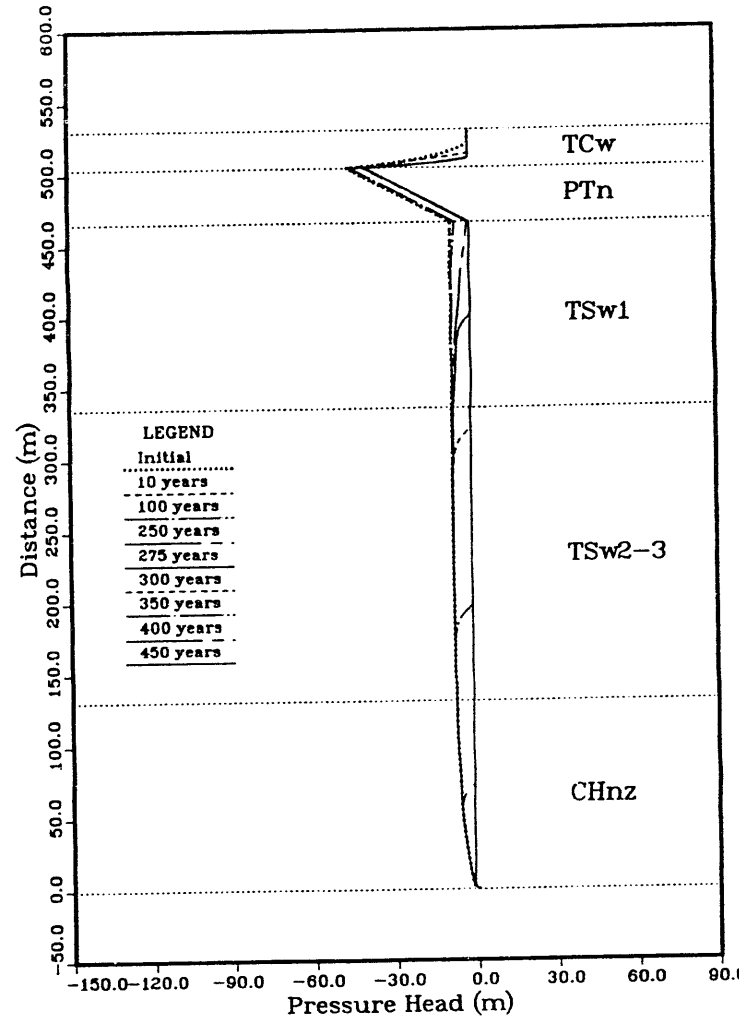

Figure 1-9-2. Pressure head versus distance above the water table at specified times; initial set of calculations; Case 9.

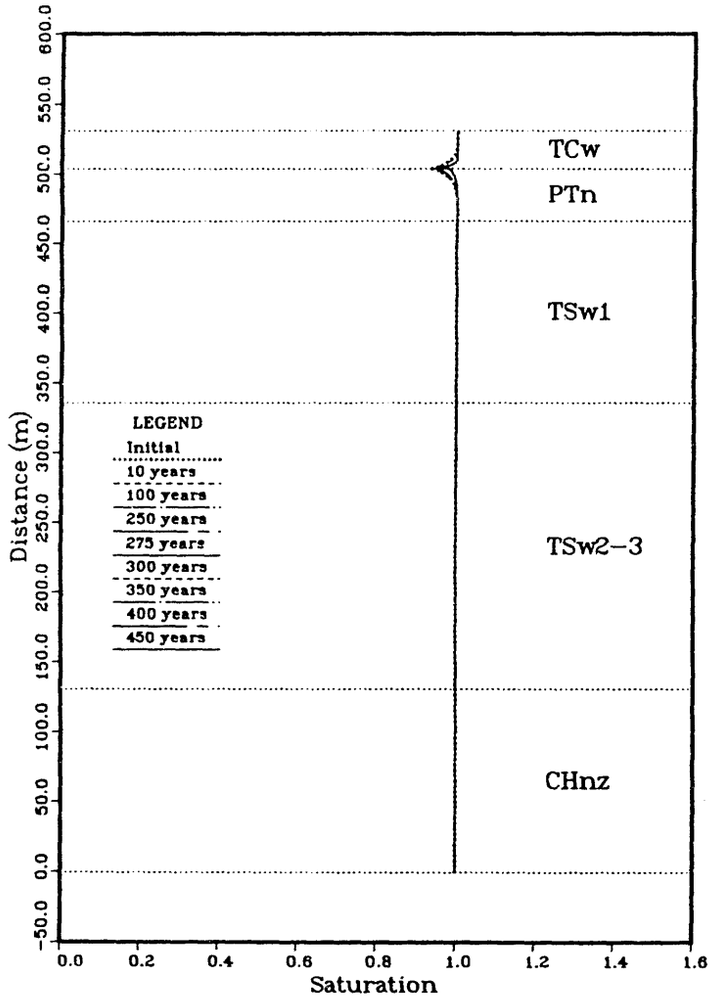

Figure 1-9-3. Matrix saturation versus distance above the water table at specified times; initial set of calculations; Case 9.

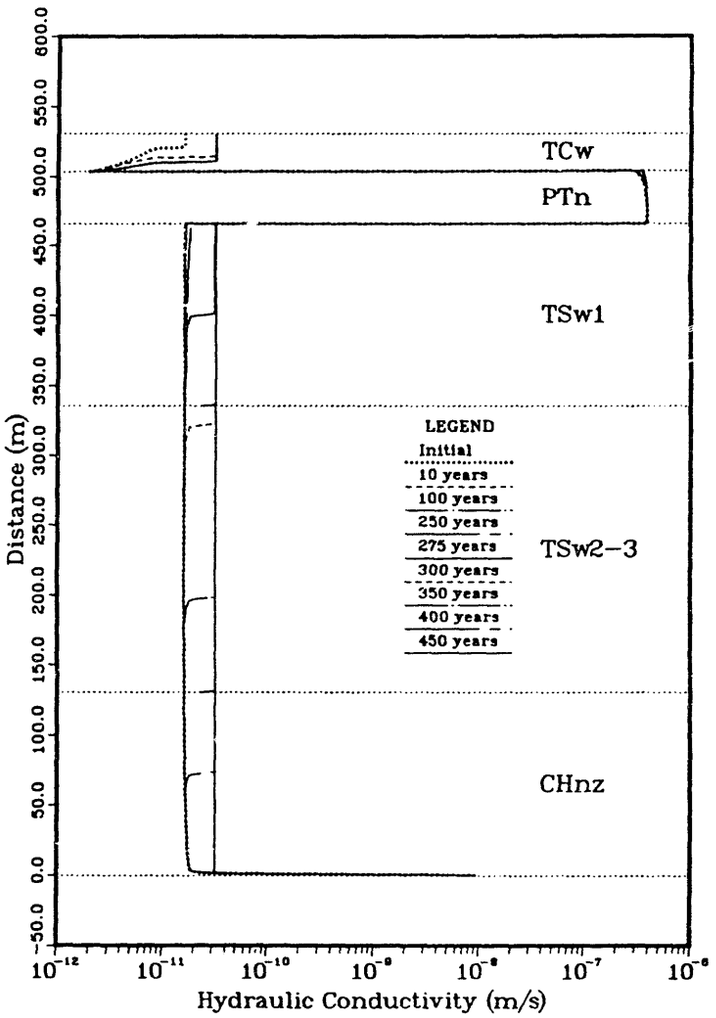

Figure 1-9-4. Hydraulic conductivity versus distance above the water table at specified times; initial set of calculations; Case 9.

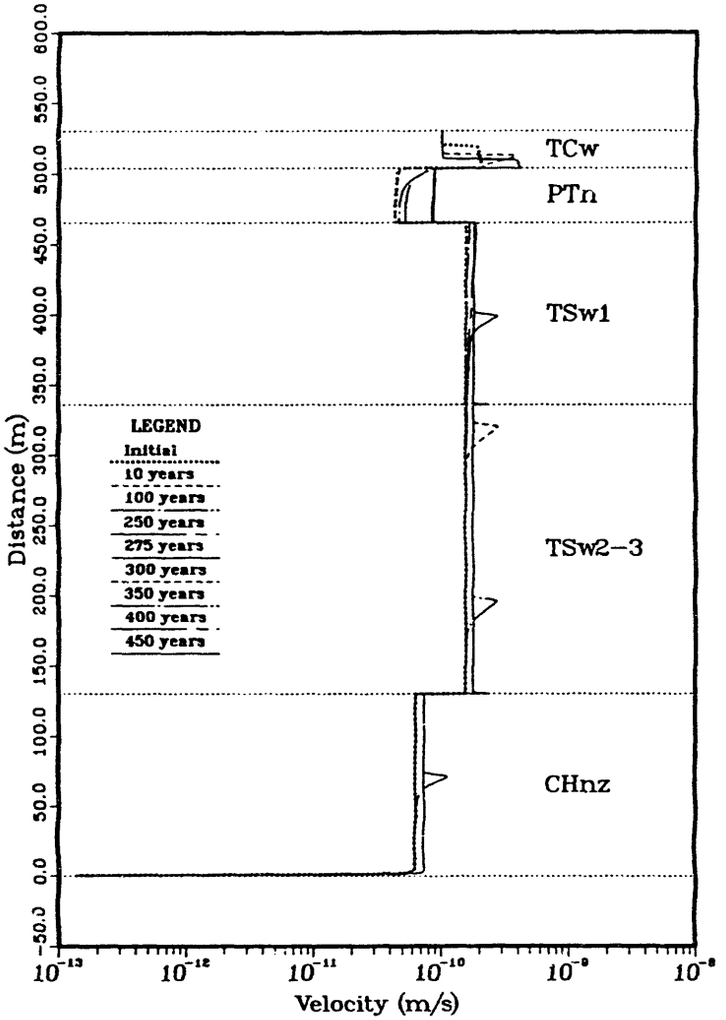

Figure 1-9-5. Average linear velocity of water in the matrix versus distance above the water table at specified times; initial set of calculations; Case 9.

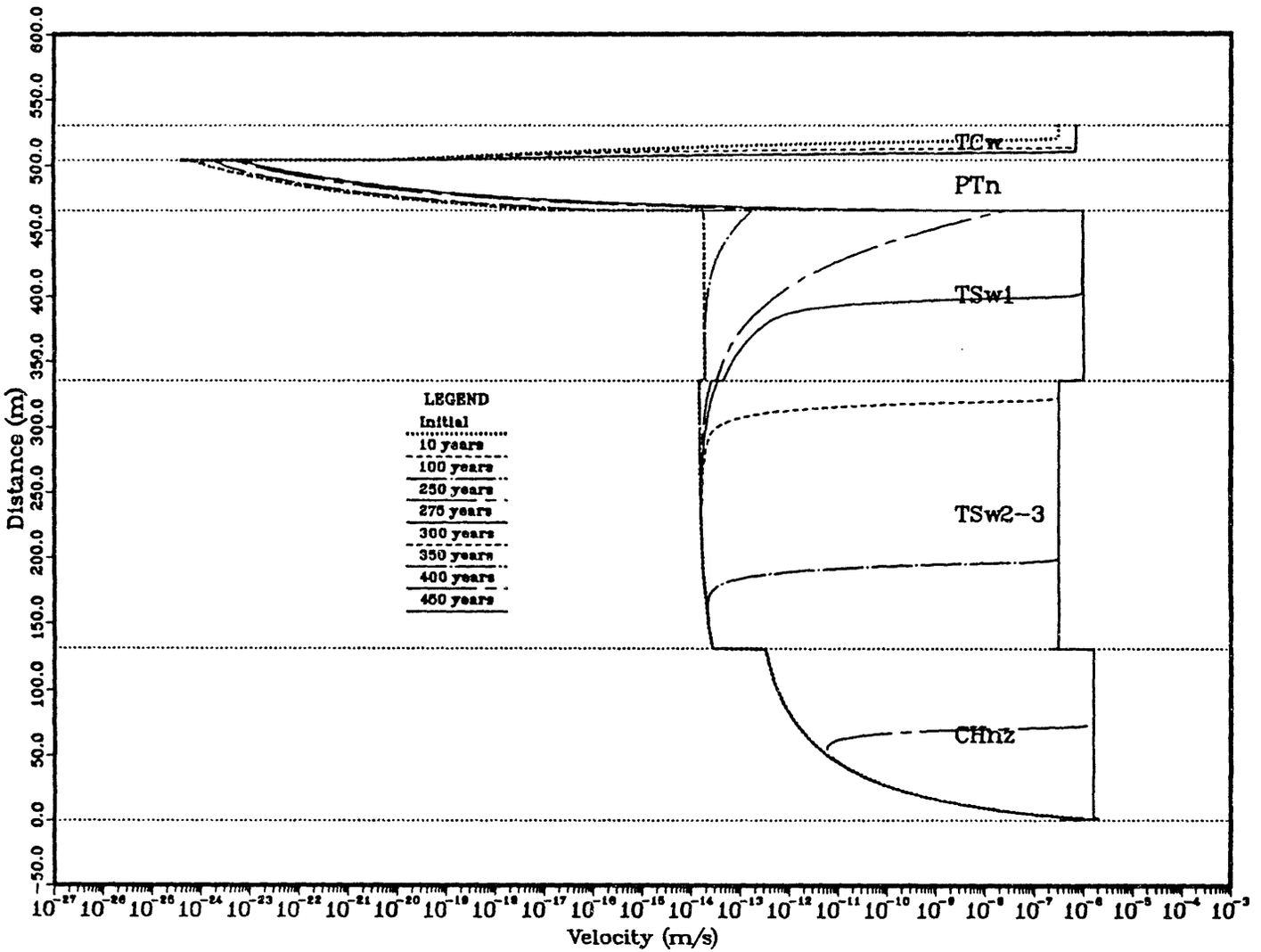

Figure 1-9-6. Average linear velocity of water in the fractures versus distance above the water table at specified times; initial set of calculations; Case 9.

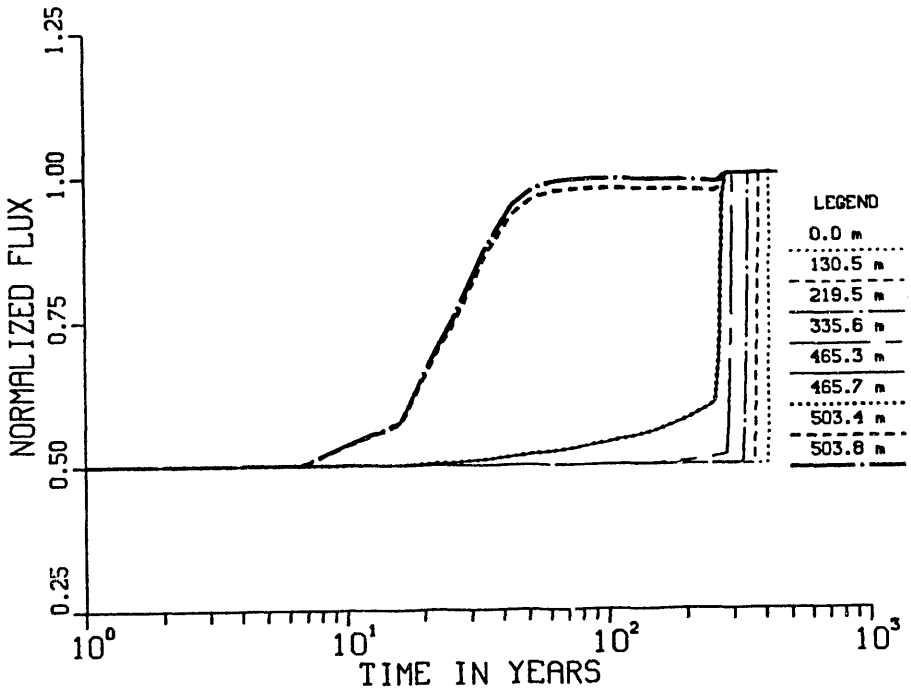

Figure 1-9-7. Normalized flux (calculated flux divided by imposed flux) versus time at specified distances above the water table; initial set of calculations; Case 9.

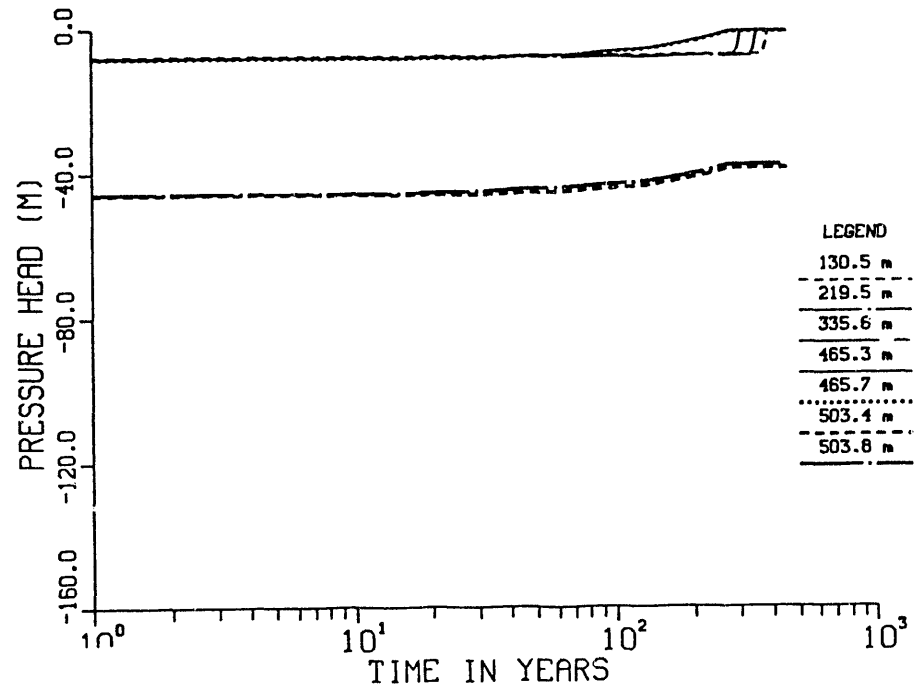

Figure 1-9-8. Pressure head versus time at specified distances above the water table; initial set of calculations; Case 9.

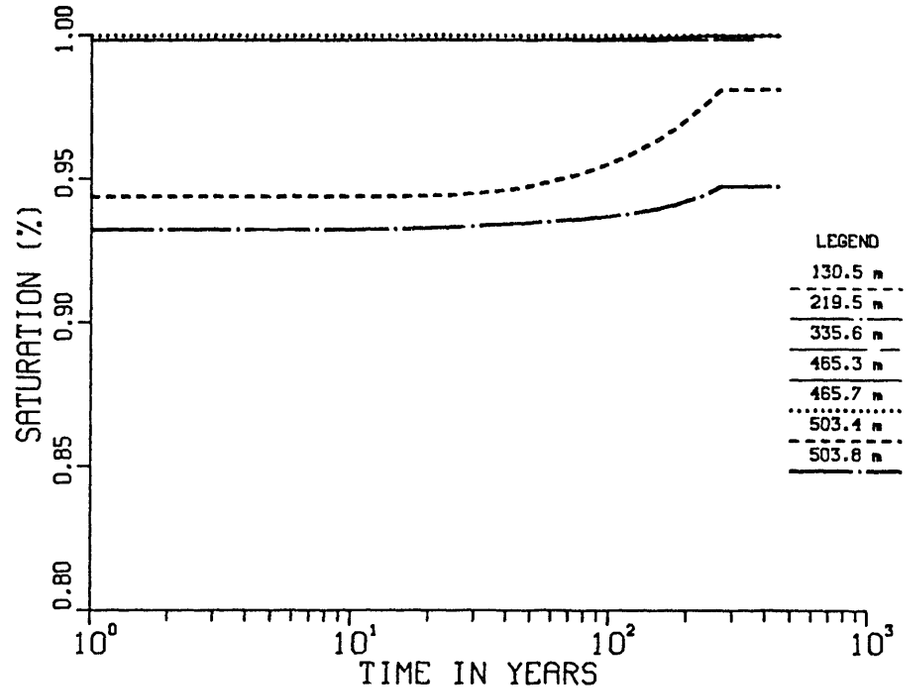

Figure 1-9-9. Matrix saturation versus time at specified distances above the water table; initial set of calculations; Case 9.

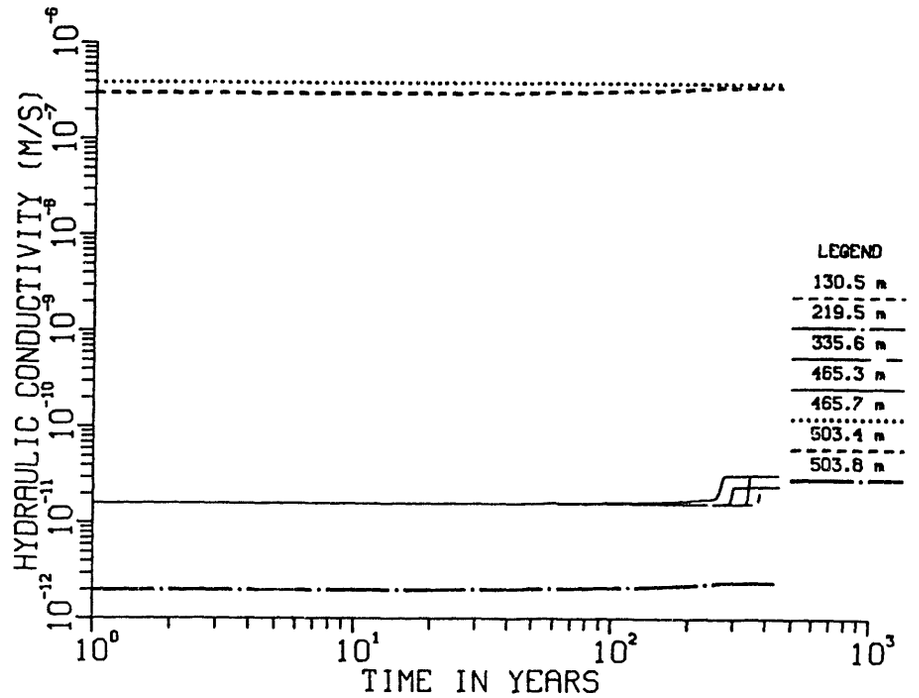

Figure 1-9-10. Hydraulic conductivity versus time at specified distances above the water table; initial set of calculations; Case 9.

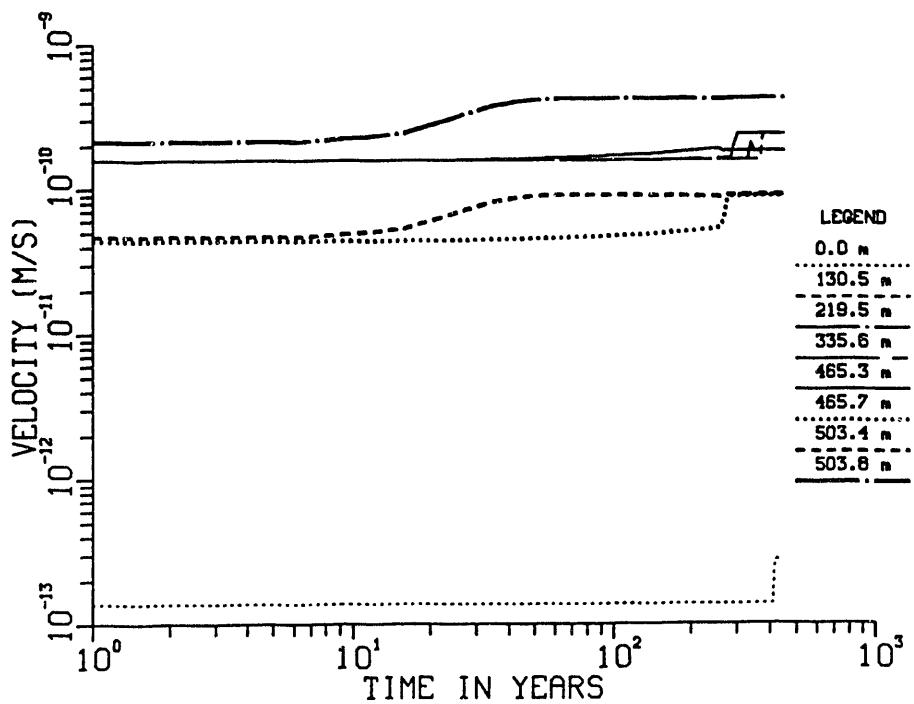

Figure 1-9-11. Average linear velocity of water in the matrix versus time at specified distances above the water table; initial set of calculations; Case 9.

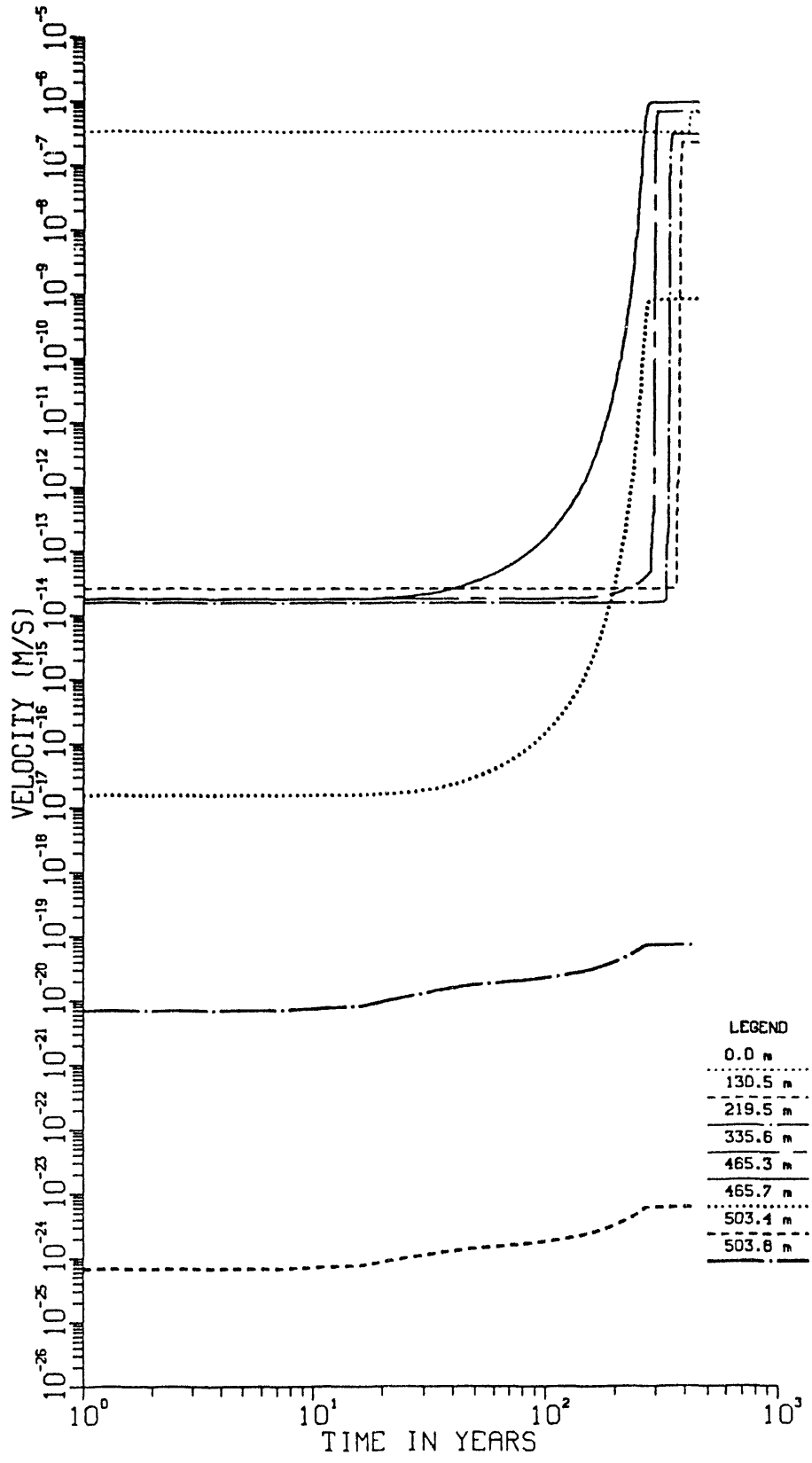

Figure 1-9-12. Average linear velocity of water in the fractures versus time at specified distances above the water table; initial set of calculations; Case 9.

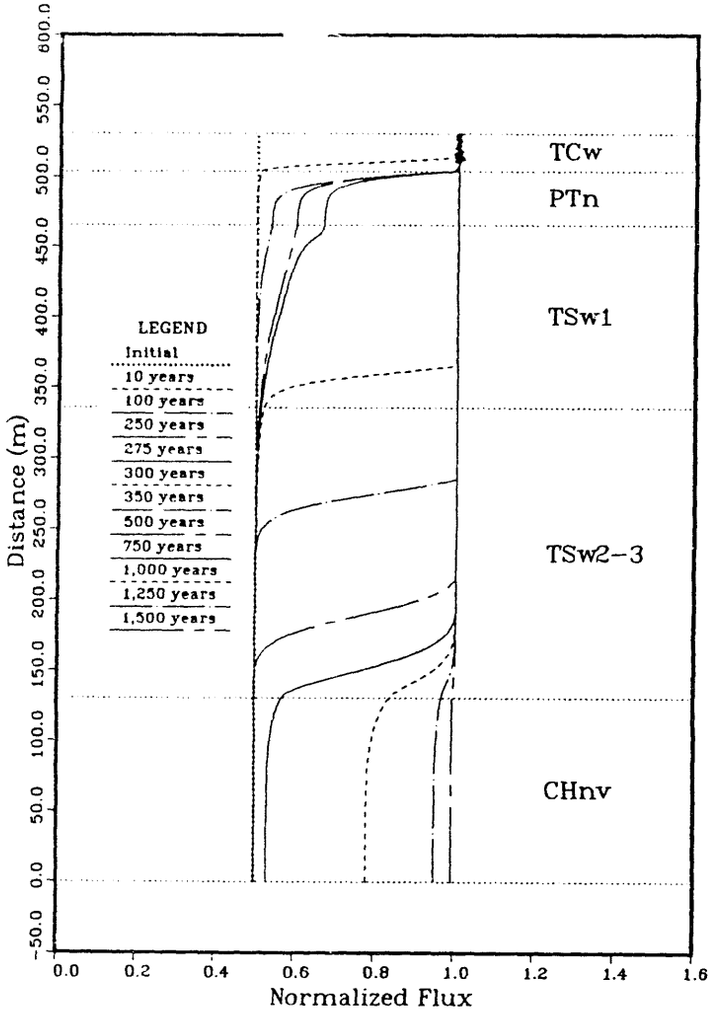

Figure 1-10-1. Normalized flux (calculated flux divided by imposed flux) versus distance above the water table at specified times; initial set of calculations; Case 10.

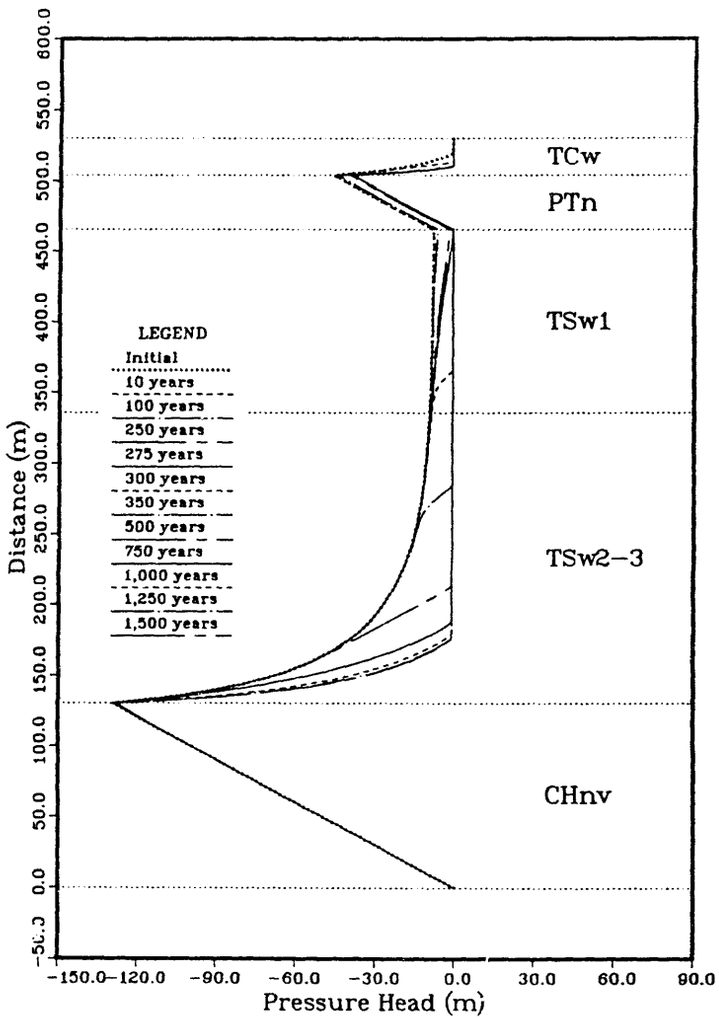

Figure 1-10-2. Pressure head versus distance above the water table at specified times; initial set of calculations; Case 10.

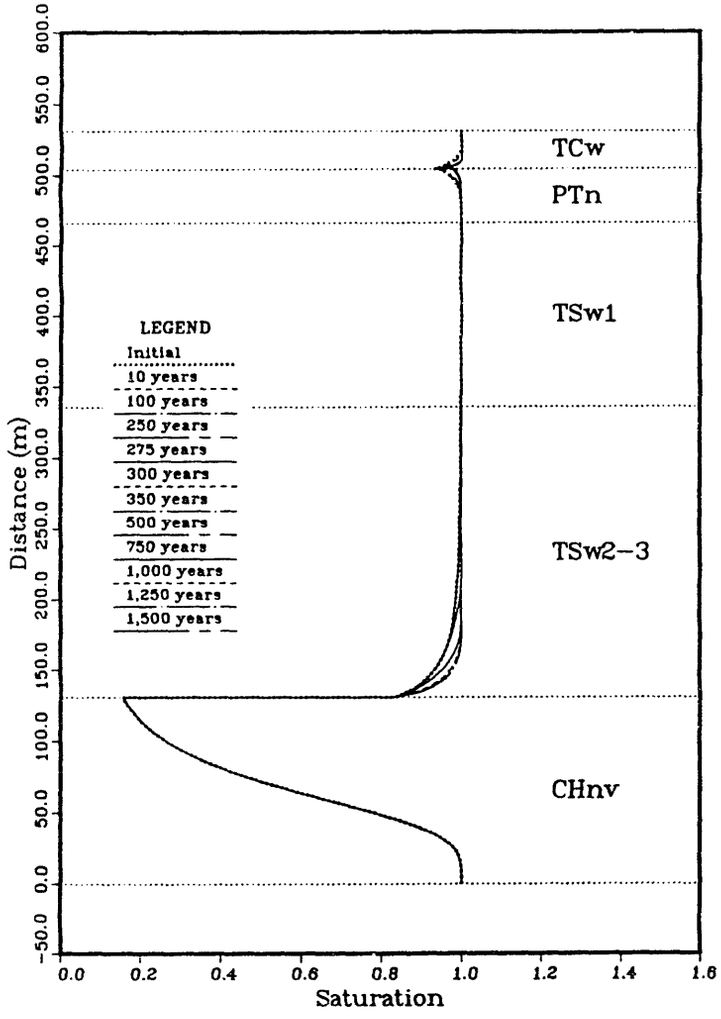

Figure 1-10-3. Matrix saturation versus distance above the water table at specified times; initial set of calculations; Case 10.

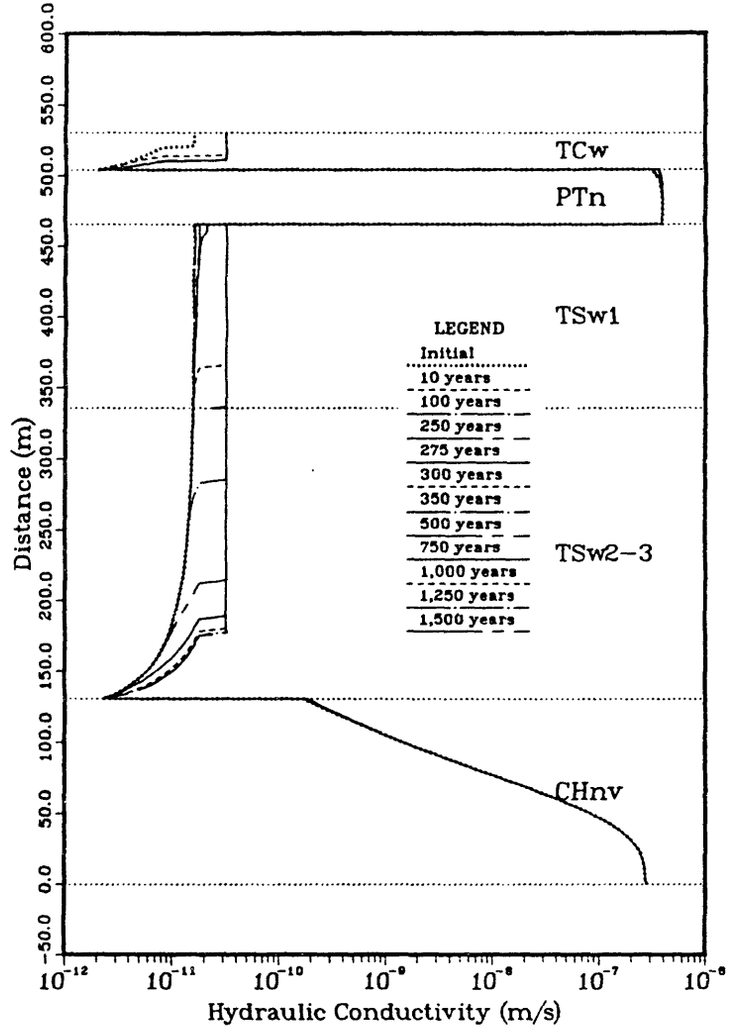

Figure 1-10-4. Hydraulic conductivity versus distance above the water table at specified times; initial set of calculations; Case 10.

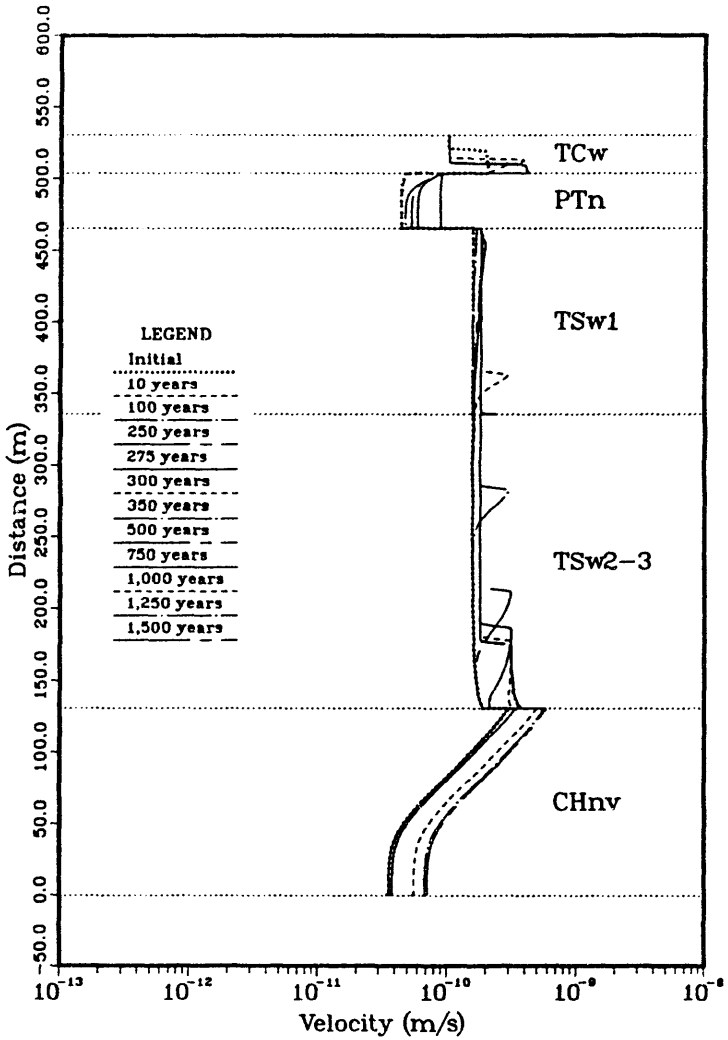

Figure 1-10-5. Average linear velocity of water in the matrix versus distance above the water table at specified times; initial set of calculations; Case 10.

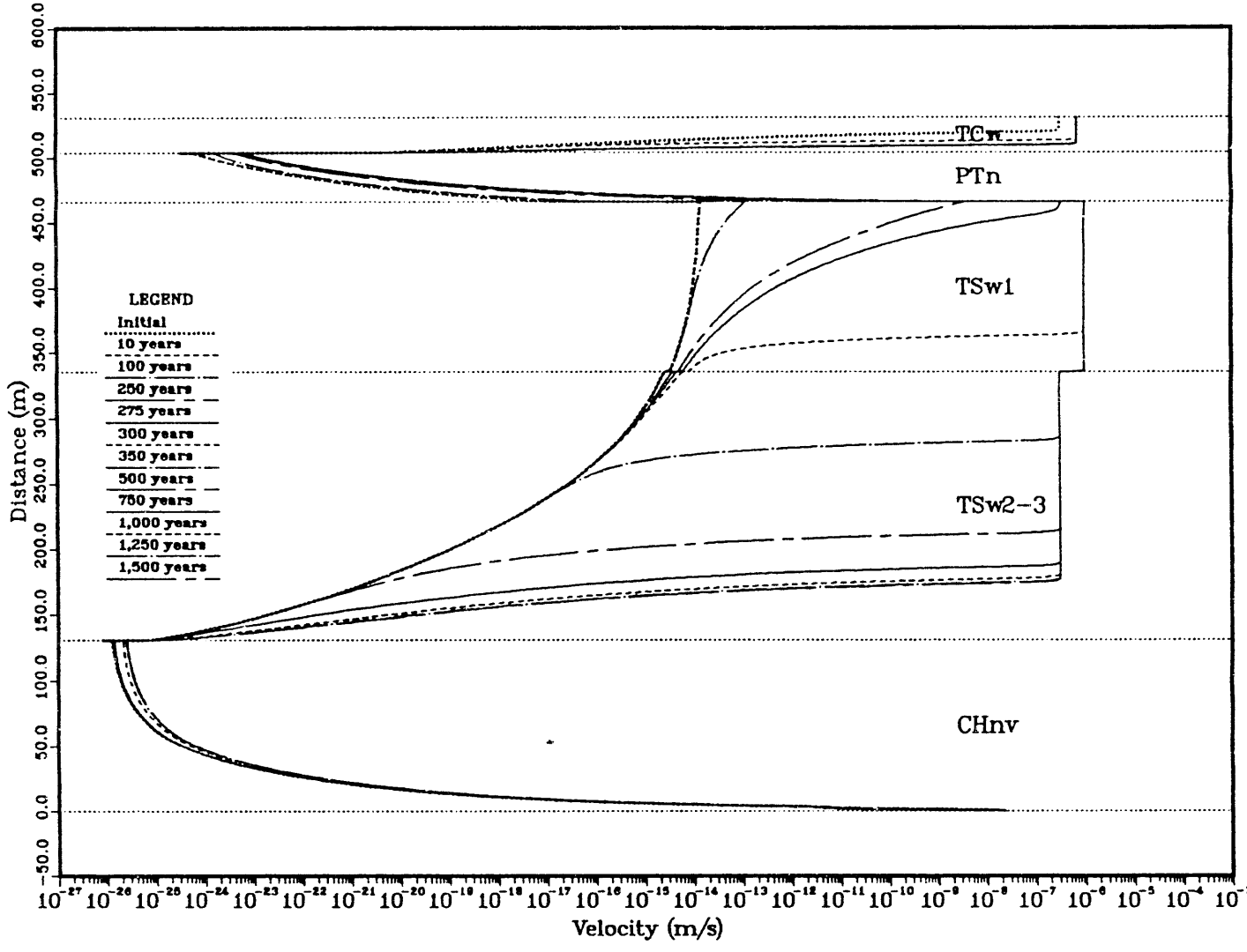

Figure 1-10-6. Average linear velocity of water in the fractures versus distance above the water table at specified times; initial set of calculations; Case 10.

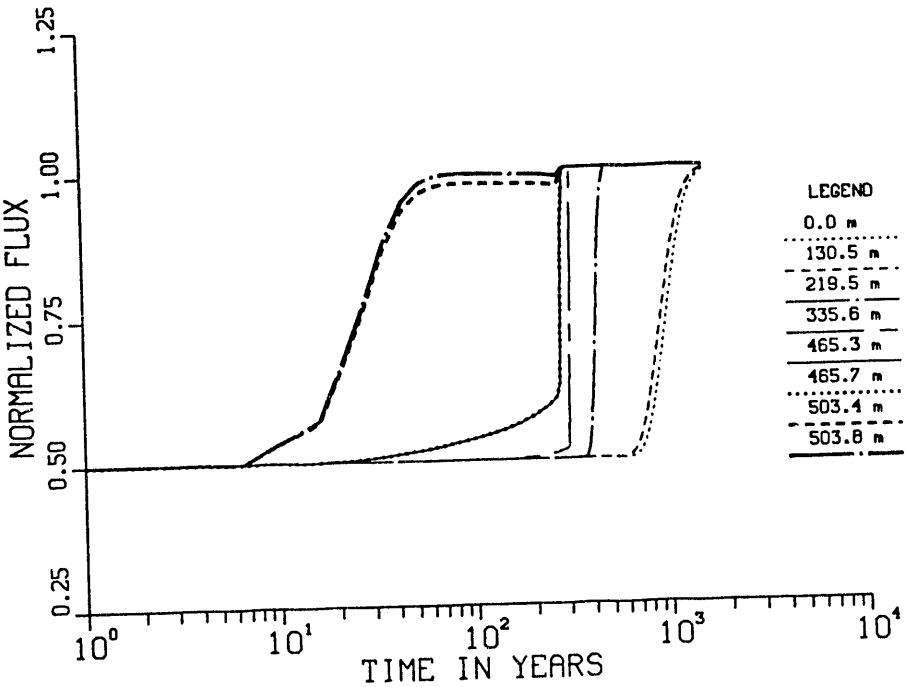

Figure 1-10-7. Normalized flux (calculated flux divided by imposed flux) versus time at specified distances above the water table; initial set of calculations; Case 10.

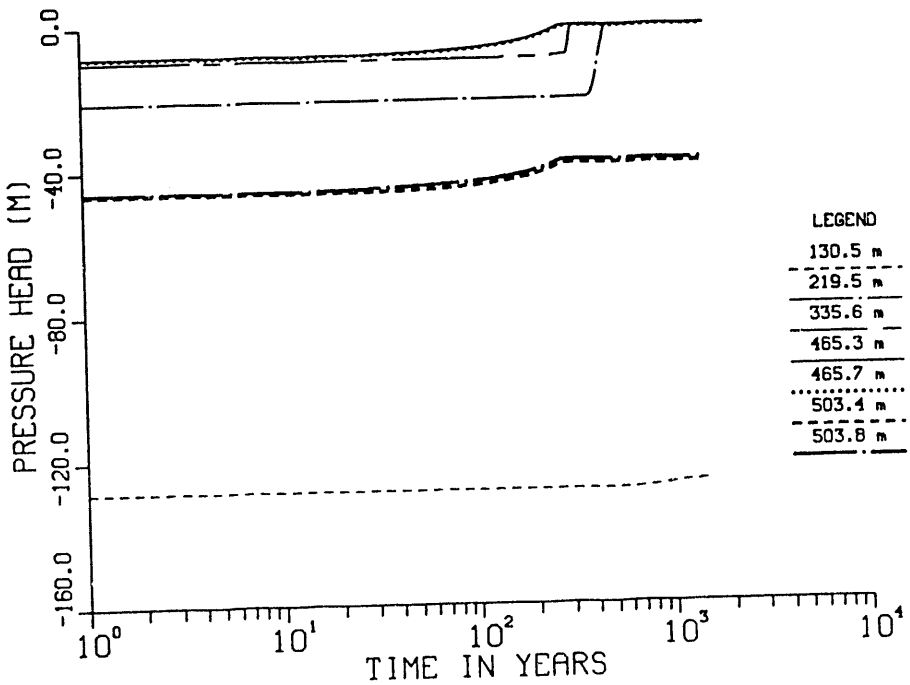

Figure 1-10-8. Pressure head versus time at specified distances above the water table; initial set of calculations; Case 10.

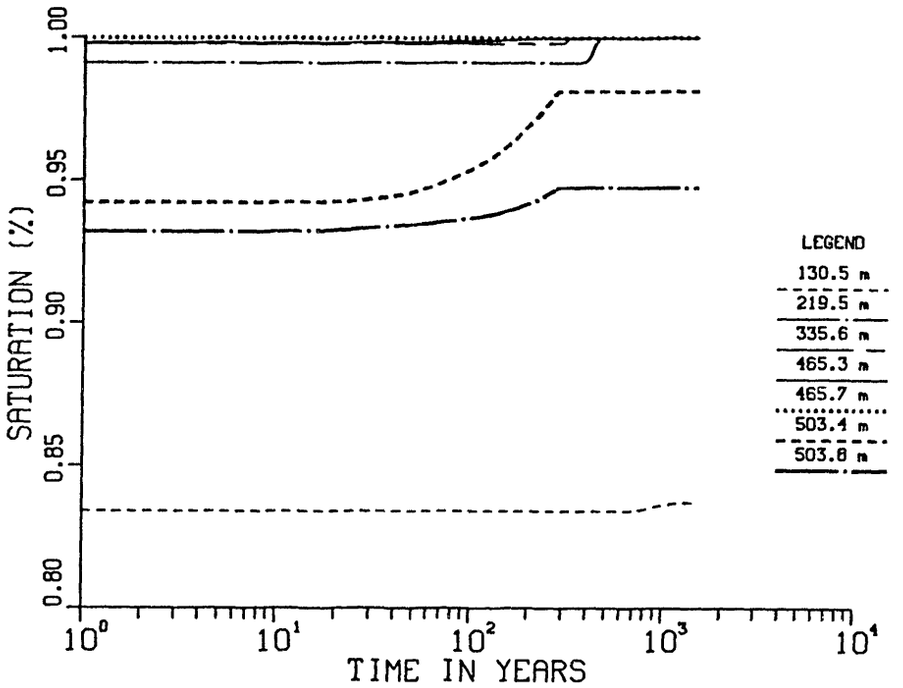

Figure 1-10-9. Matrix saturation versus time at specified distances above the water table; initial set of calculations; Case 10.

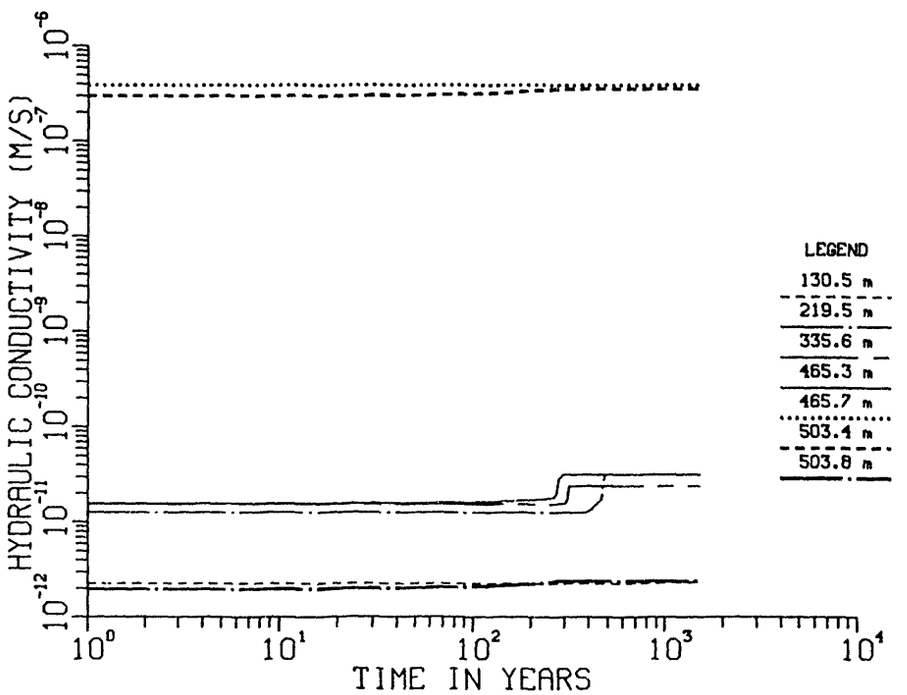

Figure 1-10-10. Hydraulic conductivity versus time at specified distances above the water table; initial set of calculations; Case 10.

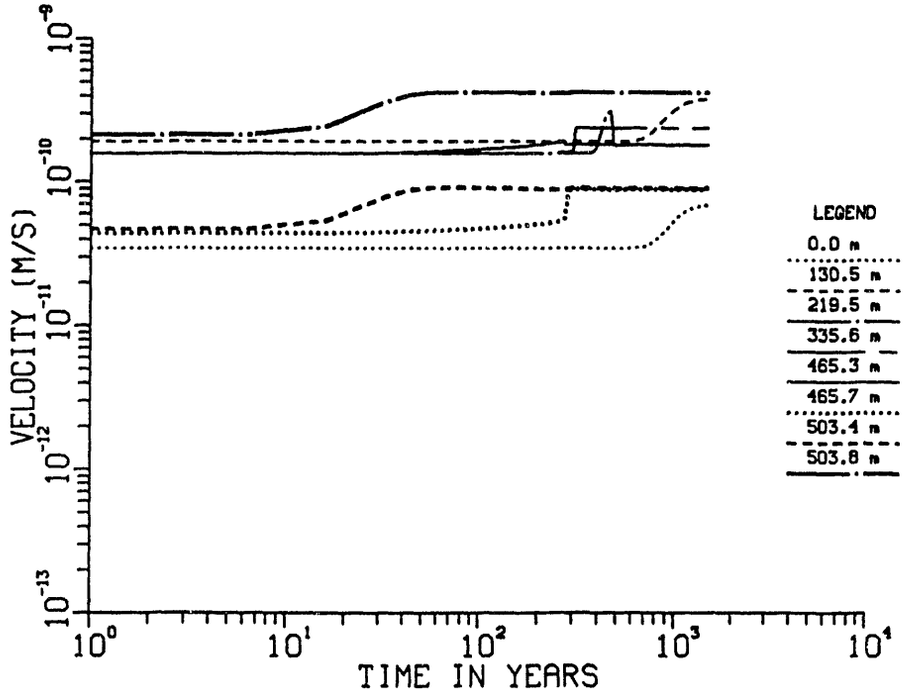

Figure 1-10-11. Average linear velocity of water in the matrix versus time at specified distances above the water table; initial set of calculations; Case 10.

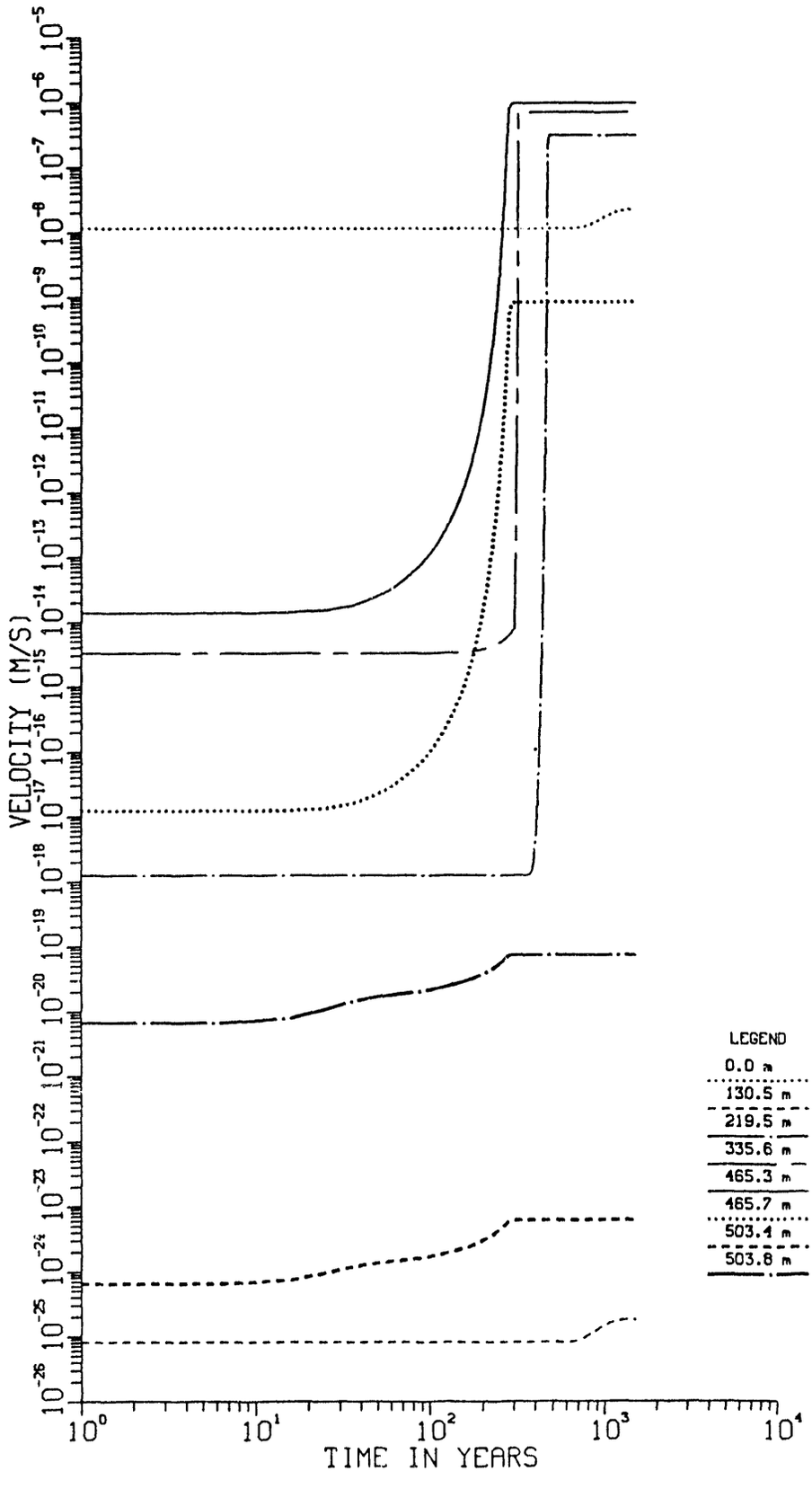

Figure 1-10-12. Average linear velocity of water in the fractures versus time at specified distances above the water table; initial set of calculations; Case 10.

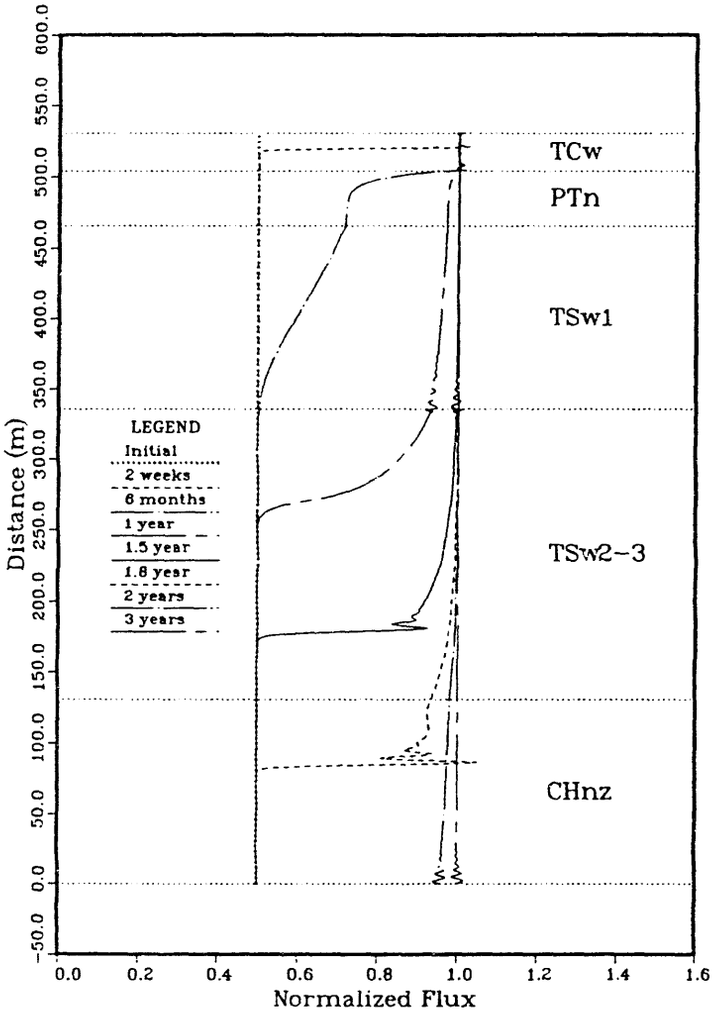

Figure 1-11-1. Normalized flux (calculated flux divided by imposed flux) versus distance above the water table at specified times; initial set of calculations; Case 11.

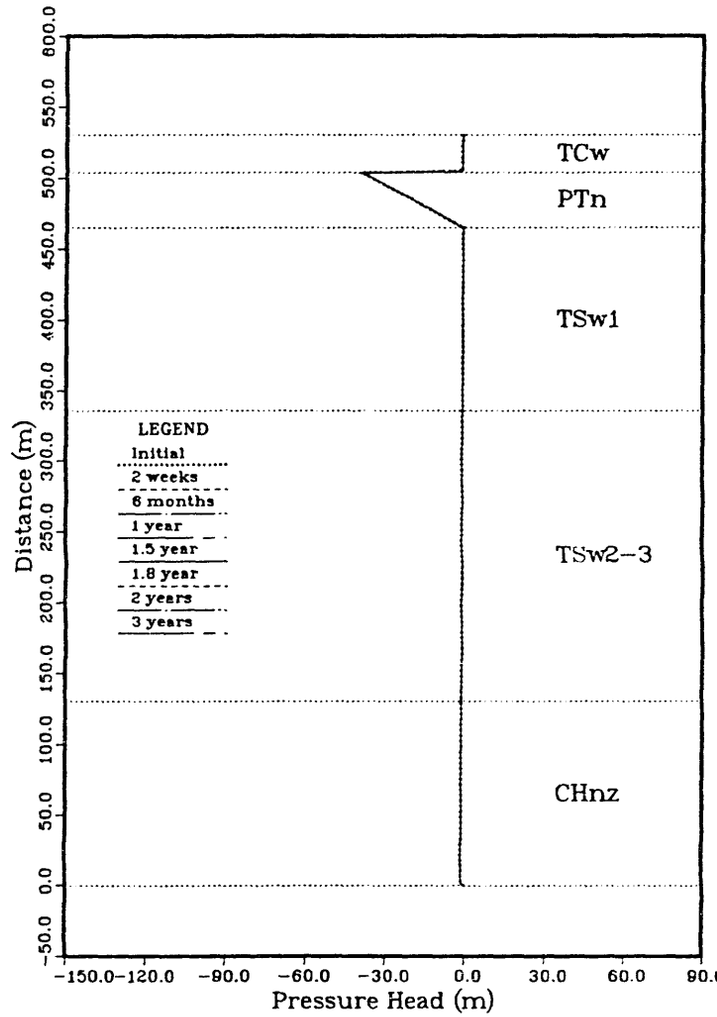

Figure 1-11-2. Pressure head versus distance above the water table at specified times; initial set of calculations; Case 11.

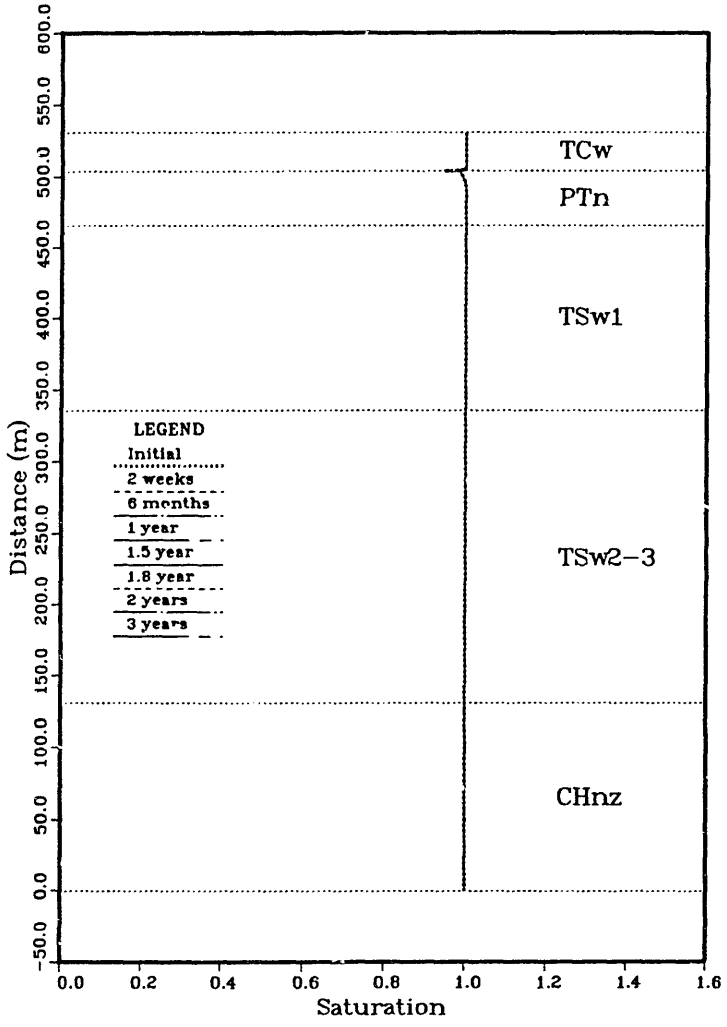

Figure 1-11-3. Matrix saturation versus distance above the water table at specified times; initial set of calculations; Case 11.

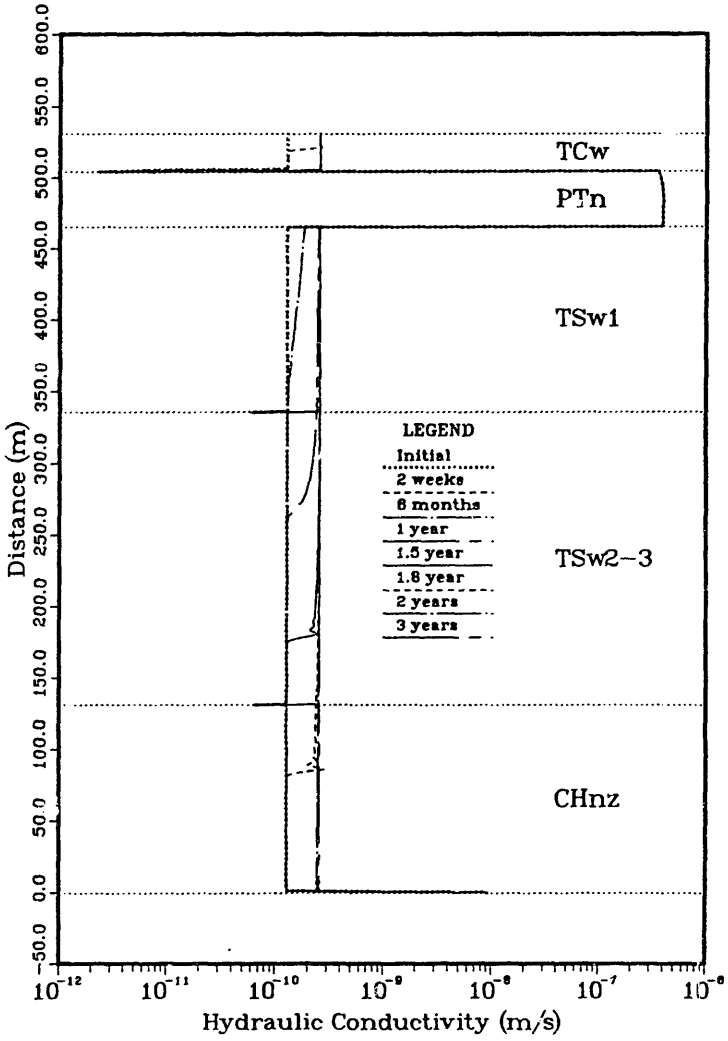

Figure 1-11-4. Hydraulic conductivity versus distance above the water table at specified times; initial set of calculations; Case 11.

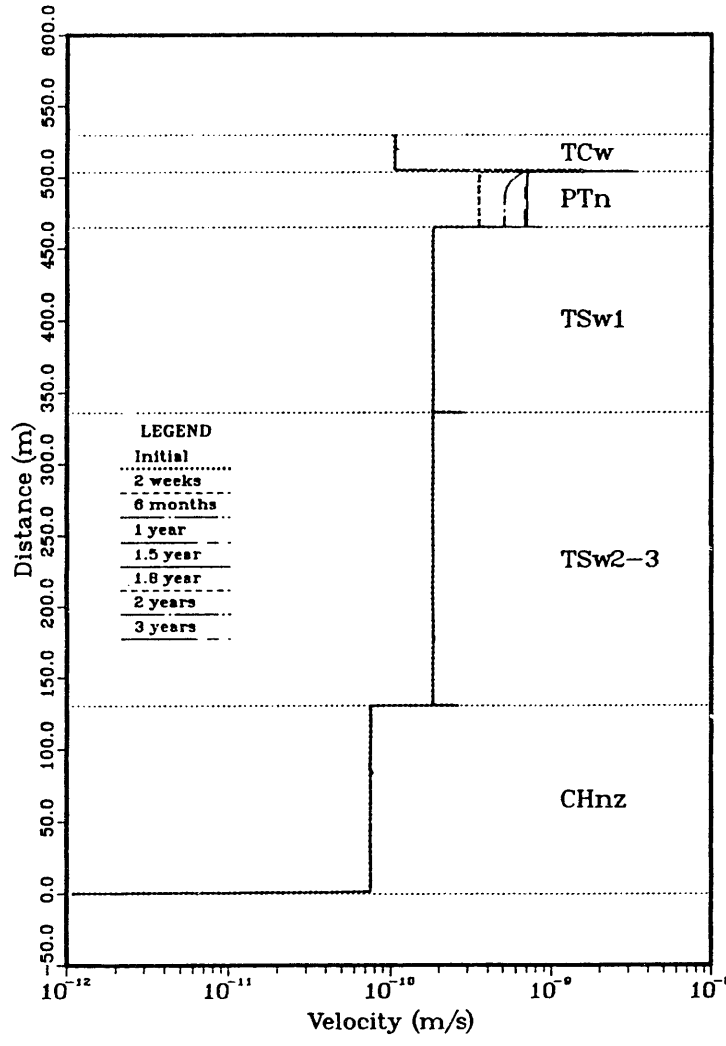

Figure 1-11-5. Average linear velocity of water in the matrix versus distance above the water table at specified times; initial set of calculations; Case 11.

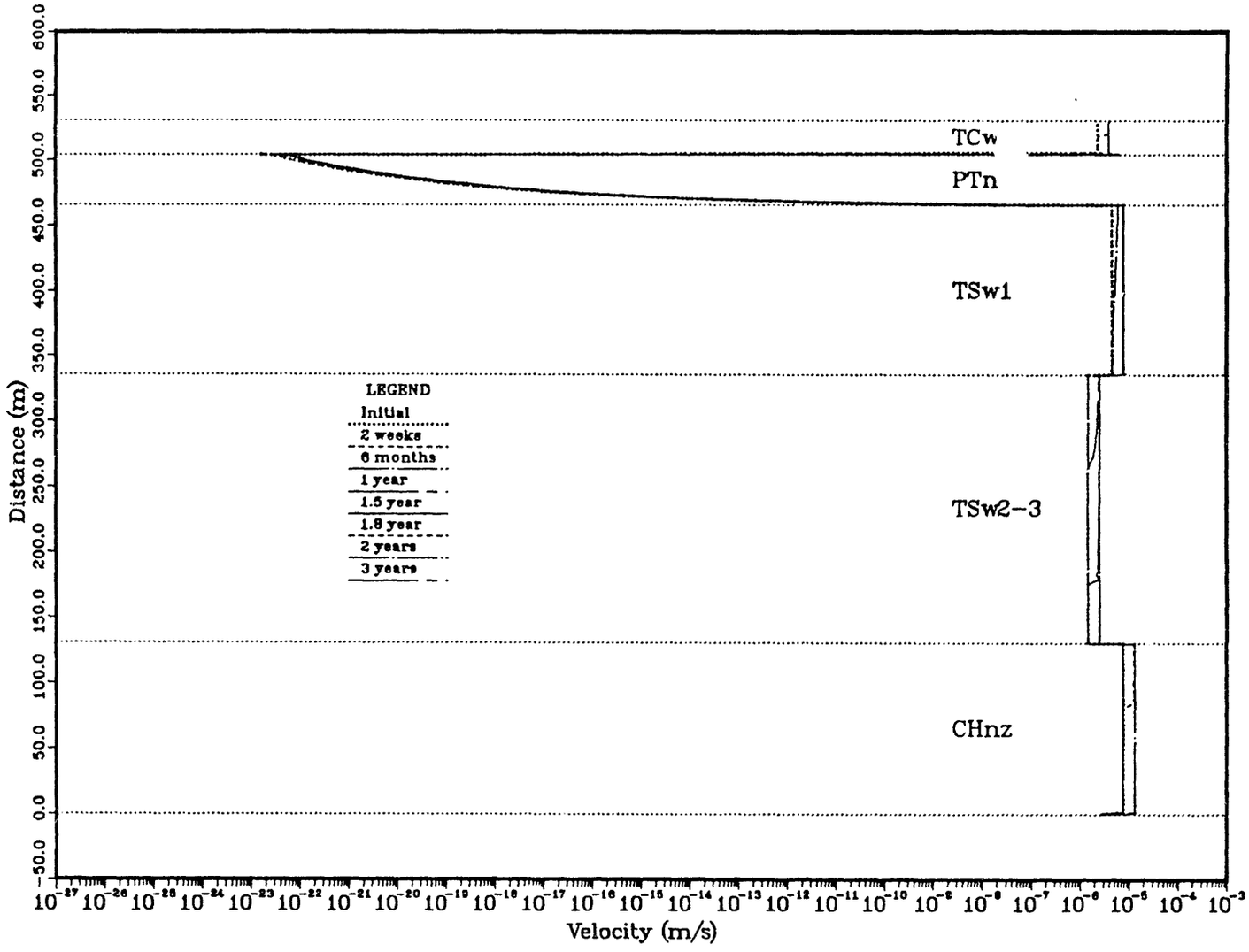

Figure 1-11-6. Average linear velocity of water in the fractures versus distance above the water table at specified times; initial set of calculations; Case 11.

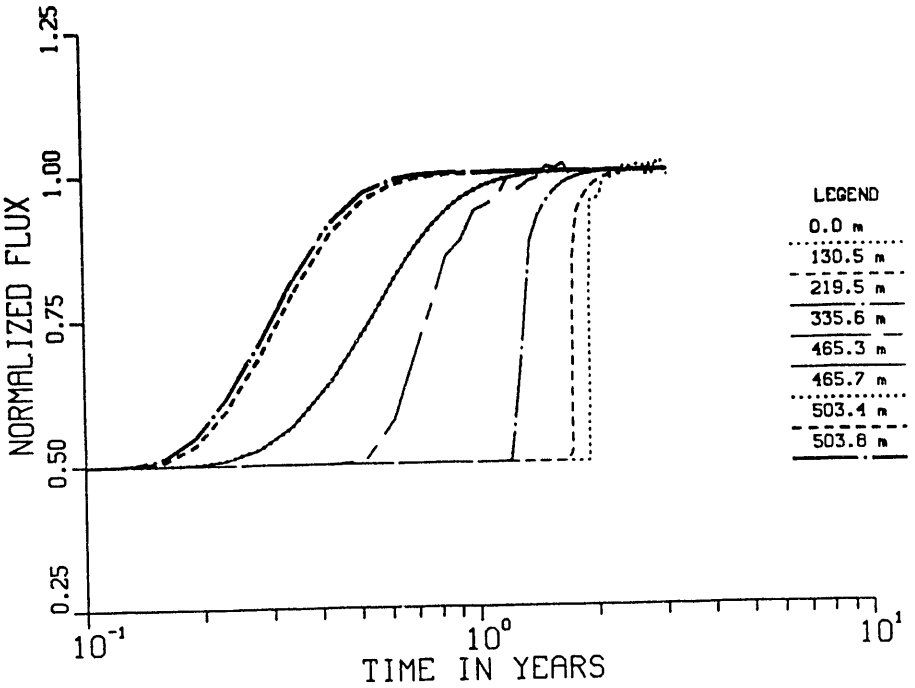

Figure 1-11-7. Normalized flux (calculated flux divided by imposed flux) versus time at specified distances above the water table; initial set of calculations; Case 11.

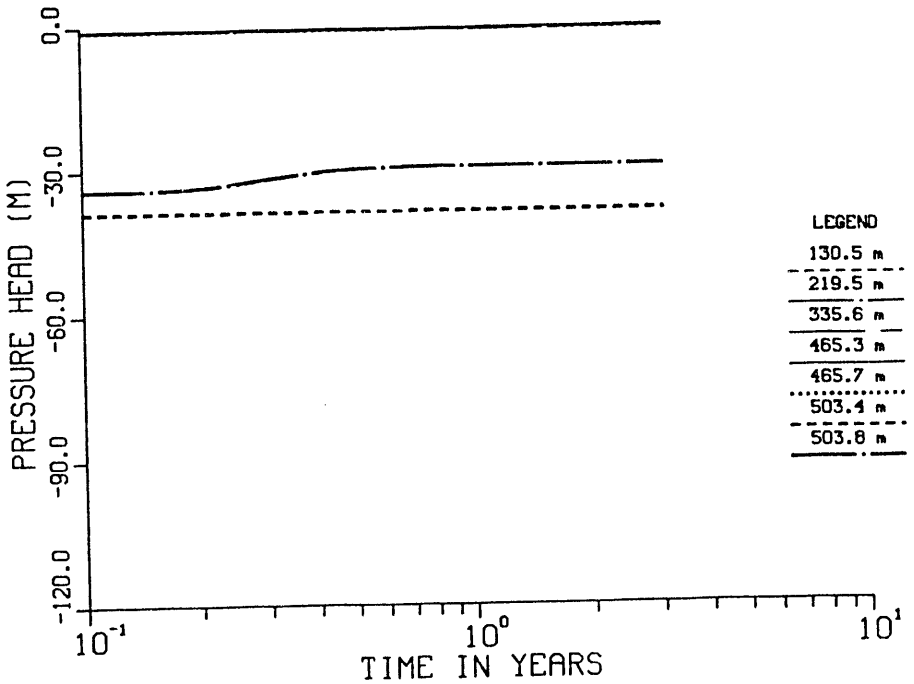

Figure 1-11-8. Pressure head versus time at specified distances above the water table; initial set of calculations; Case 11.

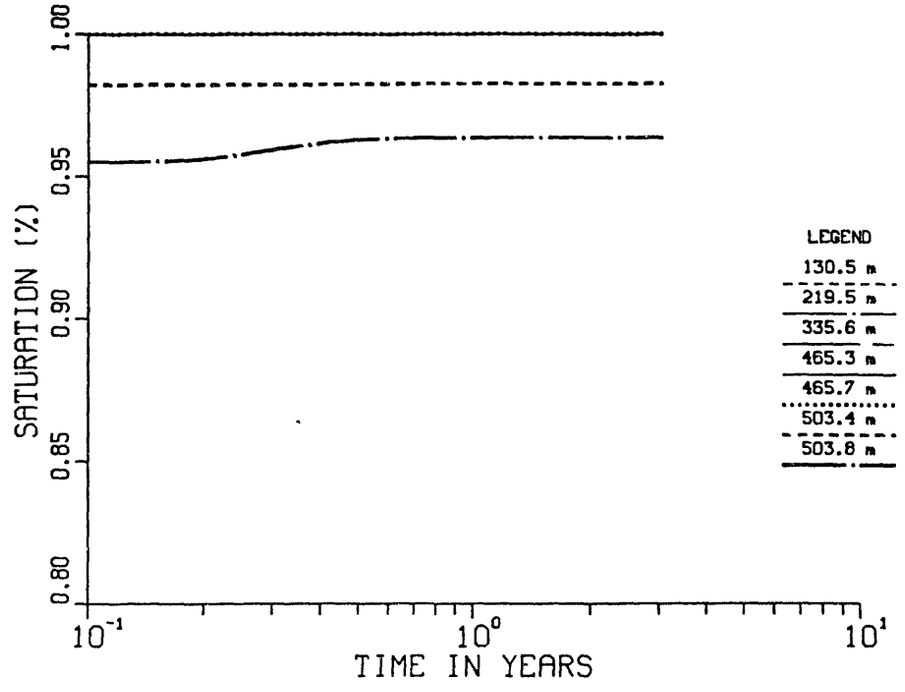

Figure 1-11-9. Matrix saturation versus time at specified distances above the water table; initial set of calculations; Case 11.

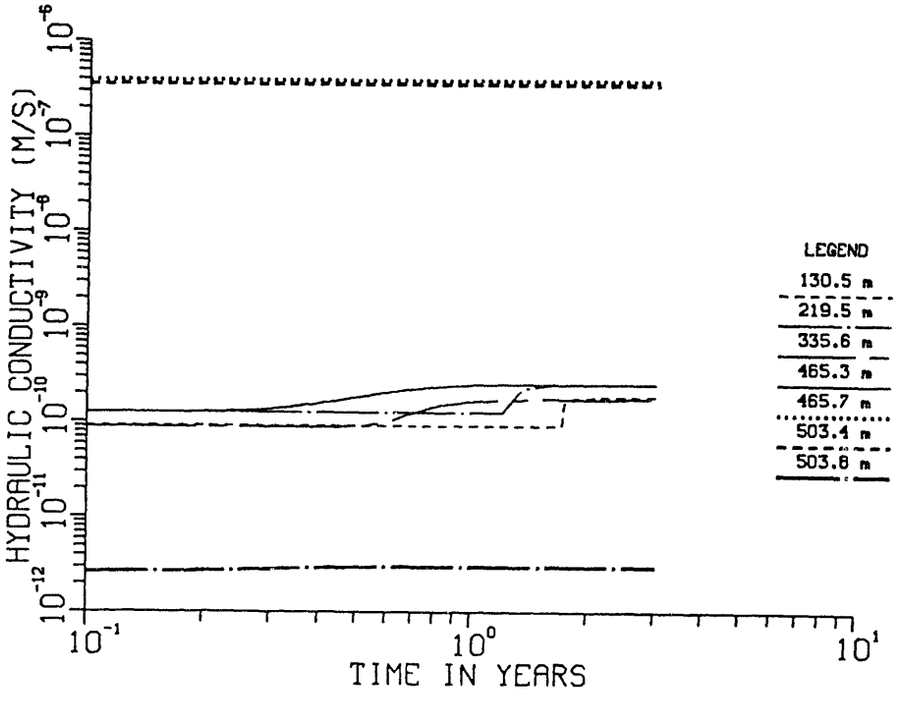

Figure 1-11-10. Hydraulic conductivity versus time at specified distances above the water table; initial set of calculations; Case 11.

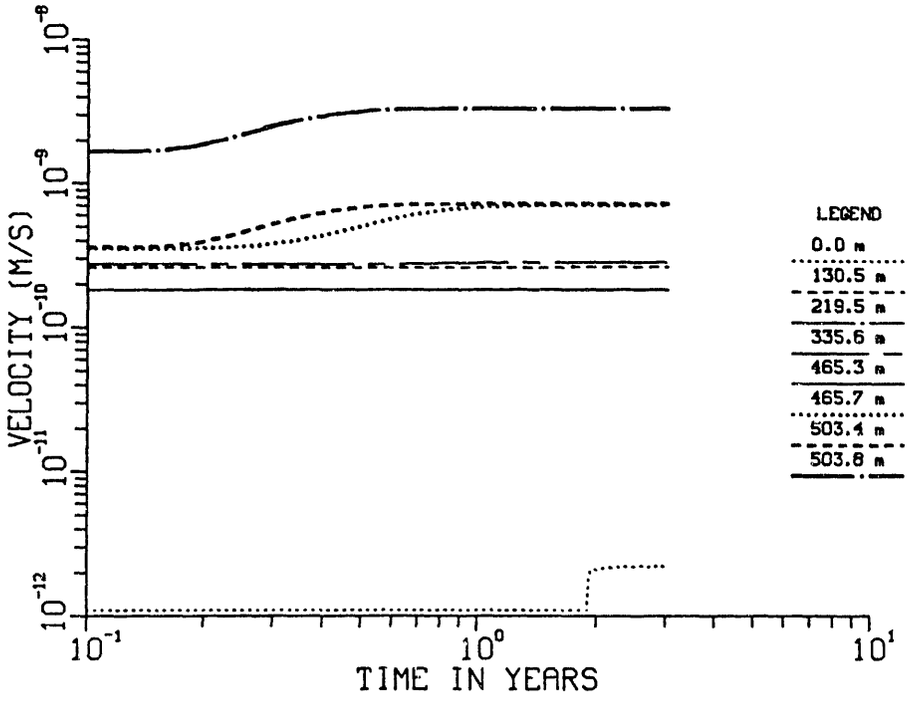

Figure 1-11-11. Average linear velocity of water in the matrix versus time at specified distances above the water table; initial set of calculations; Case 11.

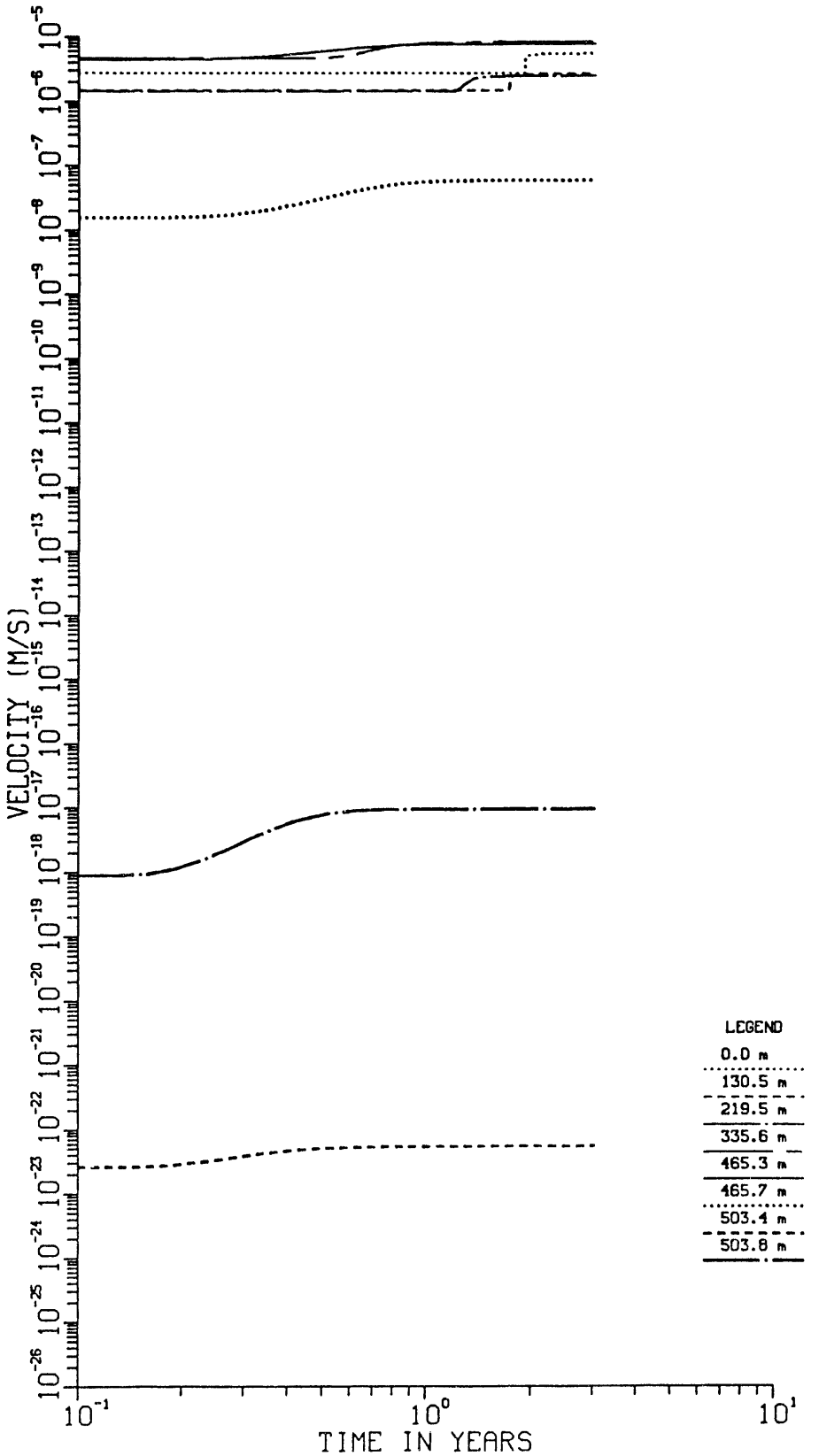

Figure 1-11-12. Average linear velocity of water in the fractures versus time at specified distances above the water table; initial set of calculations; Case 11.

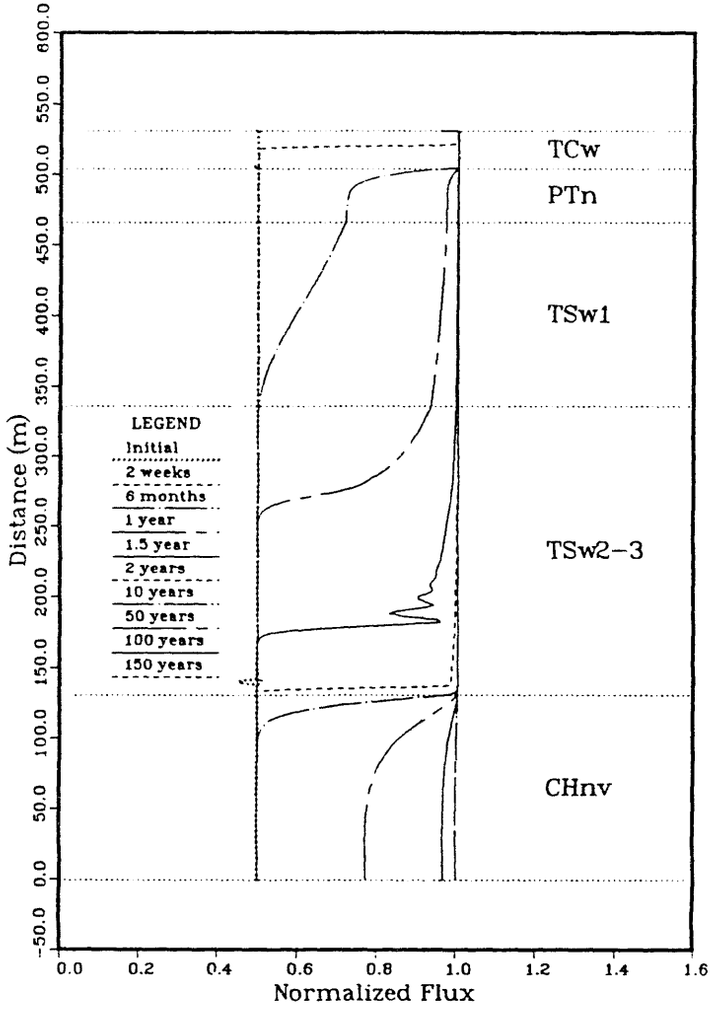

Figure 1-12-1. Normalized flux (calculated flux divided by imposed flux) versus distance above the water table at specified times; initial set of calculations; Case 12.

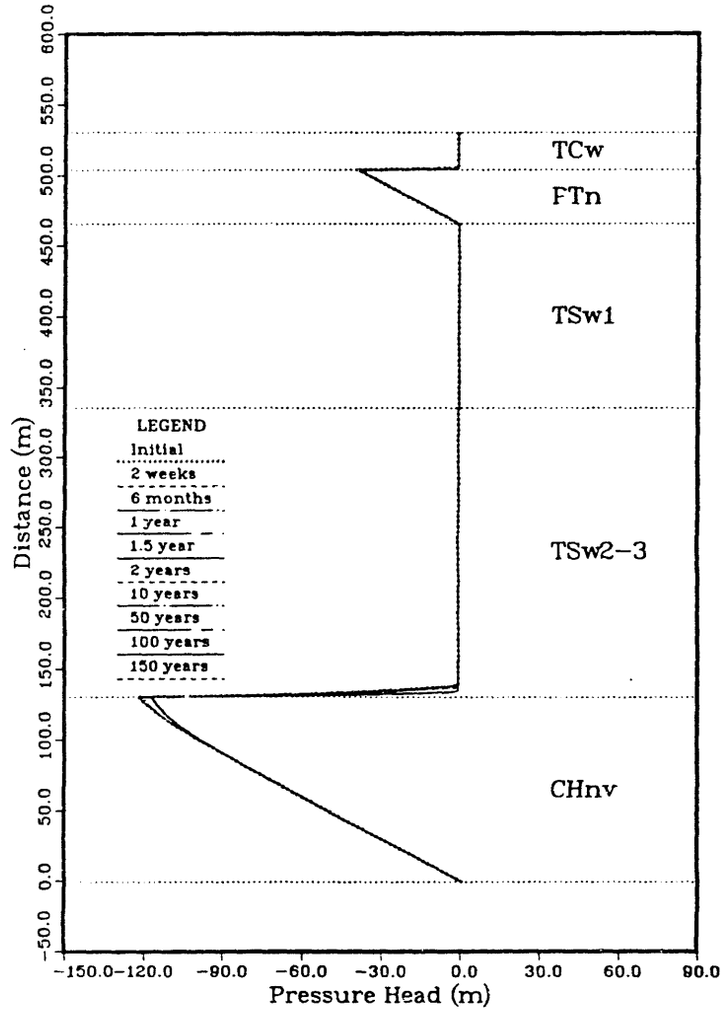

Figure 1-12-2. Pressure head versus distance above the water table at specified times; initial set of calculations; Case 12.

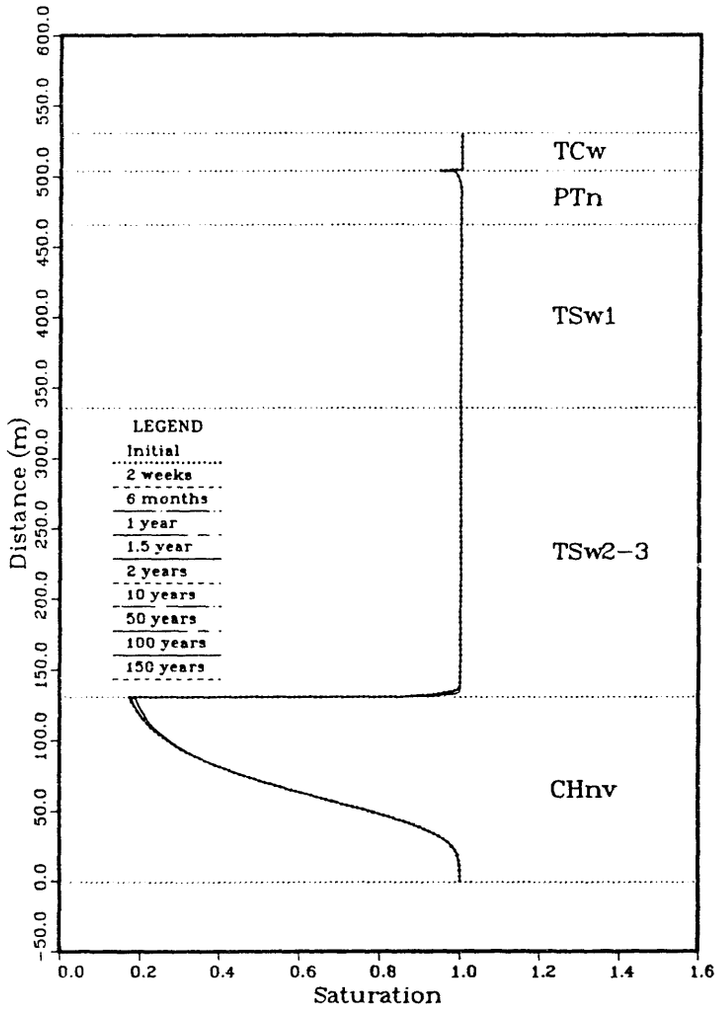

Figure 1-12-3. Matrix saturation versus distance above the water table at specified times; initial set of calculations; Case 12.

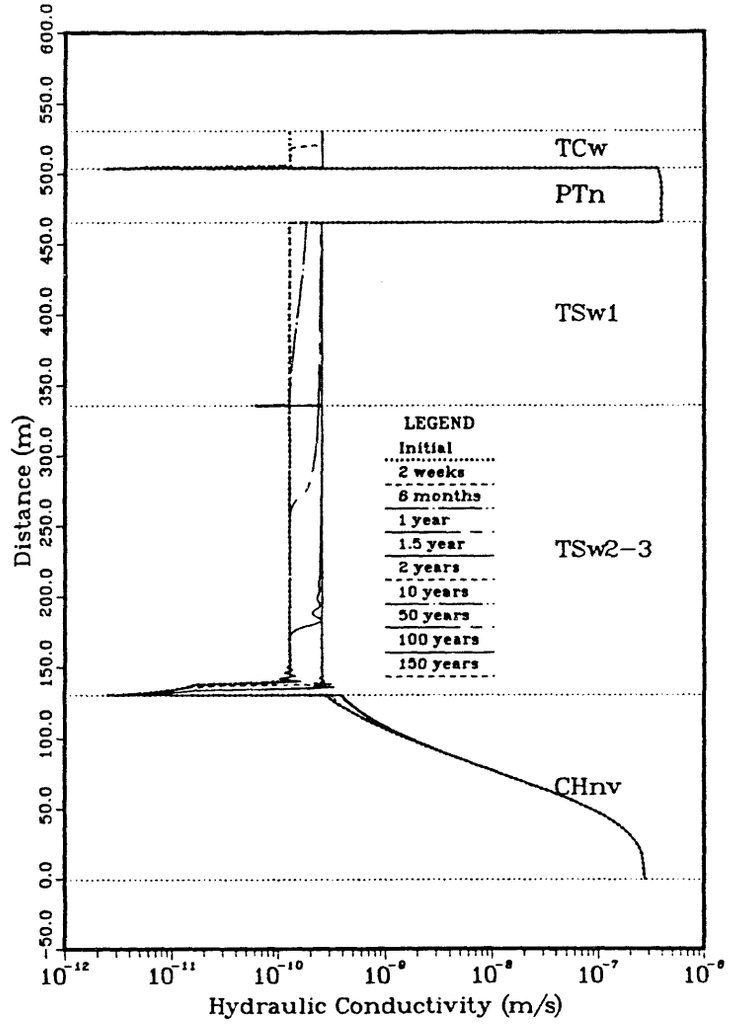

Figure 1-12-4. Hydraulic conductivity versus distance above the water table at specified times; initial set of calculations; Case 12.

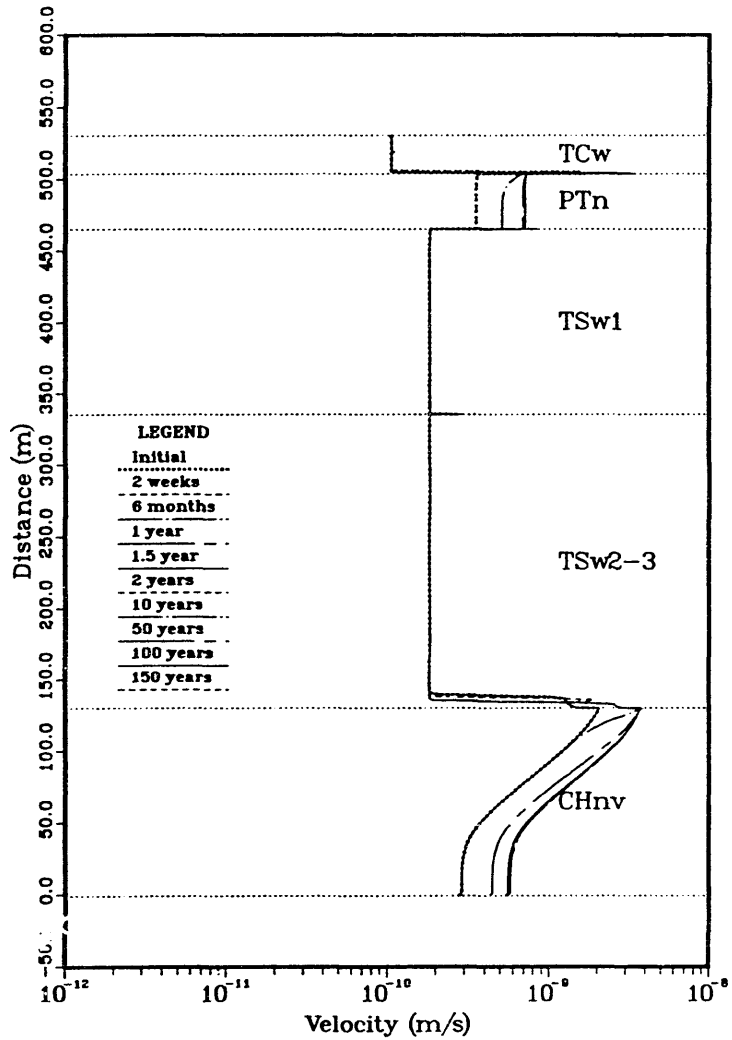

Figure 1-12-5. Average linear velocity of water in the matrix versus distance above the water table at specified times; initial set of calculations; Case 12.

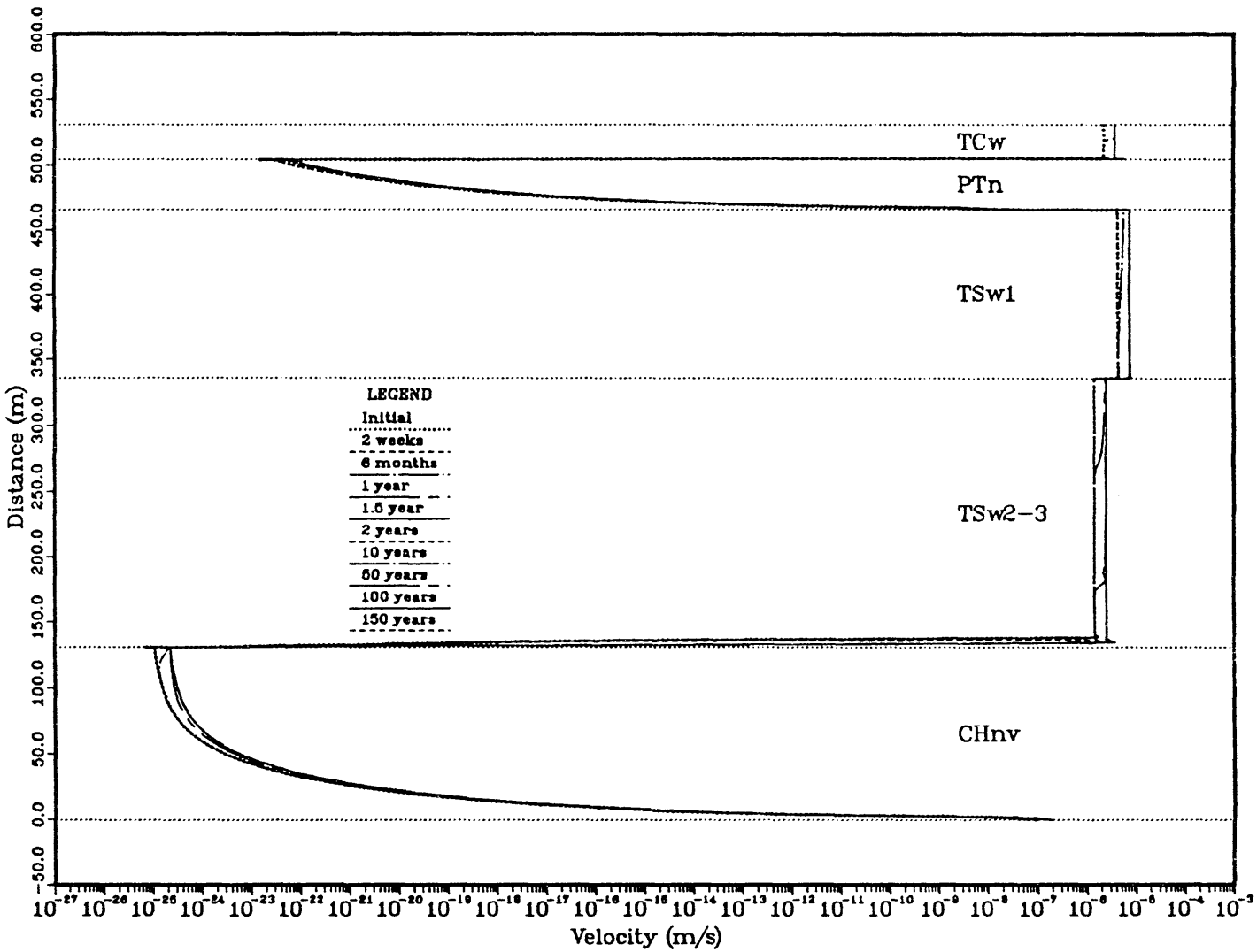

Figure 1-11-6. Average linear velocity of water in the fractures versus distance above the water table at specified times; initial set of calculations; Case 11.

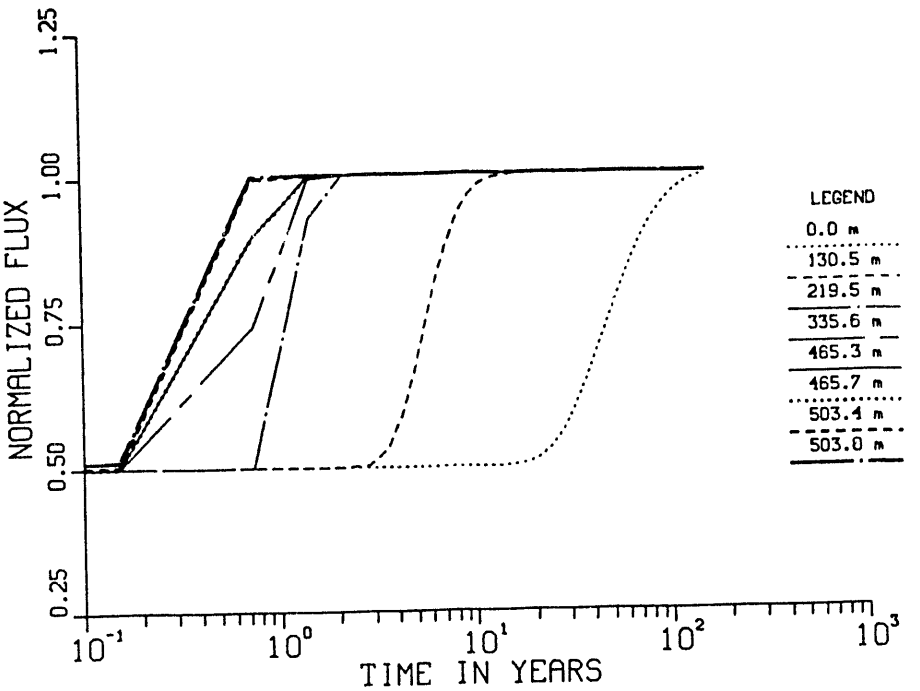

Figure 1-12-7. Normalized flux (calculated flux divided by imposed flux) versus time at specified distances above the water table; initial set of calculations; Case 12.

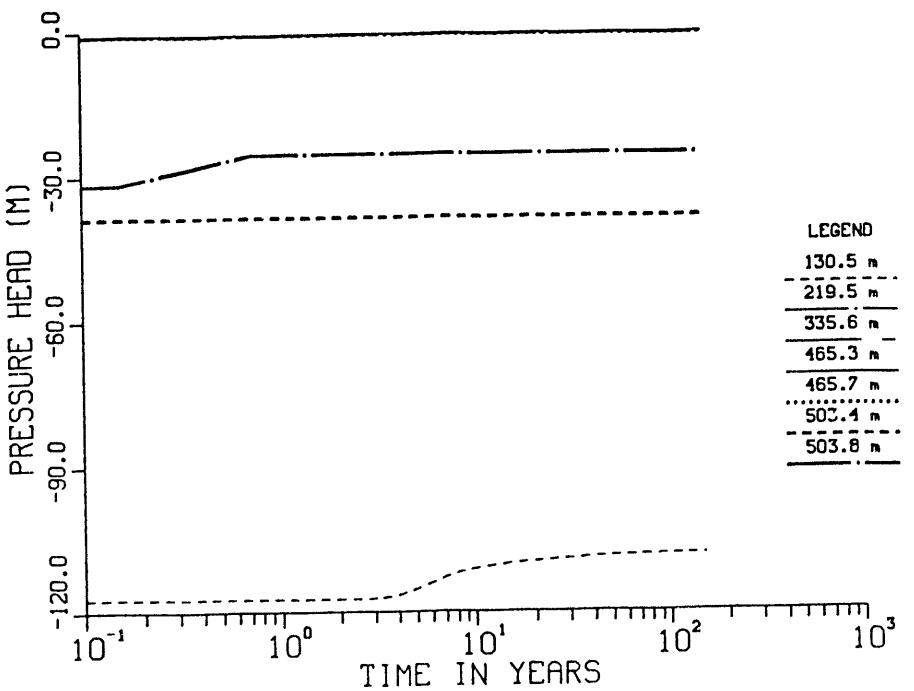

Figure 1-12-8. Pressure head versus time at specified distances above the water table; initial set of calculations; Case 12.

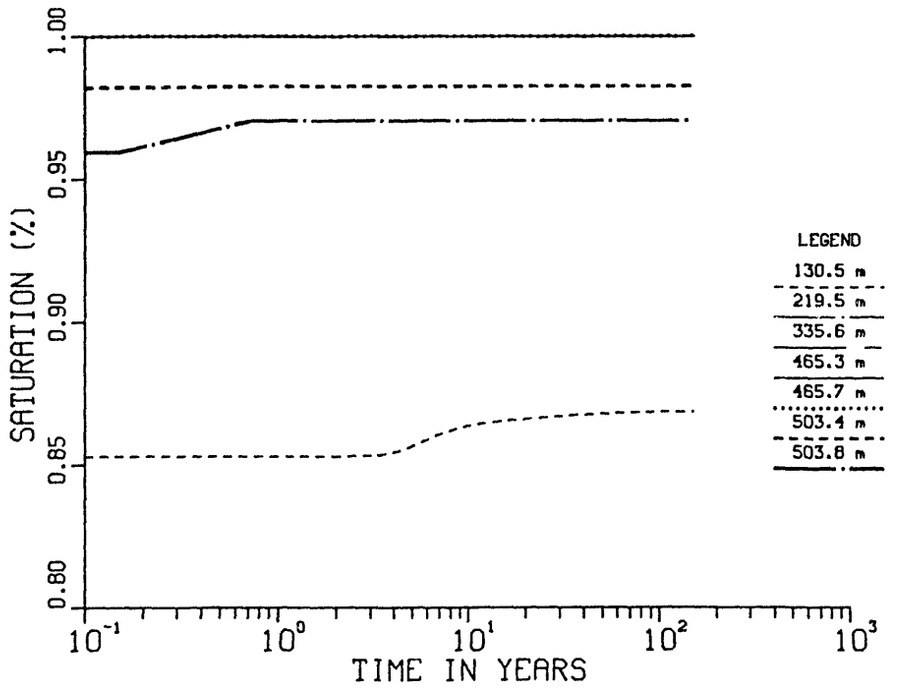

Figure 1-12-9. Matrix saturation versus time at specified distances above the water table; initial set of calculations; Case 12.

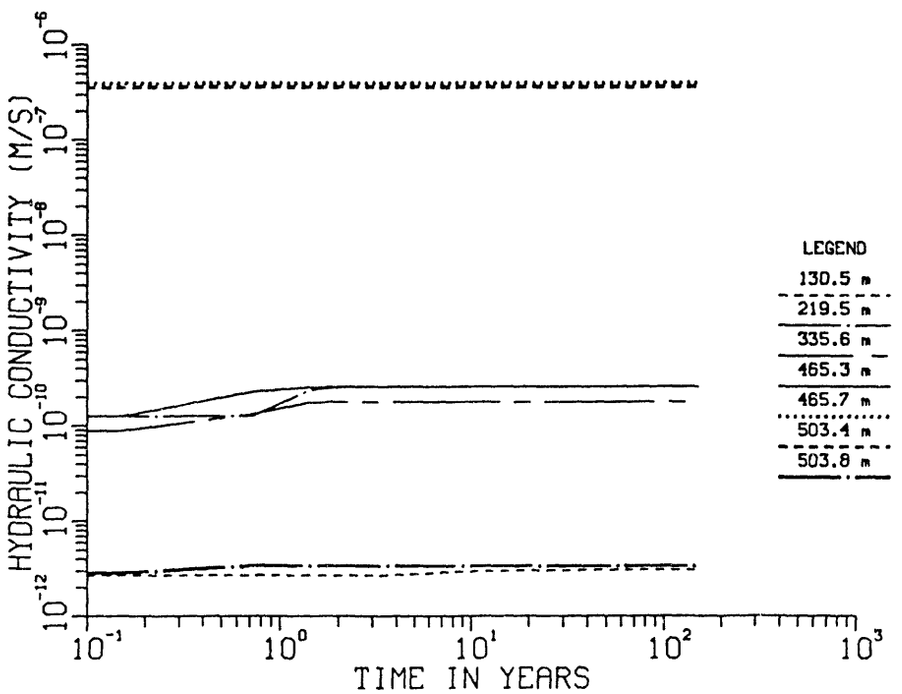

Figure 1-12-10. Hydraulic conductivity versus time at specified distances above the water table; initial set of calculations; Case 12.

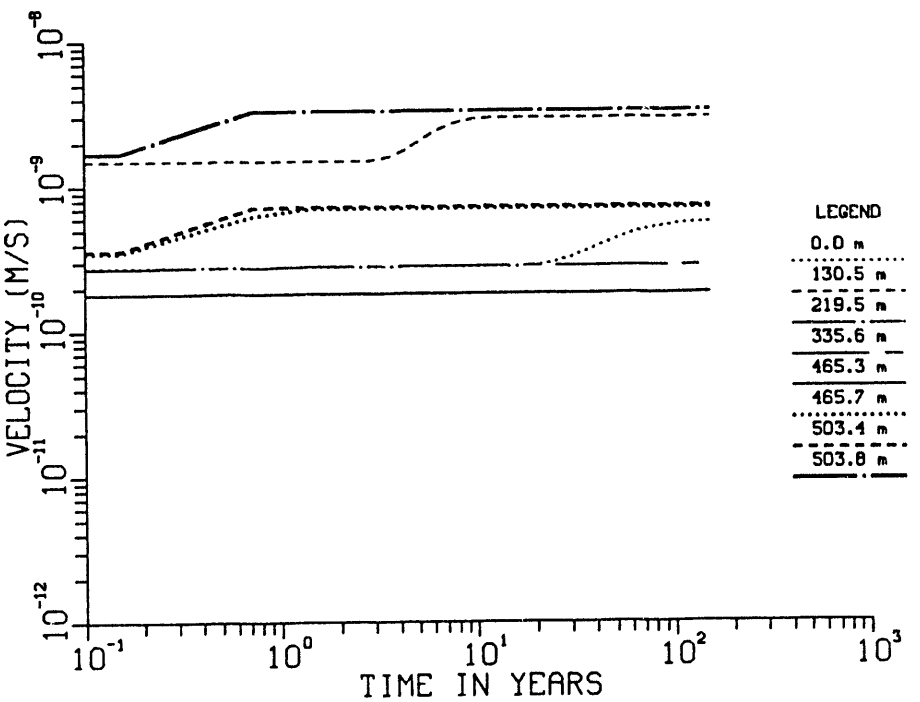

Figure 1-12-11. Average linear velocity of water in the matrix versus time at specified distances above the water table; initial set of calculations; Case 12.

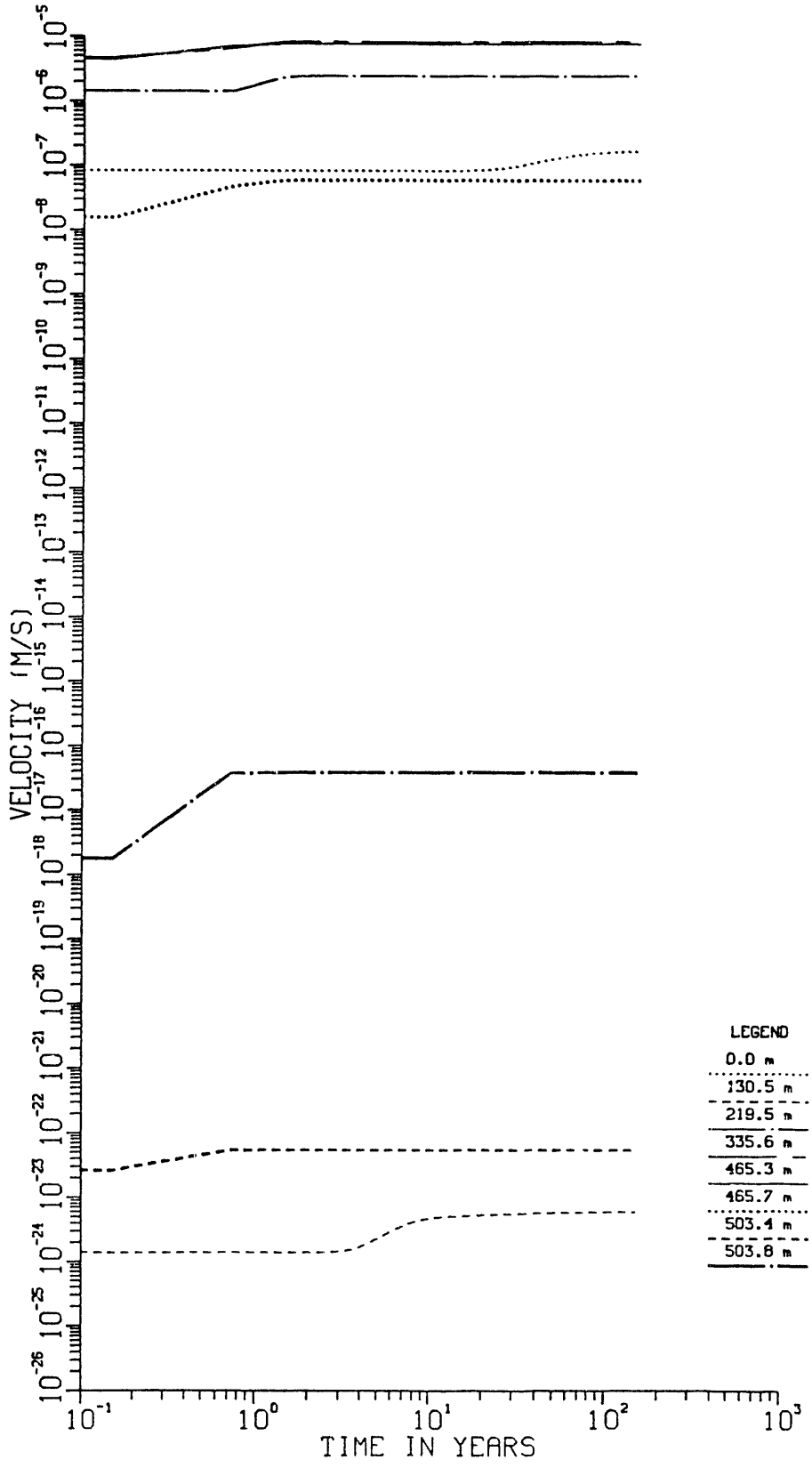

Figure 1-12-12. Average linear velocity of water in the fractures versus time at specified distances above the water table; initial set of calculations; Case 12.

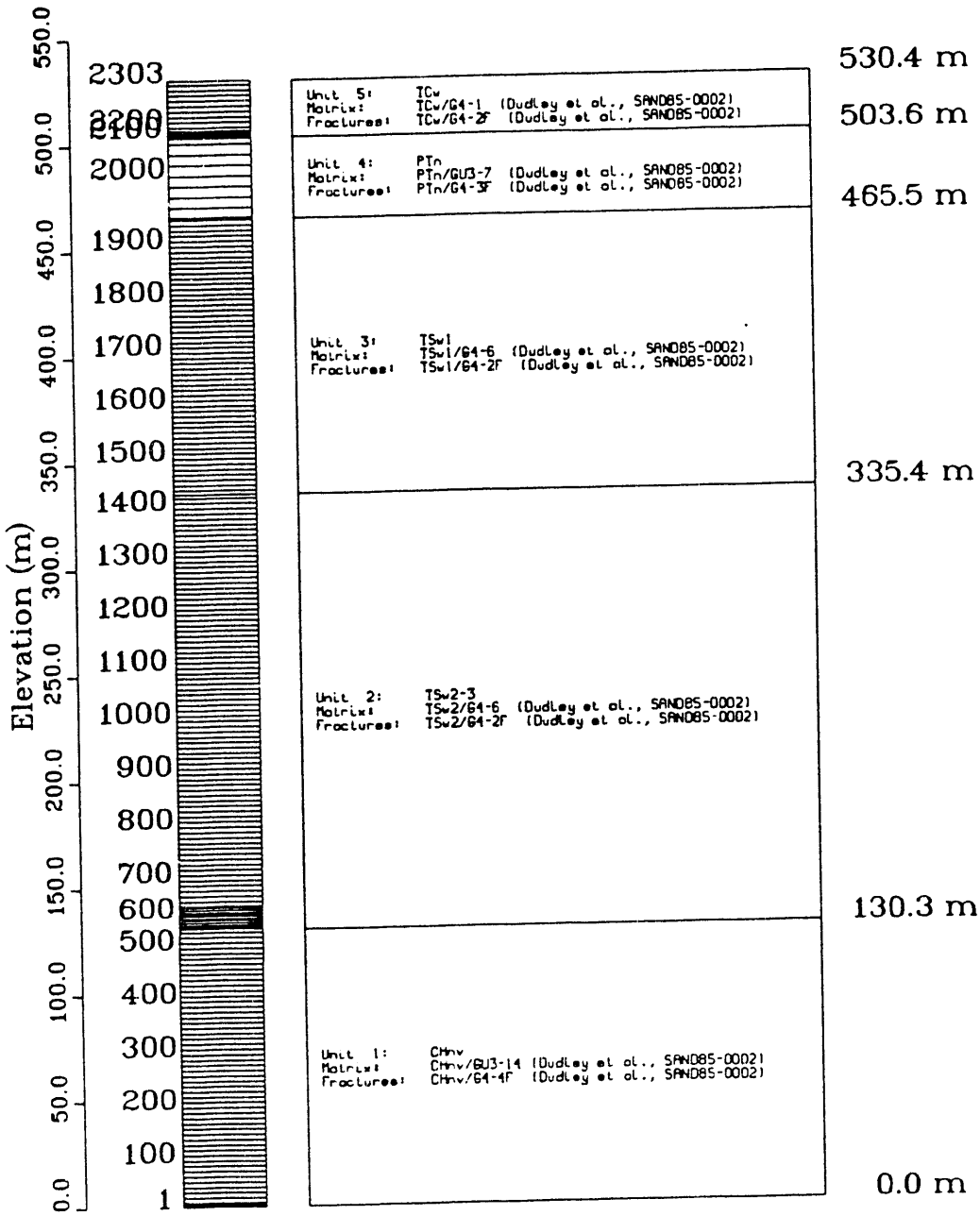

Figure 2-1. The calculational mesh (left-hand column) and the geohydrologic unit stratigraphy (right-hand column) used for all Cases of the final set of calculations.

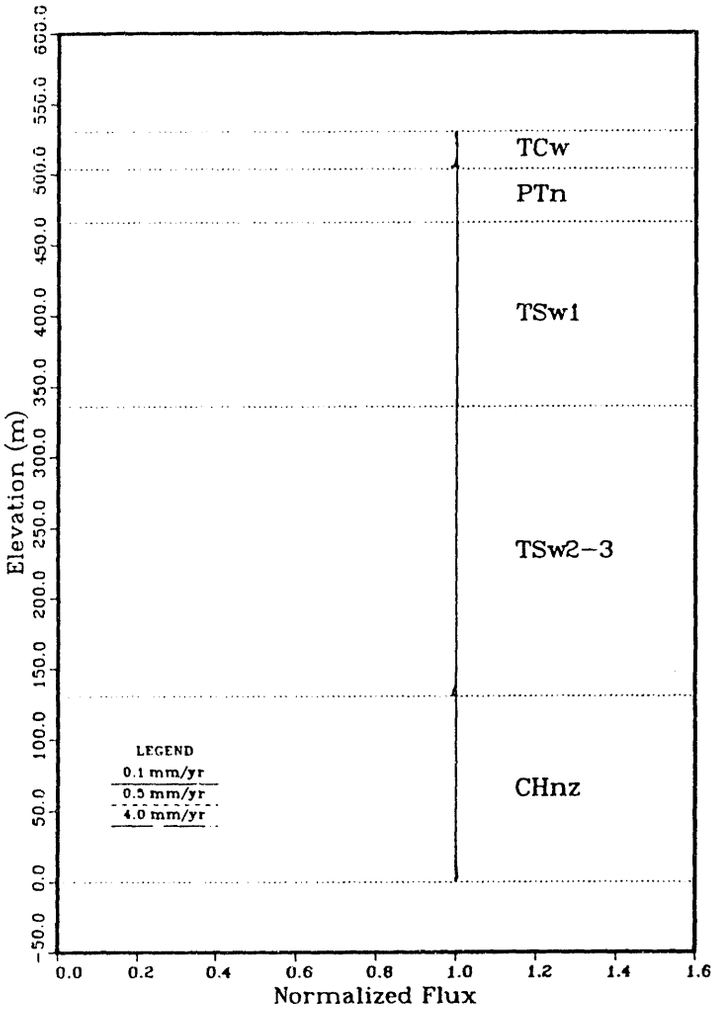

Figure 2-1/3/5-1. Normalized flux (calculated flux divided by imposed flux) versus distance above the water table; final set of calculations; Cases 1, 3, and 5.

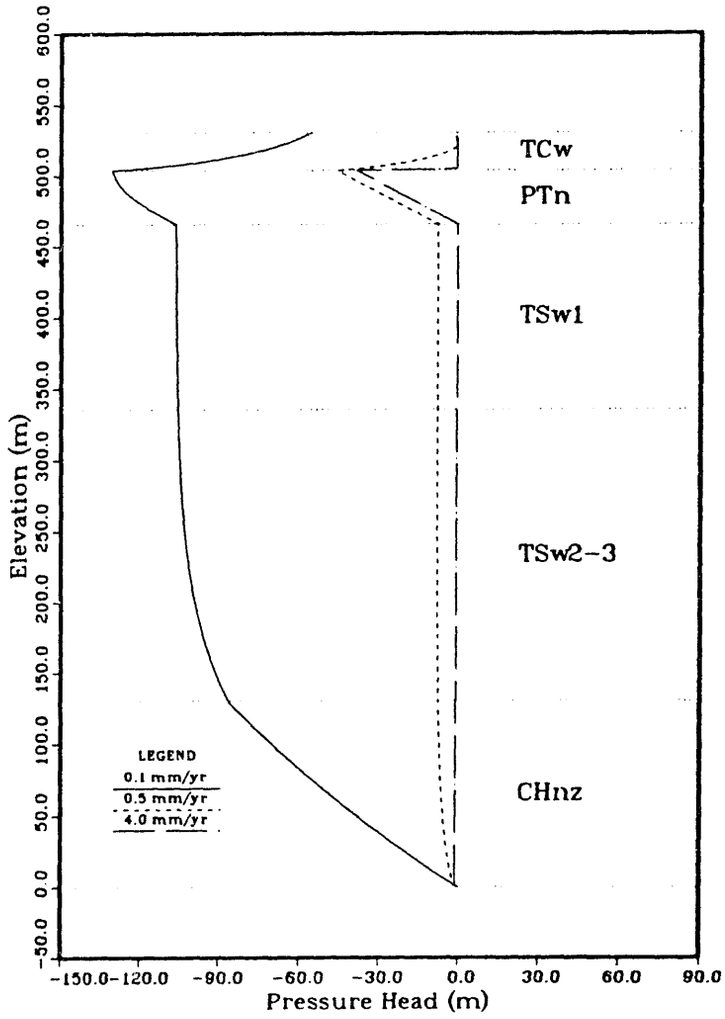

Figure 2-1/3/5-2. Pressure head versus distance above the water table; final set of calculations; Cases 1, 3, and 5.

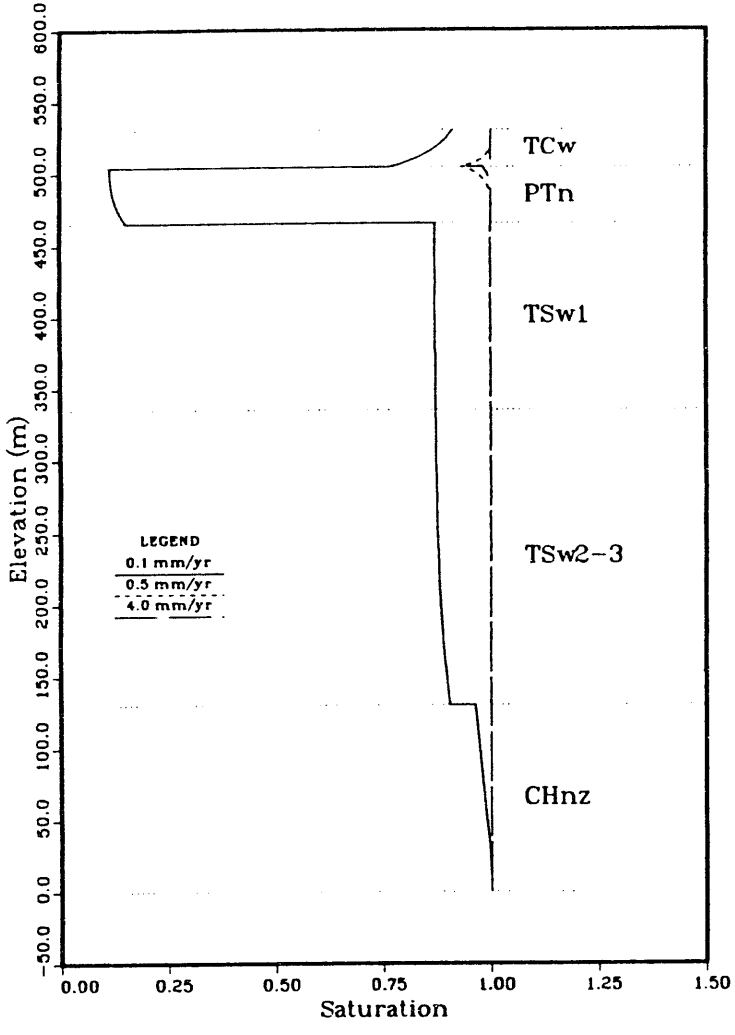

Figure 2-1/3/5-3. Matrix saturation versus distance above the water table; final set of calculations; Cases 1, 3, and 5.

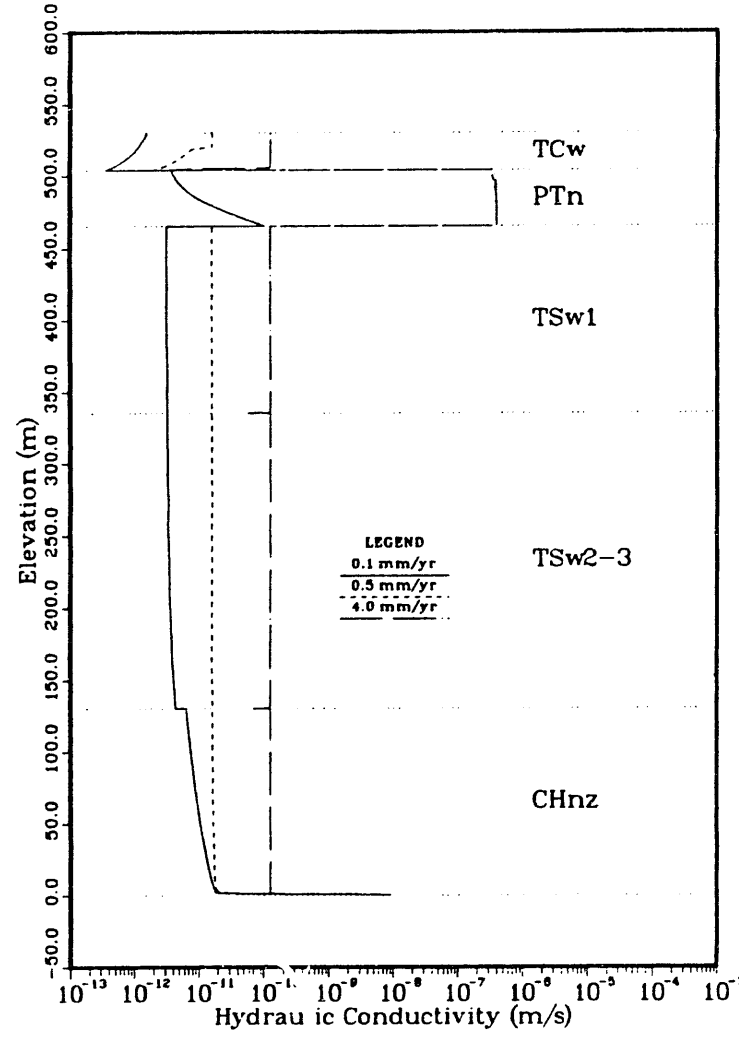

Figure 2-1/3/5-4. Hydraulic conductivity versus distance above the water table; final set of calculations; Cases 1, 3, and 5.

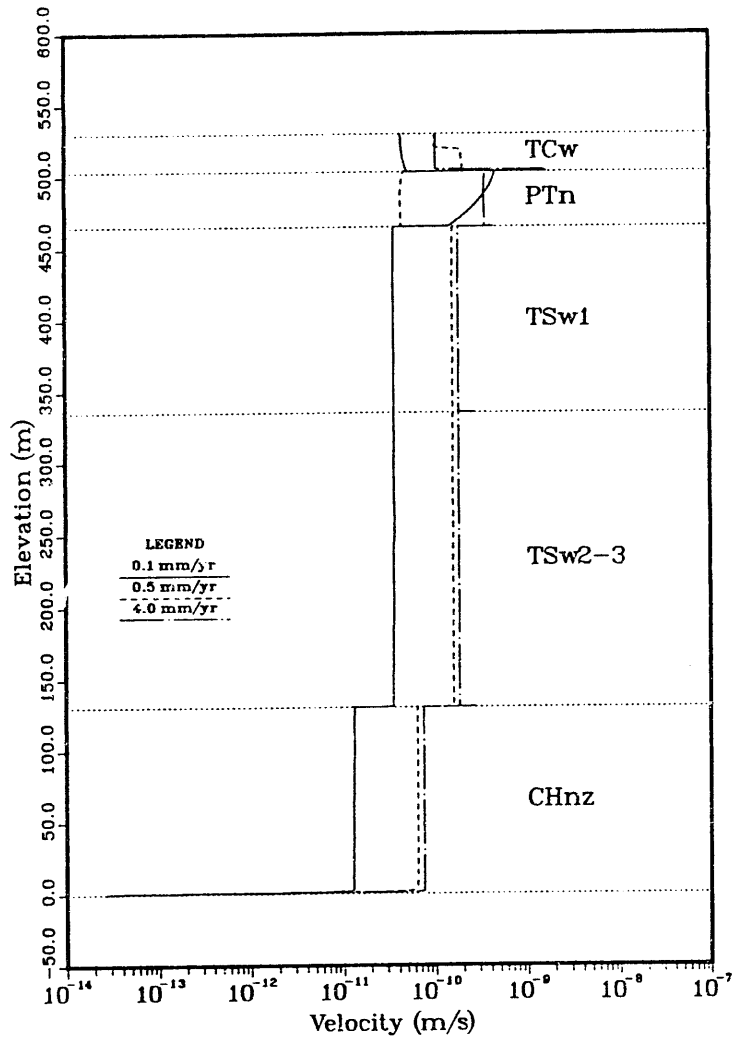

Figure 2-1/3/5-5. Average linear velocity of water in the matrix versus distance above the water table; final set of calculations; Cases 1, 3, and 5.

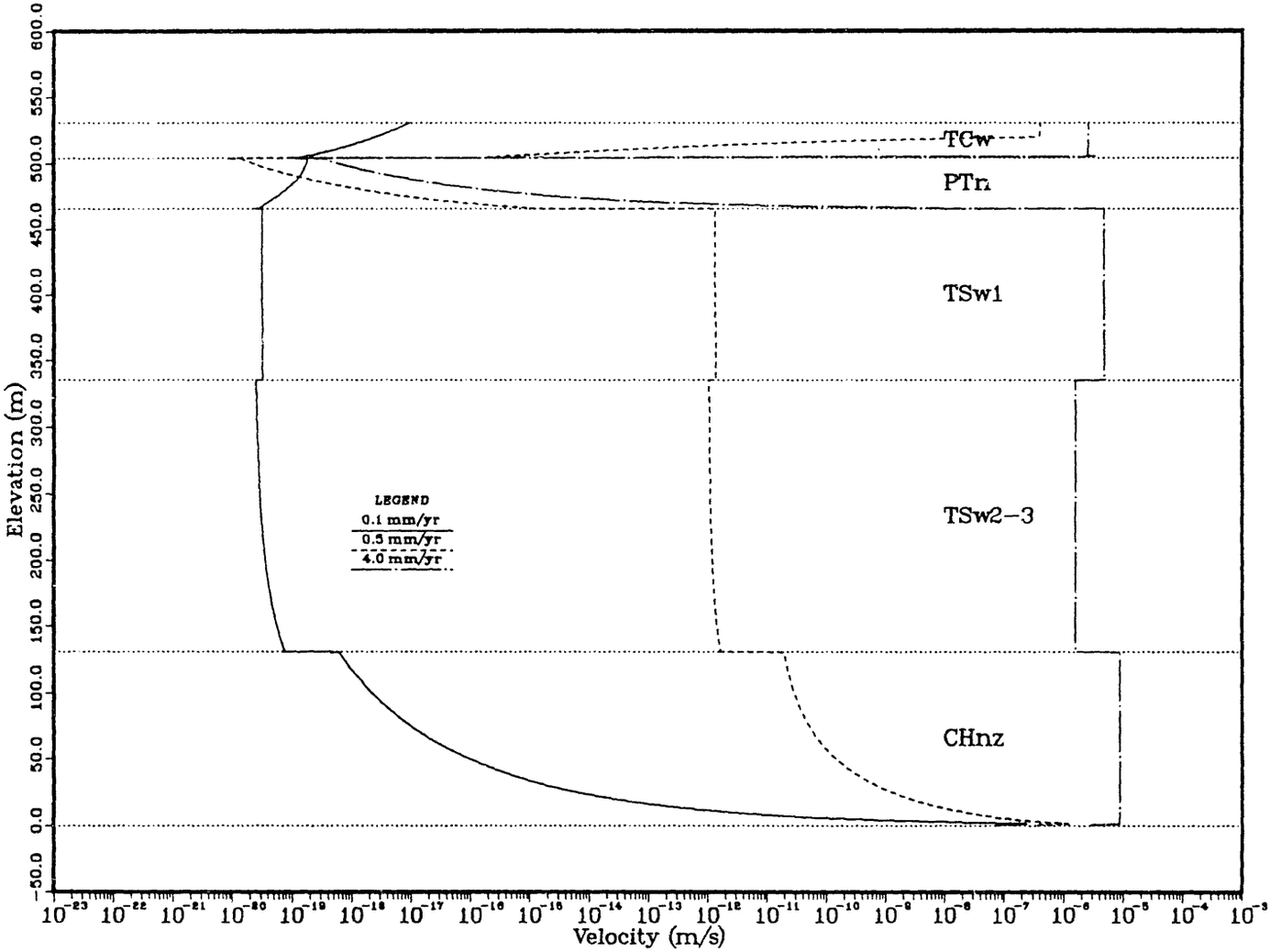

Figure 2-1/3/5-6. Average linear velocity of water in the fractures versus distance above the water table; final set of calculations; Cases 1, 3, and 5.

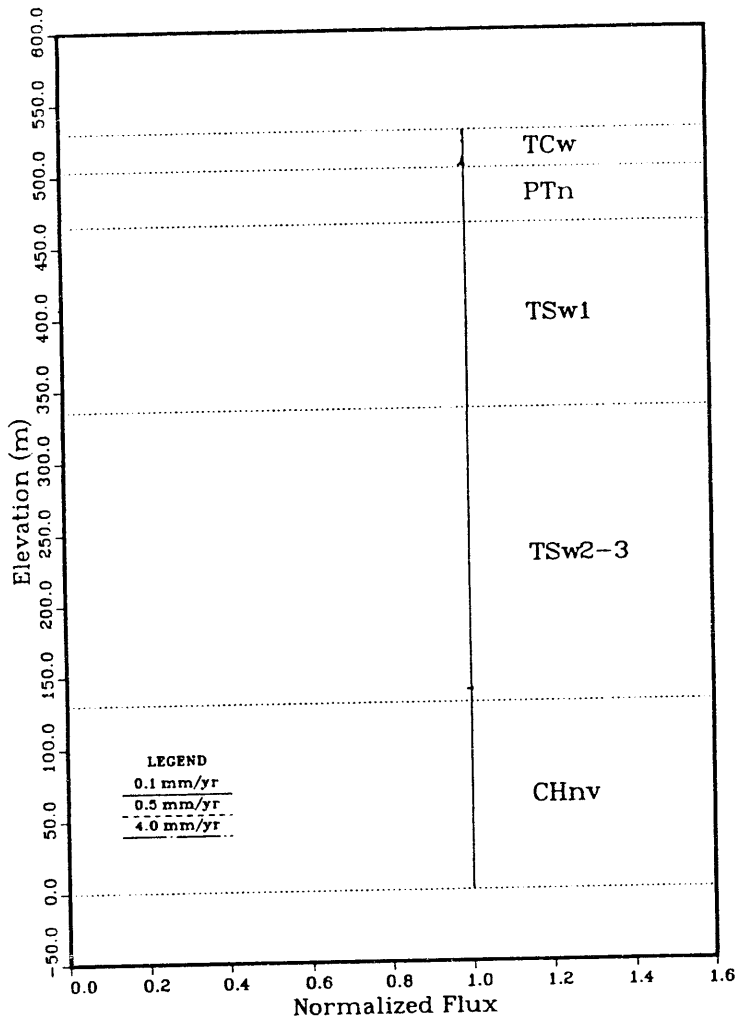

Figure 2-2/4/6-1. Normalized flux (calculated flux divided by imposed flux) versus distance above the water table; final set of calculations; Cases 2, 4, and 6.

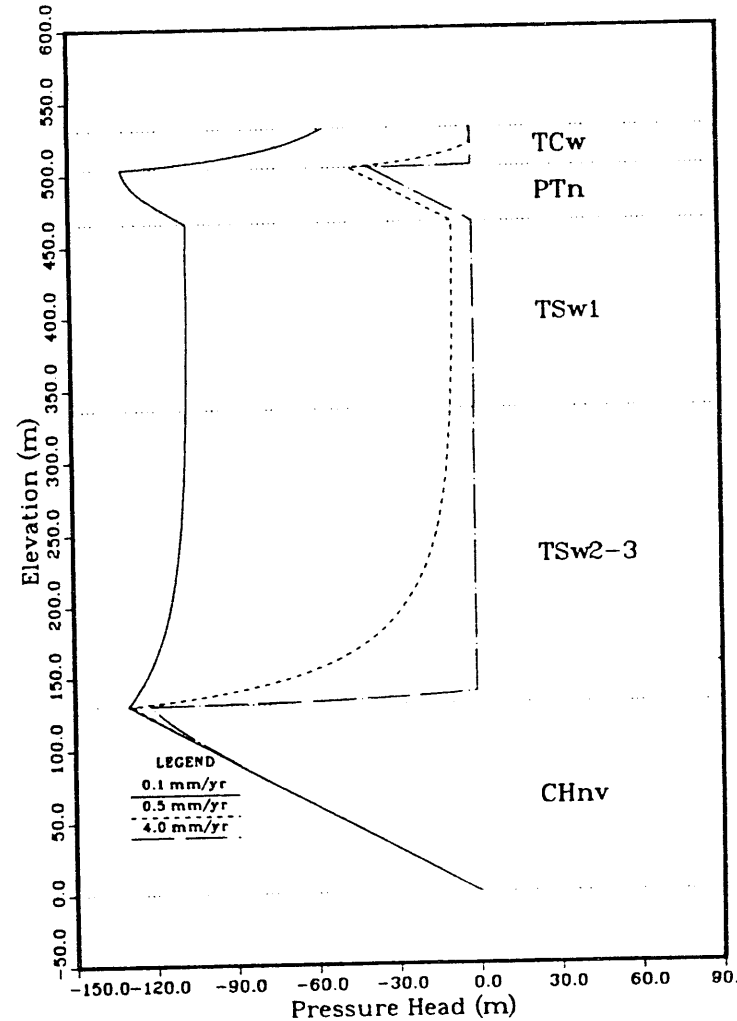

Figure 2-2/4/6-2. Pressure head versus distance above the water table; final set of calculations; Cases 2, 4, and 6.

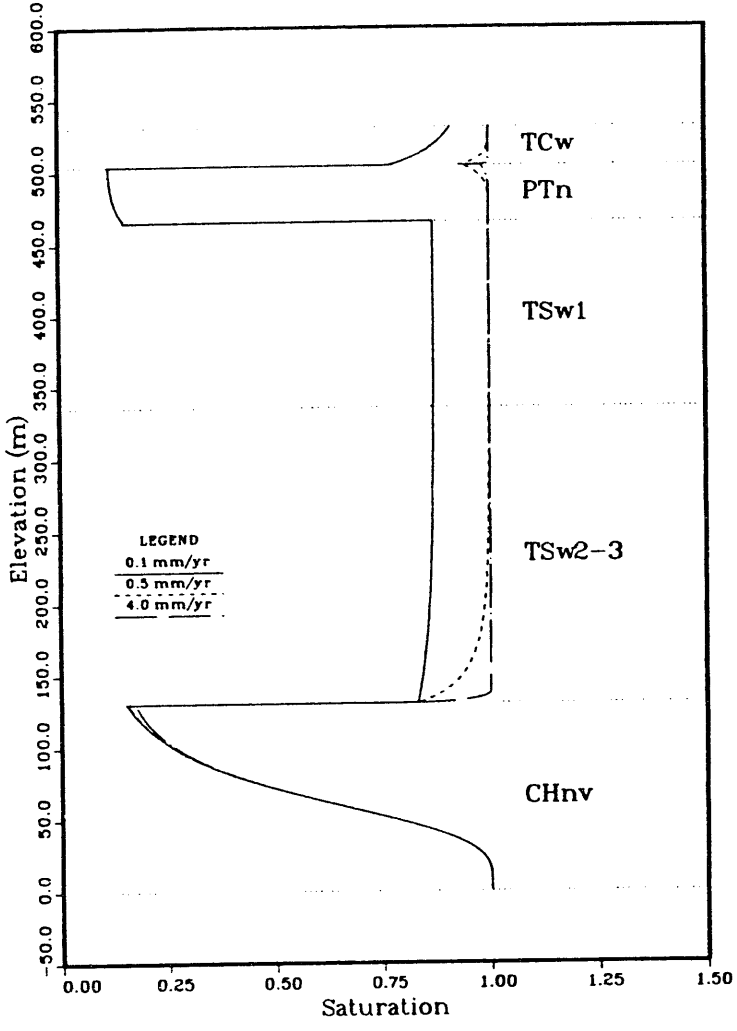

Figure 2-2/4/6-3. Matrix saturation versus distance above the water table; final set of calculations; Cases 2, 4, and 6.

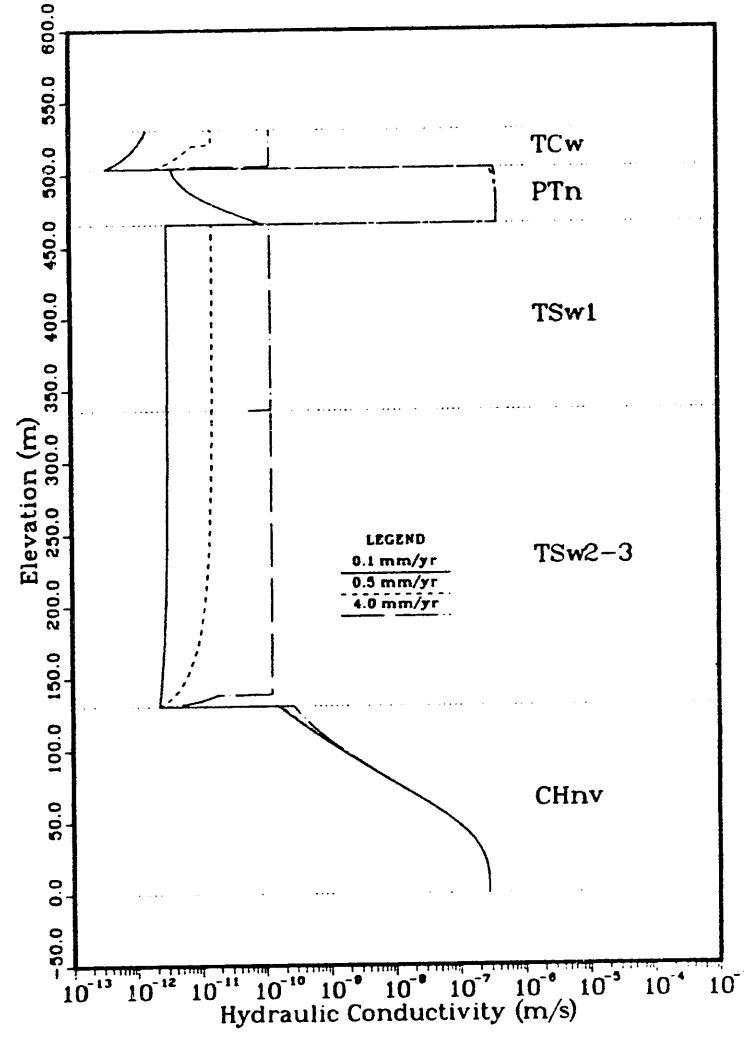

Figure 2-2/4/6-4. Hydraulic conductivity versus distance above the water table; final set of calculations; Cases 2, 4, and 6.

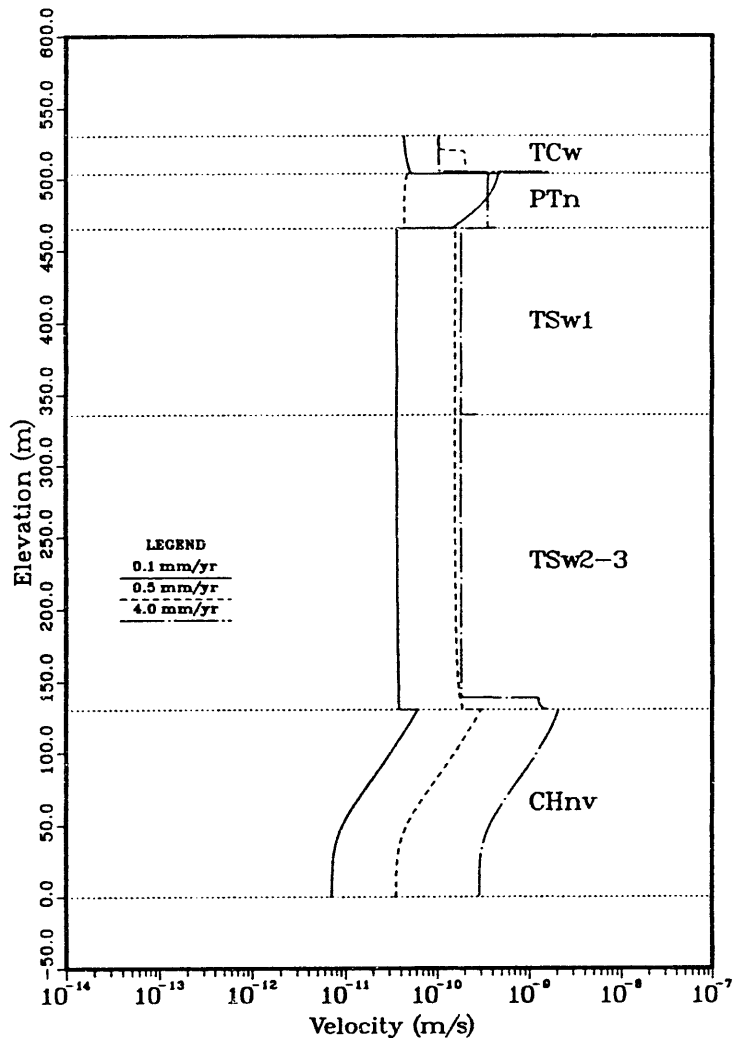

Figure 2-2/4/6-5. Average linear velocity of water in the matrix versus distance above the water table; final set of calculations; Cases 2, 4, and 6.

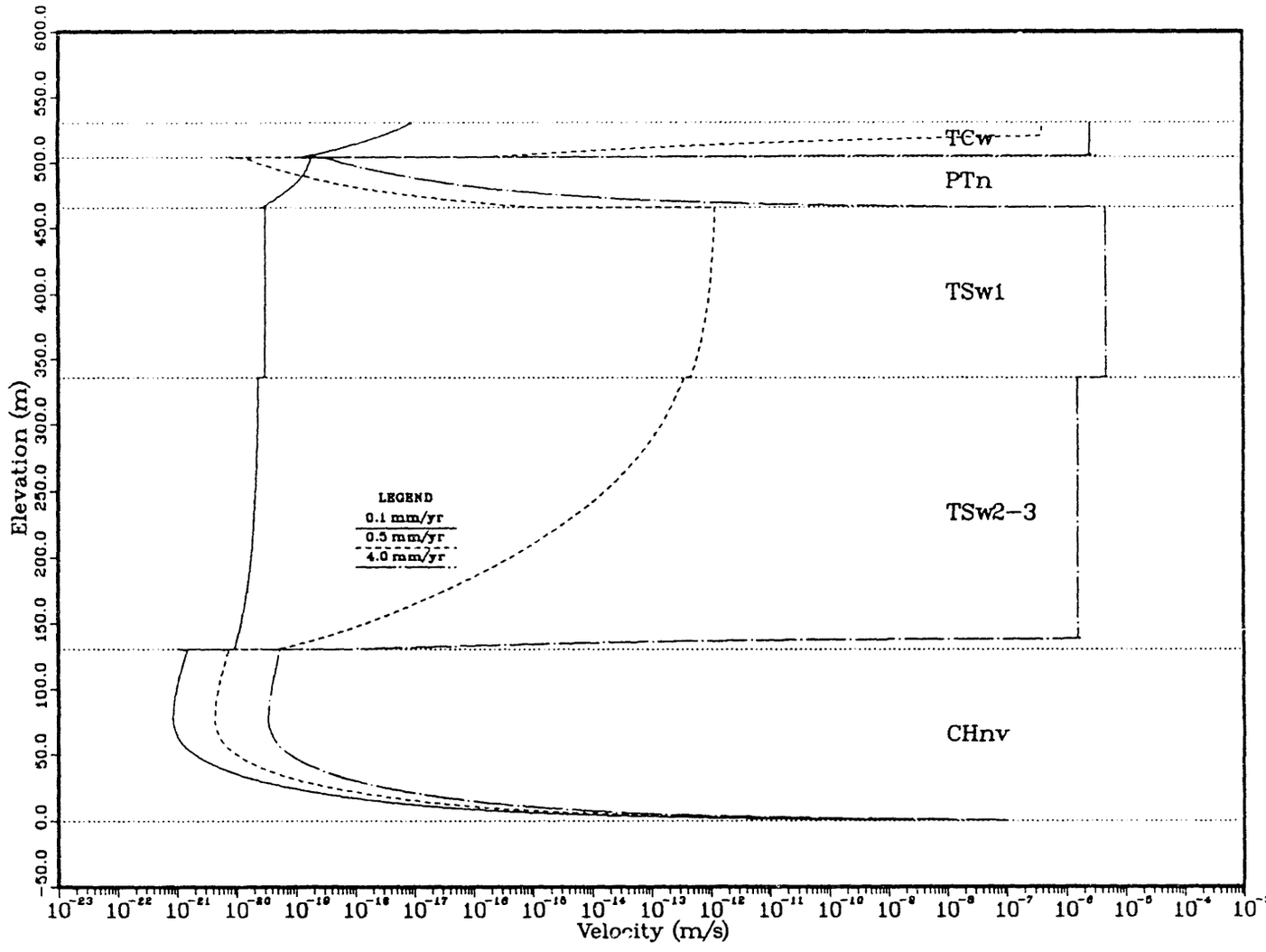

Figure 2-2/4/6-6. Average linear velocity of water in the fractures versus distance above the water table; final set of calculations; Cases 2, 4, and 6.

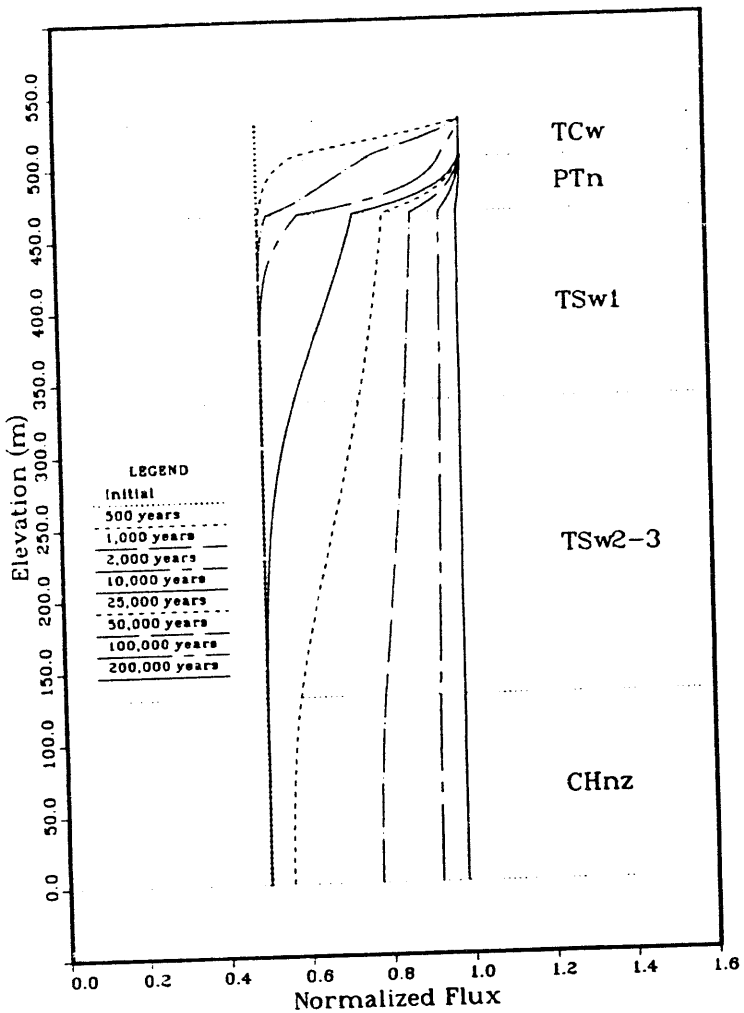

Figure 2-7-1. Normalized flux (calculated flux divided by imposed flux) versus distance above the water table at specified times; final set of calculations; Case 7.

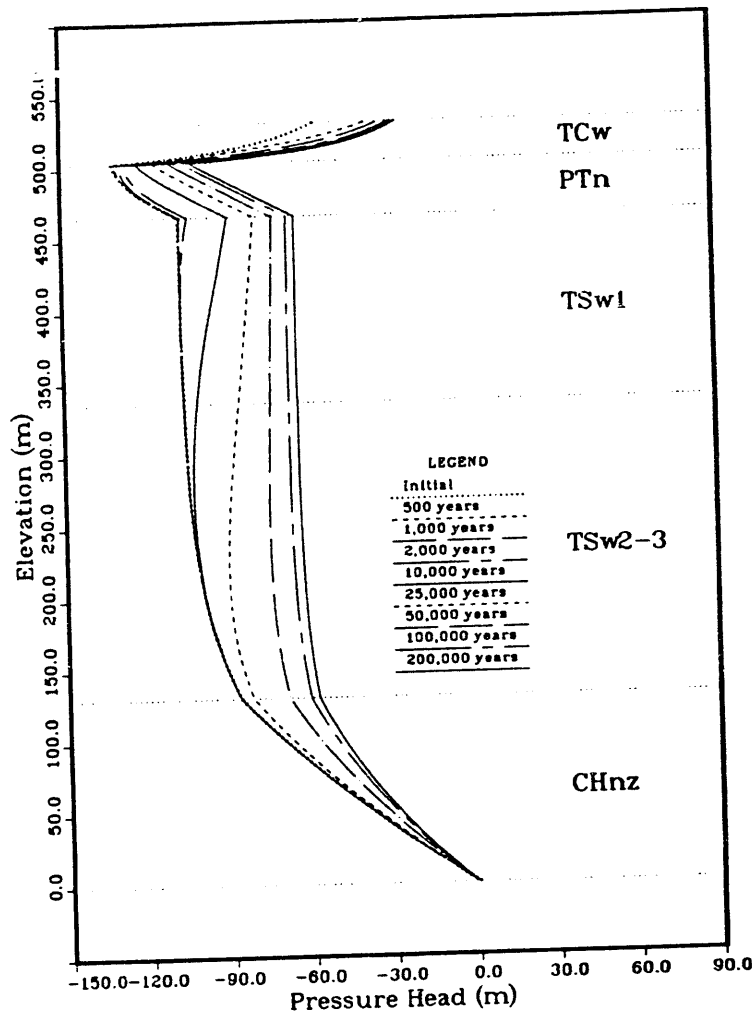

Figure 2-7-2. Pressure head versus distance above the water table at specified times; final set of calculations; Case 7.

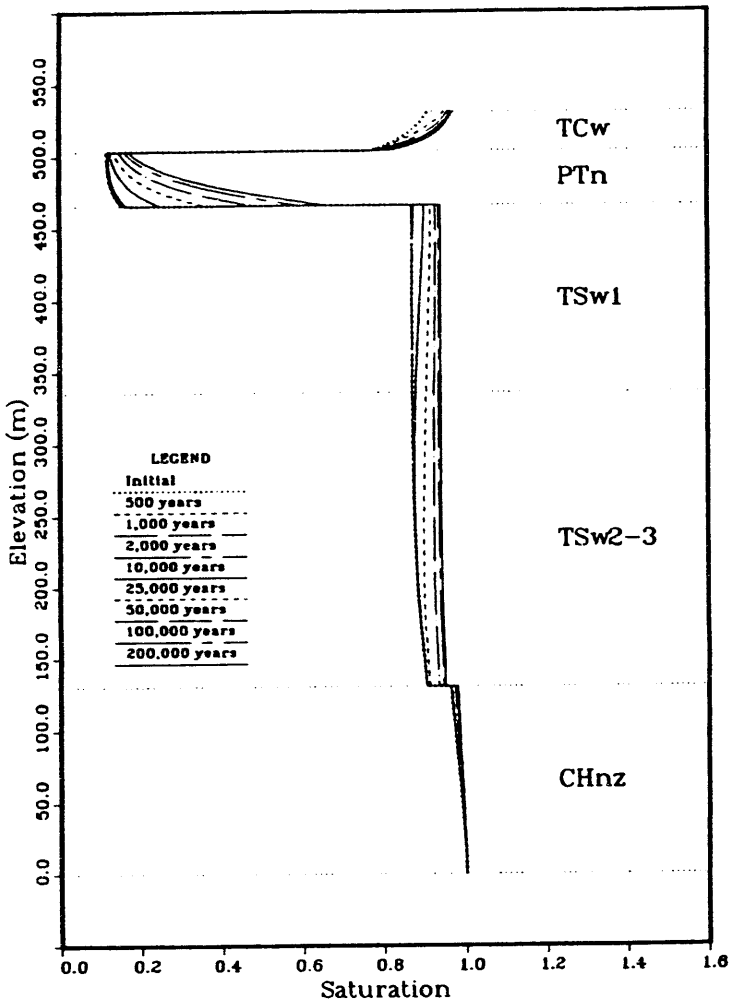

Figure 2-7-3. Matrix saturation versus distance above the water table at specified times; final set of calculations; Case 7.

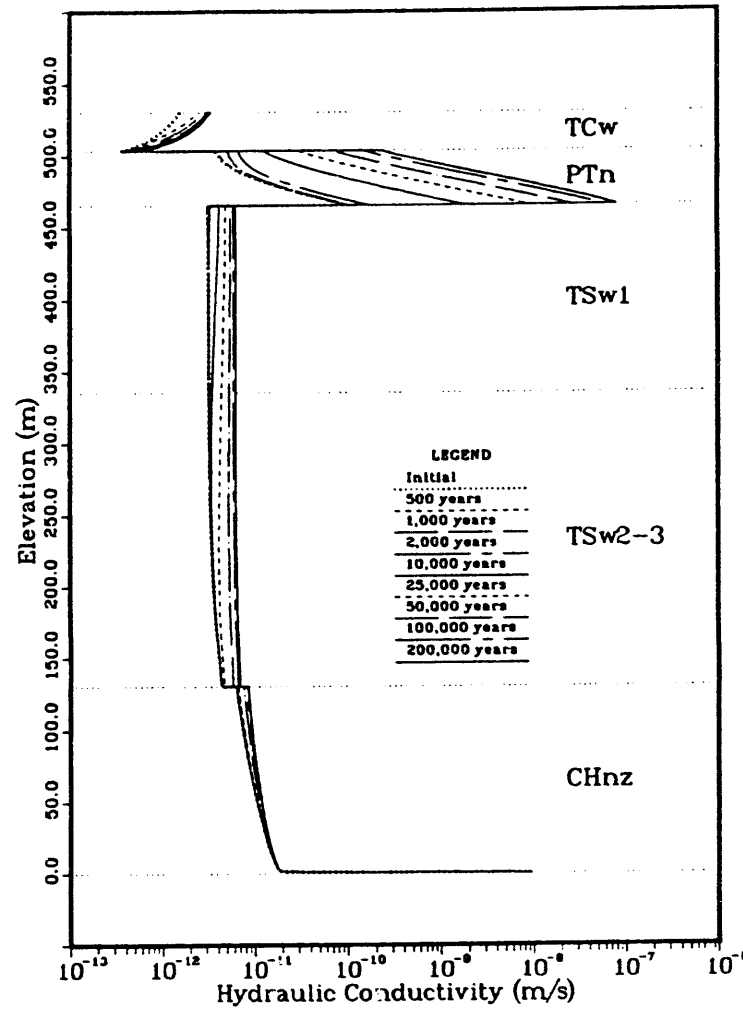

Figure 2-7-4. Hydraulic conductivity versus distance above the water table at specified times; final set of calculations; Case 7.

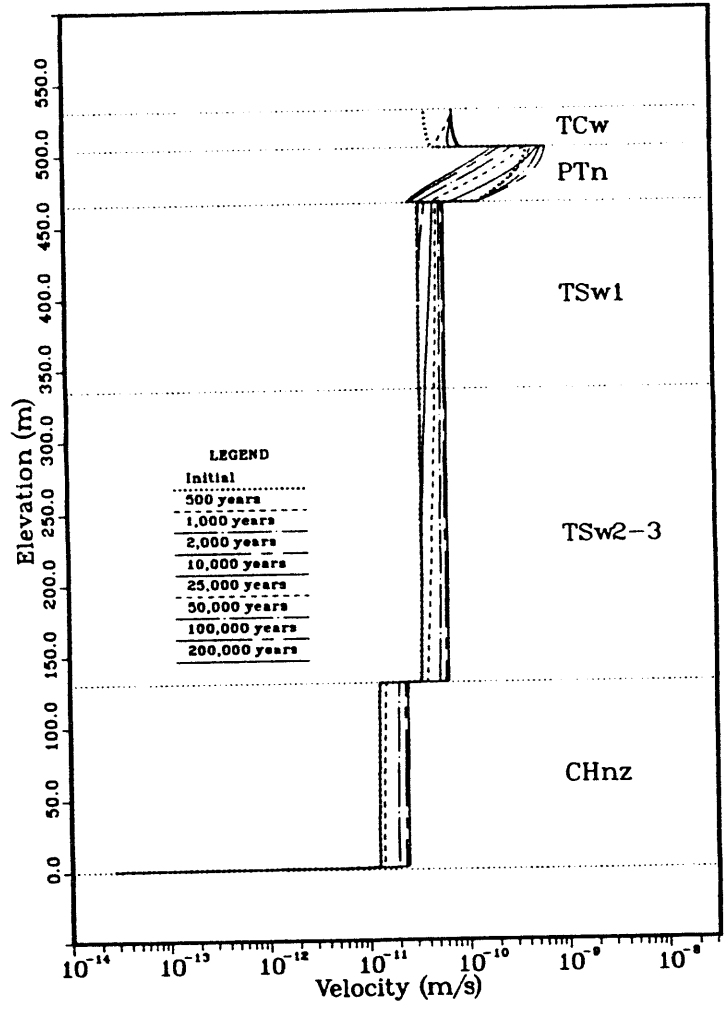

Figure 2-7-5. Average linear velocity of water in the matrix versus distance above the water table at specified times; final set of calculations; Case 7.

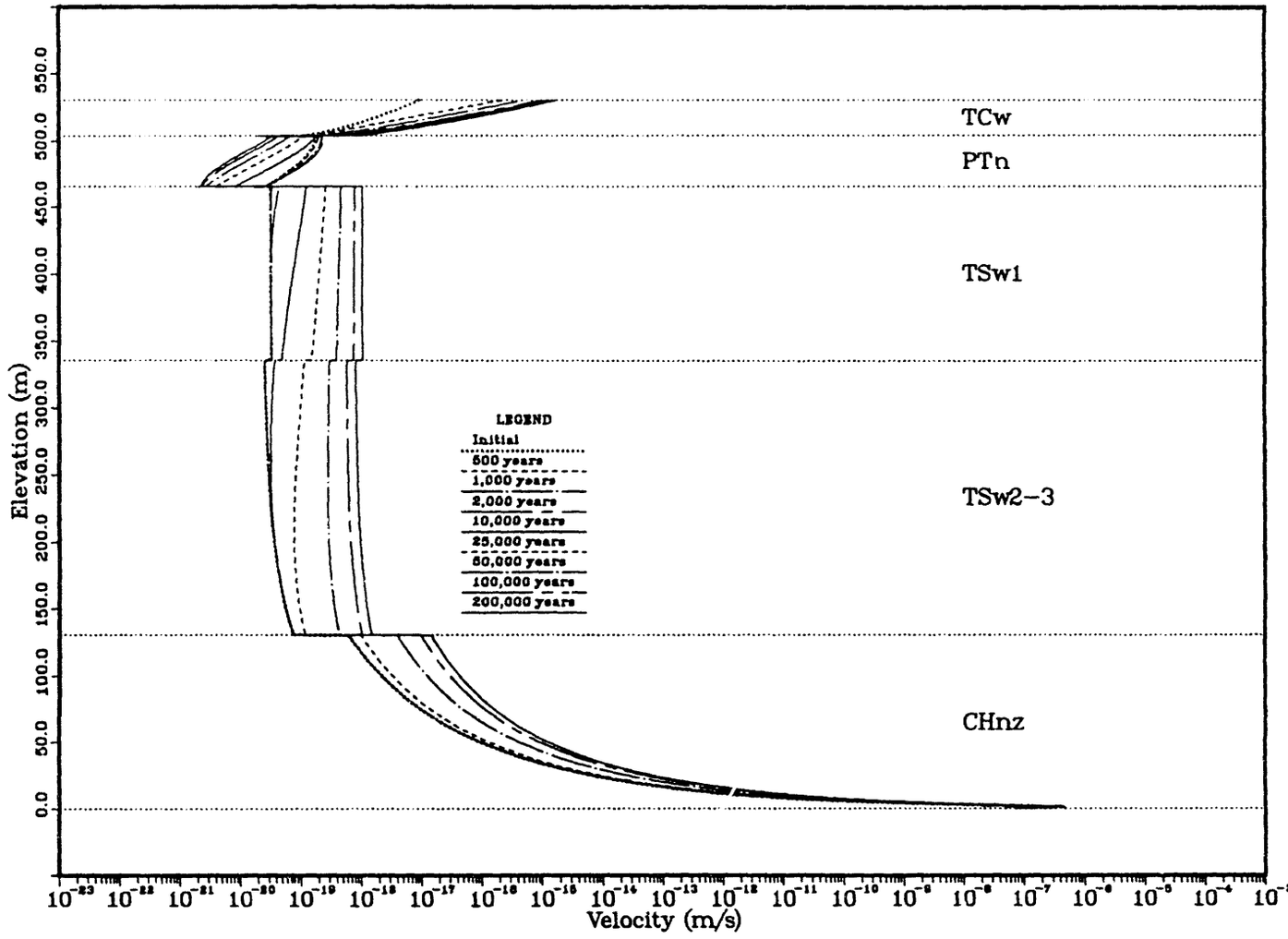

Figure 2-7-6. Average linear velocity of water in the fractures versus distance above the water table at specified times; final set of calculations; Case 7.

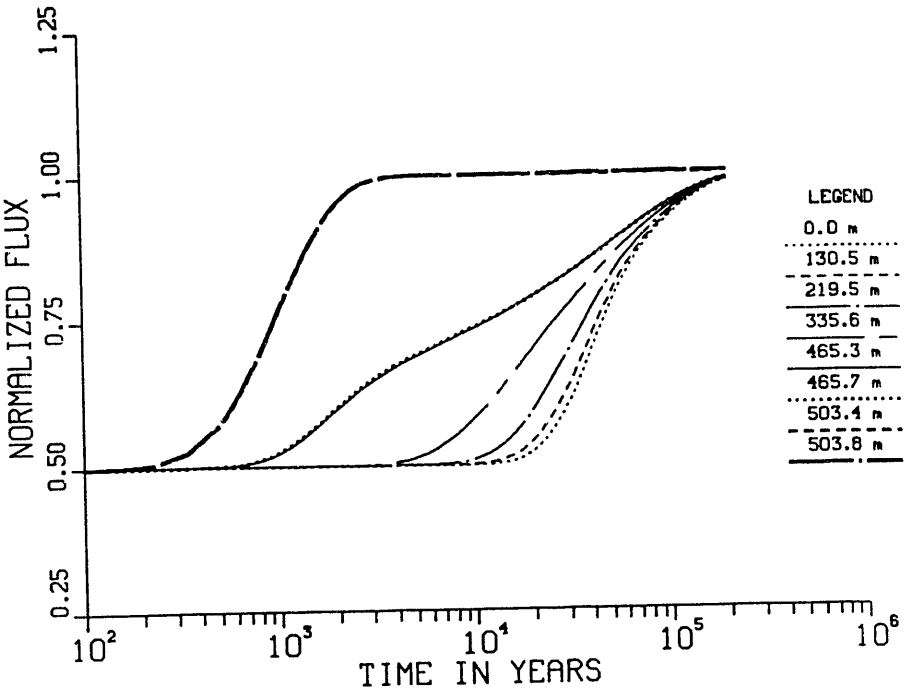

Figure 2-7-7. Normalized flux (calculated flux divided by imposed flux) versus time at specified distances above the water table; final set of calculations; Case 7.

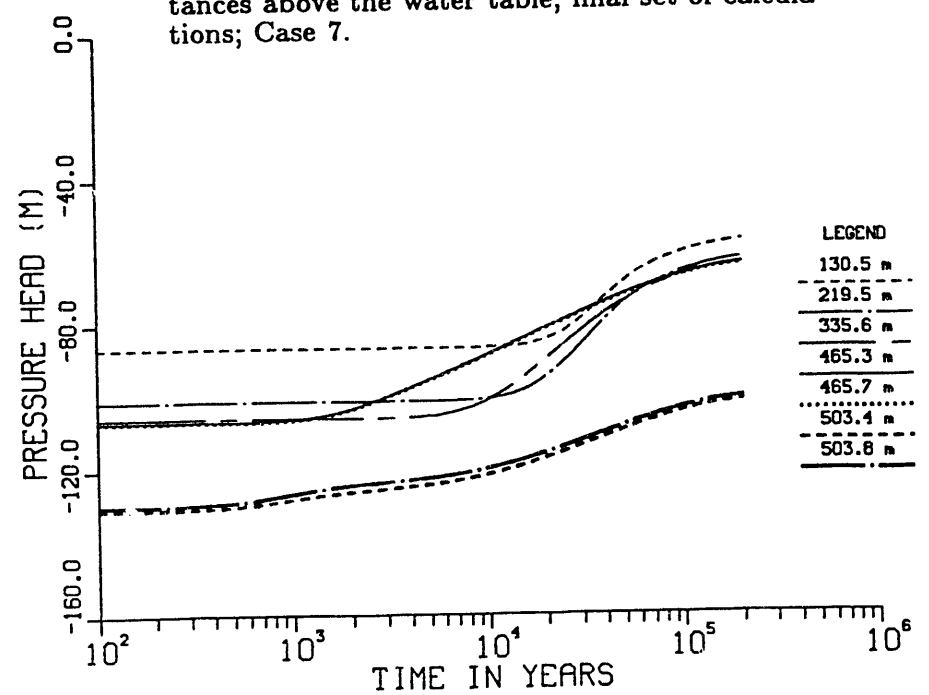

Figure 2-7-8. Pressure head versus time at specified distances above the water table; final set of calculations; Case 7.

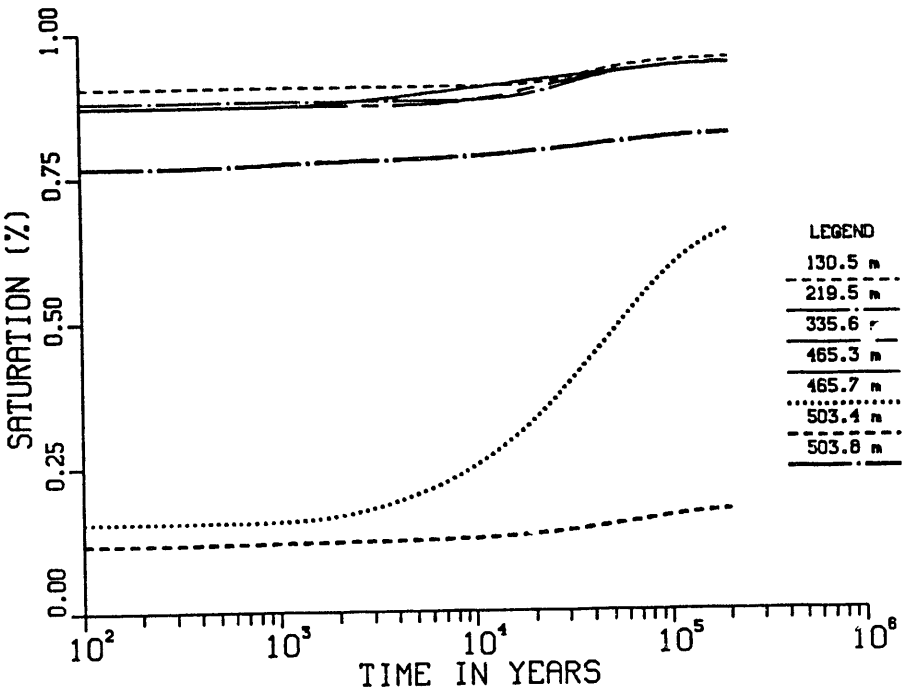

Figure 2-7-9. Matrix saturation versus time at specified distances above the water table; final set of calculations; Case 7.

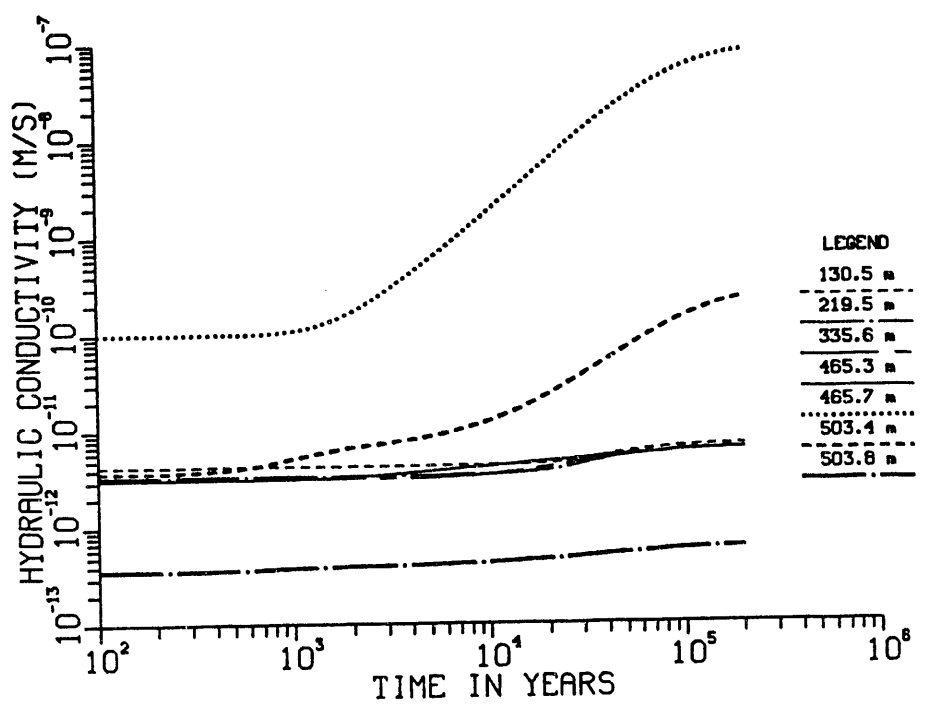

Figure 2-7-10. Hydraulic conductivity versus time at specified distances above the water table; final set of calculations; Case 7.

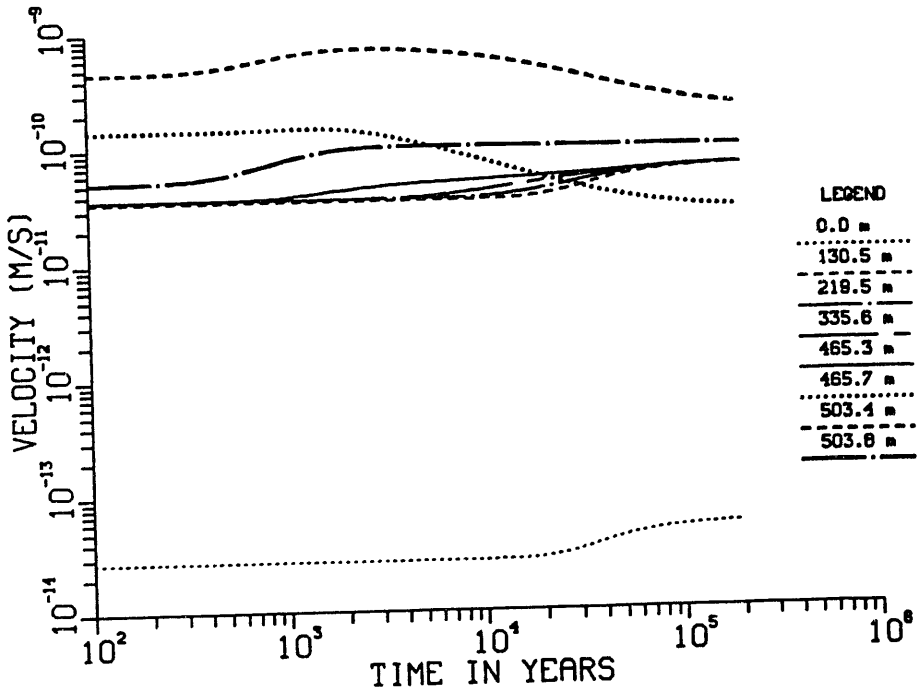

Figure 2-7-11. Average linear velocity of water in the matrix versus time at specified distances above the water table; final set of calculations; Case 7.

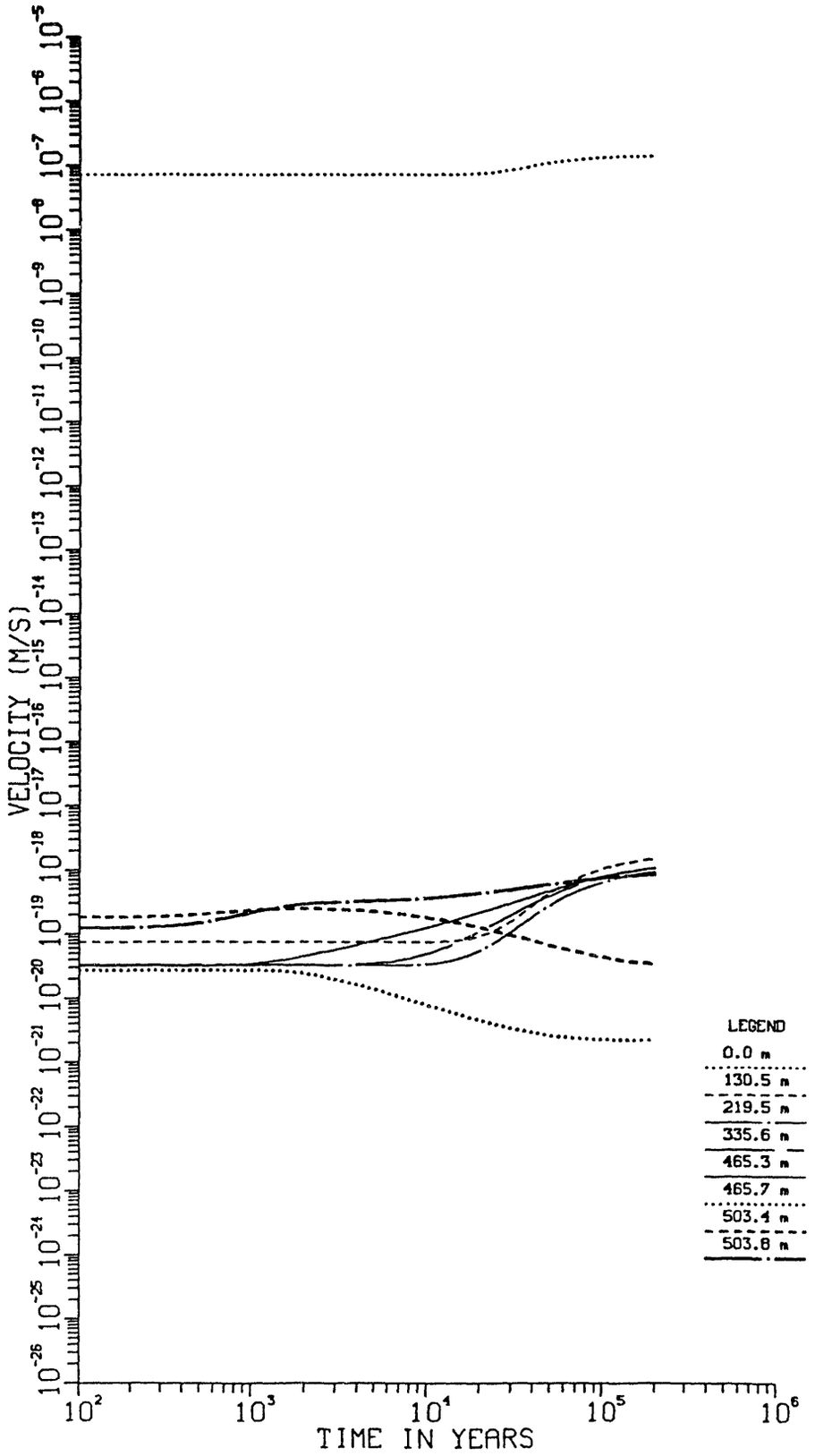

Figure 2-7-12. Average linear velocity of water in the fractures versus time at specified distances above the water table; final set of calculations; Case 7.

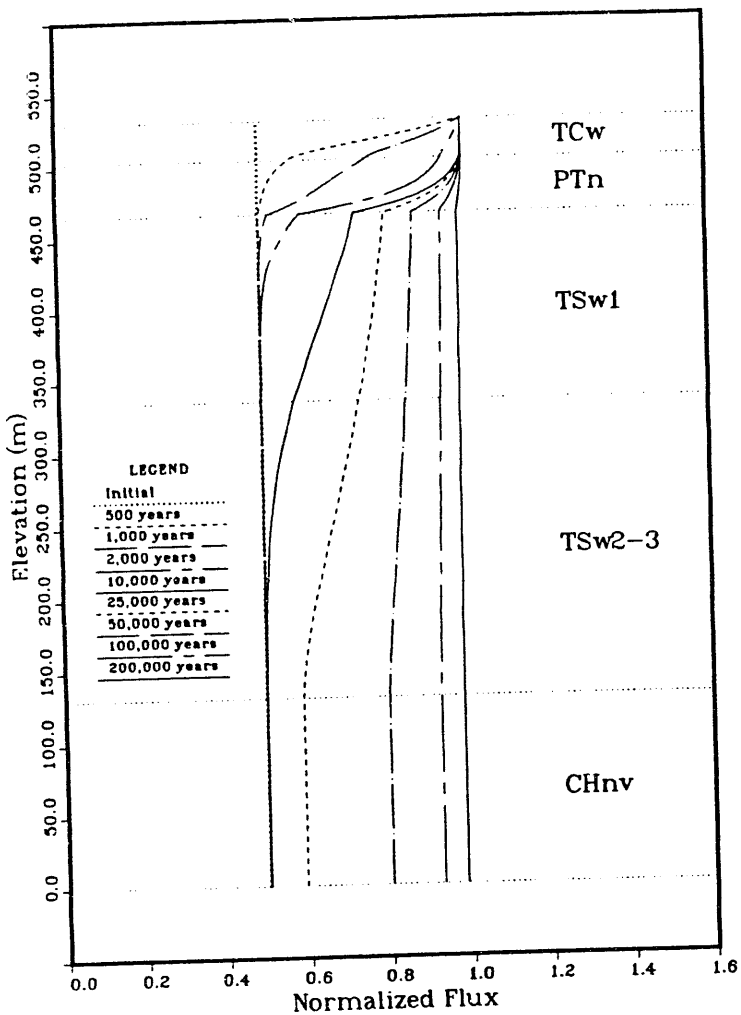

Figure 2-8-1. Normalized flux (calculated flux divided by imposed flux) versus distance above the water table at specified times; final set of calculations; Case 8.

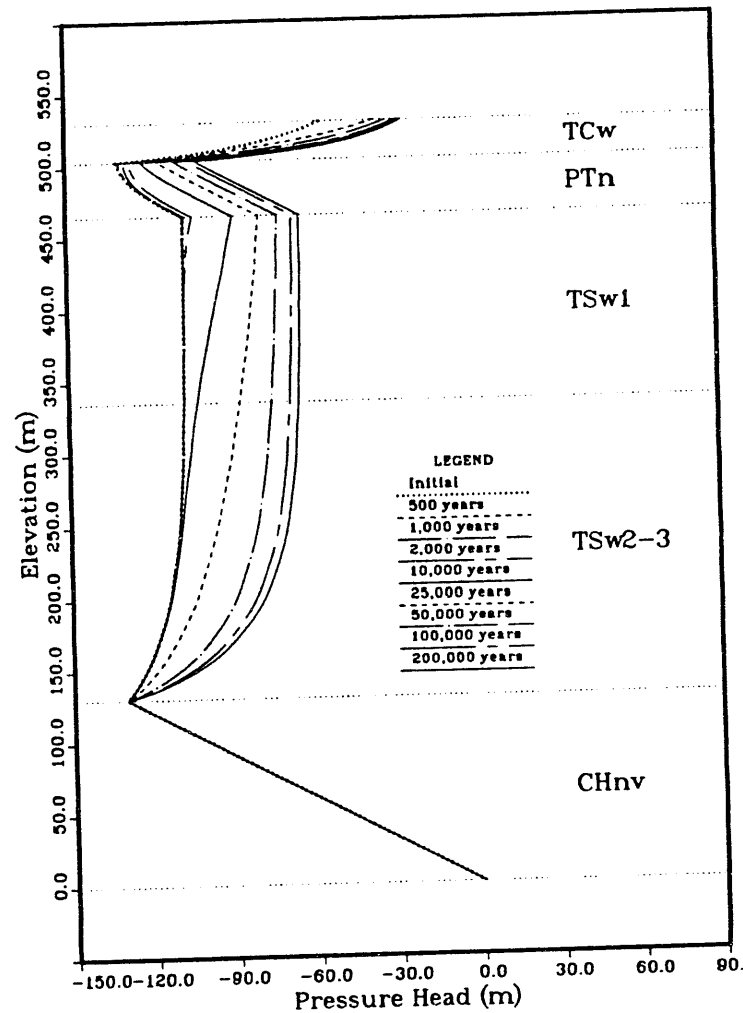

Figure 2-8-2. Pressure head versus distance above the water table at specified times; final set of calculations; Case 8.

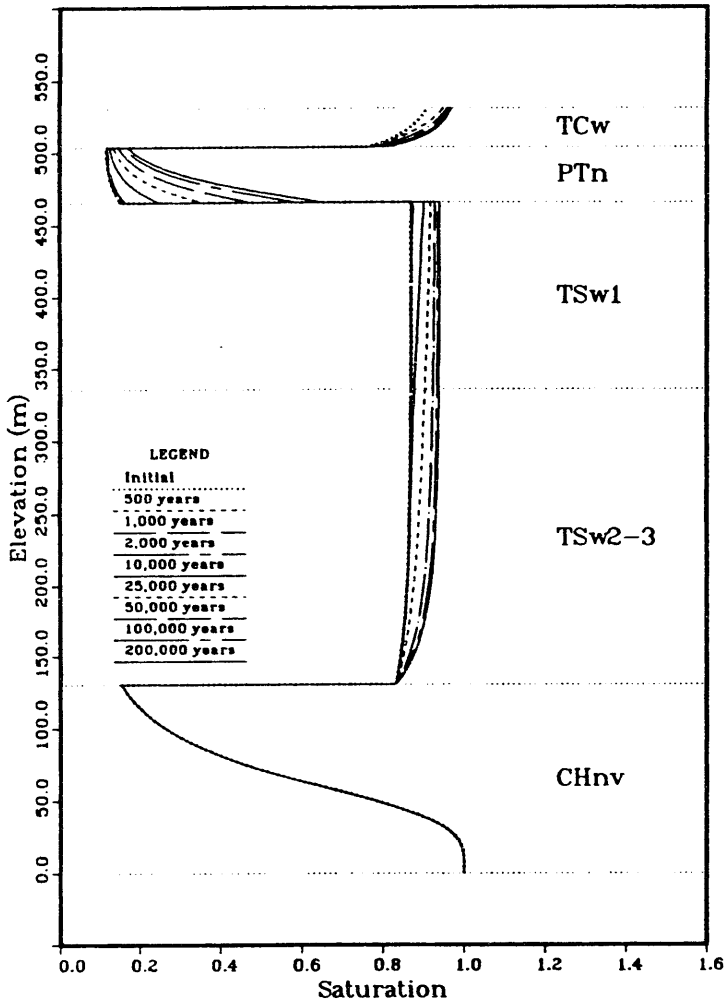

Figure 2-8-3. Matrix saturation versus distance above the water table at specified times; final set of calculations; Case 8.

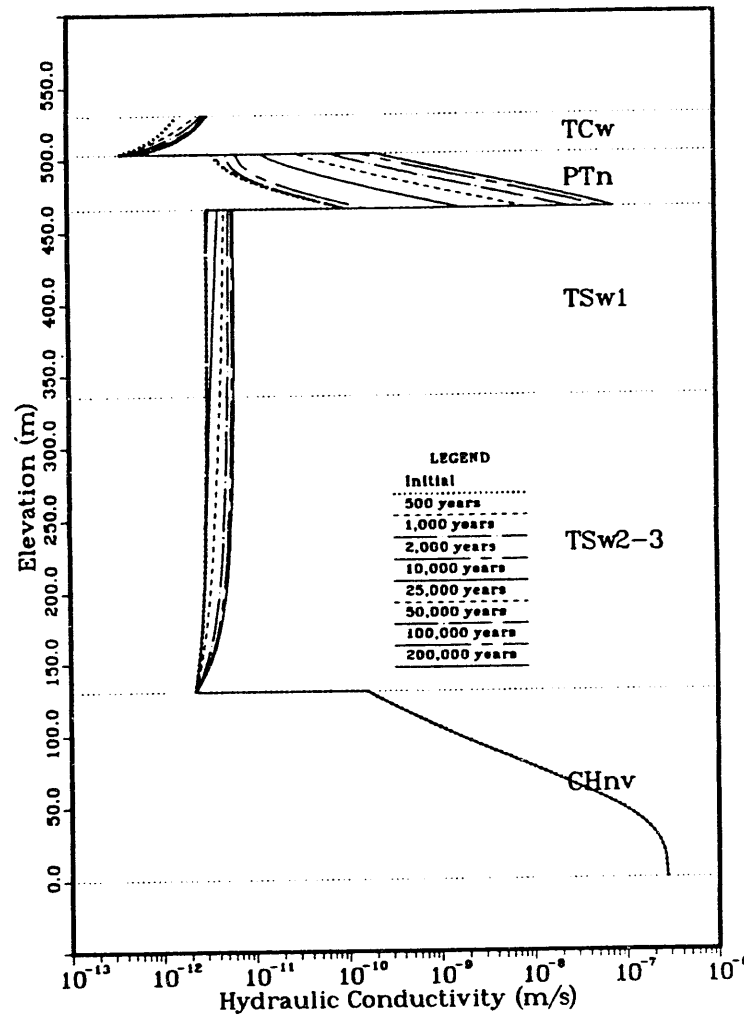

Figure 2-8-4. Hydraulic conductivity versus distance above the water table at specified times; final set of calculations; Case 8.

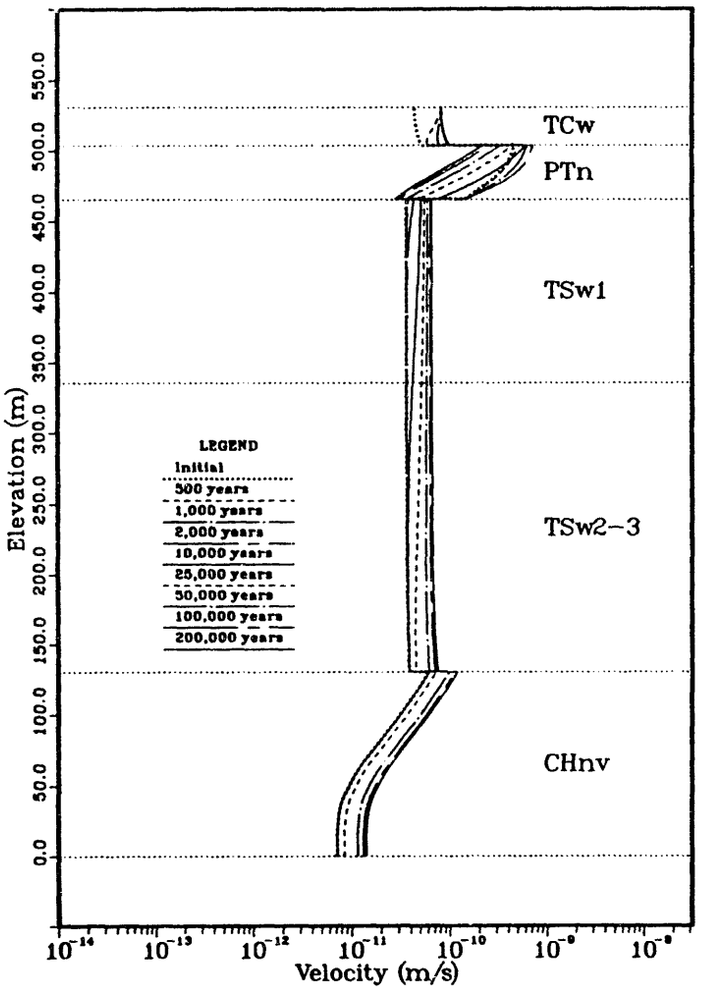

Figure 2-8-5. Average linear velocity of water in the matrix versus distance above the water table at specified times; final set of calculations; Case 8.

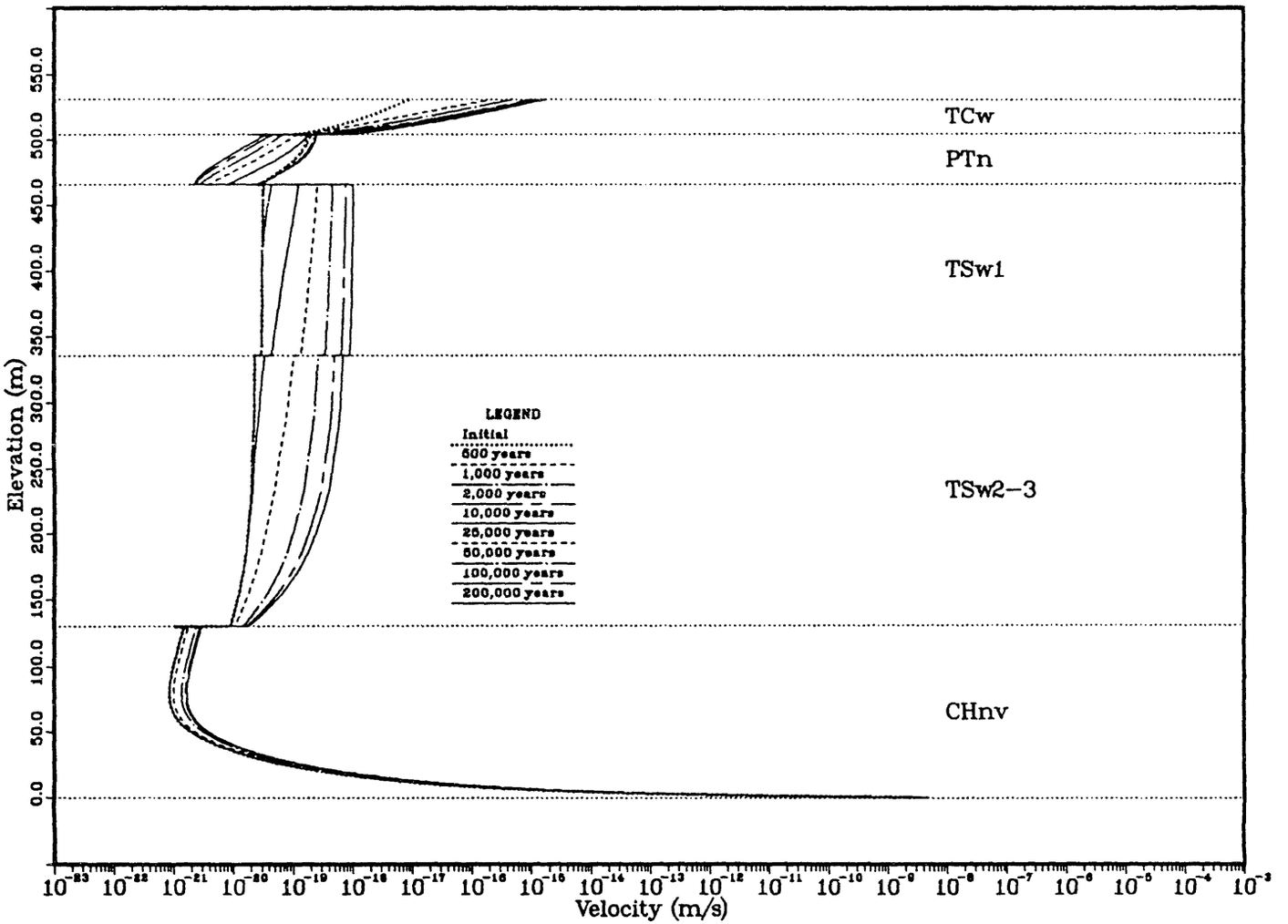

Figure 2-8-6. Average linear velocity of water in the fractures versus distance above the water table at specified times; final set of calculations; Case 8.

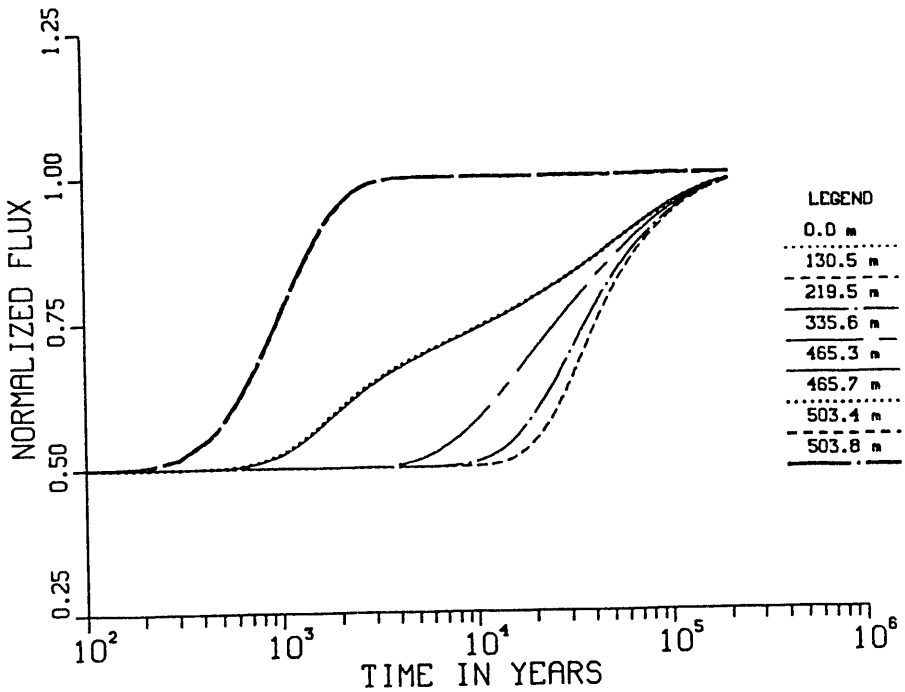

Figure 2-8-7. Normalized flux (calculated flux divided by imposed flux) versus time at specified distances above the water table; final set of calculations; Case 8.

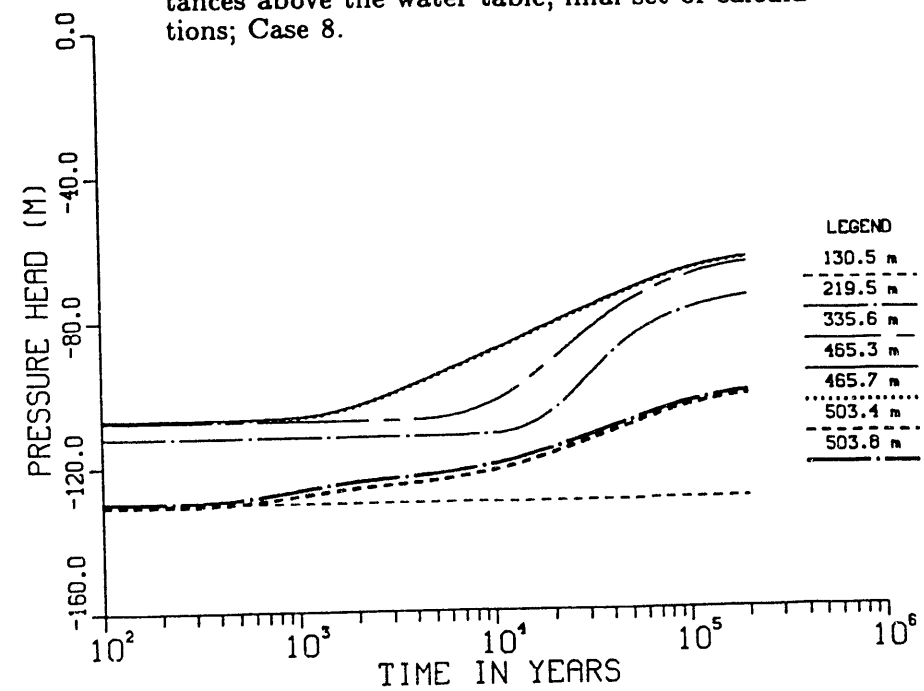

Figure 2-8-8. Pressure head versus time at specified distances above the water table; final set of calculations; Case 8.

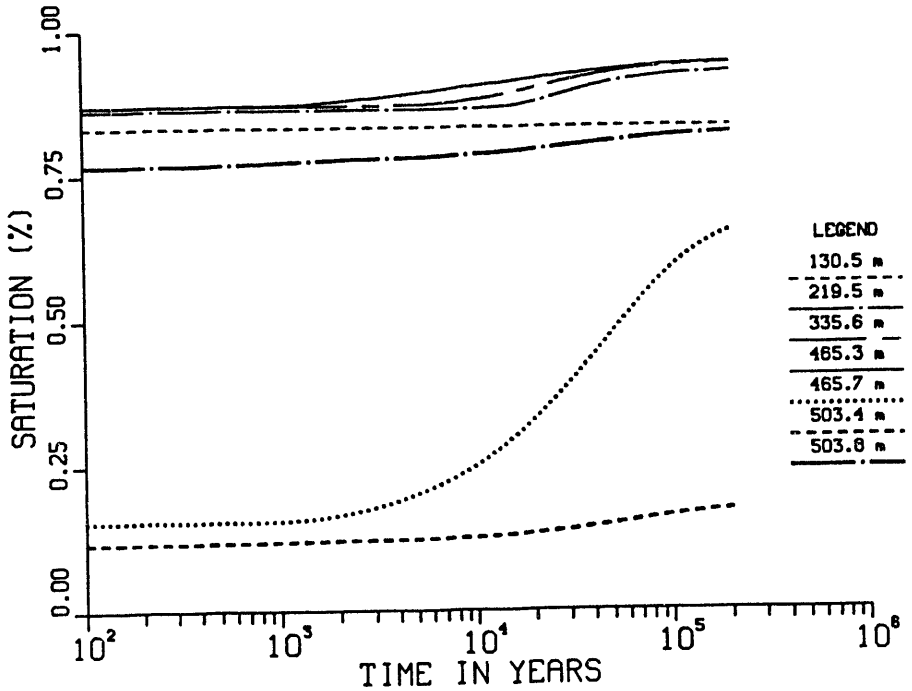

Figure 2-8-9. Matrix saturation versus time at specified distances above the water table; final set of calculations; Case 8.

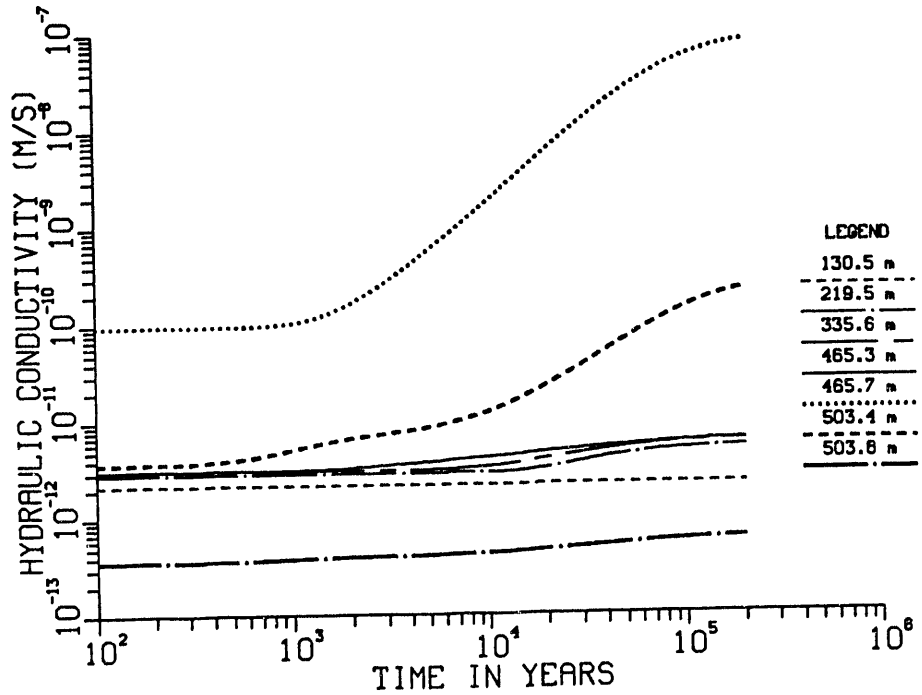

Figure 2-8-10. Hydraulic conductivity versus time at specified distances above the water table; final set of calculations; Case 8.

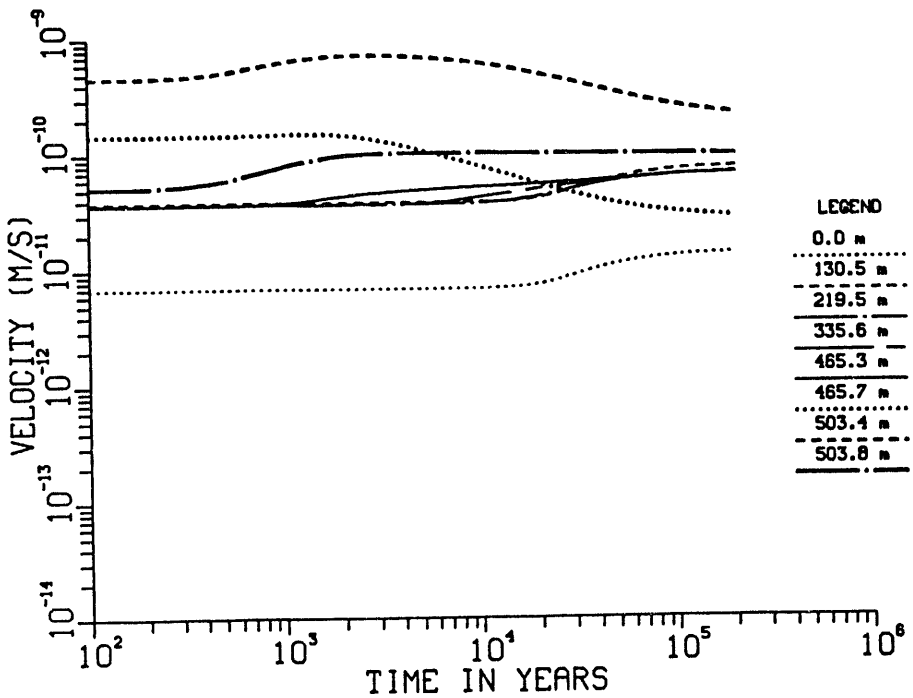

Figure 2-8-11. Average linear velocity of water in the matrix versus time at specified distances above the water table; final set of calculations; Case 8.

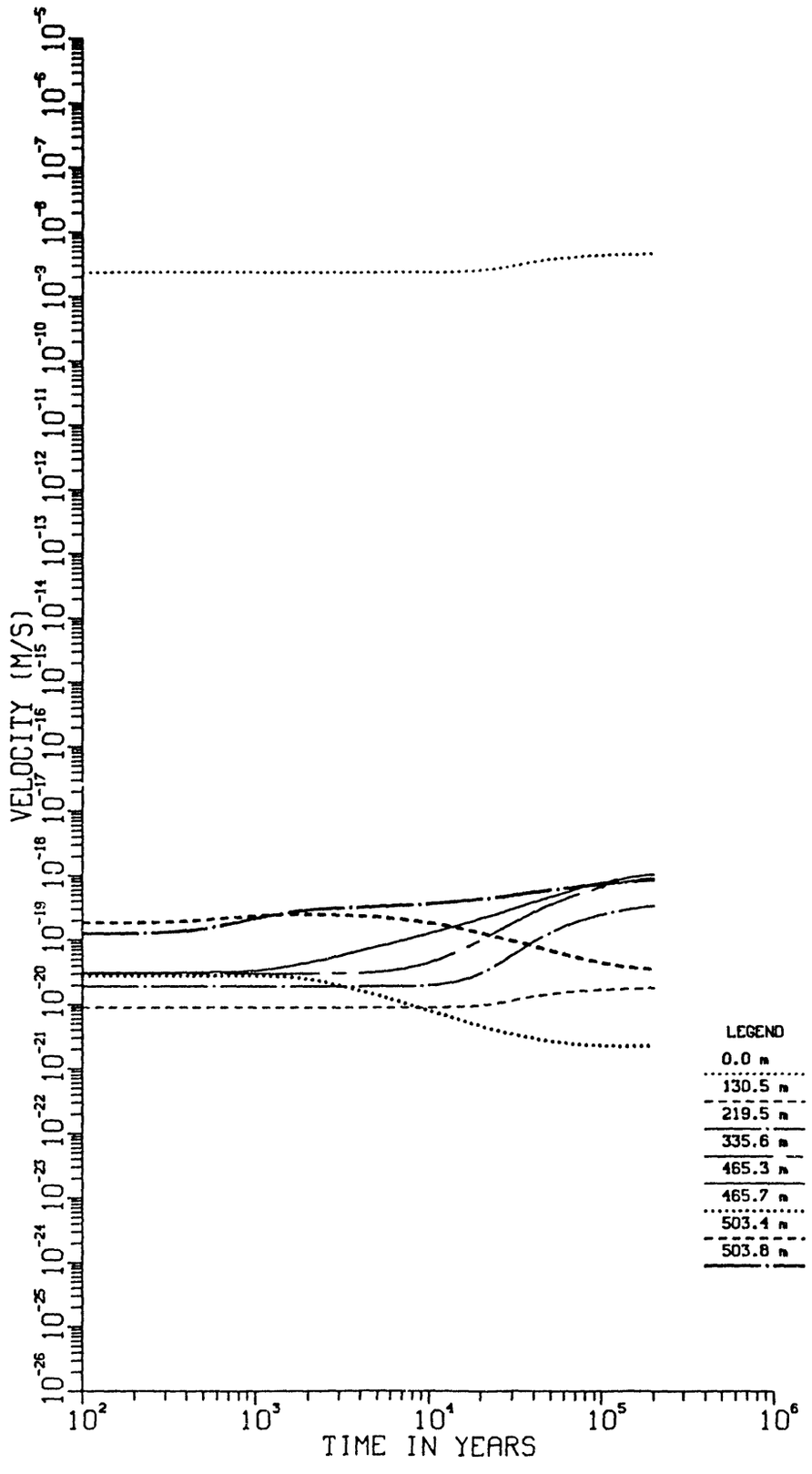

Figure 2-8-12. Average linear velocity of water in the fractures versus time at specified distances above the water table; final set of calculations; Case 8.

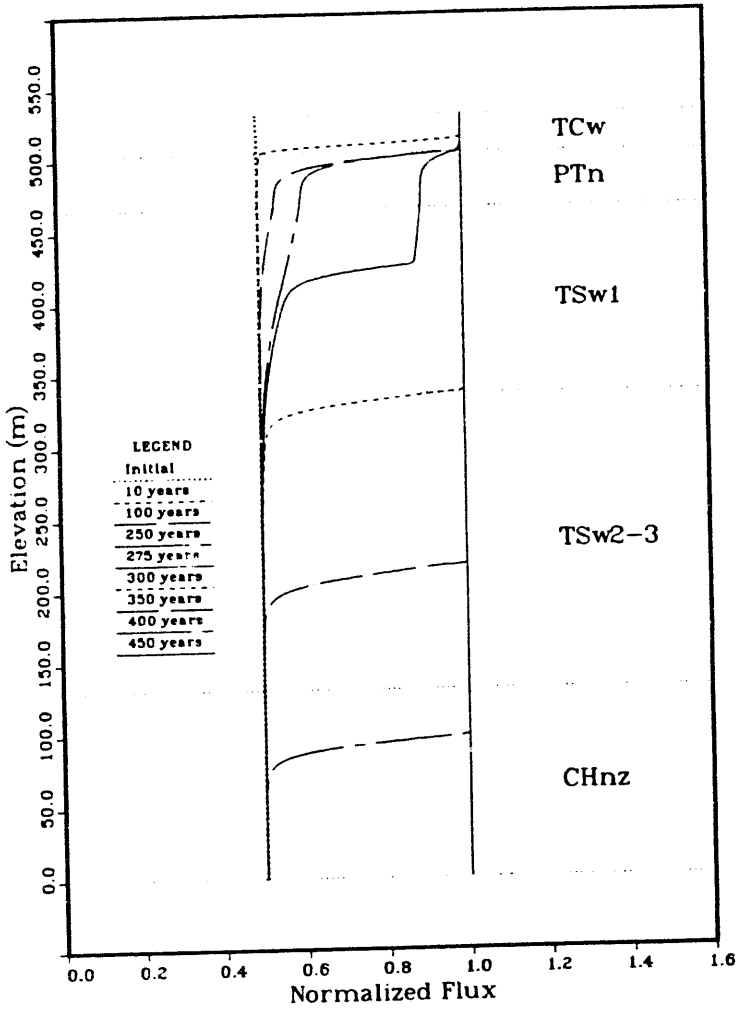

Figure 2-9-1. Normalized flux (calculated flux divided by imposed flux) versus distance above the water table at specified times; final set of calculations; Case 9.

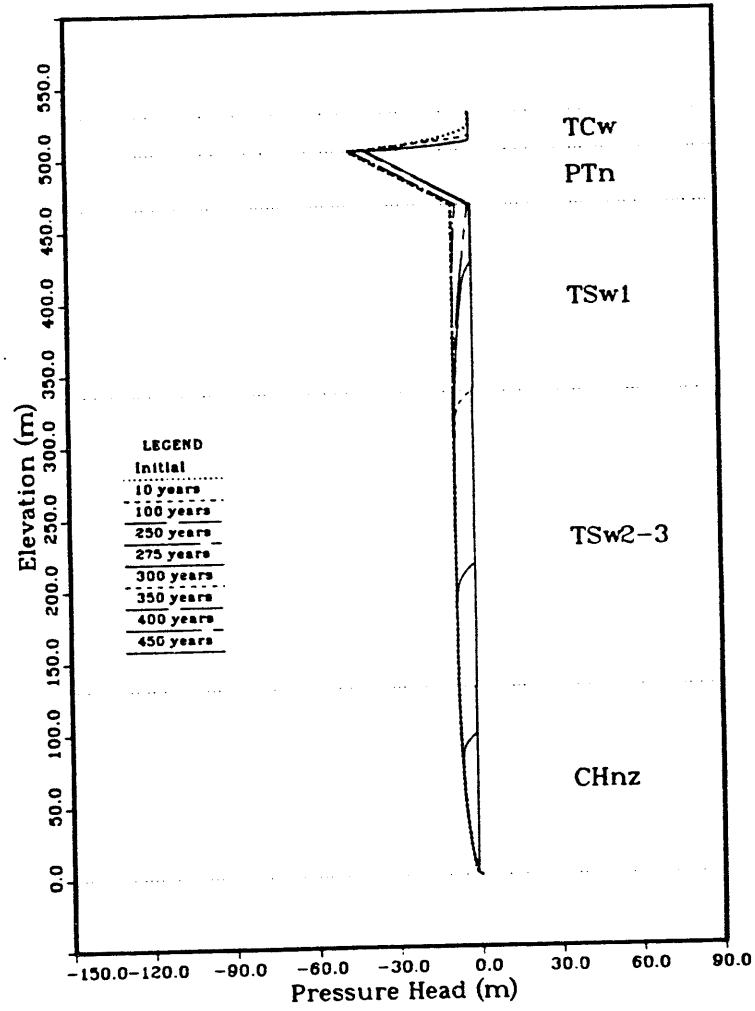

Figure 2-9-2. Pressure head versus distance above the water table at specified times; final set of calculations; Case 9.

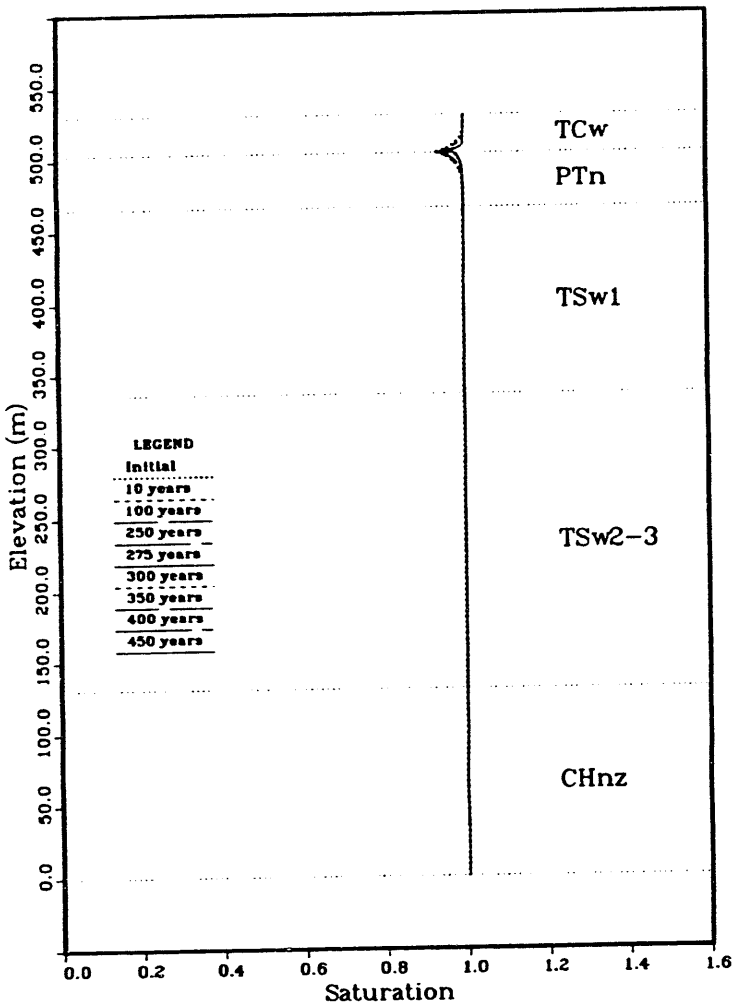

Figure 2-9-3. Matrix saturation versus distance above the water table at specified times; final set of calculations; Case 9.

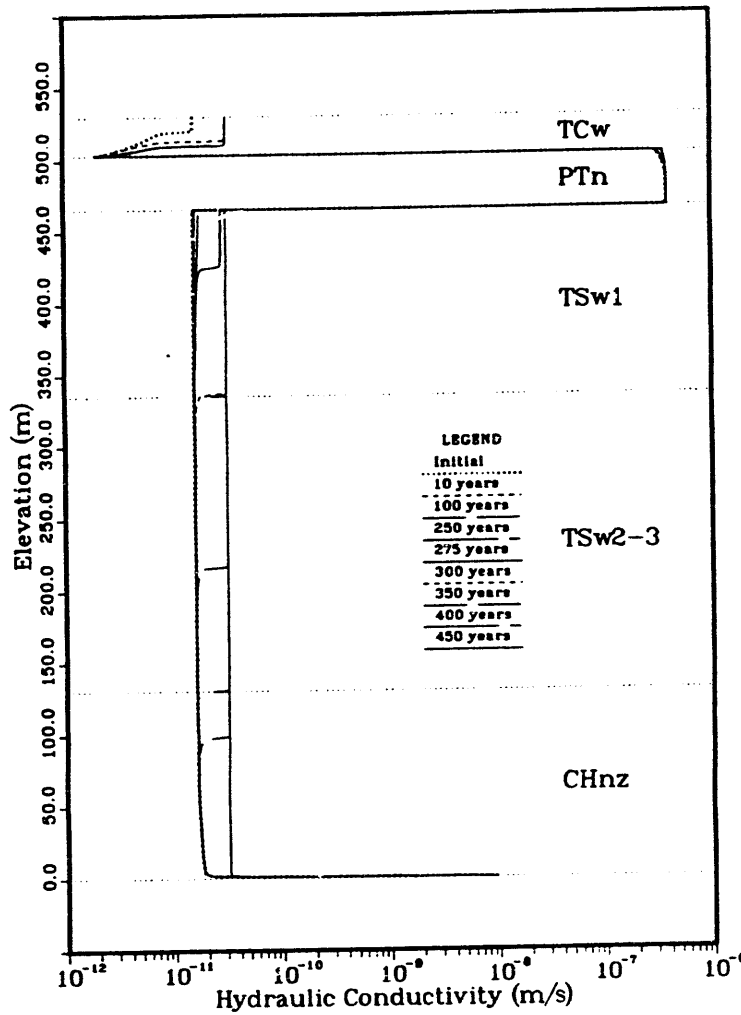

Figure 2-9-4. Hydraulic conductivity versus distance above the water table at specified times; final set of calculations; Case 9.

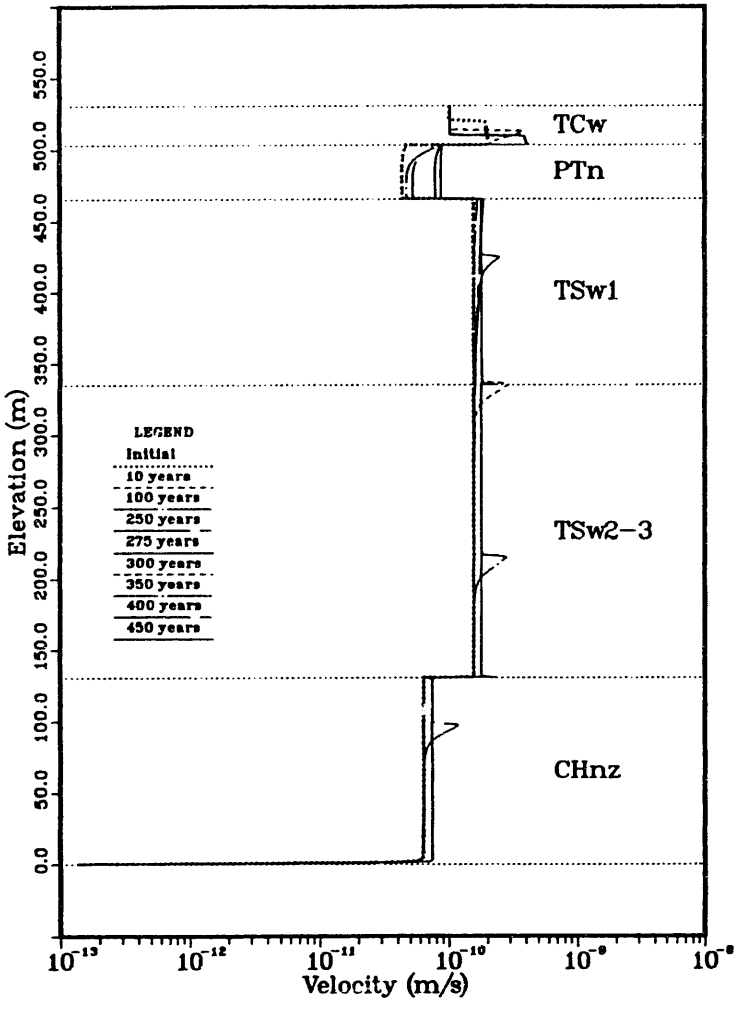

Figure 2-9-5. Average linear velocity of water in the matrix versus distance above the water table at specified times; final set of calculations; Case 9.

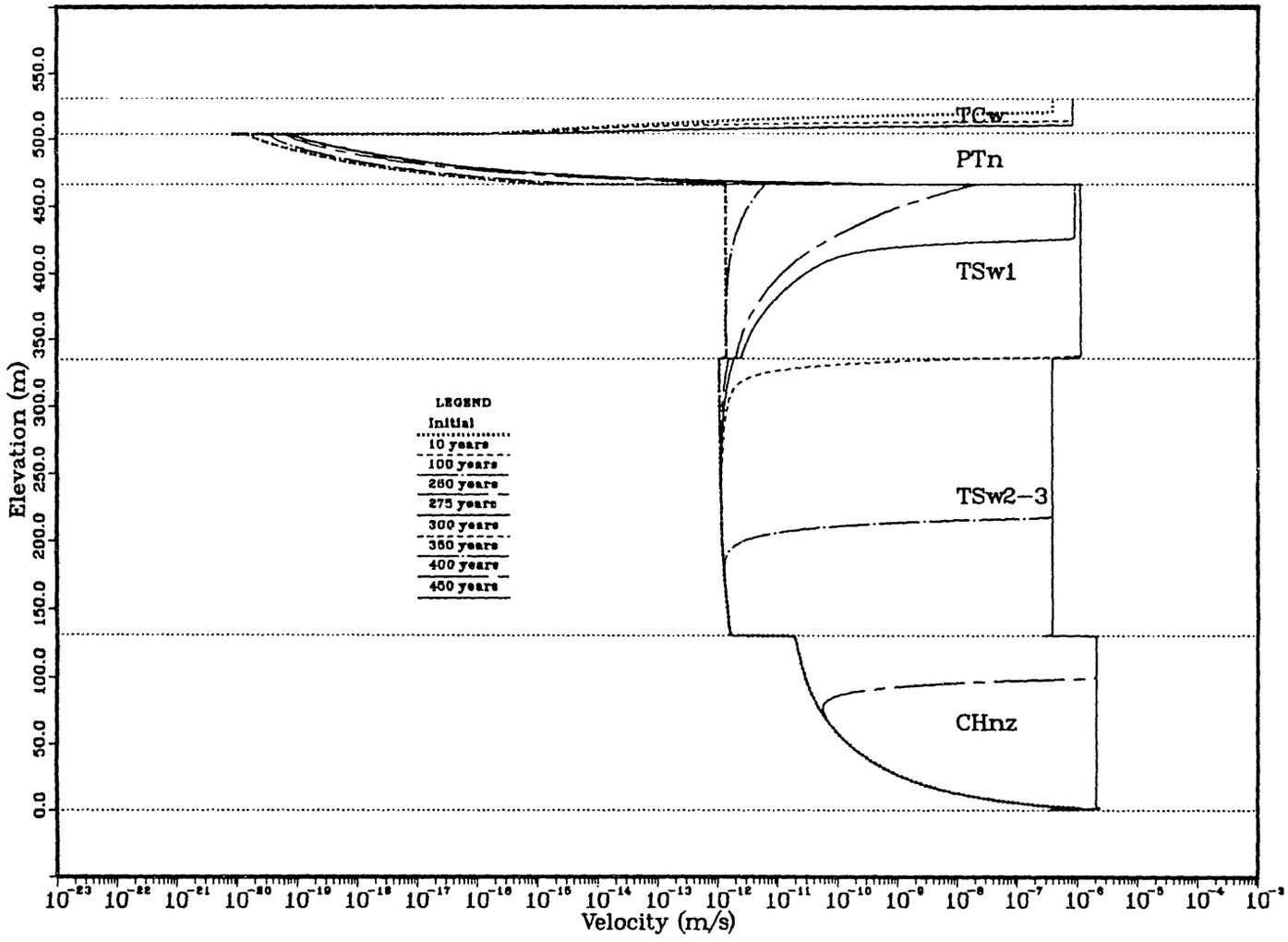

Figure 2-9-6. Average linear velocity of water in the fractures versus distance above the water table at specified times; final set of calculations; Case 9.

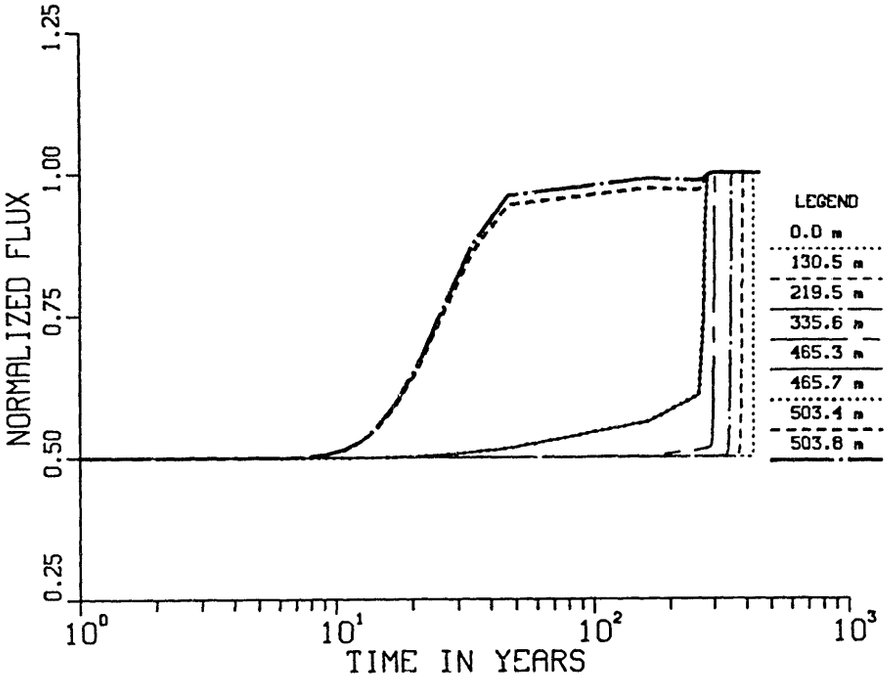

Figure 2-9-7. Normalized flux (calculated flux divided by imposed flux) versus time at specified distances above the water table; final set of calculations; Case 9.

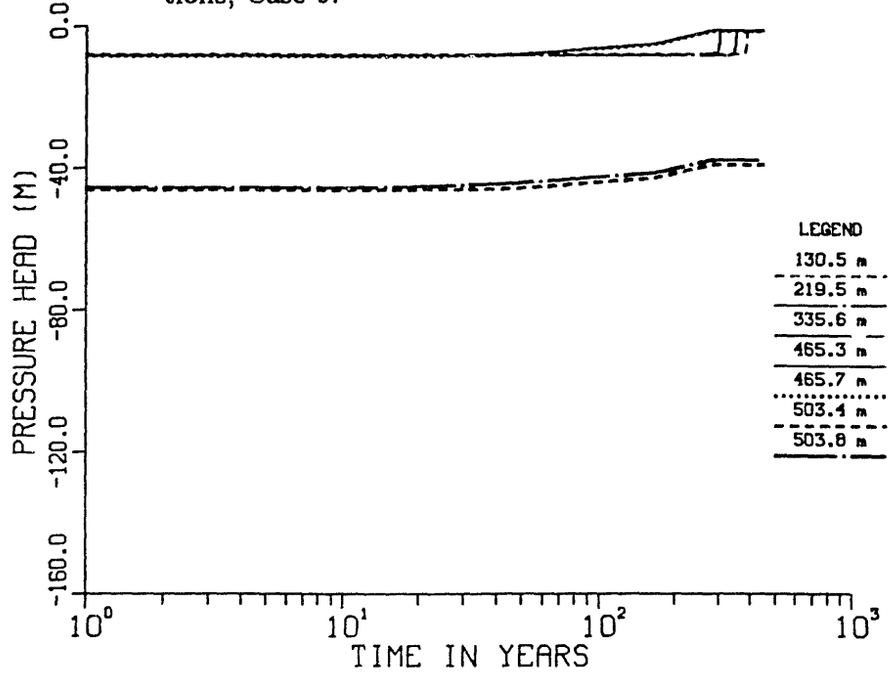

Figure 2-9-8. Pressure head versus time at specified distances above the water table; final set of calculations; Case 9.

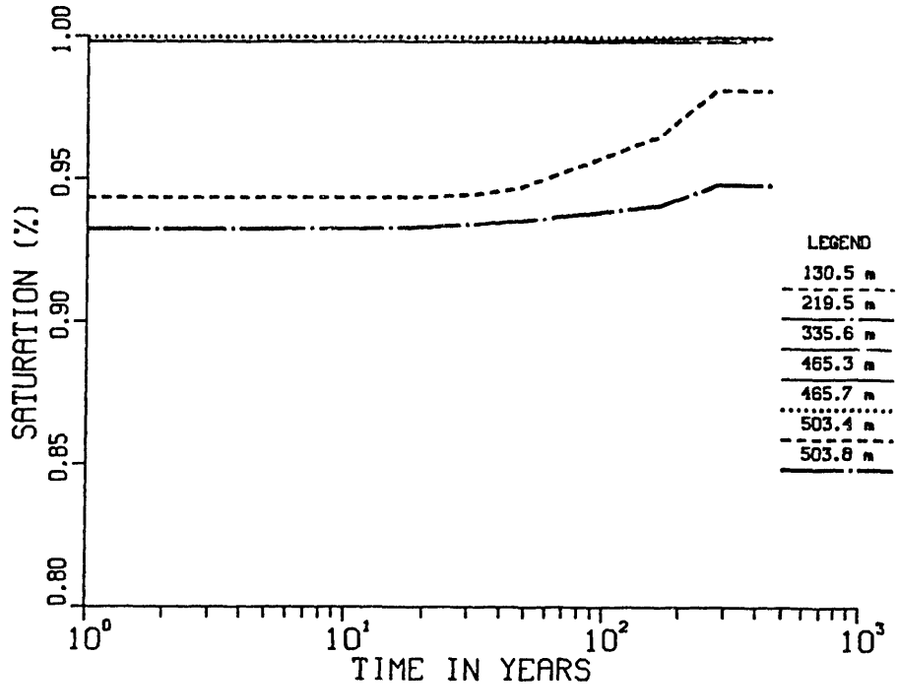

Figure 2-9-9. Matrix saturation versus time at specified distances above the water table: final set of calculations; Case 9.

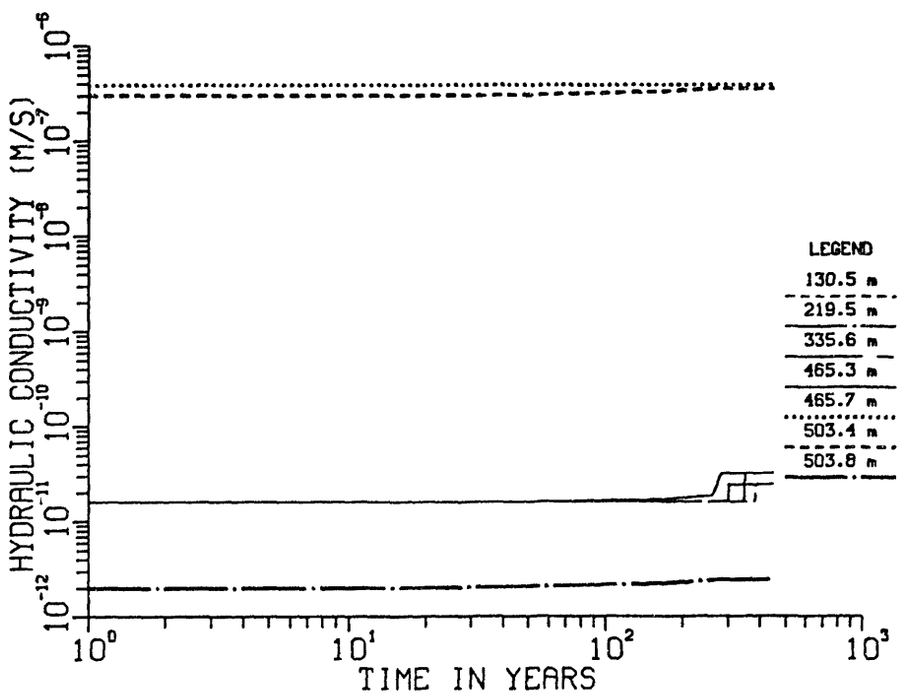

Figure 2-9-10. Hydraulic conductivity versus time at specified distances above the water table; final set of calculations; Case 9.

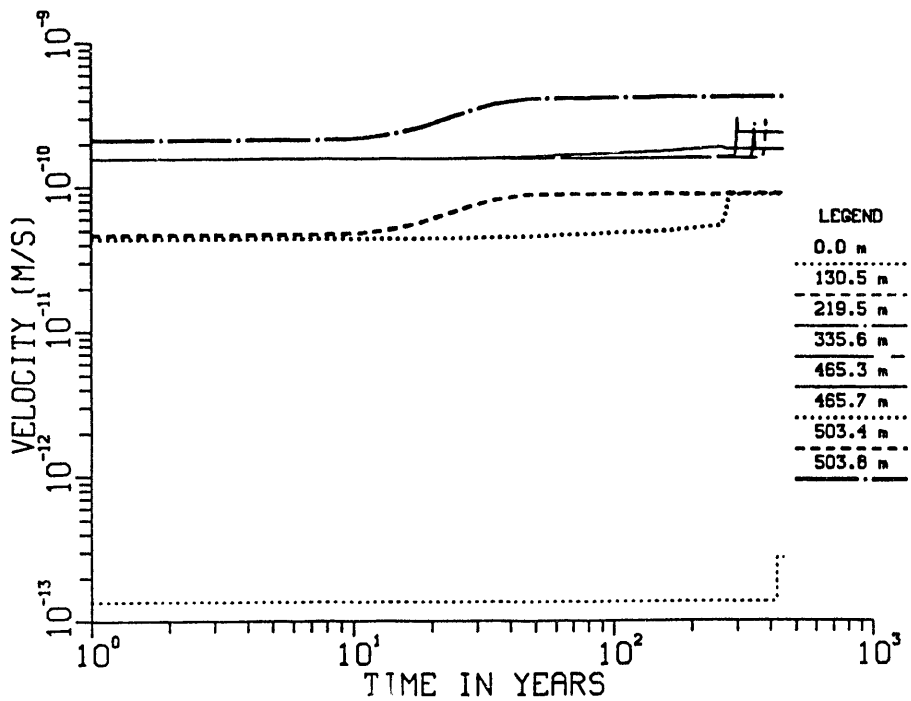

Figure 2-9-11. Average linear velocity of water in the matrix versus time at specified distances above the water table; final set of calculations; Case 9.

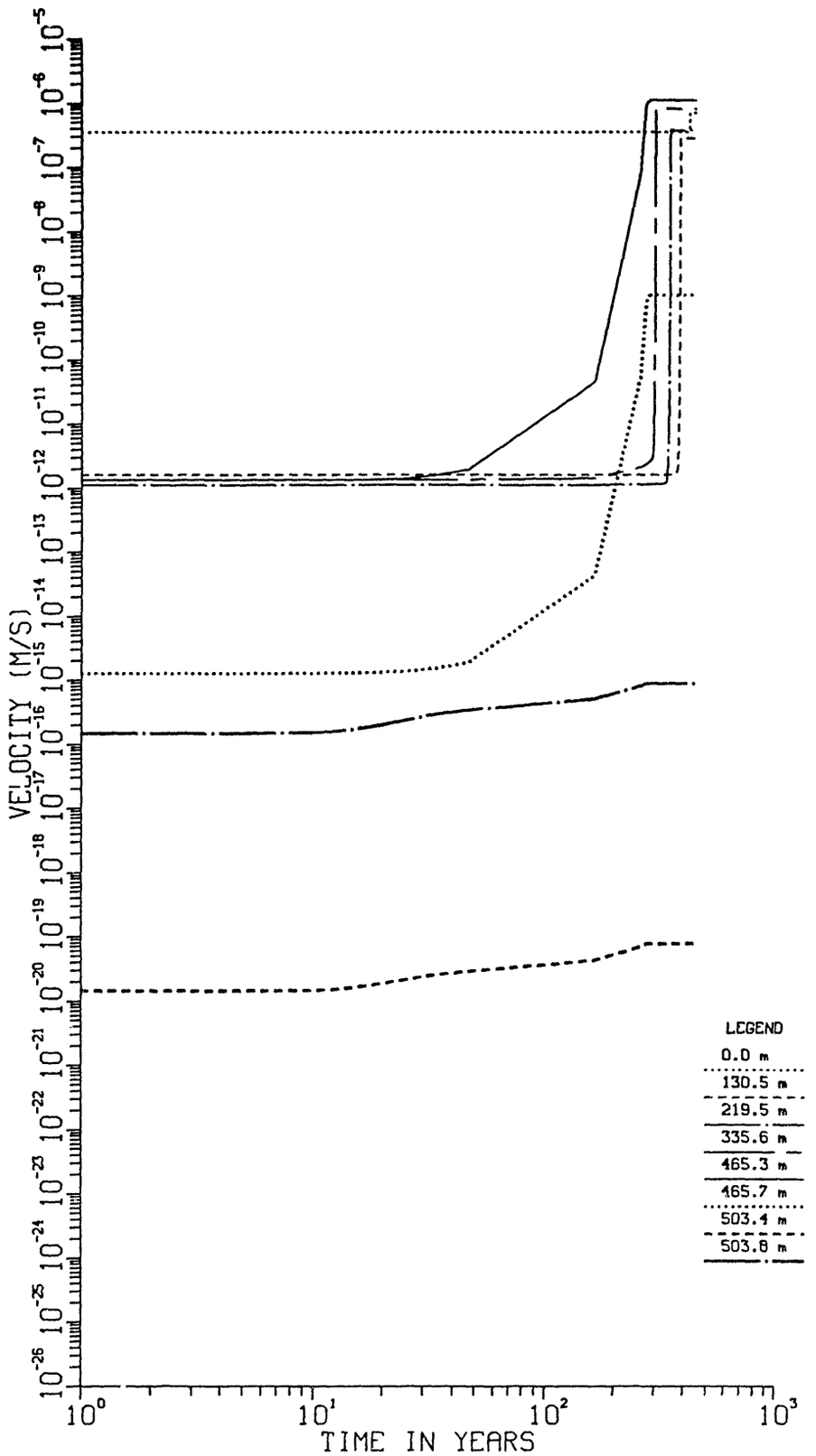

Figure 2-9-12. Average linear velocity of water in the fractures versus time at specified distances above the water table; final set of calculations; Case 9.

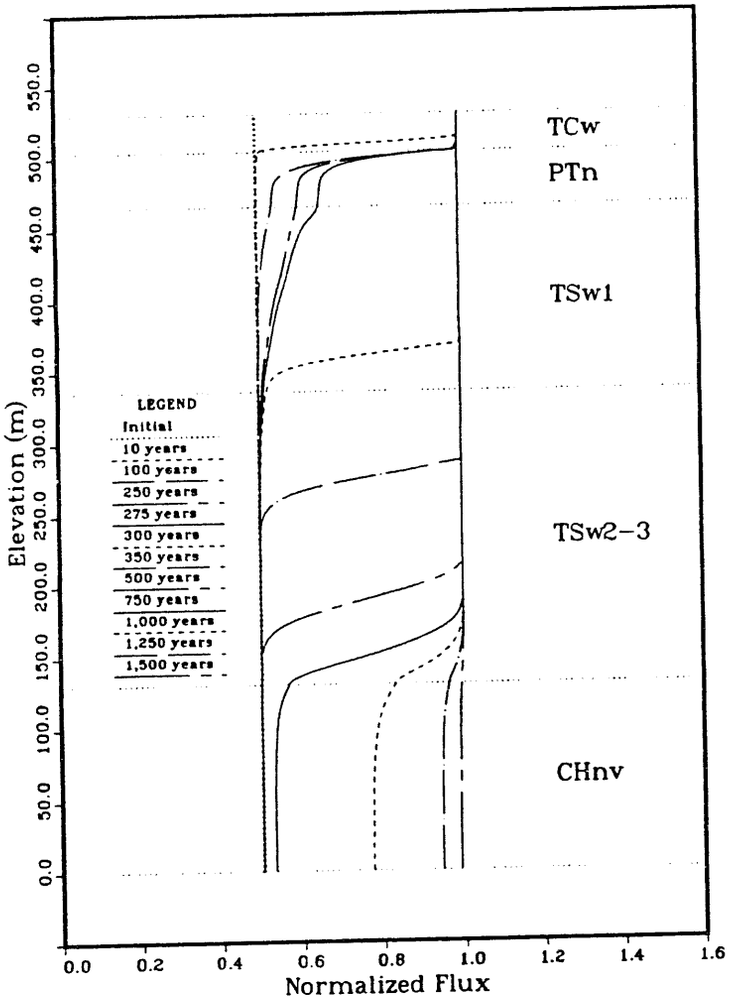

Figure 2-10-1. Normalized flux (calculated flux divided by imposed flux) versus distance above the water table at specified times; final set of calculations; Case 10.

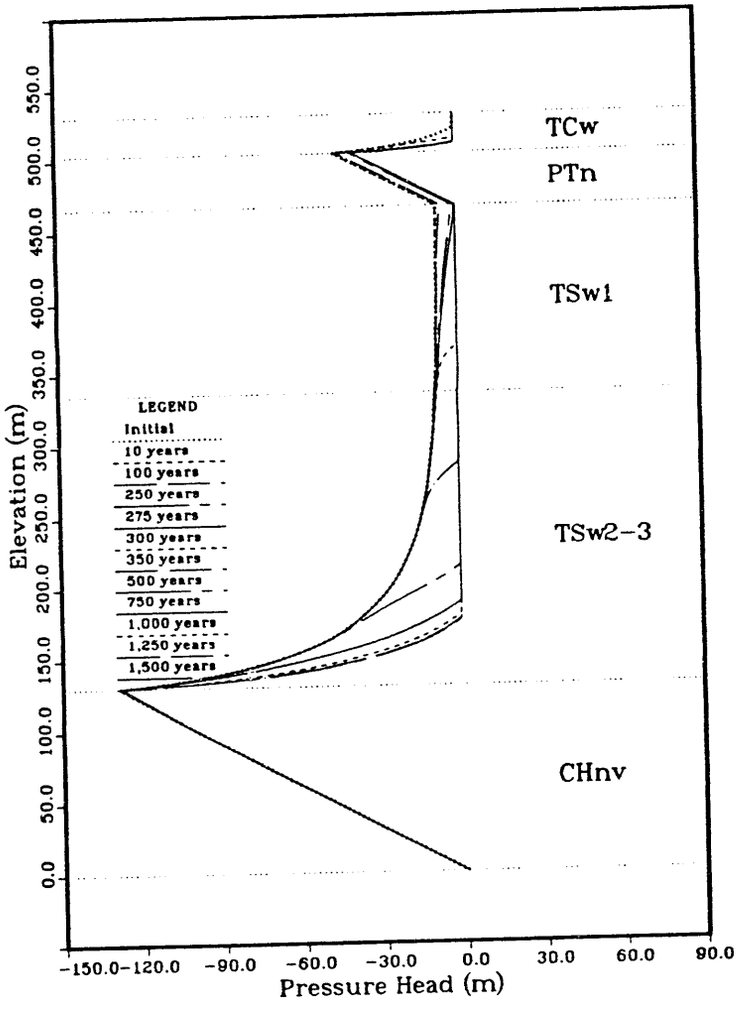

Figure 2-10-2. Pressure head versus distance above the water table at specified times; final set of calculations; Case 10.

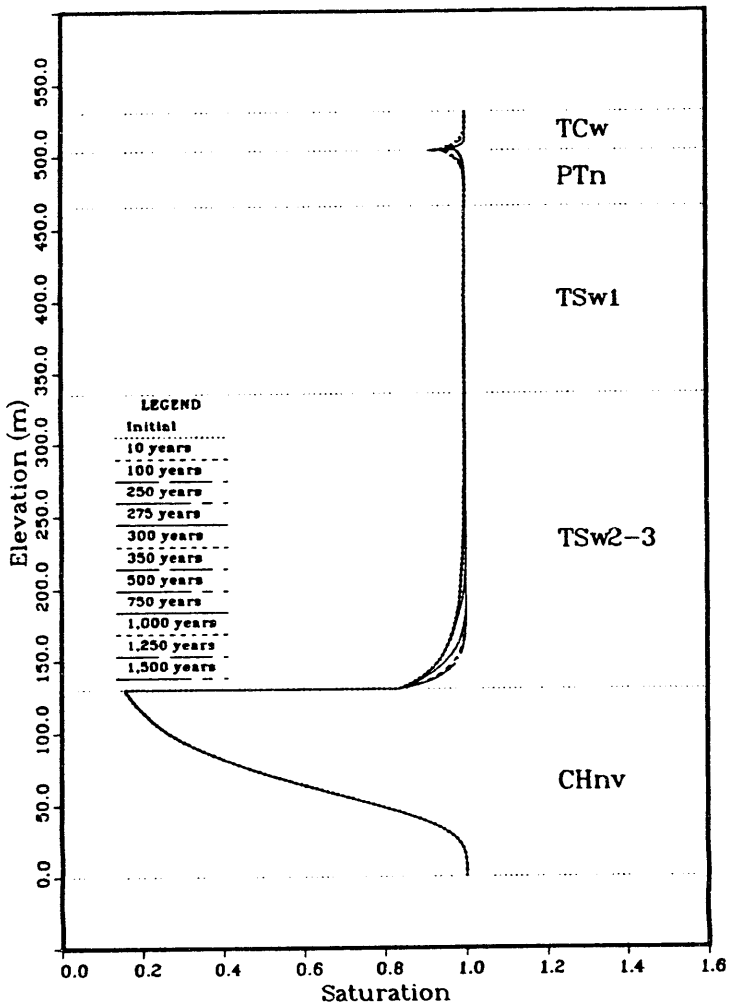

Figure 2-10-3. Matrix saturation versus distance above the water table at specified times; final set of calculations; Case 10.

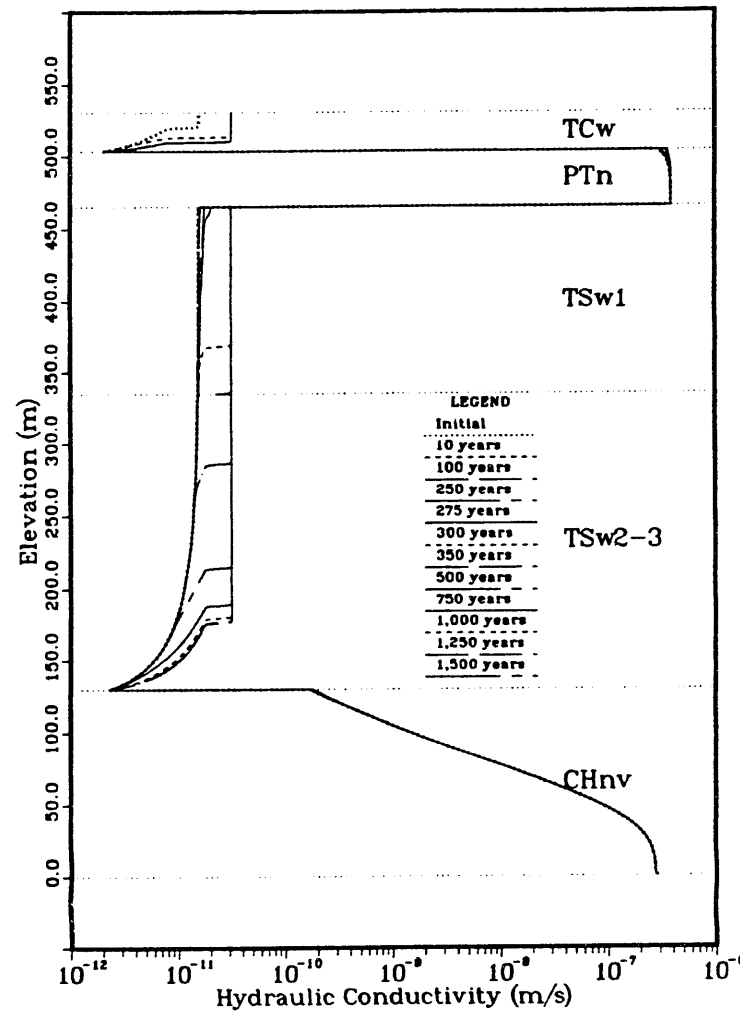

Figure 2-10-4. Hydraulic conductivity versus distance above the water table at specified times; final set of calculations; Case 10.

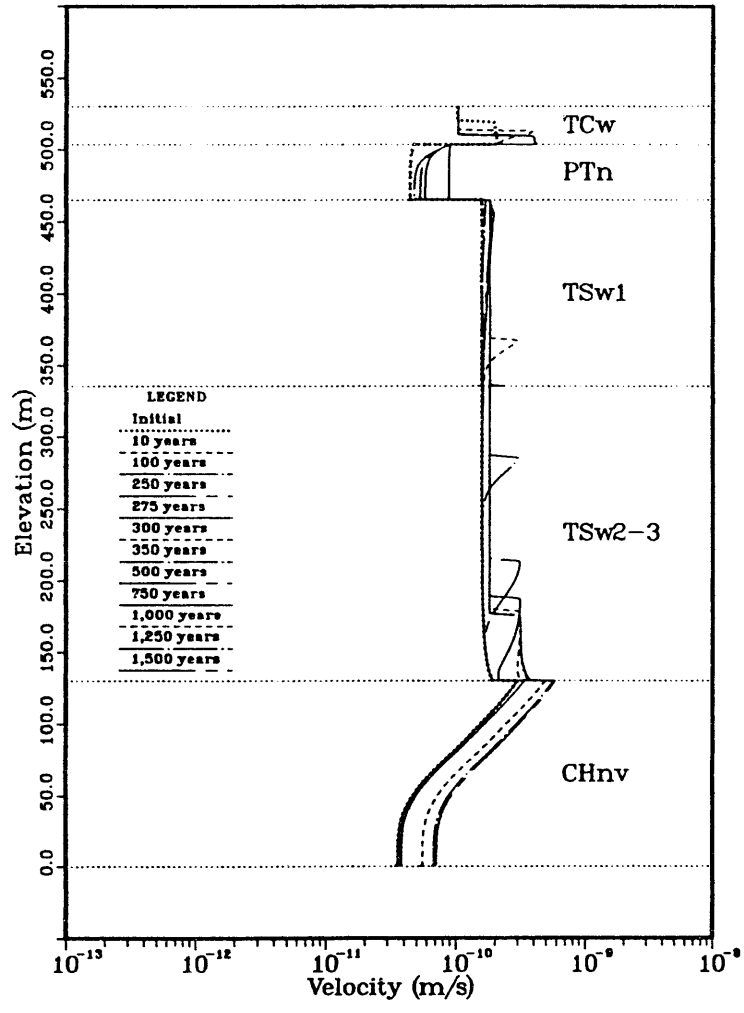

Figure 2-10-5. Average linear velocity of water in the matrix versus distance above the water table at specified times; final set of calculations; Case 10.

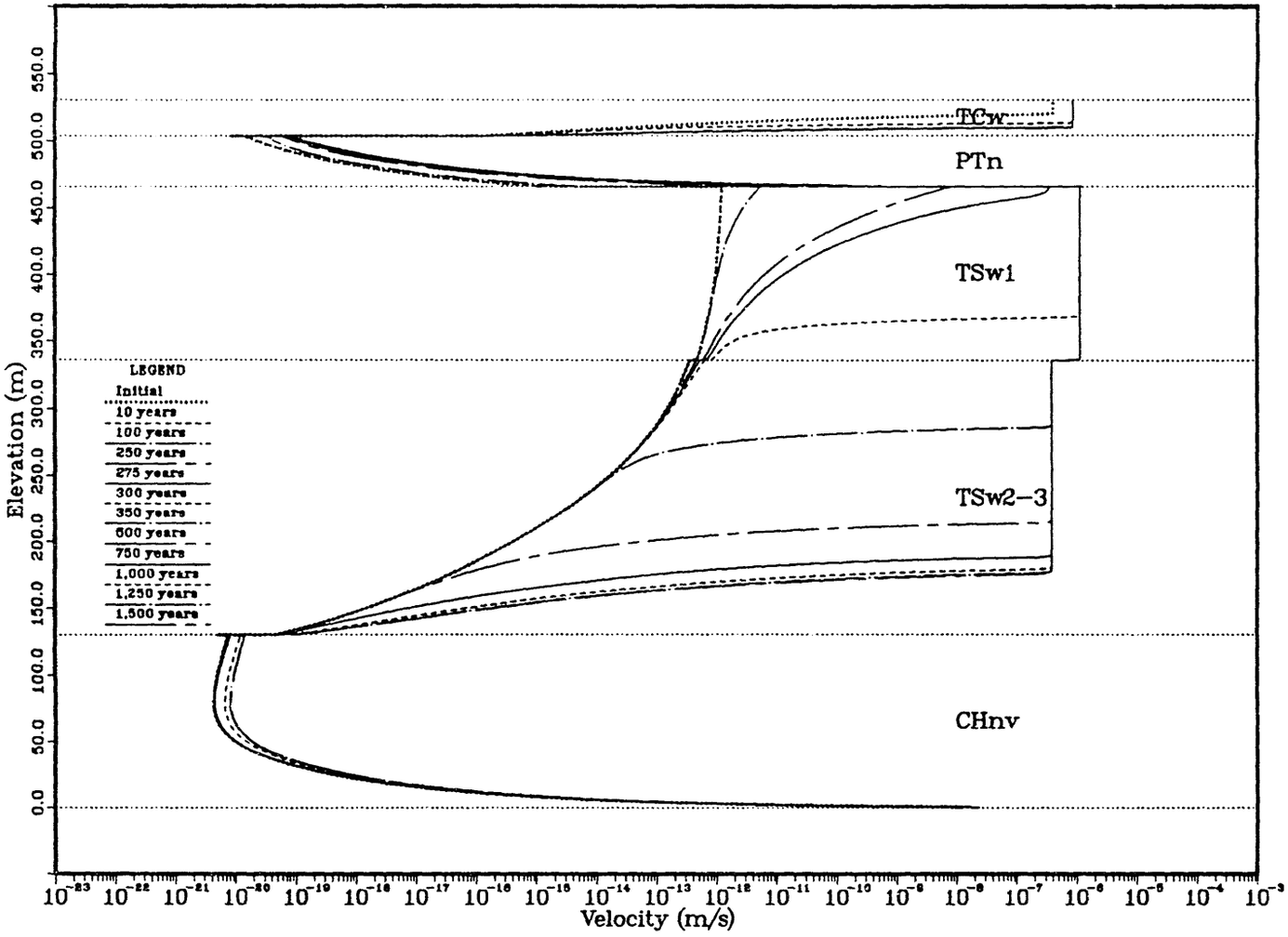

Figure 2-10-6. Average linear velocity of water in the fractures versus distance above the water table at specified times; final set of calculations; Case 10.

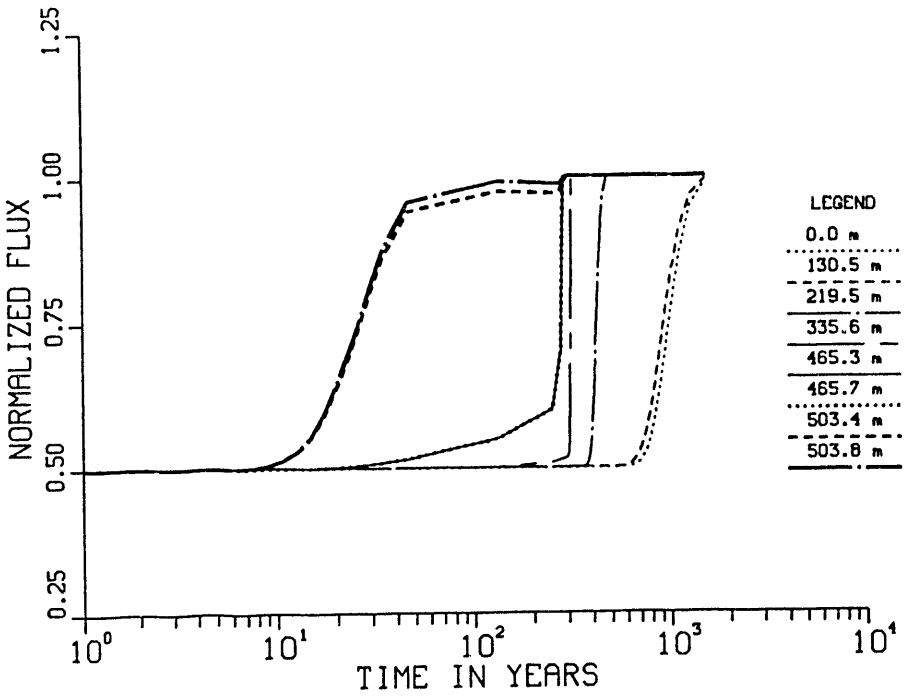

Figure 2-10-7. Normalized flux (calculated flux divided by imposed flux) versus time at specified distances above the water table; final set of calculations; Case 10.

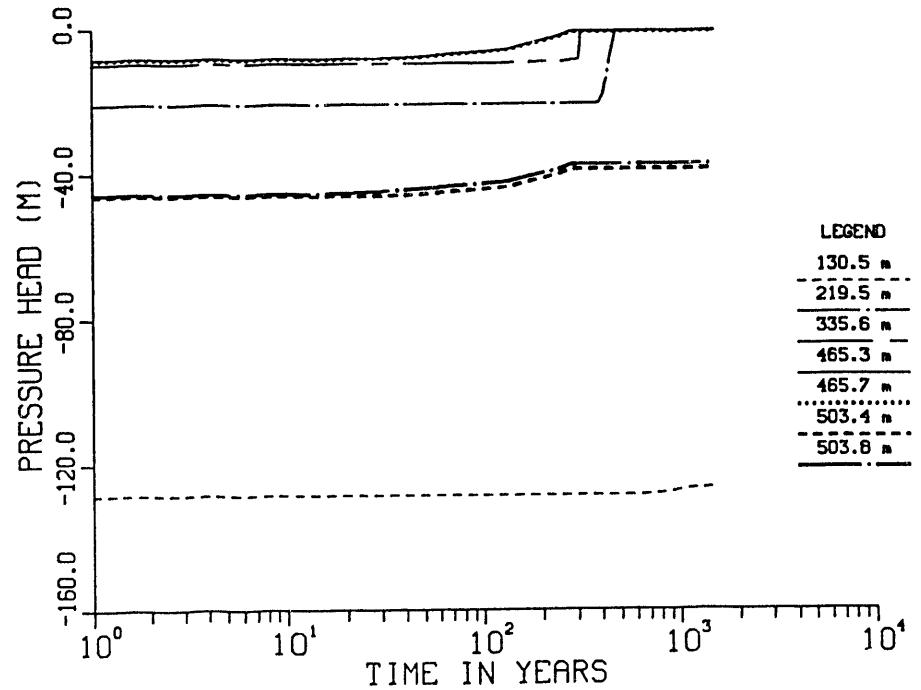

Figure 2-10-8. Pressure head versus time at specified distances above the water table; final set of calculations; Case 10.

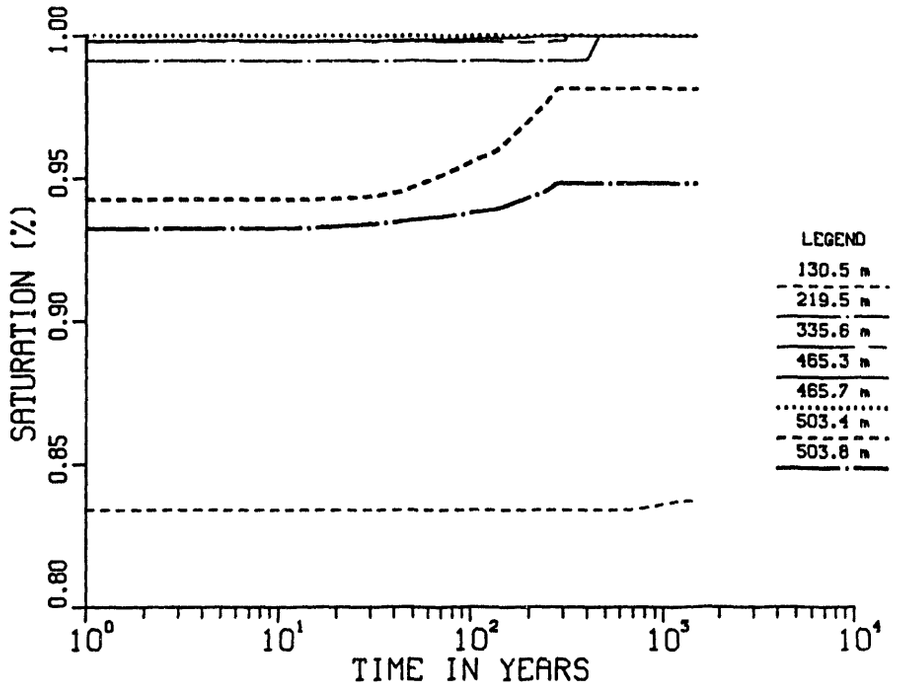

Figure 2-10-9. Matrix saturation versus time at specified distances above the water table; final set of calculations; Case 10.

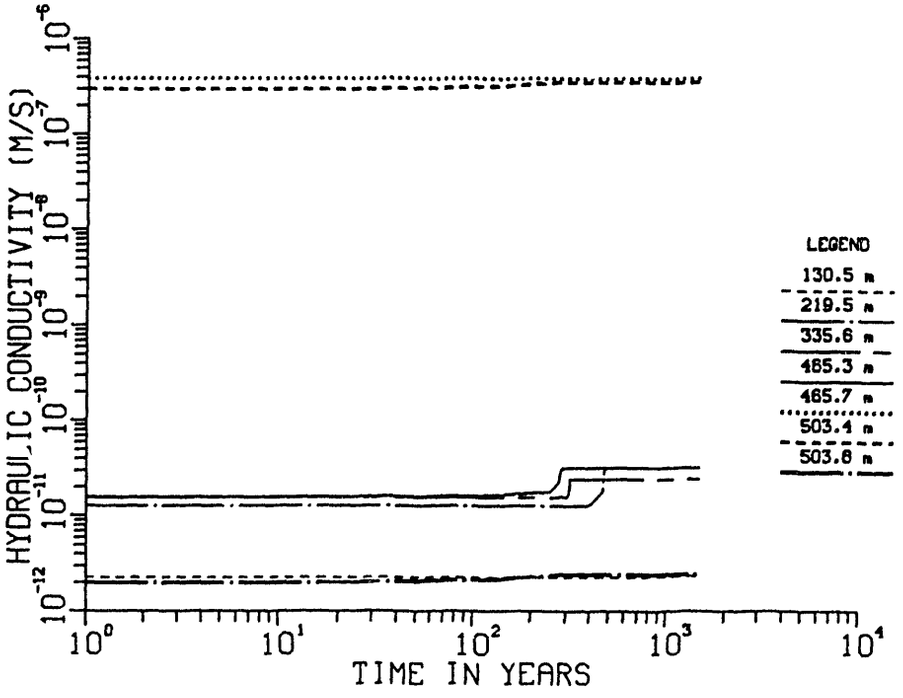

Figure 2-10-10. Hydraulic conductivity versus time at specified distances above the water table; final set of calculations; Case 10.

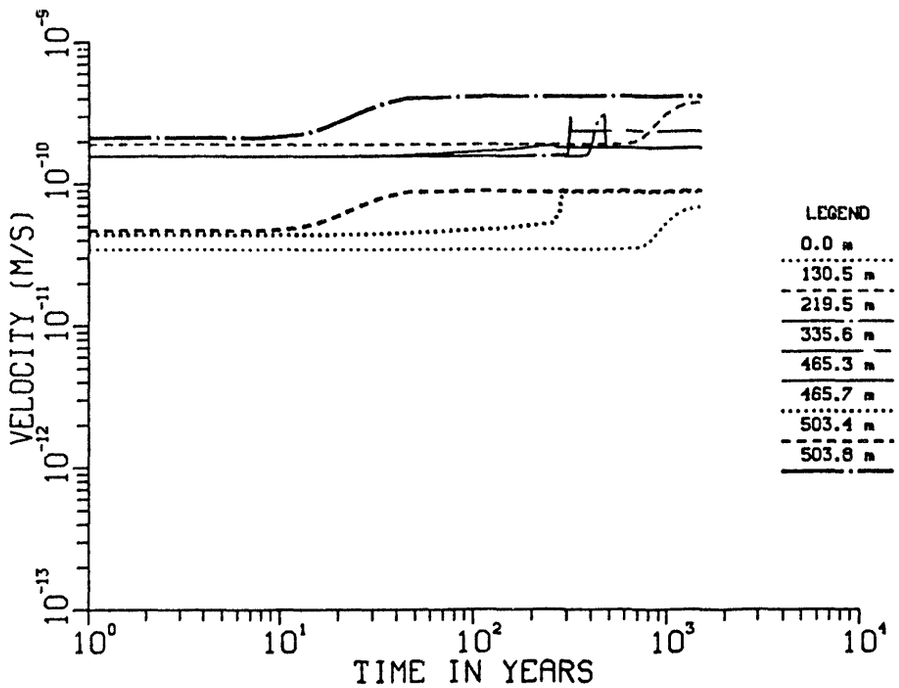

Figure 2-10-11. Average linear velocity of water in the matrix versus time at specified distances above the water table; final set of calculations; Case 10.

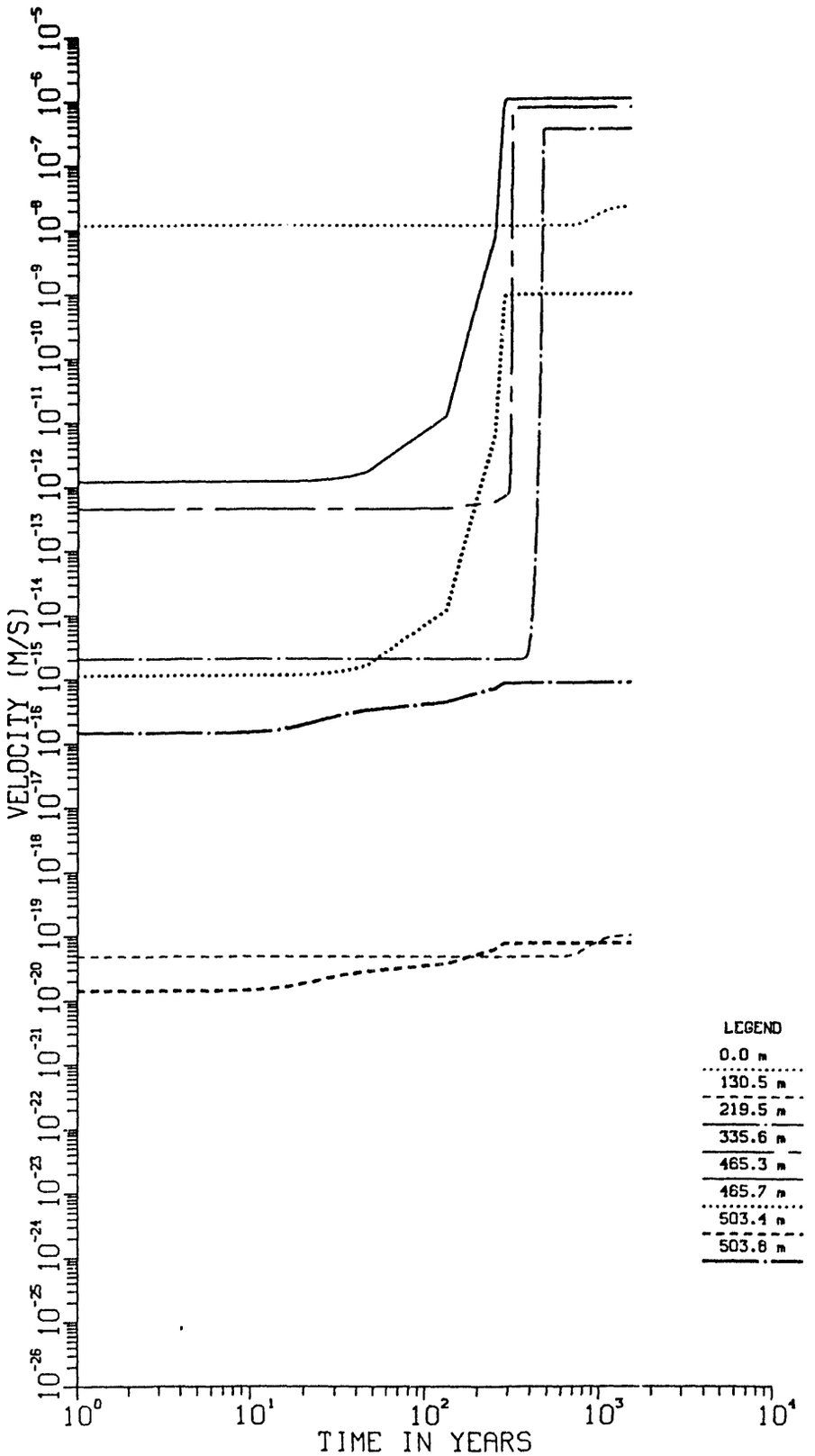

Figure 2-10-12. Average linear velocity of water in the fractures versus time at specified distances above the water table; final set of calculations; Case 10.

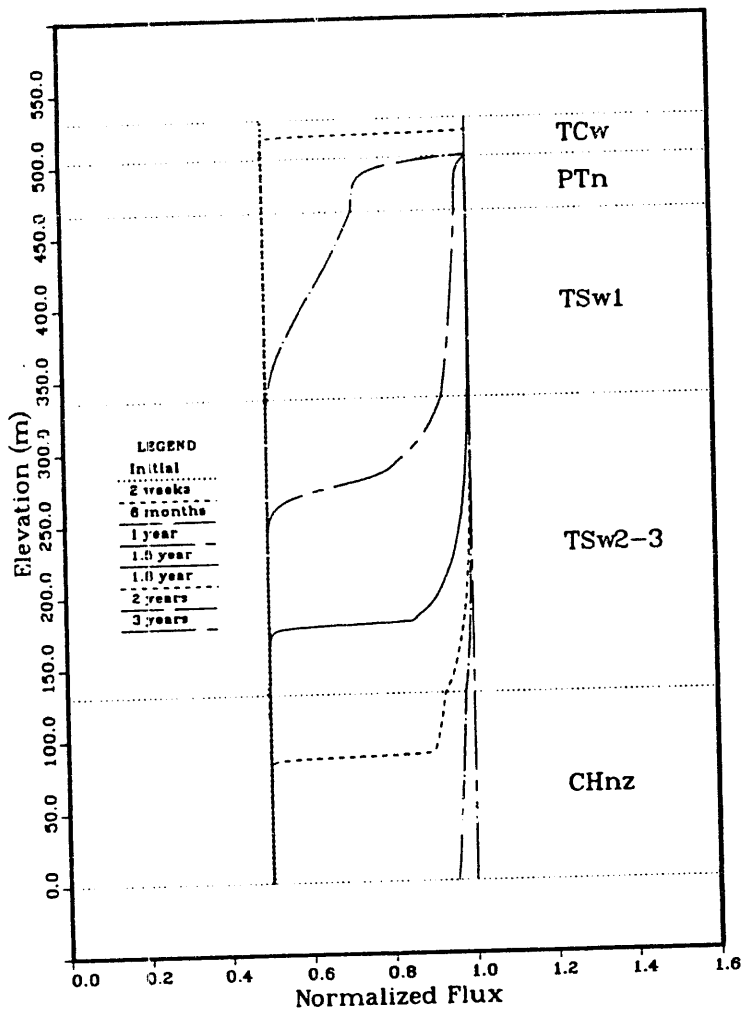

Figure 2-11-1. Normalized flux (calculated flux divided by imposed flux) versus distance above the water table at specified times; final set of calculations; Case 11.

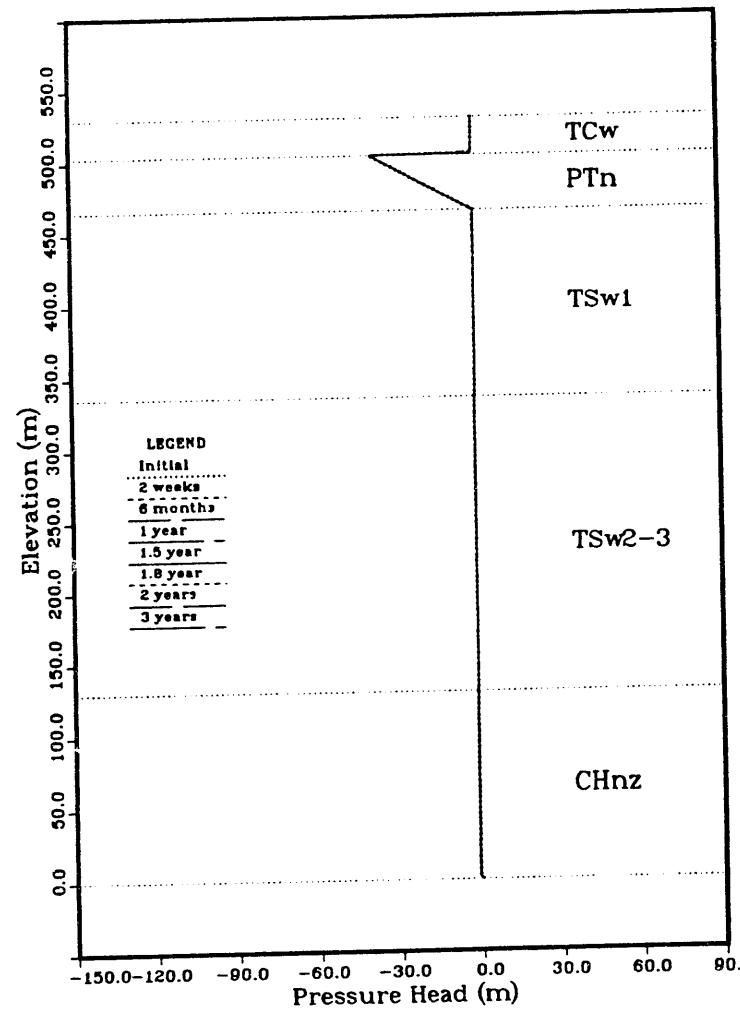

Figure 2-11-2. Pressure head versus distance above the water table at specified times; final set of calculations; Case 11.

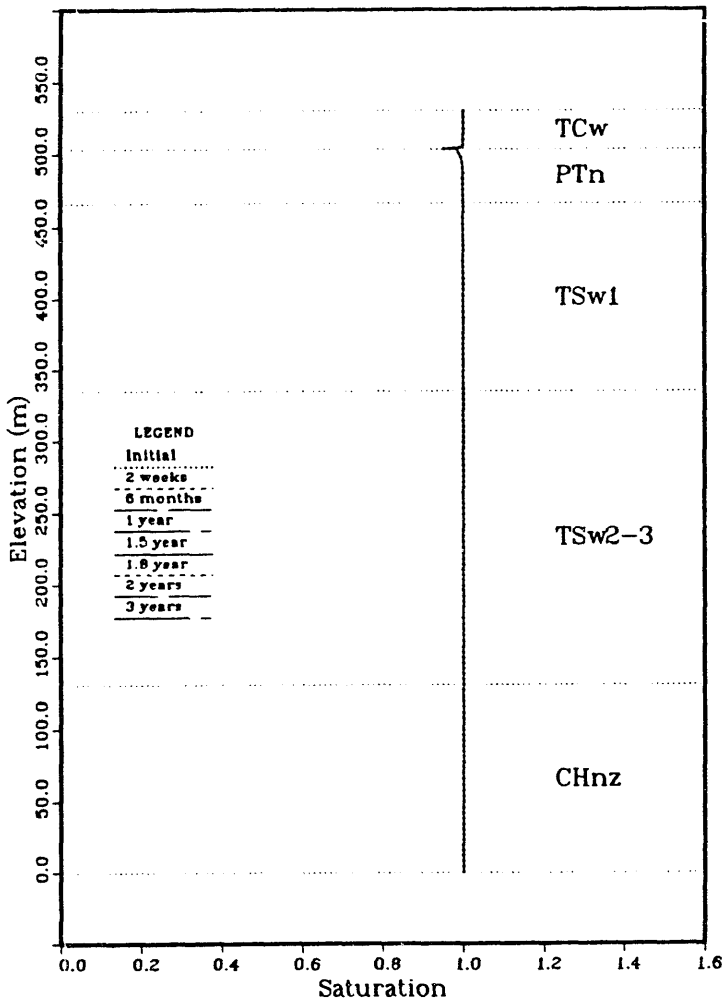

Figure 2-11-3. Matrix saturation versus distance above the water table at specified times; final set of calculations; Case 11.

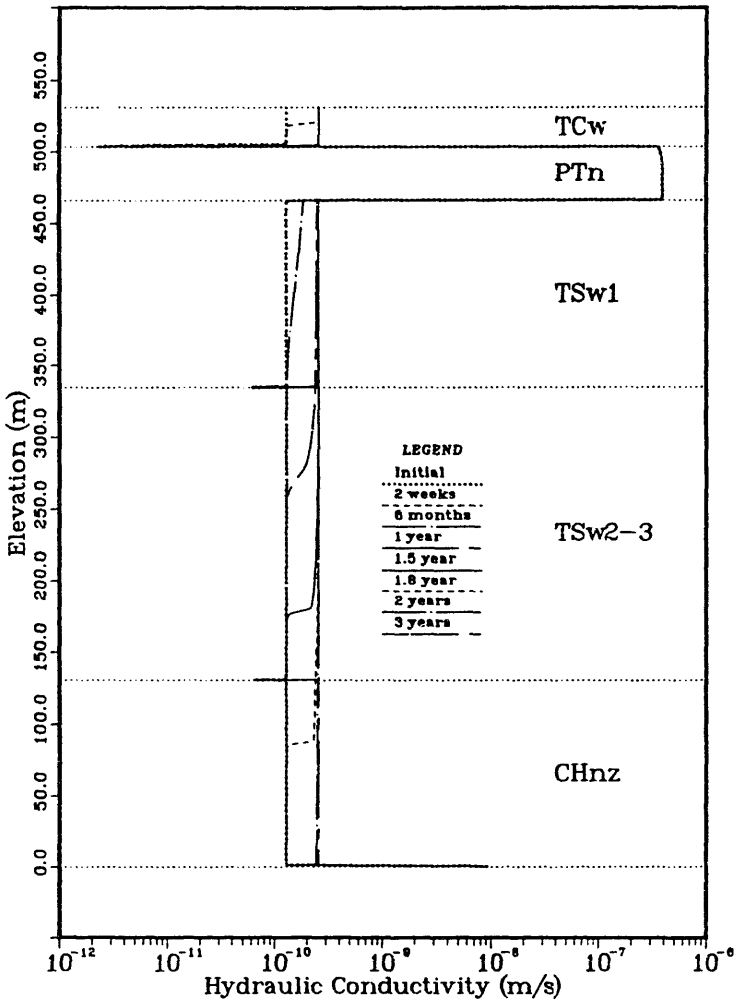

Figure 2-11-4. Hydraulic conductivity versus distance above the water table at specified times; final set of calculations; Case 11.

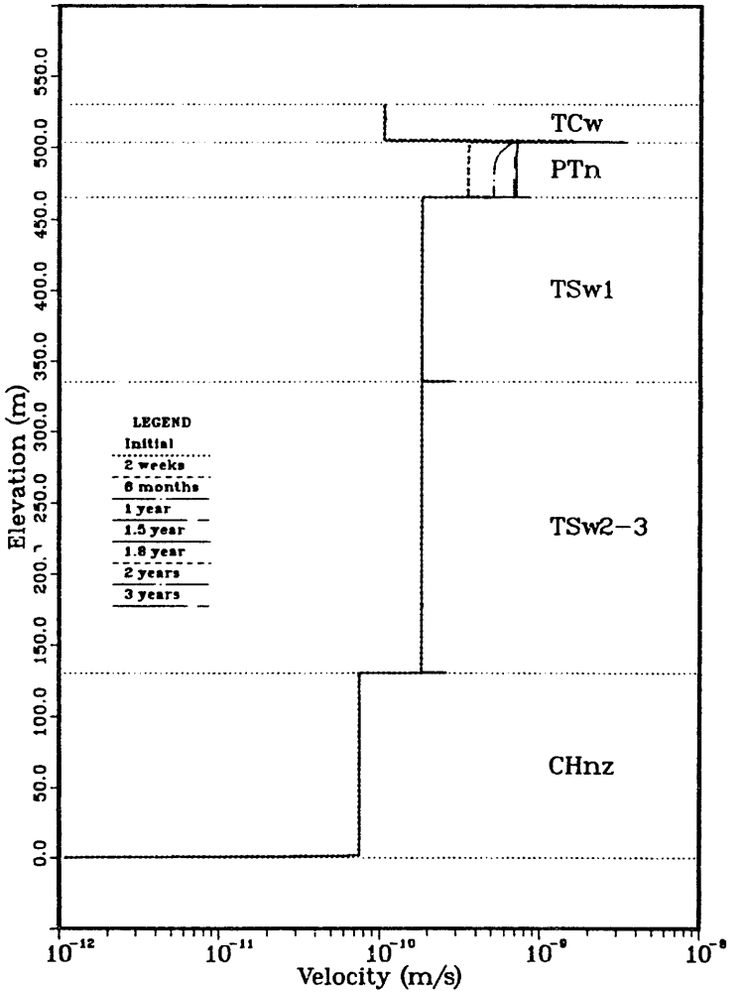

Figure 2-11-5. Average linear velocity of water in the Matrix versus distance above the water table at specified times; final set of calculations; Case 11.

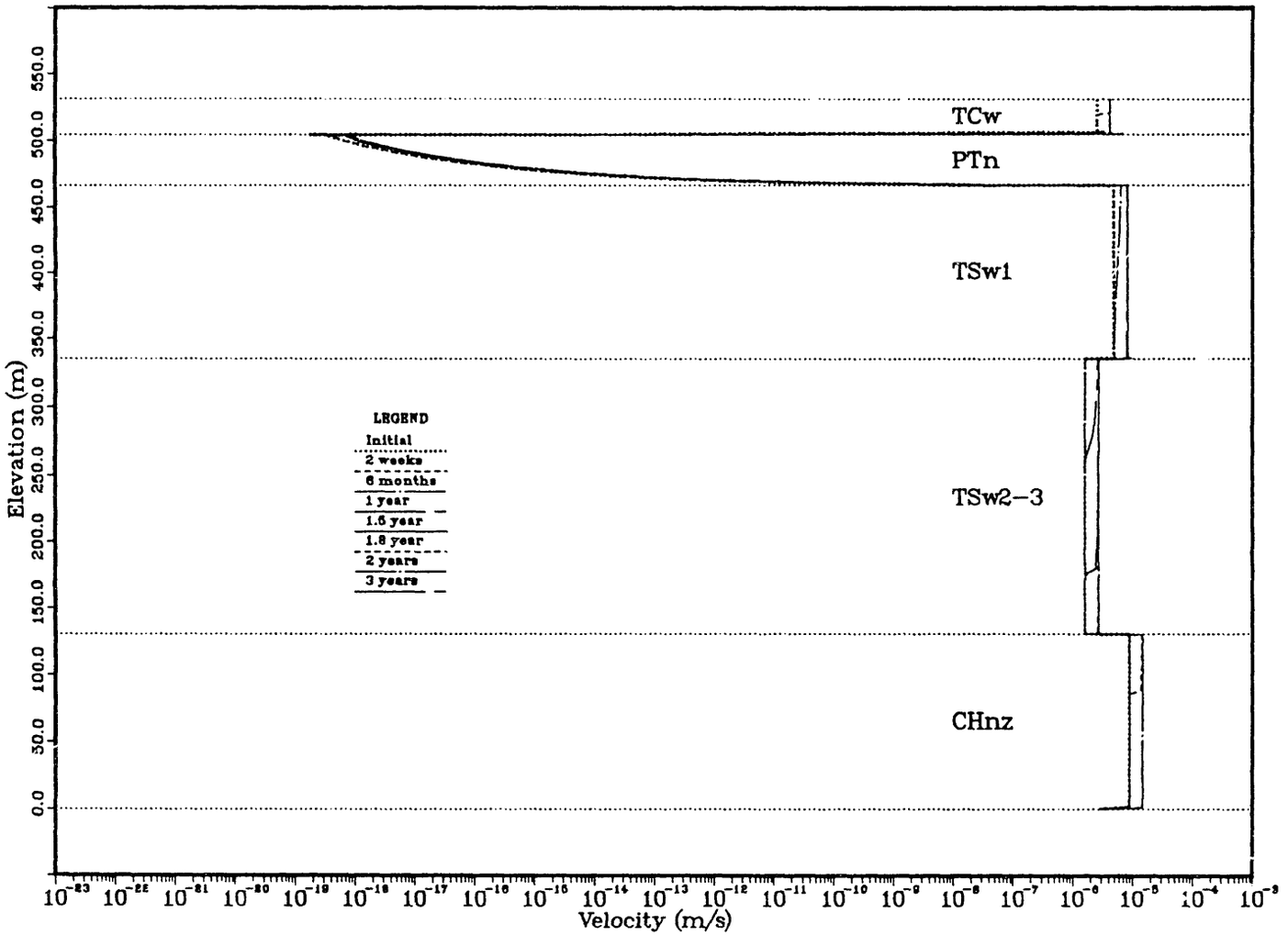

Figure 2-11-6. Average linear velocity of water in the fractures versus distance above the water table at specified times; final set of calculations; Case 11.

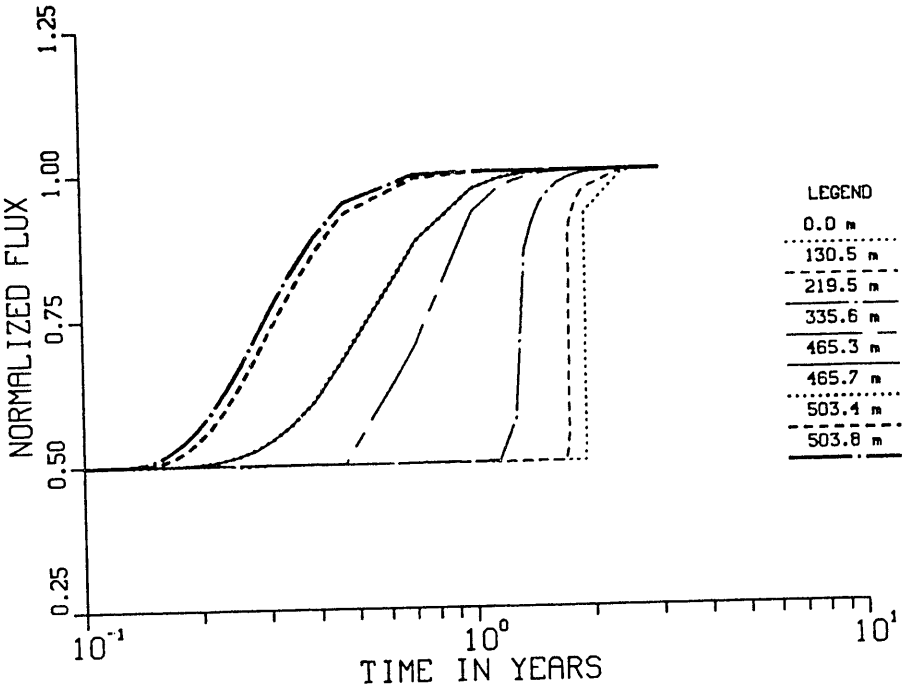

Figure 2-11-7. Normalized flux (calculated flux divided by imposed flux) versus time at specified distances above the water table; final set of calculations; Case 11.

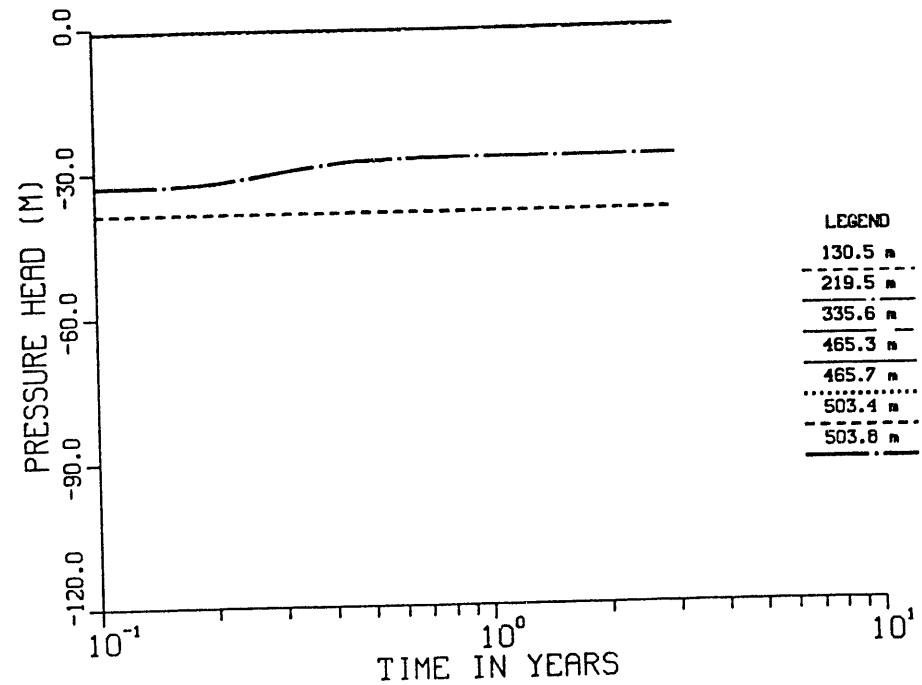

Figure 2-11-8. Pressure head versus time at specified distances above the water table; final set of calculations; Case 11.

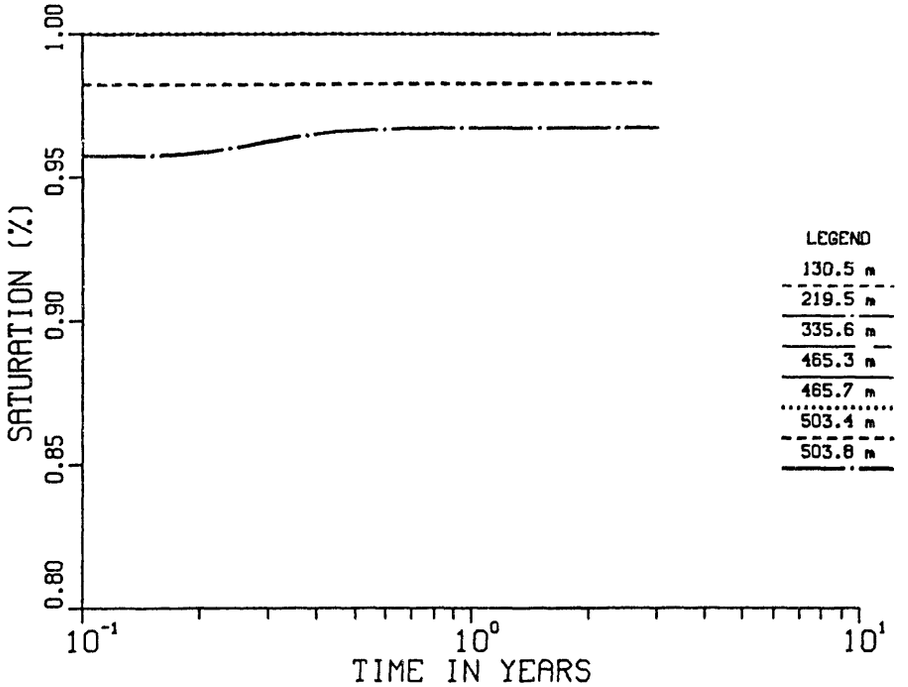

Figure 2-11-9. Matrix saturation versus time at specified distances above the water table; final set of calculations; Case 11.

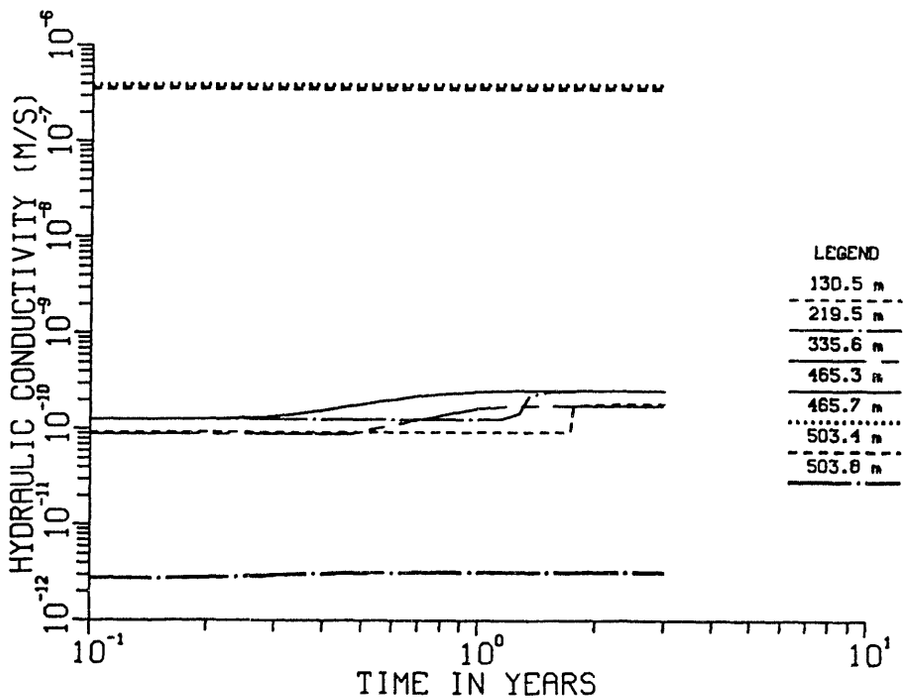

Figure 2-11-10. Hydraulic conductivity versus time at specified distances above the water table; final set of calculations; Case 11.

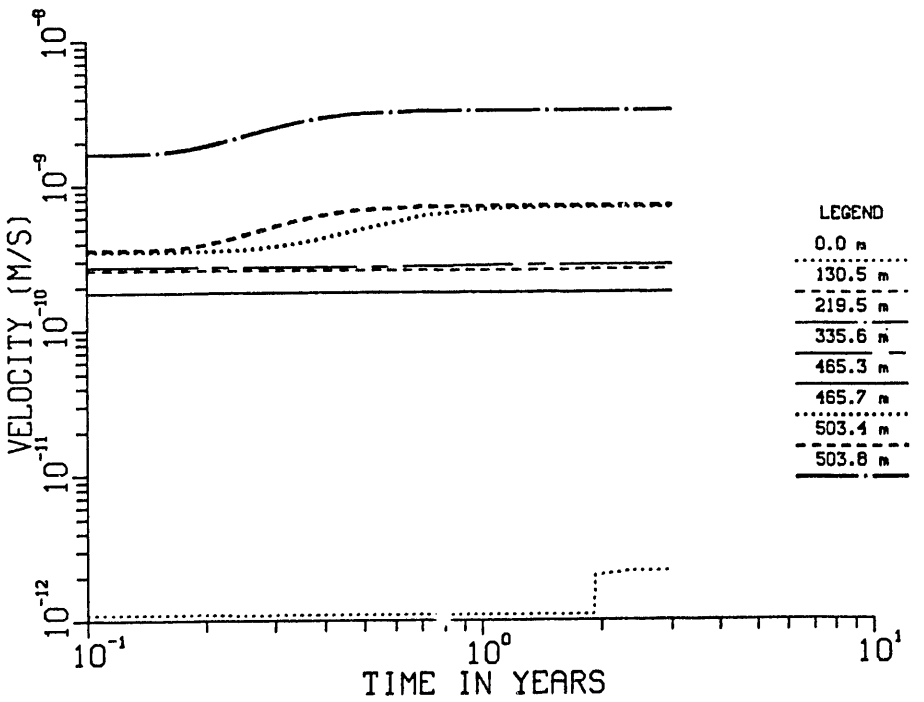

Figure 2-11-11. Average linear velocity of water in the matrix versus time at specified distances above the water table; final set of calculations; Case 11.

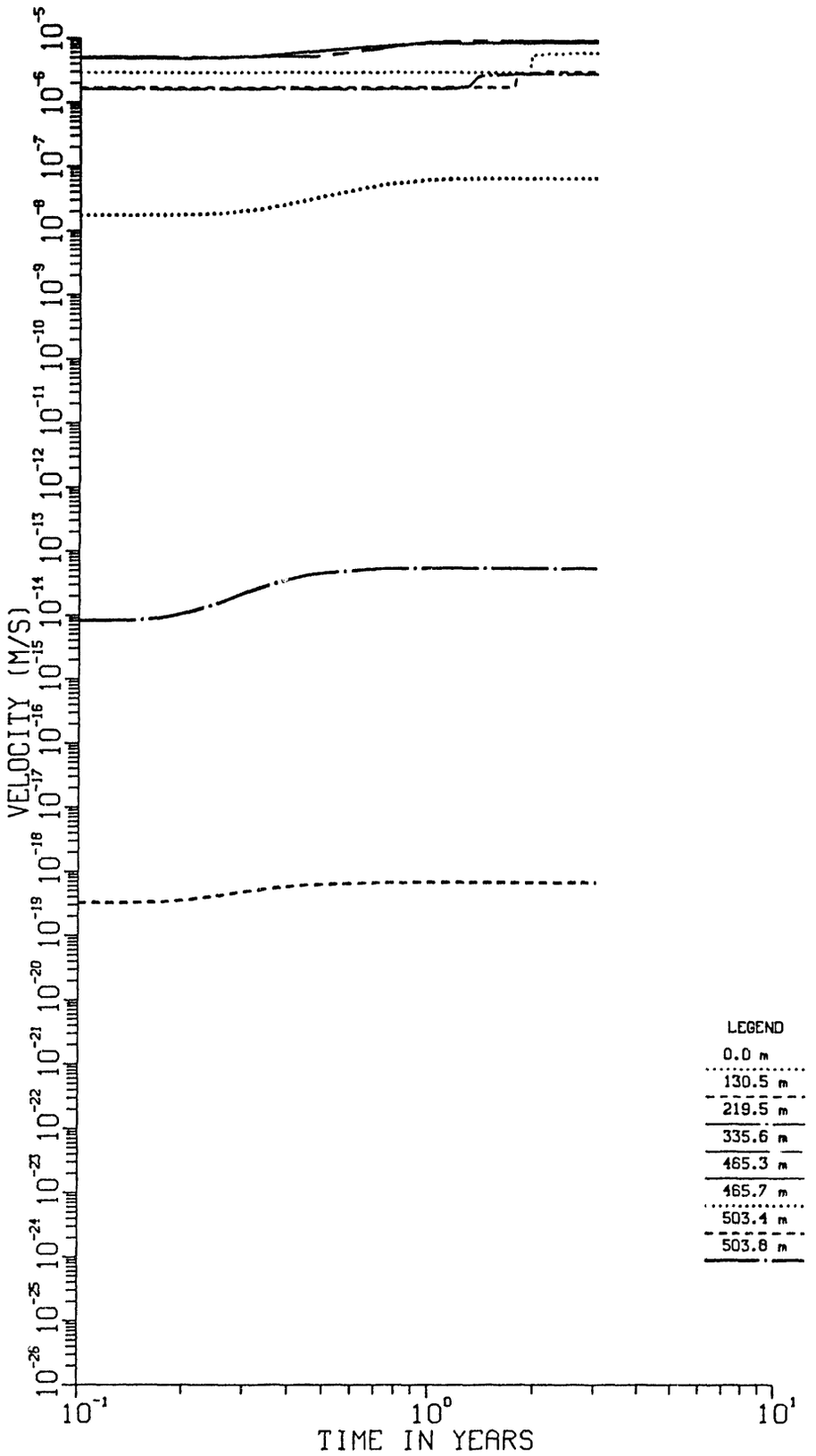

Figure 2-11-12. Average linear velocity of water in the fractures versus time at specified distances above the water table; final set of calculations; Case 11.

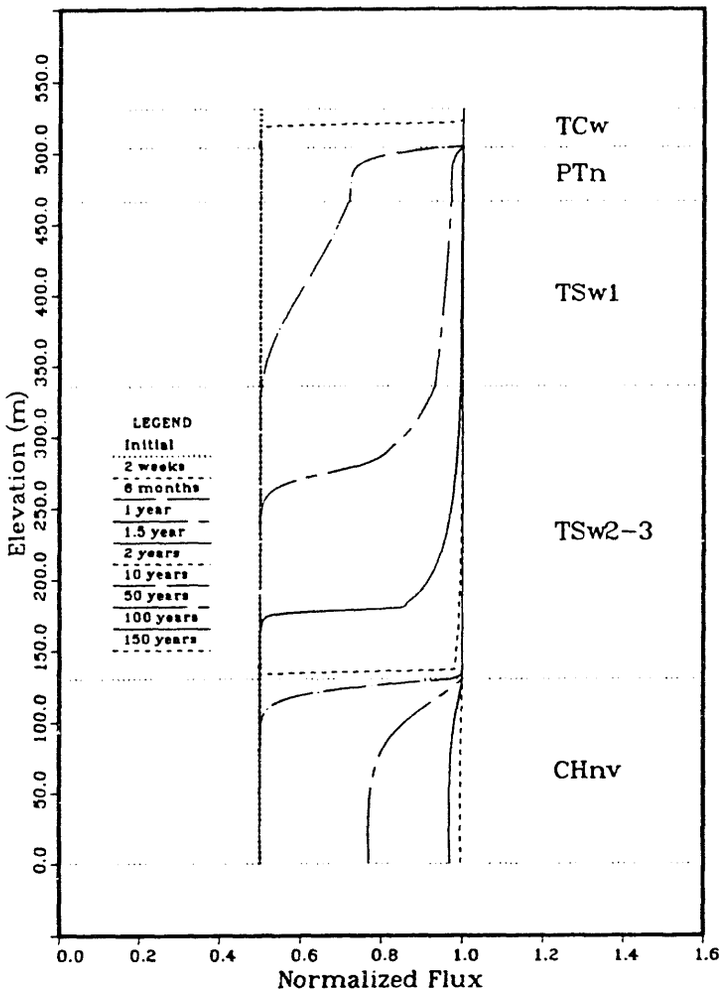

Figure 2-12-1. Normalized flux (calculated flux divided by imposed flux) versus distance above the water table at specified times; final set of calculations; Case 12.

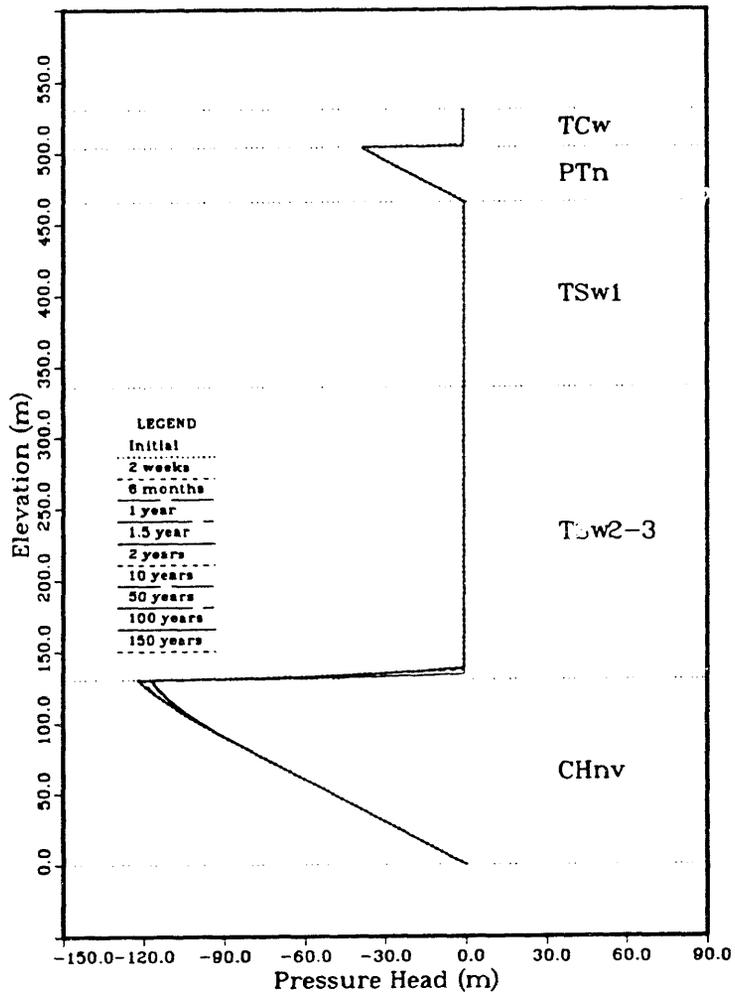

Figure 2-12-2. Pressure head versus distance above the water table at specified times; final set of calculations; Case 12.

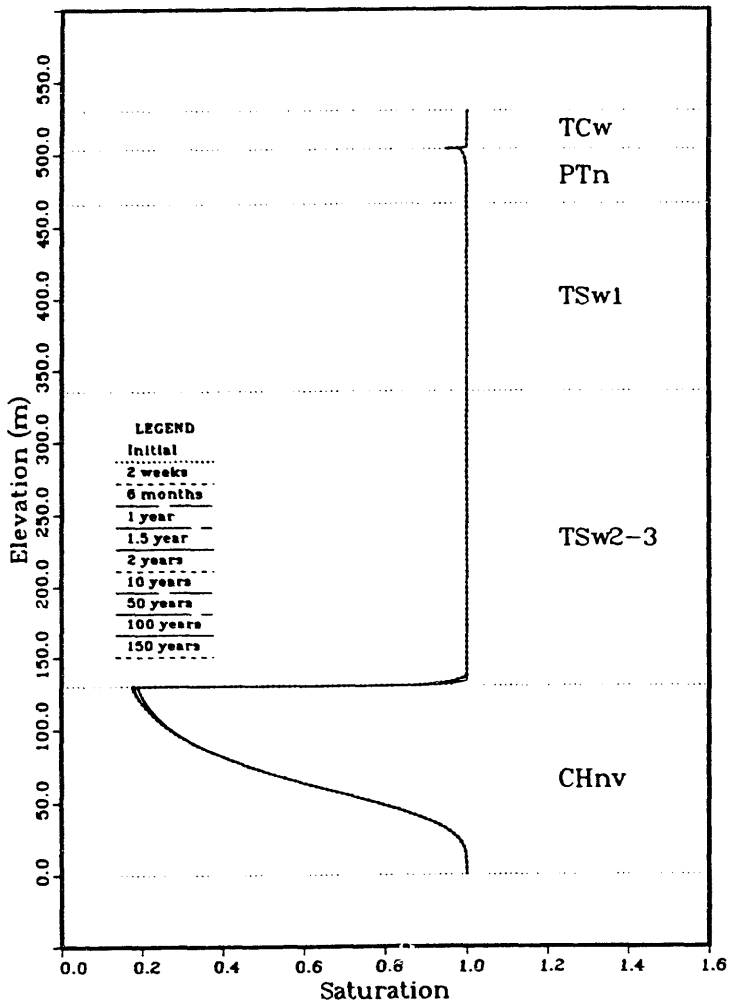

Figure 2-12-3. Matrix saturation versus distance above the water table at specified times; final set of calculations; Case 12.

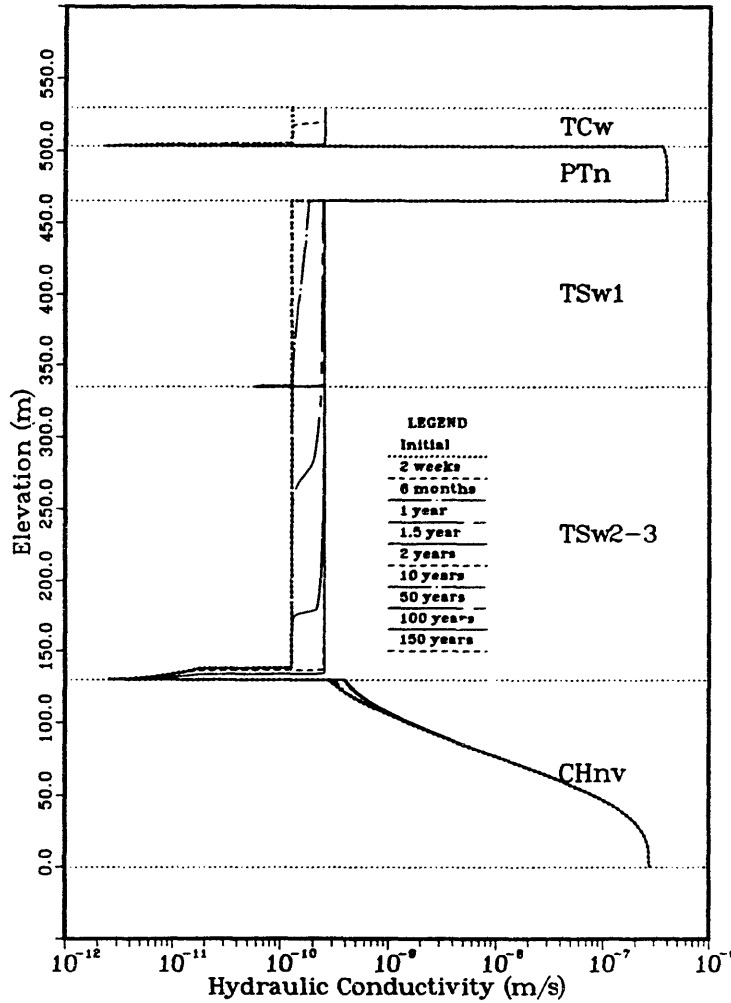

Figure 2-12-4. Hydraulic conductivity versus distance above the water table at specified times; final set of calculations; Case 12.

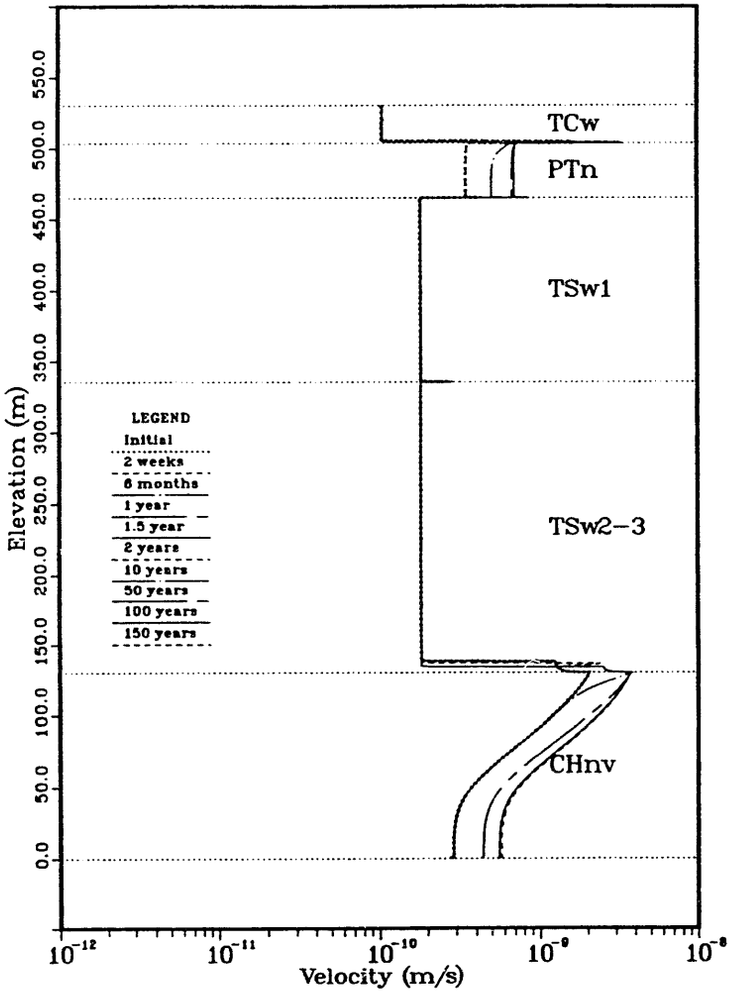

Figure 2-12-5. Average linear velocity of water in the matrix versus distance above the water table at specified times; final set of calculations; Case 12.

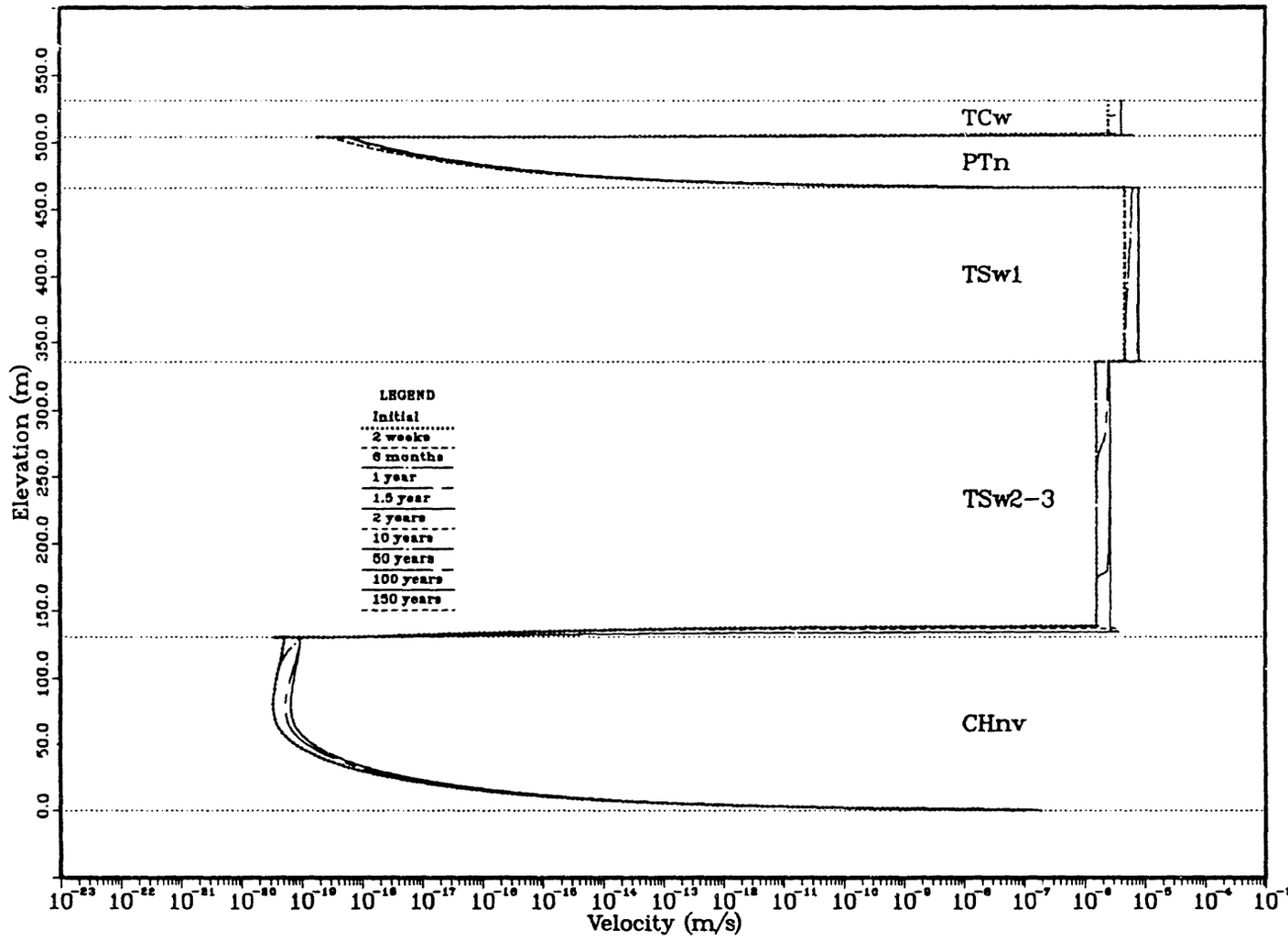

Figure 2-12-6. Average linear velocity of water in the fractures versus distance above the water table at specified times; final set of calculations; Case 12.

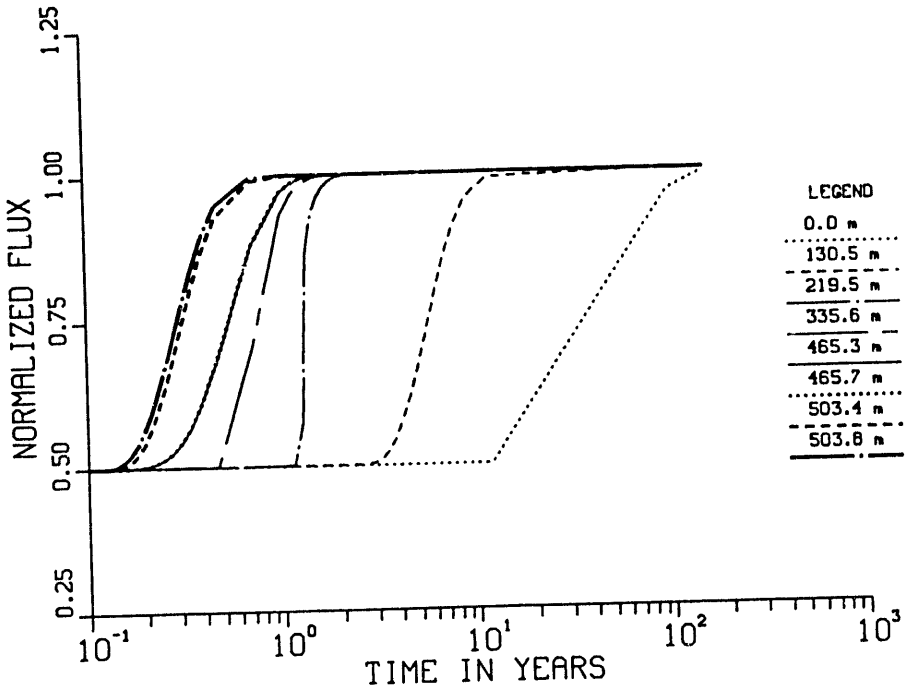

Figure 2-12-7. Normalized flux (calculated flux divided by imposed flux) versus time at specified distances above the water table; final set of calculations; Case 12.

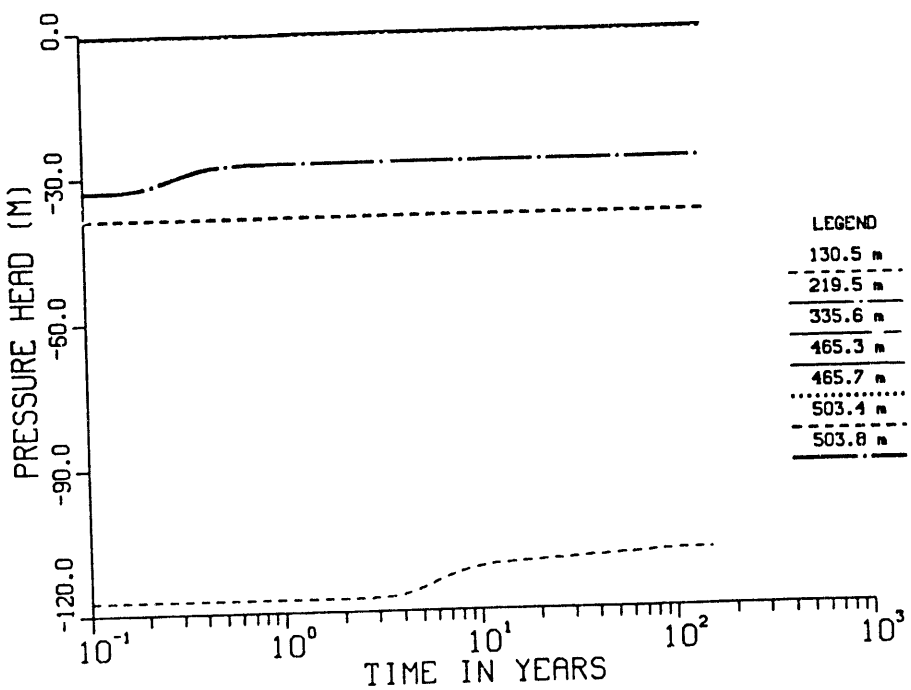

Figure 2-12-8. Pressure head versus time at specified distances above the water table; final set of calculations; Case 12.

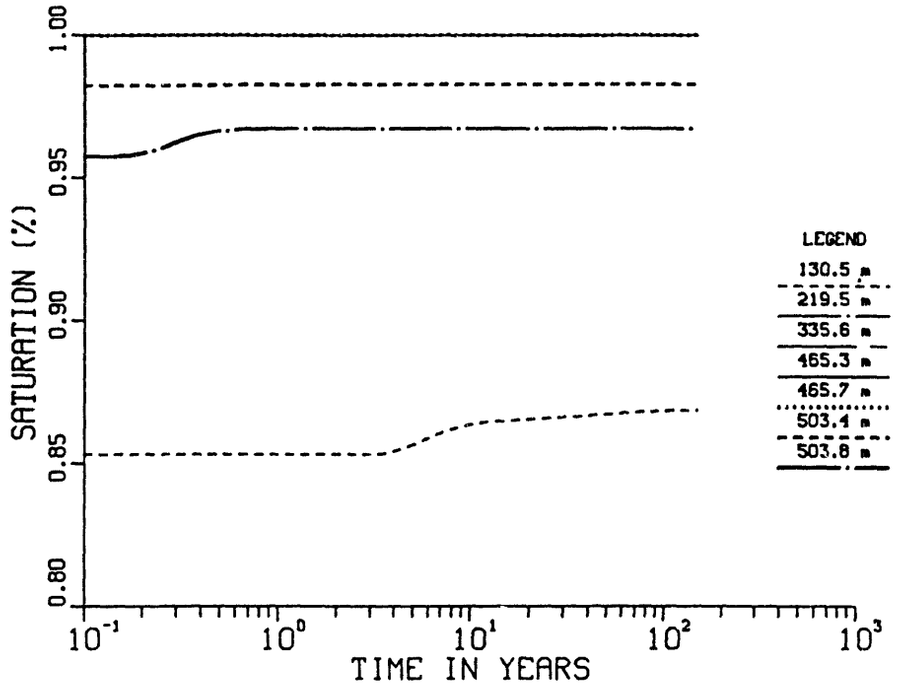

Figure 2-12-9. Matrix saturation versus time at specified distances above the water table; final set of calculations; Case 12.

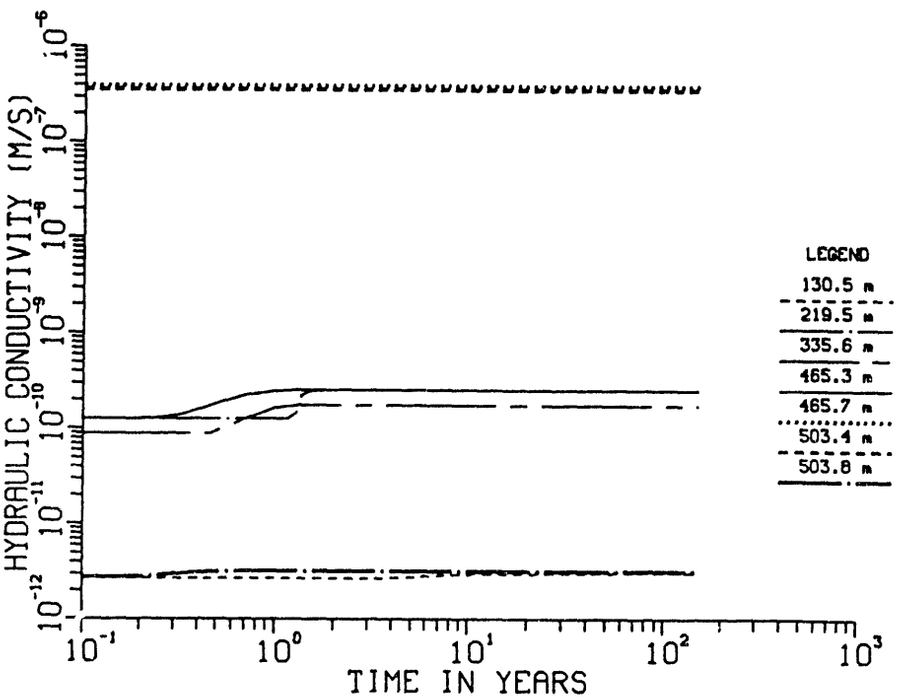

Figure 2-12-10. Hydraulic conductivity versus time at specified distances above the water table; final set of calculations; Case 12.

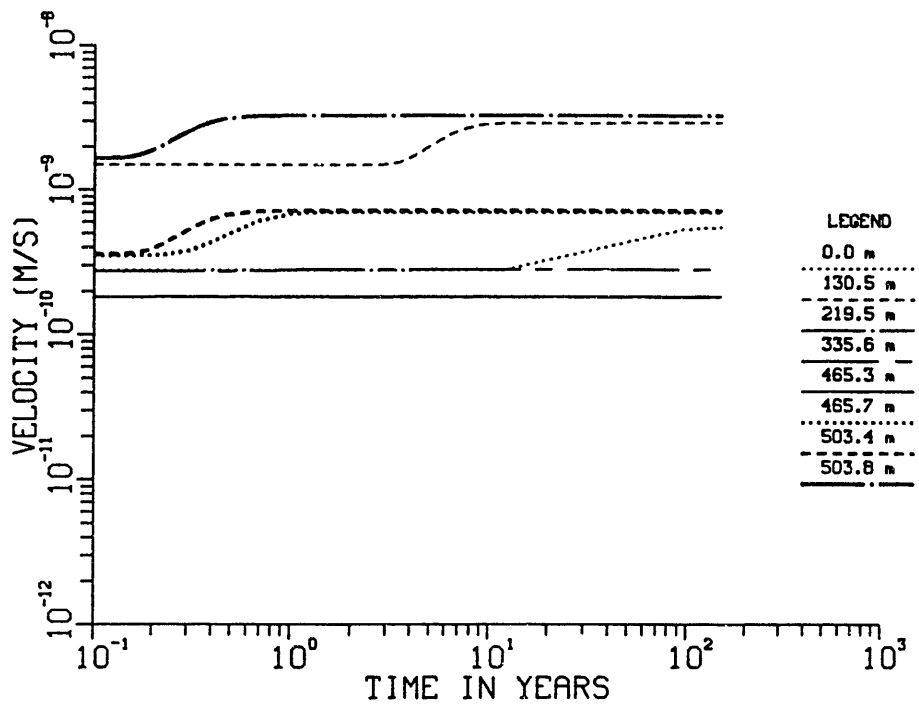

Figure 2-12-11. Average linear velocity of water in the matrix versus time at specified distances above the water table; final set of calculations; Case 12.

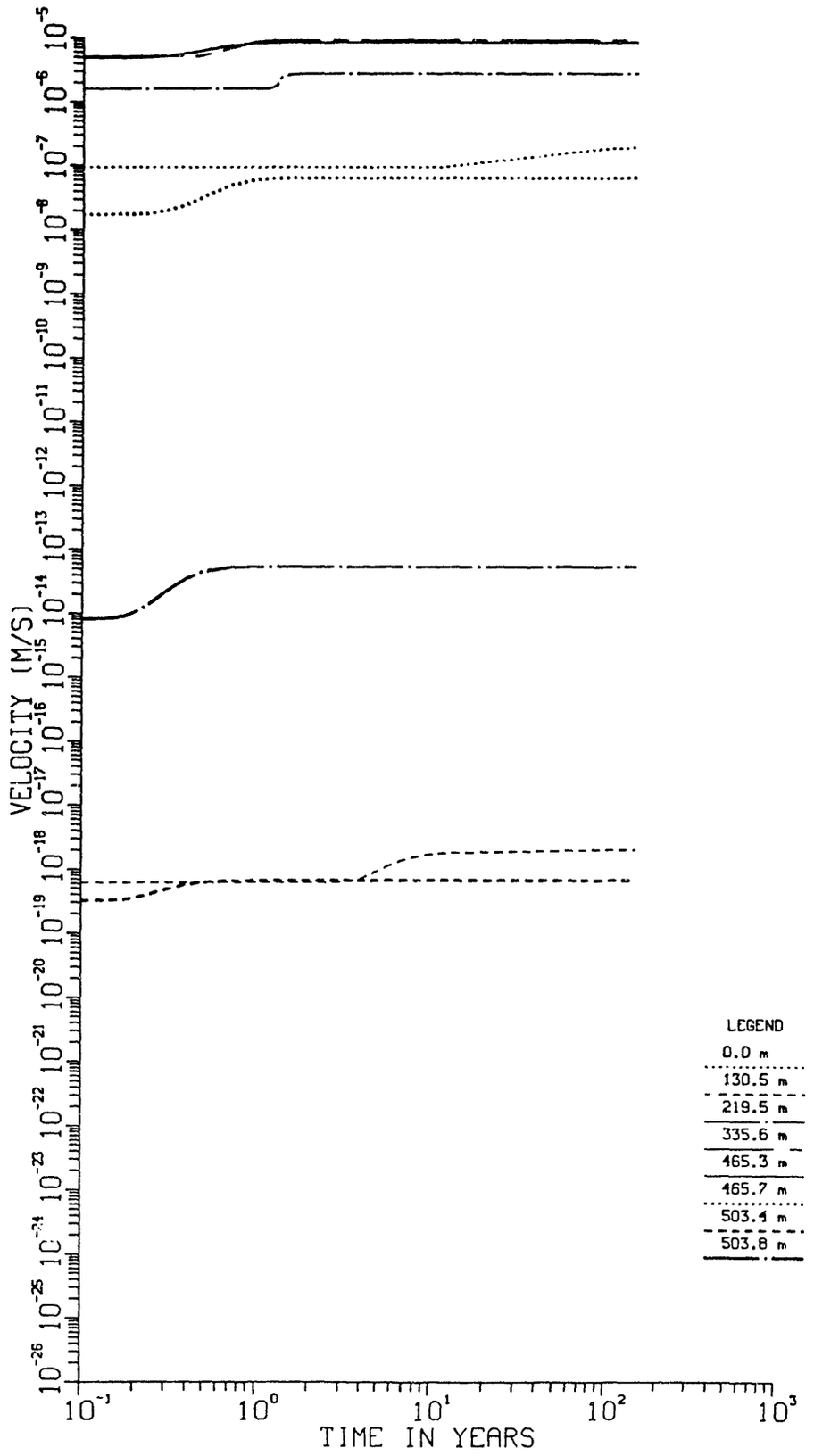

Figure 2-12-12. Average linear velocity of water in the fractures versus time at specified distances above the water table; final set of calculations; Case 12.

DISTRIBUTION LIST

1 John W. Bartlett, Director (RW-1)
Office of Civilian Radioactive Waste Management
U.S. Department of Energy
1000 Independence Avenue, S.W.
Washington, DC 20585

1 F.G. Peters, Deputy Director (RW-2)
Office of Civilian Radioactive Waste Management
U.S. Department of Energy
1000 Independence Avenue, S.W.
Washington, DC 20585

1 T.H. Isaacs (RW-4)
Office of Strategic Planning and International Programs
Office of Civilian Radioactive Waste Management
U.S. Department of Energy
1000 Independence Avenue, S.W.
Washington, DC 20585

1 J.D. Saltzman (RW-5)
Office of External Relations
Office of Civilian Radioactive Waste Management
U.S. Department of Energy
1000 Independence Avenue, S.W.
Washington, DC 20585

1 Samuel Rousso (RW-10)
Office of Program and Resources Management
Office of Civilian Radioactive Waste Management
U.S. Department of Energy
1000 Independence Avenue, S.W.
Washington, DC 20585

1 J.C. Bresee (RW-10)
Office of Civilian Radioactive Waste Management
U.S. Department of Energy
1000 Independence Avenue, S.W.
Washington, DC 20585

1 Carl P. Gertz (RW-20)
Office of Geologic Disposal
Office of Civilian Radioactive Waste Management
U.S. Department of Energy
1000 Independence Avenue, S.W.
Washington, DC 20585

1 S.J. Brocoum (RW-22)
Analysis and Verification Division
Office of Civilian Radioactive Waste Management
U.S. Department of Energy
1000 Independence Avenue, S.W.
Washington, DC 20585

1 D.E. Shelor (RW-30)
Office of Systems and Compliance
Office of Civilian Radioactive Waste Management
U.S. Department of Energy
1000 Independence Avenue, S.W.
Washington, DC 20585

1 J. Roberts (RW-33)
Office of Civilian Radioactive Waste Management
U.S. Department of Energy
1000 Independence Avenue, S.W.
Washington, DC 20585

1 G.J. Parker (RW-332)
Office of Civilian Radioactive Waste Management
U.S. Department of Energy
1000 Independence Avenue, S.W.
Washington, DC 20585

1 Associate Director (RW-40)
Office of Storage and Transportation
Office of Civilian Radioactive Waste Management
U.S. Department of Energy
1000 Independence Avenue, S.W.
Washington, DC 20585

1 Associate Director (RW-50)
Office of Contractor Business Management
Office of Civilian Radioactive Waste Management
U.S. Department of Energy
1000 Independence Avenue, S.W.
Washington, DC 20585

1 C.G. Russomanno (RW-52)
Office of Civilian Radioactive Waste Management
U.S. Department of Energy
1000 Independence Avenue, S.W.
Washington, DC 20585

1 D.U. Deere, Chairman
Nuclear Waste Technical Review Board
1100 Wilson Blvd. #910
Arlington, VA 22209-2297

1 Dr. Clarence R. Allen
Nuclear Waste Technical Review Board
1000 E. California Blvd.
Pasadena, CA 91106

1 Dr. John E. Cantlon
Nuclear Waste Technical Review Board
1795 Bramble Dr.
East Lansing, MI 48823

1 Dr. Melvin W. Carter
Nuclear Waste Technical Review Board
4621 Ellisbury Dr. NE
Atlanta, GA 30332

1 Dr. Donald Langmuir
Nuclear Waste Technical Review Board
109 So. Lookout Mountain Cr.
Golden, CO 80401

1 Dr. D. Warner North
Nuclear Waste Technical Review Board
Decision Focus, Inc.
4984 El Camino Real
Los Altos, CA 94062

1 Dr. Dennis L. Price
Nuclear Waste Technical Review Board
1011 Evergreen Way
Blacksburg, VA 24060

1 Dr. Ellis D. Verink
Nuclear Waste Technical Review Board
4401 NW 18th Place
Gainesville, FL 32605

5 Carl P. Gertz, Project Manager
Yucca Mountain Site Characterization Project Office
Nevada Operations Office
U.S. Department of Energy
P.O. Box 98608—MS 523
Las Vegas, NV 89193-8608

1 C.L. West, Director
Office of External Affairs
Nevada Operations Office
U.S. Department of Energy
P.O. Box 98518
Las Vegas, NV 89193-8518

12 Technical Information Office
Nevada Operations Office
U.S. Department of Energy
P.O. Box 98518
Las Vegas, NV 89193-8518

1 P.K. Fitzsimmons, Director
Health Physics and Environmental Division
Nevada Operations Office
U.S. Department of Energy
P.O. Box 98518
Las Vegas, NV 89193-8518

1 Repository Licensing and Quality Assurance Project Directorate
Division of Waste Management
U.S. Nuclear Regulatory Commission
Washington, DC 20555

1 Senior Project Manager for Yucca Mountain Repository Project Branch
Division of Waste Management
U.S. Nuclear Regulatory Commission
Washington, DC 20555

1 NRC Document Control Desk
Division of Waste Management
U.S. Nuclear Regulatory Commission
Washington, DC 20555

1 P.T. Prestholt
NRC Site Representative
301 E. Stewart Ave.
Las Vegas, NV 89101

1 E.P. Binnall
Field Systems Group Leader
Building 50B/4235
Lawrence Berkeley Laboratory
Berkeley, CA 94720

1 Center for Nuclear Waste Regulatory Analyses
6220 Culebra Road
Drawer 28510
San Antonio, TX 78284

3 L.J. Jardine
Technical Project Officer for YMP
Lawrence Livermore National Laboratory
Mail Stop L-204
P.O. Box 808
Livermore, CA 94550

4 R.J. Herbst
Technical Project Officer for YMP
Los Alamos National Laboratory
N-5 Mail Stop J521
P.O. Box 1663
Los Alamos, NM 87545

1 H.N. Kalia
Exploratory Shaft Test Manager
Los Alamos National Laboratory
Mail Stop 527
101 Convention Center Drive
Suite 820
Las Vegas, NV 89109

1 J.F. Divine
Assistant Director for Engineering Geology
U.S. Geological Survey
106 National Center
12201 Sunrise Valley Dr.
Reston, VA 22092

6 L.R. Hayes
Technical Project Officer for YMP
U.S. Geological Survey
Mail Stop 425
P.O. Box 25046
Denver, CO 80225

1 V.R. Schneider
Asst. Chief Hydrologist
Office of Program Coordination and Technical Support
U.S. Geological Survey
12201 Sunrise Valley Dr.
Reston, VA 22092

1 R.B. Raup, Jr.
Geological Division Coordinator
Yucca Mountain Site Characterization Project
U.S. Geological Survey
Mail Stop 913
P.O. Box 25046
Denver, CO 80225

1 D.H. Appel, Chief
Hydrologic Investigations Program
U.S. Geological Survey
Mail Stop 421
P.O. Box 25046
Denver, CO 80225

1 E.J. Helley
Branch of Western Regional Geology
U.S. Geological Survey
Mail Stop 427
345 Middlefield Road
Menlo Park, CA 94025

1 Chief
Nevada Operations Office
U.S. Geological Survey
101 Convention Center Dr.
Suite 820 — MS 509
Las Vegas, NV 89109

1 D. Zesiger
U.S. Geological Survey
101 Convention Center Dr.
Suite 820 — MS 509
Las Vegas, NV 89109

1 R.V. Watkins, Chief
Project Planning and Management
U.S. Geological Survey
P.O. Box 25046
Denver, CO 80225

1 A.L. Flint
U.S. Geological Survey
Mail Stop 721
P.O. Box 327
Mercury, NV 89023

1 D.A. Beck
U.S. Geological Survey
1600 E. Tropicana, Suite 115
Las Vegas, NV 89132

1 P.A. Glancy
U.S. Geological Survey
Federal Building, Room 224
Carson City, NV 89701

1 Sherman S.C. Wu
Branch of Astrogeology
U.S. Geological Survey
2255 N. Gemini Dr.
Flagstaff, AZ 86001

1 J.H. Sass
Branch of Tectonophysics
U.S. Geological Survey
2255 N. Gemini Dr.
Flagstaff, AZ 86001

1 DeWayne A. Campbell
Technical Project Officer for YMP
Bureau of Reclamation
Code D-3790
P.O. Box 25007
Denver, CO 80225

1 S.M. Dash
Science Applications International Corporation
14062 Denver West Parkway, Suite 255
Golden, CO 80401

1 K.W. Causseaux
NHP Reports Chief
U.S. Geological Survey
421 Federal Center
P.O. Box 25046
Denver, CO 80225

1 V.M. Glanzman
U.S. Geological Survey
913 Federal Center
P.O. Box 25046
Denver, CO 80225

1 J.H. Nelson
Technical Project Officer for YMP
Science Applications International Corporation
101 Convention Center Dr.
Suite 407
Las Vegas, NV 89109

2 SAIC-T&MSS Library
Science Applications International Corporation
101 Convention Center Drive
Suite 407
Las Vegas, NV 89109

1 Elaine Ezra
YMP GIS Project Manager
EG&G Energy Measurements, Inc.
Mail Stop D-12
P.O. Box 1912
Las Vegas, NV 89125

1 R.E. Jackson, Program Manager
Roy F. Weston, Inc.
955 L'Enfant Plaza SW
Washington, DC 20024

1 Technical Information Center
Roy F. Weston, Inc.
955 L'Enfant Plaza SW
Washington, DC 20024

1 D. Hedges, Vice President
Quality Assurance
Roy F. Weston, Inc.
4425 Spring Mountain Rd., Suite 300
Las Vegas, NV 89102

1 D.L. Fraser, General Manager
Reynolds Electrical & Engineering Co.
Mail Stop 555
P.O. Box 98521
Las Vegas, NV 89193-8521

1 R.F. Pritchett
Technical Project Officer for YMP
Reynolds Electrical & Engineering Co.
Mail Stop 408
P.O. Box 98521
Las Vegas, NV 89193-8521

1 B.W. Colston
General Manager and President
Las Vegas Branch
Raytheon Services Nevada
Mail Stop 416
P.O. Box 95487
Las Vegas, NV 89193-5487

1 R.L. Bullock
Technical Project Officer for YMP
Raytheon Services Nevada
Suite P250, Mail Stop 403
101 Convention Center Dr.
Las Vegas, NV 89109

1 R.E. Lowder
Technical Project Officer for YMP
MAC Technical Services
101 Convention Center Dr.
Suite 1100
Las Vegas, NV 89109

1 C.K. Hastings, Manage
PASS Program
Pacific Northwest Laboratories
P.O. Box 999
Richland, WA 99352

1 A.T. Tamura
Science and Technology Division
Office of Scientific and Technical Information
U.S. Department of Energy
P.O. Box 62
Oak Ridge, TN 37831

1 Carlos G. Bell, Jr.
Professor of Civil Engineering
Civil and Mechanical Engineering Department
University of Nevada, Las Vegas
4505 South Maryland Parkway
Las Vegas, NV 89154

1 C.F. Costa, Director
Nuclear Radiation Assessment Division
U.S. Environmental Protection Agency
Environmental Monitoring Systems Laboratory
P.O. Box 93478
Las Vegas, NV 89193-3478

1 ONWI Library
Battelle Columbus Laboratory
Office of Nuclear Waste Isolation
505 King Avenue
Columbus, OH 43201

1 T. Hay, Executive Assistant
Office of the Governor
State of Nevada
Capitol Complex
Carson City, NV 89710

3 R.R. Loux, Jr.
Executive Director
Nuclear Waste Project Office
State of Nevada
Evergreen Center, Suite 252
1802 North Carson Street
Carson City, NV 89701

1 C.H. Johnson
Technical Program Manager
Nuclear Waste Project Office
State of Nevada
Evergreen Center, Suite 252
1802 North Carson Street
Carson City, NV 89701

1 John Fordham
Water Resources Center
Desert Research Institute
P.O. Box 60220
Reno, NV 89506

1 Dr. Martin Mifflin
Water Resources Center
Desert Research Institute
2505 Chandler Avenue
Suite 1
Las Vegas, NV 89120

1 Eric Anderson
Mountain West Research-Southwest, Inc.
2901 N. Central Ave. #1000
Phoenix, AZ 85012-2730

1 Department of Comprehensive Planning
Clark County
225 Bridger Avenue, 7th Floor
Las Vegas, NV 89155

1 Planning Department
Nye County
P.O. Box 153
Tonopah, NV 89049

1 Lincoln County Commission
Lincoln County
P.O. Box 90
Pioche, NV 89043

5 Judy Foremaster
City of Caliente
P.O. Box 158
Caliente, NV 89008

1 Economic Development Department
City of Las Vegas
400 East Stewart Avenue
Las Vegas, NV 89101

1 Community Planning and Development
City of North Las Vegas
P.O. Box 4086
North Las Vegas, NV 89030

1 Director of Community Planning
City of Boulder City
P.O. Box 367
Boulder City, NV 89005

1 Commission of the European Communities
200 Rue de la Loi
B-1049 Brussels
BELGIUM

2 M.J. Dorsey, Librarian
YMP Research and Study Center
Reynolds Electrical & Engineering Co., Inc.
Mail Stop 407
P.O. Box 98521
Las Vegas, NV 89193-8521

1 Amy Anderson
Argonne National Laboratory
Building 362
9700 So. Cass Ave.
Argonne, IL 60439

1 Robert W. Prindle
Deuel and Associates, Inc.
7208 Jefferson NE
Albuquerque, NM 87109

1 K. Birdsell
Los Alamos National Laboratory
Mail Stop F665
P.O. Box 1663
Los Alamos, NM 87545

1 T.N. Narasimhan
Earth Sciences Division
Lawrence Berkeley Laboratory
University of California
Berkeley, CA 94720

The number in the lower right-hand corner is an accession number used for Office of Civilian Radioactive Waste Management purposes only. It should not be used when ordering this publication.

END

DATE FILMED

12/30/91